Charles University in Prague

Faculty of Mathematics and Physics

DOCTORAL THESIS

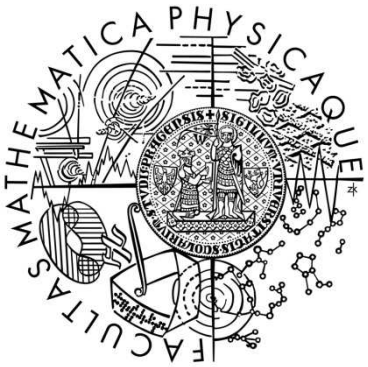

Naďa Tesařová

Investigation of magnetization dynamics in GaMnAs by ultrafast laser spectroscopy

Department of Chemical Physics and Optics

Supervisor of the doctoral thesis: Doc. RNDr. Petr Němec, Ph.D.

Study programme: Physics
Specialization: Quantum Optics and Optoelectronics

Prague 2012

ACKNOWLEGEMENT

This thesis could not be finished without the great help and support of all the people that I have been collaborating with during my doctoral studies. Here I would like to thank to those who influenced and helped me the most.

My biggest gratitude belongs to my supervisor Petr Němec, who I had the chance to be lead, supported and inspired by. I am very thankful for his invaluable help with the experimental work and his patient discussions and fitting remarks to all my achieved results. I would also like to thank all my colleagues and especially Eva Schmoranzeroá, who I had the pleasure to closely collaborate with. My thanks also belong to František Trojánek, for his software support and prompt help in the laboratory and to Petr Malý for his beneficial remarks.

I highly acknowledge the excellent collaboration with colleagues from the Academy of Sciences – Vít Novák and Kamil Olejník for providing us with high-quality samples, Karel Výborný, Tomáš Jungwirth and Jairo Sinova for their inevitable theoretical support.

I am very grateful to Dr. John Černe who gave me the opportunity to realize part of my doctoral studies at University at Buffalo and guided me through the experimental work in infrared spectroscopy. My thanks also belong to my fellow colleagues Chase T. Ellis and Gigi Acbas.

I declare that I carried out this doctoral thesis independently, and only with the cited sources, literature and other professional sources.

I understand that my work relates to the rights and obligations under the Act No. 121/2000 Coll., the Copyright Act, as amended, in particular the fact that the Charles University in Prague has the right to conclude a license agreement on the use of this work as a school work pursuant to Section 60 paragraph 1 of the Copyright Act.

In Prague 12.12.2012

Naďa Tesařová

Název práce: ***Studium dynamiky magnetizace v GaMnAs pomocí ultrarychlé laserové spektroskopie***

Autor: ***Naďa Tesařová***

Katedra / Ústav: Katedra chemické fyziky a optiky

Vedoucí doktorské práce: Doc. RNDr. Petr Němec, Ph.D., Katedra chemické fyziky a optiky

Abstrakt: Tato doktorská práce se zabývá studiem dynamik magnetizace ve feromagnetickém polovodiči (Ga,Mn)As pomocí metod magneto-optické (MO) spektroskopie. Charakter dynamik magnetizace po dopadu laserového pulzu byl zkoumán za různých experimentálních podmínek na široké sadě optimalizovaných vzorků (Ga,Mn)As obsahujících koncentraci Mn atomů v rozmezí od 1,5% do 14%. Díky důkladné analýze měřených MO signálů se nám podařilo vyvinout novou metodu, která umožňuje určit laserovým pulsem vyvolanou trajektorii magnetizace v reálném prostoru bez nutnosti jakéhokoliv numerického modelování. Studium naměřených MO signálů nám také umožnilo určit základní mikromagnetické vlastnosti (Ga,Mn)As, jakými jsou například magnetická anizotropie, Gilbertův faktor tlumení, nebo tzv. spin stiffness. Dále jsme zjistili, že světlem vyvolaná precese magnetizace může mít tři různé příčiny - zahřátí vzorku vlivem přenosu energie z laserových pulzů, přenos úhlového momentu hybnosti z kruhově polarizovaných fotonů a působení nerovnovážné spinové polarizace děr vyvolané relativistickou spin-orbitální interakcí. Zatímco první z těchto mechanizmů je dobře znám, ty dva zbývající mechanismy, které odpovídají optické analogii „spin trasfer torque“ a „spin-orbit torque“, zatím nebyly v literatuře popsány.

Klíčová slova: magnetický polovodič (Ga,Mn)As, dynamika magnetizace, ultrarychlá laserová spektroskopie, magneto-optika

Title: ***Investigation of magnetization dynamics in GaMnAs by ultrafast laser spectroscopy***

Author: ***Naďa Tesařová***

Department / Institute: Department of Chemical Physics and Optics

Supervisor of the doctoral thesis: Doc. RNDr. Petr Němec, Ph.D., Department of Chemical Physics and Optics

Abstract: This doctoral thesis is dedicated to the study of magnetization dynamics in ferromagnetic semiconductor (Ga,Mn)As using magneto-optical (MO) spectroscopy methods. The character of the magnetization dynamics after the impact of the laser pulse was investigated under different experimental conditions in an extensive set of optimized (Ga,Mn)As samples with Mn doping ranging from 1.5% to 14%. The thorough analysis of the measured MO signal enabled us to develop a new method that can be used to determine the laser pulse-induced real-space magnetization trajectory without any numerical modelling. Moreover, the investigation of the measured MO signals allowed us to determine the basic micromagnetic properties of (Ga,Mn)As, such as the magnetic anisotropy, the Gilbert damping or the spin stiffness. In addition to this, we found out that the light-induced magnetization precession can be caused by three distinct mechanisms - the sample heating due to the energy transfer from the laser pulses, the angular momentum transfer from the circularly polarized photons, and the influence of the non-equilibrium hole polarization induced by the relativistic spin-orbit interaction. The first of these mechanisms is rather well known but the two remaining ones, which are the optical analogues of the spin-transfer torque and the spin-orbit torque, were not reported in the literature so far.

Key words: magnetic semiconductor (Ga,Mn)As, magnetization dynamics, ultrafast laser spectroscopy, magneto-optics

PREFACE

Over the past few years, there has been a considerable interest and progress in investigation and understanding of the spin-related phenomena. The majority of the research was focused on the spin states and dynamics in magnetic metals and it led to a development of devices with improved or completely new functionalities, which are typically based on the giant magnetoresistance (GMR) or similar effects. These effects are used in devices such as hard disc read heads, non-volatile memory chips or in magnetometers. However, the discovery of the magnetic order in semiconductors has opened a new perspective for the spin-based electronics (spintronics). For example, the incorporation of Mn ions into the conventional GaAs semiconductor showed unprecedented features of magnetism in (Ga,Mn)As, where the Mn atoms act as localized magnetic moments on one hand, and introduce free holes into the system on the other hand. The high concentrations of holes give rise to a strong, so called carrier-mediated, ferromagnetic order between the Mn spins, enabling the direct control of magnetism by external means (optically, by electrical field, etc.). A part of (Ga,Mn)As research is also devoted to fast manipulation of the magnetic order by ultrashort laser pulses as it is a challenging topic with potential impact on the time scale of information manipulation and processing.

This thesis is dedicated to the study of magnetization dynamics after the impact of the ultrashort (femtosecond) laser pulse on (Ga,Mn)As by means of the time-resolved magneto-optical (MO) spectroscopy. The analysis of the MO signals enabled investigation of the basic micromagnetic material properties, such as the magnetic anisotropy, Gilbert damping parameter, or the spin stiffness. Moreover, the MO spectroscopy served us as a very useful tool for revealing some of the predicted, yet experimentally unobserved physical phenomena. The time-integrated MO spectroscopy was utilized in order to investigate the electronic structure, thus the origin of the magnetic interactions in (Ga,Mn)As. This thesis can be considered as experimental but it is also supplemented with some simple calculations that were beneficial for the interpretation of the experimental results. The overwhelming part of the experiments was performed in the laser laboratory of the Department of Quantum Optics and Optoelectronics at Charles University in Prague and the smaller part in the Department of Physics at University at Buffalo.

I have taken advantage of the possibility to write my thesis in the form of commented set of published or submitted articles. I have chosen this form because the output of my work during the past four years is very clearly and systematically documented in the already written articles, which give the reader a comprehensive insight on my work. Hence, the thesis is divided into two parts – the first part gives a general overview of the theoretical and experimental findings in the magneto-optical research of (Ga,Mn)As. The main emphasis is put on the description of the laser-induced magnetization dynamics, its origin and its significance in characterizing the basic micromagnetic properties of (Ga,Mn)As. This overview was written with respect to the results presented in the second part, given by a set of articles in the Appendices 1 – 8.

Contents

1. Introduction

The current electronics based on the carrier charge transport for information storage and processing is reaching its limits due to the ongoing miniaturization of transistors. According to the Moore's law, the progress of complementary metal-oxide-semiconductor (CMOS) technology has increased rapidly, i.e. the number of transistor that can be integrated on one chip has been doubled every two years. With the advanced laser photolithography the gate size has shrank to 20 nm and the transistor density has already reached over ~ 10^6/mm^2 with the switching speeds up to 10 GHz [1]. The future semiconductor logic device with the suggested 10 nm gate width will, however, face the essential energy problems, since the projected gate-switching energy (the energy needed to switch between two logical states "0" and "1") in 2020 for low-standby-power and fast CMOS transistors is three orders of magnitude larger than the theoretical minimum [1, 2]. Thus the CMOS technology is approaching its "dead end" not only because of the unsatisfying energy management but also for the physical limitations on the transistor gates. In order to fulfill the increasing demands on more powerful technologies, we need to create a new class of energy saving (non-volatile) and high speed switching (THz) devices that would exploit new physical approaches. Spintronics provides a possibility of utilizing the carrier spin, as an addition or alternative to its charge, for the information transport and storage which could not only improve the performance but also add new functionalities to the existing devices [1, 3]. The electrical and spin properties are, however, characterized by different properties. The electrical properties are given by carrier mobility, electrical conductivity or electrical current whereas the spin properties are described by magnetization, magnetic resonant frequencies and spin relaxation rates. The tools that control the electron charge and spin are also different – while the electronic devices are manipulated by the applied voltages, the spin state is predominantly controlled by magnetic fields. This diversity drives the need for a search of new materials in which both approaches could be merged. Current spintronics is based mainly on ferromagnetic (FM) metals, exploited for example in commercially successful spin valves which are used in hard disc read heads or magnetic random memories (MRAM). Spin valves are based on the giant/tunneling magnetoresistance principles, where the resistance magnitude is changes by the applied magnetic field. The possibility of changing the physical properties by electrical field is a feature of semiconductors. The biggest obstacle in smooth integration of magnetic materials into information processing circuits is the lack of efficient control of their magnetization. As it was previously mentioned, this is vastly achieved with external magnetic fields which - in contrast to electric fields - cannot be applied locally. The demonstration of ferromagnetism in diluted magnetic semiconductors (DMS) raised hopes for applications based on single element combining the information storage capabilities of magnetic metals with the logic functionalities of semiconductors.

DMS are alloys consisting of a non-magnetic semiconductor doped with small percentage of magnetic impurities (most commonly Mn atoms). It was shown that such a small doping with magnetic ions (~ several percent) will not deteriorate the optical or

transport properties of the host and will introduce large magnetic and magneto-optical effects [4, 5]. The extensive study of DMS and their heterostructures has started with II-IV semiconductors, mostly CdTe and ZnSe [6, 7], but it was soon discovered that the FM order is present only at very low temperatures (below 2 K [6]), so the research has subsequently moved to III-V compounds. Nowadays, the most thoroughly investigated DMS is (Ga,Mn)As, with the highest Curie temperature (T_C) among all the DMS, $T_C \sim 190$ K [8, 9]. In (Ga,Mn)As the FM order is established by an exchange interaction between the charge carriers (holes) and the localized Mn spins (see Chap. 2) [6]. The carrier concentration is relatively low, of the order of 10^{20} to 10^{21} cm^{-3} (depending on Mn doping), as opposed to 10^{23} cm^{-3} in metals [10], so it is possible to control the amount of carriers by external electric fields, which not only influences the electronic properties but also the stability of ferromagnetic phase and other magnetic properties [11]. Despite the fact that T_C of (Ga,Mn)As is still far below the room temperature and its further increase is questionable [10, 12], it has already played a crucial role in exploring new physics, ideas and concepts in spintronics that has not been accessible in metals. In the following paragraph we summarize some of the most interesting phenomena that were observed in (Ga,Mn)As – some of them serve "only" as a proof of spintronic concepts but some have stimulated a discovery of related phenomena in conventional metals magnets, which are highly relevant for current spintronic applications [4, 10].

As already mentioned, the tunneling magnetoresistance (TMR) is one of the building blocks of spintronics, which is currently commercially utilized for the information readout in FM metals. The well-established growth of heterostrustructures and microfabrication techniques in semiconductors enabled fabrication of the high quality tunnel junctions which showed large TMR in III-V compounds as well [13, 14]. In particular, an intrinsic TMR effect with magnetoresistance up to 100% was observed in a device containing two (Ga,Mn)As electrodes separated by ZnSe tunneling barrier [14]. Besides the conventional two FM electrode devices (also called the Mott devices), (Ga,Mn)As served as a key material for observing the tunneling anisotropic magnetoresistance (TAMR) which comprise only one FM electrode. This phenomenon originates from the spin-orbit coupling (SOC) which causes that the conductivity depends on the orientation of the magnetization relative to the crystal axis or the current direction, so there is no need for the reference electrode. Devices based on the SOC are generally called the Dirac devices as the SOC was elucidated in Dirac equation [15]. The TAMR was primarily observed in (Ga,Mn)As [16] and subsequently detected in conventional metals [17]. Another type of magnetoresistance – the Coulomb blockade anisotropic magnetoresistance (CBAMR) – was observed in (Ga,Mn)As single electron transistor (SET) [18]. In this effect the electron can tunnel through a tunneling barrier due to the Coulomb blockade oscillations, which can show both positive and negative spin-valve-like characteristics depending on the SET gate voltage. This new type of magnetoresistance should be generic to SETs fabricated in FM systems with large SOC and we note that for, e.g. FePt FM metal this effect was predicted to be observable even at room temperature [18]. Such effect could be utilized in the next generation devices, analogous to the field effect transistors (FET), where the spin transport and the magnetoresistance magnitude would be controlled by a voltage applied to the gate. Another step towards a fundamentally new information processing paradigm was again realized in (Ga,Mn)As – a monolithic read-write

device. In this single device, the information is written as a magnetic state ("0" and "1" are represented by two *perpendicular* orientations of magnetization) by current-induced switching and readout of the state is done by means of the TAMR effect [19]. The current densities that are needed to switch the magnetization from one state to another are on the order of ~ 10^5 Acm^{-2}, which is 1 to 2 orders of magnitude lower than the densities needed in metallic memory elements [19]. Such device has a lot of technological advantages as it allows for manufacturing the integrated circuits consisting of identical multifunctional elements, which can be easily and cheaply produced. We finish the list of intriguing phenomena observed in (Ga,Mn)As by mentioning the reversible control of magnetization orientation using the spin-orbit magnetic field, i.e., by so called spin-orbit torque (SOT). In contrary to the spin transfer torque (STT), where a spin polarized current induces a torque on magnetization via the angular momentum transfer [20, 21, 22], in SOT the equilibrium orientation of magnetization is changed by an *unpolarized* current due to the relativistic spin-orbit coupling [23, 24]. A device based on the SOT principle was constructed by Chernyshov et *al.* [23] and performs a non-volatile memory cell, with two states (2 bits) encoded in the magnetization direction which is controlled by the unpolarized current passing through the device in one crystallographic direction. The authors suggest that the functionality of the device could be increased into 4 bits, if the current is injected in two orthogonal directions.

Despite the fact that (Ga,Mn)As is thoroughly investigated material, as could be seen from the previous paragraph, its properties are still not understood completely. For example, there is an ongoing debate about the character of its electronic band structure, mainly the position of the Fermi level for Mn doping exceeding 1 % [25, 26, 27]. There is also a large scatter in the micromagnetic parameters magnitude that seemed to be lacking any monotonous dependence on Mn doping. This thesis is dedicated to the study of some of the basic (Ga,Mn)As properties (electronic band structure) and parameters (anisotropy constants, spin stiffness or Gilbert damping coefficient), employing both, the time-integrated and time-resolved magneto-optical methods. Moreover, we report on two newly discovered physical phenomena, concretely on the optical counterparts of STT and SOT.

2. Ferromagnetic semiconductor (Ga,Mn)As

The significance of (Ga,Mn)As can be seen from several aspects. i) The incorporation of Mn atoms causes only a small perturbation of the GaAs host, which is the mainstream semiconductor used in high-mobility transistors, lasers and other electronic devices. Incorporating the FM order into this highly used semiconductor is thus very attractive. ii) The magnetism in (Ga,Mn)As is mediated by the charge carriers (as will be discussed later in more detail), so the magnetic properties can be controlled, in addition to magnetic, also by the electric field. iii) Nowadays, the growth techniques and the subsequent postgrowth treatment are well managed and the structures on the nanometer scale can be fabricated by the advanced microfabrication methods. All these attributes, together with a potential for future applications, motivate the extensive research of (Ga,Mn)As. This chapter is devoted to a brief overview of its most essential properties, focusing especially on the magnetic ones.

2.1 Magnetic order

When a magnetic Mn atom is incorporated into GaAs, it occupies the cation (Ga) sublattice (Mn_{Ga}) in the zinc-blend host structure [25, 28]. As can be seen from nominal atomic composition of each element: [Ar]$3d^{10}4s^2p^1$ for Ga, [Ar]$3d^5 4s^2$ for Mn, and [Ar]$3d^{10}4s^2p^3$ for As, Mn_{Ga} not only provides a localized spin $S = 5/2$ due to five 3*d* electrons, but also acts as an acceptor, because of the missing 4*p* valence electron. The concentration of provided holes and Mn moments is crucial for establishing the FM order in the system. One could assume that the concentration of Mn ions corresponds to the same concentration of holes and Mn moments. This is, however, not true in the real systems, since Mn atoms can also occupy the less energetically stable interstitial (Mn_I) positions (see Fig. 1), acting as double donors and compensating the concentration of holes [28]. Moreover, the Mn_I also couples antiferromagnetically to Mn_{Ga}, reducing the overall magnetic moment [28]. The number of Mn atoms that *effectively* contribute to the ferromagnetic order can be defined as: $Mn_{eff} = Mn_{sub} - Mn_I$, where Mn_{sub} and Mn_I stand for substitutional and interstitial Mn atoms, respectively [26].

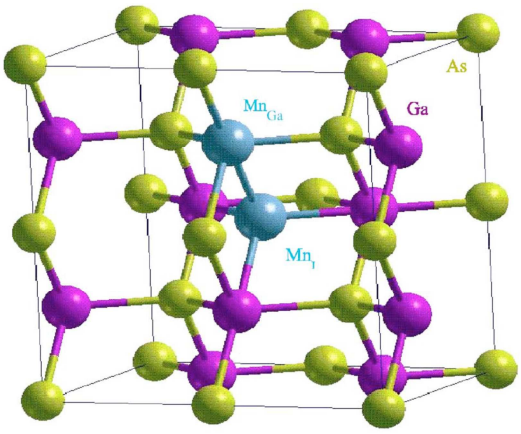

Fig. 1: (Ga,Mn)As unit cell. The most energetically favorable position of Mn atom in the GaAs host cell is in the position of Ga (Mn_{Ga}). The less common interstitial position is depicted as Mn_I. [27]

The origin of ferromagnetism in (Ga,Mn)As was studied both, theoretically and experimentally and the proposed explanation can be found in Refs. 25, 28, 29, 30, here, only the basic picture is given. In this elementary framework – which is still a matter of controversy [25, 27, 31] – the ferromagnetic coupling between Mn spins is mediated by the free carriers (holes). The strong *p-d* hybridization between holes and localized Mn *d* electrons results into their antiferromagnetic (AF) interaction, which can be described by the exchange parameter J_{pd}. The spin polarized holes transfer their AF coupling with Mn spins further into the lattice, causing the long-range overall FM order between the localized Mn spins [28]. Experimentally, the FM in $Ga_{1-x}Mn_xAs$ is observed when the Mn doping reaches ~ 1% (x = 1% corresponds to Mn concentration of 2.2×10^{20} cm^{-3} [27]), which is well above the equilibrium solubility limit in GaAs and therefore the non-equilibrium molecular beam epitaxy (MBE) technique is used for the growth. The overall strength of the magnetic order is characterized by the Curie temperature T_C that is, in the simplified approach, directly proportional to the effective Mn and hole concentrations, x_{eff} and p, respectively [29, 30]. In addition, T_C was found to be the most simple and reliable parameter for characterizing the quality of (Ga,Mn)As samples. The highest attainable T_C leads simultaneously to layers with maximized uniformity and minimized compensation by unintentional impurities and defects [8, 32]. In order to produce high quality samples with the lowest concentration of defects, the samples have to be grown and subsequently annealed under optimized conditions, which vary for each nominal Mn doping x. For detailed description of the growth and annealing conditions see Němec et *al*. [33] in Appendix 8.

2.2 Electronic band structure

In the first approximation, (Ga,Mn)As has very similar band structure to GaAs, consisting of a conduction and valence band, where the later one is split into three sub-bands (heavy, light and split-off bands), due to the spin-orbit interaction [34, 35]. However, the *exact* electronic structure of this material is still widely discussed, lacking an unambiguous explanation mainly for higher concentrations of Mn ions [31, 36]. The picture is clear and well accepted only for a single Mn impurity in GaAs host structure, where it forms a separate impurity level which is detached (~ 0.1 eV) from the top of the valence band (VB). This impurity level is formed due to three main contributions [36]: i) long-range acceptor hydrogenic-like potential, ii) short-range central cell potential, which is specific for a given impurity and iii) spin-dependent hybridization of Mn *d*-levels with As *p*-levels. This single impurity model persists only for low Mn concentrations ($x \ll 1\%$), where the free carrier density is below the metal-to-insulator transition [31, 36]. In this scenario, the Fermi level resides in a narrow impurity band (IB). For concentrations $x > 1.5\%$, where the conductivity increases by several orders of magnitude [33, 36] and where the material becomes a degenerate semiconductor (i.e. with a metallic-like conductivity), two physical scenarios exist, named the *valence* and *impurity* band, respectively [26, 31, 33, 36, 37, 38, 39, 40]. In the VB model, the detached impurity band broadens with increasing Mn doping, and for sufficiently screened hydrogenic-like potential, it merges into the valance band. The states at the Fermi energy (E_F) retain the *p*-orbital character of the host semiconductor [28, 32, 36]. On

the other hand, the IB model predicts the persistence of the impurity band (as well as E_F) within the band gap also for the high-doped (Ga,Mn)As layers with metallic-like conduction [26, 37, 38, 39, 40]. While the VB model is built on the tight-binding approximation Hamiltonian, treated using the Anderson model (for magnetic impurities) and the coherent potential approximation (for disorder) [36], the IB model lacks suitable theoretical background and its whole framework is based only on the experimental results that contradict the predictions of the VB model.

For further discussion about the electronic structure of (Ga,Mn)As see Chap. 3, where the character of bands (and the related origin of FM order) is reviewed in the light of static magneto-optical measurements (magnetic circular dichroism in particular).

2.3 Magnetic anisotropy

For typical Mn doping levels 1% - 10% in (Ga,Mn)As, the magnetocrystalline anisotropy dominates over the shape anisotropy, that is prevailing in conventional ferromagnets [41]. Magnetocrystalline anisotropy describes the ferromagnet energy dependence on the magnetization orientation with respect to the crystallographic axes, and is originating mainly from a strong spin-orbit coupling of holes in the valence band [35]. The overall magnetic anisotropy (MA) is given by a sum of different anisotropy fields and the external magnetic field. In (Ga,Mn)As, the MA is dominated by the cubic and uniaxial anisotropies (in a case when no external magnetic field is applied) [41]. The cubic anisotropy reflects the zinc-blend symmetry of the GaAs host in which [100], [010] and [001] crystallographic directions are equivalent. However, in (Ga,Mn)As the symmetry between the in-plane and out-out-of-plane directions is distorted, due to additional compressive strain induced by the substrate (in the case of GaAs substrate). The cubic anisotropy is thus replaced by the biaxial (more often called in-plane "cubic", K_c) and the out-of-plane (K_{out}) anisotropies [28, 41]. The uniaxial in-plane anisotropy (K_u) is not associated with any measurable strain in the epilayer and is likely of the extrinsic origin (caused by the low-temperature MBE growth) [41, 42], favoring the [-110] crystallographic direction. MA is given by a total free energy functional F, which can be written as [41, 43]:

$$F = M\left[\begin{array}{l} K_c \sin^2\theta\left(\frac{1}{4}\sin^2 2\varphi \sin^2\theta + \cos^2\theta\right) - K_{out}\cos^2\theta - \frac{K_u}{2}\sin^2\theta(1-\sin 2\varphi) - \\ - H_{ext}\left[\cos\theta\cos\theta_H + \sin\theta\sin\theta_H\cos(\varphi-\varphi_H)\right] \end{array}\right], \quad (1)$$

where the angles φ (φ_H) and θ (θ_H) describe the orientation of magnetization (external magnetic field H_{ext}) from the [100] and [001] crystallographic axes, respectively. The minimum of the free energy functional determines the equilibrium position of magnetization, usually denoted as the *easy axis* (EA). It is important to remark, that the EA position is very sensitive to the "inherent" material properties, such as the hole concentration (p) and the magnetic moment magnitude (M) and also to the "external" conditions, such as temperature (T) or strain, as every magnetic anisotropy component K_i is a function of p, M, T and strain [41, 44, 45]. We note that (Ga,Mn)As is a highly disordered material, mainly because of the

non-equilibrium low temperature growth by the MBE technique, which causes a high number of different defects (see Chap. 2.1) [46]. This influences the number of uncompensated holes (p) and also the magnetic moment magnitude. In order to increase the hole concentration and the overall magnetic quality, the samples are annealed and/or etched after the growth [33, 46].

The magnitude of the magnetic anisotropies can be determined by at least three independent methods, e.g. by the ferromagnetic resonance (FMR) [47, 48], by the superconducting quantum interference device (SQUID) [49] or by the time-resolved magneto-optical spectroscopy. As part of this thesis is devoted to the determination of the magnetic anisotropy constants from the time-dependent magneto-optical signal, the detailed description of this method can be found in Chap. 6, or see Němec et *al*. [33] in Appendix 8.

2.4 (Ga,Mn)As samples used in this thesis

All the experimental results presented in this thesis (see Appendices 1 – 8) were obtained on the set of $Ga_{1-x}Mn_xAs$ samples, which are summarized in Table 1. The samples were grown at the Institute of Physics of the Academy of Sciences in Prague by the non-equilibrium MBE method. All the samples were of very high-quality, with relatively high Mn doping, spanning the range from x = 1.5% to 14%. The details about the growth and post-growth treatment can be found in Ref. 33 (see Appendix 8). All samples are in-plane magnets in which the biaxial anisotropy is competing with the uniaxial. In the lowest Mn doping (x = 1.5%), the biaxial anisotropy dominates and the EA lies in the [100] or [010] crystallographic direction. With increasing Mn concentration, the uniaxial anisotropy starts being comparable with the biaxial, shifting the EA towards the [-110] direction. The uniaxial anisotropy dominates for x > 9% and the EA is aligned with [-110] crystallographic direction. The samples show increasing magnetic moment M_S, T_C and p with increasing Mn concentration [33].

sample	x (%)	d (nm)	T_C (K)	M_S (emu/cm^3)	p (10^{21} cm^{-3})
F010	1.5	20	29	8.9	0.15
F007	2.5	20	60	11.5	-
F002	3	20	77	16.2	0.66
F016	3.8	20	96	24.7	-
E101	4.5	19	111	27.8	1.03
F020	5.2	20	132	333	1.08
D071	7	50	150	47.4	-
E115	7	20	159	51.0	1.41
E122	9	20	179	63.7	1.55
F056	14	20	182	78.1	1.81

Table 1: Table summarizing the basic characteristics of the $Ga_{1-x}Mn_xAs$ samples used in this thesis: x is the nominal Mn doping, d is the film thickness, T_C is the Curie temperature, M_S is the saturated magnetic moment and p is the hole concentration.

3. Static magneto-optics in (Ga,Mn)As

The interconnection between the magnetic, electric and optical effects in (Ga,Mn)As, together with the direct gap band structure, make this FM semiconductor an ideal system for investigating its basic properties by the optical spectroscopy. Moreover, in the presence of the ferromagnetic order, the spin degeneracy of the conductance and valence bands is removed (in analogy with the Zeeman splitting) [44], which gives rise to an appearance of the magneto-optical (MO) effects [50, 51, 52]. MO spectroscopy is extremely beneficial as it enables to study the electronic structure of DMS and it provides an insight into the exchange mechanism between the holes and the local magnetic moments. Moreover, the MO spectroscopy enables to discriminate between the intrinsic (induced by the Mn moments) and extrinsic (induced by the impurities or defects) origin of the FM phase [31, 53], so it is very convenient to use it as a complementary technique to the standard magnetization measurement techniques like SQUID. The most common MO effects, which are typically employed for the investigation of (Ga,Mn)As properties, are described in the following section.

The term "MO effects" comprises a large number of phenomena where the interaction of polarized light with a magnetized medium leads to a change of polarization state of the incident light [54]. The polarized light can be represented in orthogonal basis as a sum of two linear (*s* and *p*) or circular (σ^+ and σ^-) polarizations. The MO interactions lead to a change of the complex index of refraction ($\hat{n} = n + ik$) for two orthogonal polarizations and, consequently, the polarization of transmitted/reflected light is rotated and/or the ellipticity is changed. The polarization changes induced by the real part of the index of refraction cause a magnetic birefringence, whereas the imaginary part causes a magnetic dichroism [54]. Both effects are complementary and appear simultaneously because of the Kramers–Kronig relations between *n* and *k*.

MO effects can be sorted on the basis of the geometry between the incident light propagation (***k***) and the orientation of magnetization (***M***). In the case of normal incidence, with ***k*** parallel to ***M***, the energy levels are split into doublets (known as the longitudinal Zeeman effect) and the transitions between the spin-split levels and the ground state occur for σ^+ or σ^- [55]. The MO effects that appear in this configuration are odd functions of magnetization, i.e. they change sign when the magnetization orientation is reversed and they are proportional to the magnetization magnitude. These effects are also generally called as the first order MO effects. For ***k*** perpendicular to ***M***, the energy levels are split into triplets (known as the transversal Zeeman effect) and the middle and peripheral levels correspond to *s* and *p* linear polarizations, respectively [55]. The effects occurring in this geometry are even (quadratic) functions of magnetization, i.e. their sign is *not* changed when the magnetization direction is reversed and they are proportional to magnetization square. The effects in this geometry are also called as the second order or quadratic MO effects.

Since this thesis is focused on the study of (Ga,Mn)As properties by MO effects, the ones used in our experiments – the magnetic circular/linear dichroism and birefringence – are

briefly introduced. For simplicity, the transmission geometry and the normal incidence of light are considered in the following section.

Magnetic circular dichroism (MCD) is caused by a different absorption coefficient for σ^+ and σ^- circularly polarized light when $\boldsymbol{k}$ is parallel to $\boldsymbol{M}$. For linearly polarized incident light, $\boldsymbol{M}$ induces a change in the amplitude ratio between σ^+ and σ^-, which causes the rise of ellipticity (see Fig. 2a). The spectral dependence of MCD is essential for revealing the magnetic nature (i.e. antiferromagnetic or ferromagnetic) of the exchange interaction between the local Mn moments and the free carriers in (Ga,Mn)As [31, 32, 39]. Due to this feature, the MCD spectra were extensively studied in samples with different Mn doping and carrier concentrations, see e.g. Refs. 26, 32, 37, 53. The huge amount of the experimental results led to a dichotomy in the electronic band structure of (Ga,Mn)As, forming two competing theories – the VB and IB models (see Chap. 2.2). The IB model is promoted because of the observed rigidity of the near-band gap feature in the MCD spectra with increasing doping [26, 37], supported by the red-shift of the peak in the infrared (IR) absorption [38]. However, it was later shown by Jungwirth et *al*. (see Ref. 32 in Appendix 1), that this trend is not generic, as the blue-shift of the sharp MCD spectral feature at the band-gap energy (as well as the IR absorption peak) with increasing Mn doping was observed, in accordance with the predictions of the VB model with the AF *p-d* interaction. Despite the yet unsolved question about the character of the band structure in (Ga,Mn)As, the MCD spectroscopy proved to be a powerful tool for investigation of the intrinsic nature of FM in DMS.

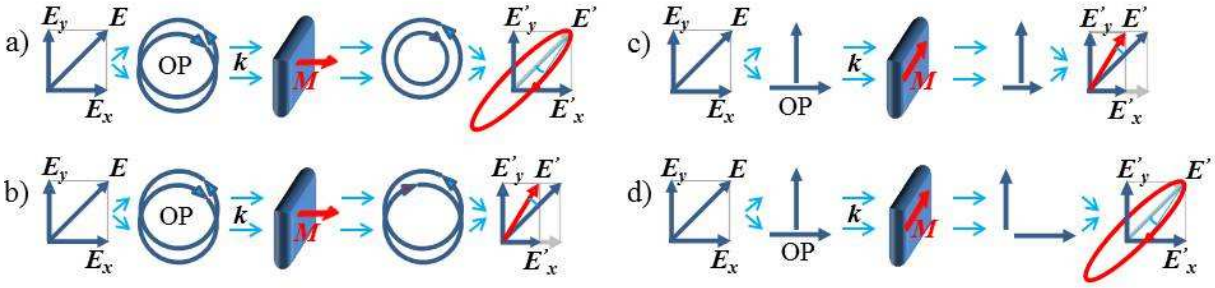

Fig. 2: Schematic illustration of magnetic circular dichroism (a), magnetic circular birefringence (b), magnetic linear dichroism (c) and magnetic linear birefringence (d). $\boldsymbol{E_x}$ and $\boldsymbol{E_y}$ are the *x* and *y* components of the incident light polarization $\boldsymbol{E}$ which is subsequently decomposed into two orthogonal polarizations (OP) in the given basis. The polarization of the transmitted light is changed after passing through the magnetized sample and the new polarization is depicted as $\boldsymbol{E}'$(with the $\boldsymbol{E}'_x$ and $\boldsymbol{E}'_y$ components). $\boldsymbol{M}$ represents the direction of magnetization and it is parallel to the incoming light direction ($\boldsymbol{k}$) in (a) and (b) and perpendicular to $\boldsymbol{k}$ in (c) and (d).

Magnetic circular birefringence (MCB) is a complementary effect to MCD, which is induced by a different index of refraction for σ^+ and σ^-. The difference in the refraction indices causes a phase shift between these two orthogonal polarizations, which in turn leads to rotation of the light polarization plane (see Fig. 2b). This effect is more commonly called the Polar Faraday or Kerr effect in transmission or reflection geometry, respectively. The static Polar Kerr effect (PKE) is widely used MO effect that is well established for probing the magnetic arrangement, FM interactions or the mechanisms of the magnetization reversals [53, 56, 57]. In addition, PKE is an AC-analogy to the anomalous Hall effect (AHE), as it is

directly proportional to the transversal component of conductivity (σ_{xy}), and can thus supplement the AHE measurements in the finite-frequency domain [53, 58]. PKE is also extensively used in the time-resolved MO measurements for observing the out-of-plane component of the magnetization dynamics, see e.g. Refs. 59, 60, 61 and the references therein.

Magnetic linear dichroism (MLD) is detected in a geometry when ***k*** is perpendicular to ***M*** and is caused by a difference in the absorption coefficient for *s* and *p* polarizations, resulting into rotation of the linearly polarized light (see Fig. 2c). This effect was found to be very small in conventional metals and was typically omitted in the studies of their MO properties [54, 62, 63]. In (Ga,Mn)As, however, a "giant" MLD signal was discovered recently [52, 64]. Its magnitude is spectrally dependent and it was found that it can even exceed the magnitude of PKE in some spectral regions, see e.g. Tesařová et *al*. in Refs. 65 and 66 (Appendices 2 and 5, respectively). Analogously to PKE, it can be perceived as the finite-frequency extension of the anisotropic magneto-resistance (AMR), and thus it can be exploited in elucidating the unclear origin of the AMR [67]. It was also shown that MLD is very valuable for a reconstruction of the real-space magnetization dynamics as it provides the access to the in-plane component of magnetization. For further analysis of the MLD see Chap. 4 or Tesařová et *al*. [66] in Appendix 5.

Magnetic linear birefringence (MLB) is a complementary effect to MLD. It is caused by a different index of refraction for *s* and *p* polarizations, which shifts their mutual phase and, consequently, it leads to the light elliptically change (see Fig. 2d).

It is important to note that such a simple and elegant division of the MO effects, based on the real and imaginary part of the complex index of refraction, is possible only in the transmission geometry. Although the manifestation of these effects stays the same in the reflection geometry, their origin might differ in such extent, that the change of the absorption and refraction index cannot be strictly separated [68]. In this thesis, all the mentioned MO effects were used mainly in the reflection geometry as an experimental tool for studying the manifestation of the FM order under different conditions, and, therefore, the exact origin of these MO effects was not of the fundamental importance.

In the following part of this thesis, we will show how the presented MO effects can be exploited in determining the basic material properties by other means than just the conventional measurements of the hysteresis loops or the MO spectra. The MO effects will be used in the time-resolved pump and probe spectroscopy (see Appendix 9) to study the magnetization dynamics. We show that this technique is not only favorable for determining the essential material parameters of (Ga,Mn)As but it also enabled us to reveal some new and intriguing physical phenomena in this material system.

4. Laser-induced precession of magnetization

The ever-increasing demand for speeding up the information storage and processing in the magnetic media leads to an intense research in fast manipulation of the magnetization state. While the transistor-based electronics is currently working in a few gigahertz clock-speed regime (~ 300 ps), the storage on magnetic hard discs, where the information is stored in magnetized domains (logic states "0" and "1" represent two different magnetization orientations), requires few nanoseconds, creating so called the ultrafast technology gap [69]. One of the alternatives to the magnetic field-induced magnetization switching is the current induced torque (CIT; also known as the spin transfer torque) [15]. The magnetization manipulation by CIT originates from the angular momentum transfer, where the magnetic layer orientation is flipped due to the angular momentum carried by the spin polarized current (see Chap. 5.2). The time scale of such CIT induced magnetization switching is on the order of several hundred picoseconds [70]. However, the observation of subpicosecond demagnetization by 60 fs laser pulses (in Ni films) [71] has opened a new perspective of the ultrafast magnetization manipulation by means of optics. Pumping the magnetic system with the optical laser pulses strongly disturbs the equilibrium between the lattice, carriers and magnetization [69, 72] and leads to several quasi-equilibrium dynamical processes that can provide insight into the strength and timescale of various microscopic interactions [72], or can reveal some new photoinduced phenomena, as will be discussed in more detail in Chap. 5.

The aim of the following chapters is to elucidate one of such dynamical processes – the laser pulse-induced magnetization precession – and to demonstrate the strength of the MO spectroscopy in determination of the real-space magnetization trajectory and in investigation of the basic material properties of (Ga,Mn)As. Moreover, we show how this experimental technique can be exploited in revealing new physical phenomena.

4.1 Magnetization dynamics observed by MO spectroscopy

The impact of a strong laser pulse induces a change of the equilibrium conditions between the reservoirs of spins, free carriers and phonons in the (Ga,Mn)As sample [73]. Because the magnetic properties of (Ga,Mn)As are strongly dependent on the interaction between the spins and charge carriers, the impact of the laser pulse induces a precession of magnetization (even if no external magnetic field is applied), which can be detected as an oscillatory MO signal. In (Ga,Mn)As the oscillatory motion of magnetization was for the first time observed in 2005 by Oiwa et *al*. [74]. Since then, the photoinduced magnetization dynamics in (Ga,Mn)As have been studied by many different groups, see e.g. Refs. 59, 60, 61, 75, 76 77, 78.

In these studies the observed MO signals were found to be independent of the excitation polarization, at least for time delays > 100 ps as can be seen from Fig. 3a. This indicated that the detected MO signal (rotation of the light polarization plane $\Delta\theta$) – that reflects the oscillations of FM coupled Mn spins – was not connected with the light angular momentum

transfer. The magnetic origin of the measured MO signal was further investigated by Tesařová et *al*. in Ref. 79 (see Appendix 3), where the pump-induced change of rotation ($\Delta\theta$) and ellipticity ($\Delta\eta$) were measured simultaneously (see Fig. 3b).

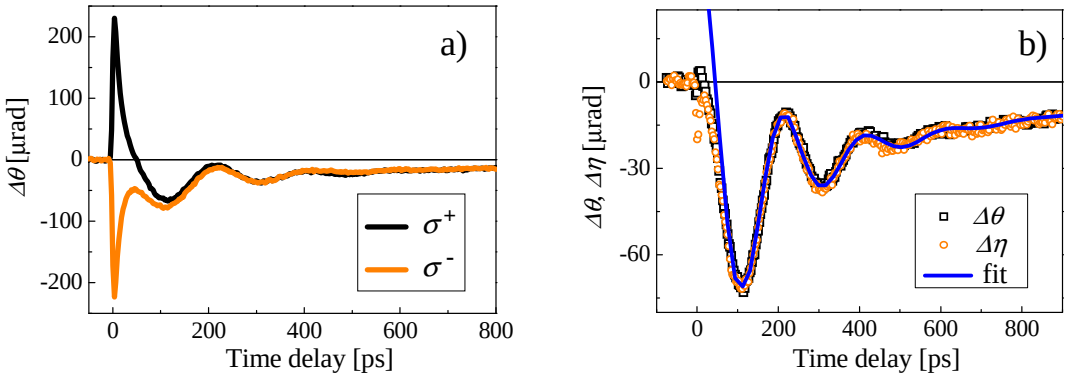

Fig. 3: MO signals measured as a function of time delay between pump and probe laser pulses. a) Dynamics of the probing light polarization rotation $\Delta\theta$ measured for two circular pump polarizations (σ^+ and σ^-). b) Polarization-independent part, $(\sigma^+ + \sigma^-)/2$, of the rotation ($\Delta\theta$) and ellipticity ($\Delta\eta$) (points) measured under identical conditions. The solid line corresponds to the fit by a damped harmonic function: $MO(\Delta t) = Acos(2\pi f\Delta t + \Phi)e^{-\frac{\Delta t}{t_G}} + Ce^{-\frac{\Delta t}{t_p}}$, where A = 82 μrad, t_G = 145 ps, f = 196.6 GHz, Φ = 59°, C = -42 μrad, t_p = 700 ps. Experimental data were taken for (Ga,Mn)As with 3% Mn concentration, at T = 15 K and with no external magnetic field applied. 80 fs pulses from the Ti:sapphire laser were tuned to 1.63 eV with pump intensity 46 μJcm^{-2}.

The data show similar behavior from time delays > 10 ps, confirming the FM origin of the measured MO signal at longer time scales and suggesting the non-magnetic (so-called optical) contribution right after the impact of the laser pulse [79, 80]. From the numerous experimental observations, it was concluded that the magnetization oscillations are caused by the laser-induced change of the magnetic anisotropy (MA), see e.g. Refs. 59, 76, 78. Since the MA is a function of *p*, *T* and strain, their slight photo-induced change influences the overall MA, thus the EA position of magnetization (see Chap. 2.3). However, the exact mechanisms of the anisotropy change remains an open question, where both the *thermal* (change in the sample temperature) and the *non-thermal* (change in the carrier concentration) origin of the MA change was considered [59, 61, 77]. The magnetization dynamics were investigated as a function of temperature [59, 61, 76, 78, 81], excitation intensities [24, 59, 61, 76, 78] and energies [80], carrier concentrations [24, 61, 78] or thermal annealing [61], but the experimental observations obtained by different groups led to ambiguous interpretations of the magnetization dynamics origin [24, 61, 76, 77]. We note that the diversity may come from the distinct quality of the studied samples. As mentioned above (in Chap. 2.3), (Ga,Mn)As is a highly disordered material system and its magnetic properties depend on various parameters, such as growth conditions, film thickness, post-growth treatment and so on. All these factors may lead to different observations of the magnetization dynamics, even at similar experimental conditions. The latest studies of Tesařová et *al*. in Ref. 24 (see Appendix 7) on a high quality samples suggest, that in principle, both mechanisms (thermal and non-thermal) are present and are not easily distinguishable. It was shown, that at lower excitation intensities

(I < 70 μJcm^{-2}), the thermal mechanism prevails, but for higher intensities, the temperature increase is saturated and the magnetization dynamics is dominated by the non-thermal effects (see Chapter 5 for detailed discussion). Nevertheless, it was also found that the impact of the laser pulse does not always lead to the precession of magnetization (see Appendix 4) [82]. In samples with strong uniaxial (i.e. the EA oriented in [-110] crystallographic direction), or cubic anisotropy (i.e. the EA oriented in [100] or [010] crystallographic direction), no magnetization oscillations were observed – at least for the excitation intensities I < 28 μJcm^{-2} – as the impact of the laser pulse is not sufficient to reorient the equilibrium EA position. It was concluded that the laser-induced change of the EA, which triggers the magnetization dynamics, can be observed only in samples where the cubic and uniaxial anisotropies are "comparable", so that the equilibrium EA is oriented between [010] and [-110] crystallographic directions. Moreover, it was shown that the MA has a strong influence not only on the precessional frequency (as will be discussed in Chap. 6), but also on the amplitude of the oscillations, as observed by Tesařová et *al*. in Ref. 82 (see Appendix 4 for further details).

The measured data of magnetization precession can be phenomenologically fitted by a sum of damped harmonic function and a non-oscillatory pulse-like background function [59, 60, 66]:

$$MO\ (\Delta t) = Acos(2\pi f \Delta t + \Phi)e^{-\frac{\Delta t}{t_G}} + Ce^{-\frac{\Delta t}{t_p}}, \quad (2)$$

where A and C are the amplitudes of the harmonic and pulse-like functions, respectively, f is the frequency of precessing Mn spins, Φ is an initial phase, t_G is the Gilbert damping time (see Chap. 6), and t_p is the damping time of the pulse-like function. As seen from Fig. 3b, only the quasi-equilibrium part of the MO signal, reflecting the precessional motion of magnetization, can be fitted well by Eq. 2. In fact, this formula describes a phenomenological model, in which the MO signal can be decomposed into the damped magnetization oscillations around the quasi-equilibrium EA and the laser-induced tilt of the equilibrium EA position [Supplementary material in 21, 82].

The situation can be in more detail described as the following: Before the impact of the laser pulse, the magnetization is aligned with the equilibrium EA, given by the free energy minimum (see Fig. 4a and Eq. 1 in Chap. 2.3). The impact of the laser pulse changes the overall MA, which leads to the shift of the EA (Fig. 4b). At this moment, the instant position of magnetization and the EA are not aligned, so the magnetization starts to approach the transient EA position by an oscillatory motion, which can be perceived as the precession of magnetization around some inherent effective magnetic field [77, 81]. As the laser-induced changes are decaying, the transient EA is returning to its equilibrium position and the precession of magnetization is damped by the Gilbert damping at the same time (Fig. 4c).

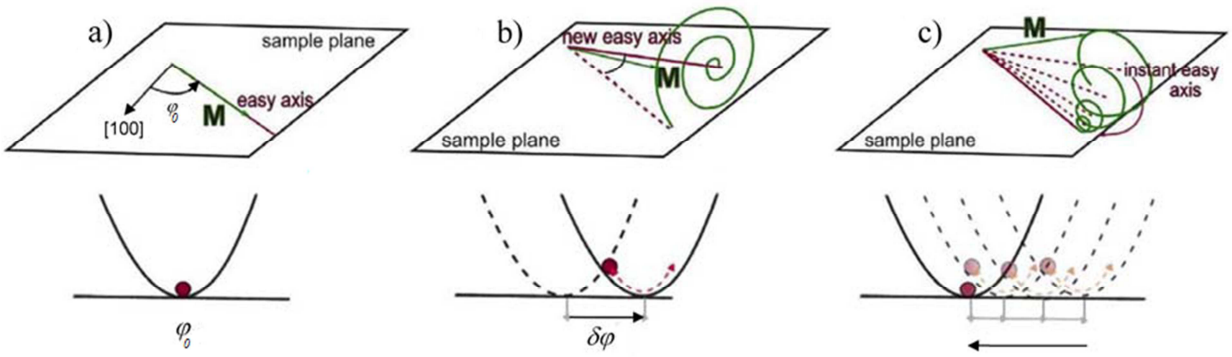

Fig. 4: Schematic illustration of the pulse-induced precession of magnetization. a) In equilibrium, the magnetization is aligned with the EA position, which lies in the sample plane at the angle φ_0 from the [100] crystallographic direction. b) The impact of a strong laser pulse induces a transient change of the MA, which leads to the reorientation of the easy axis and subsequently to the precession of magnetization. c) The recombination of the photoinduced carriers and the heat dissipation slowly restore the equilibrium conditions, making the EA return to its original position. Simultaneously, the magnetization precession in damped by the Gilbert damping. [43]

The anisotropy-dependent precession of magnetization can be of a practical use as it can be controlled by external means – either optically by another laser pulse [60], or electrically by a piezo-transducer [21]. The electrical control by piezo-stressing allows the manipulation of the overall strain in the sample, which enables either to enhance or completely suppress the magnetization dynamics, see Ref. 21 in Appendix 6. We note that the laser-induced magnetization precessions can be also used for determination of the basic properties of (Ga,Mn)As, such as the MA constants K_i, the Gilbert damping constant α, or the spin stiffness parameter D (as will be discussed in detail in the Chap. 6) – in a way rather similar to ferromagnetic resonance experiments [FMR]. Before proceeding to such specific characteristics of (Ga,Mn)As, let's have a closer look at the real-space magnetization trajectory after the impact of the laser pulse.

4.2 Real-space magnetization dynamics

MO spectroscopy is a very powerful tool for the investigation of the magnetization trajectory in the real space as it reflects both the in-plane and out-of-plane motion of magnetization sensed by MLD and PKE, respectively. In order to separate these two contributions in the measured MO signals, their distinct polarization dependences can be used as will be demonstrated in the following sections. The polarization dependence of PKE and MLD will be derived first for the static MO signals and, subsequently, it will be applied to the analytical model of magnetization dynamics described by Eq. 2. We stress that the detailed understanding of the measured dynamical MO signal, together with the polarization dependence of PKE and MLD, enables to perform a full quantitative 3D reconstruction of the magnetization precessional motion without any numerical modeling.

4.2.1 Polarization dependence of static MO signal

As mentioned in Chap. 3, there are four different MO effects that can change the polarization state of light when reflected from the magnetized media (taking just the reflection geometry with small angles of incidence into account). In the following discussion, the polarization dependence of only two of them, causing the *rotation* of the light polarization plane, will be investigated – PKE (sensitive to out-of-plane projection of ***M***) and MLD (sensitive to in-plane projection of ***M***), but the obtained results can be also applied for MCD and MLB, causing the light ellipticity change. In general, the orientation of magnetization can be characterized by the polar and azimuthal angles φ_0 and θ_0, respectively (see Fig. 5a for the angle definition). In the case of PKE, the rotation of light polarization ($\Delta\beta$) is proportional to the projection of magnetization to the direction of light propagation and it is insensitive the incident polarization orientation (see Figs. 5b and 2b):

$$\Delta\beta^{PKE} = \beta' - \beta = P^{PKE} cos\theta_0, \tag{3}$$

where P^{PKE} is the corresponding MO coefficient of the sample, which can be measured when the magnetization is oriented by a strong external magnetic field out of the sample plane (θ_0 = 0˚).

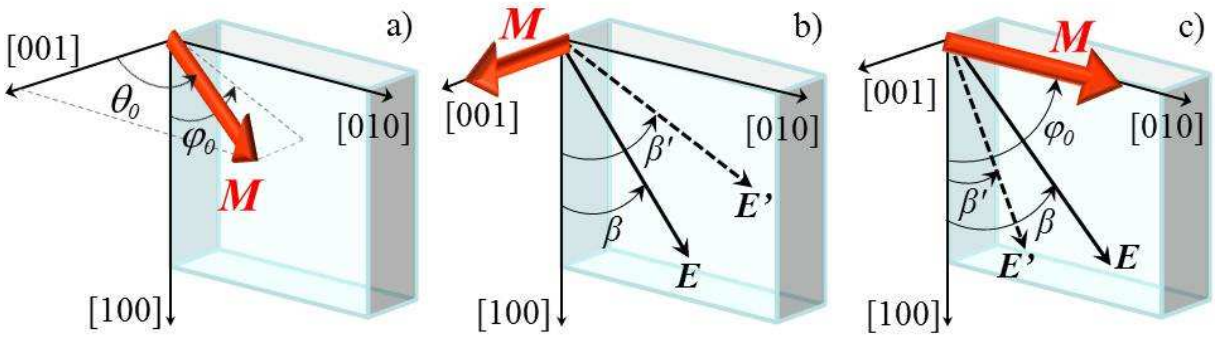

Fig. 5: a) Definition of the polar angle φ_0 and azimuthal angle θ_0, that determine the position of magnetization ***M*** in the sample. b) Rotation of light polarization plane $\Delta\beta$ due to PKE, which is proportional to the out-of plane orientation of magnetization. PKE does not depend on the incident light polarization β. c) Rotation of the light polarization plane $\Delta\beta$ due to MLD, which is sensitive to in-plane position of ***M*** and depends on the incident light polarization orientation β; $\Delta\beta^{MLD} = P^{MLD} sin2(\varphi_0 - \beta)$. The incident polarizations are labeled ***E*** and the transmitted/reflected polarizations are labeled ***E'*** in b) and c), respectively.

In the case of MLD, the rotation of light polarization is proportional to the projection of magnetization to the direction perpendicular to light propagation (see Fig. 2c) and it strongly depends on the incident polarization orientation β. The polarization dependence of the MLD can be analytically calculated using the trigonometric relation between the magnetization orientation in the sample plane, given by the angle φ_0, and the incident and reflected light polarizations, given by the angles β and β' (see Fig. 5c and Ref. 65 in Appendix 2 for more details):

$$\Delta\beta^{MLD} = \beta' - \beta = P^{MLD} sin[2(\varphi_0 - \beta)], \tag{4}$$

where P^{MLD} is the MO coefficient defined as $P^{MLD} = 0.5(r_{\parallel}/r_{\perp} - 1)$ and $r_{\parallel}$ ($r_{\perp}$) describes the reflection coefficients for light polarized parallel (perpendicular) to magnetization orientation, respectively. Eq. 4 shows, that the polarization rotation $\Delta\beta$ due to MLD is maximized when the angle between $\boldsymbol{M}$ and the incident polarization orientation is ±45˚. In this case $\Delta\beta$ is given solely by P^{MLD}, thus this geometry is also used in order to determine the magnitude of P^{MLD} (the position of magnetization is fixed by a strong magnetic field). On the other hand, $\Delta\beta$ is zero when the incident polarization is parallel or perpendicular to $\boldsymbol{M}$ (i.e., $\varphi_0 - \beta$ = 0˚ or 90˚, respectively). In more general case, when the magnetization is not oriented in the sample plane, but has an arbitrary orientation given by φ_0 and θ_0, the polarization rotation due to MLD can be written as:

$$\Delta\beta^{MLD} = P^{MLD} sin^2\theta_0 sin[2(\varphi_0 - \beta)], \tag{5}$$

The overall rotation of light polarization is given by the sum of PKE and MLD contributions $\Delta\beta^{PKE}$ and $\Delta\beta^{MLD}$, respectively:

$$MO^{stat} = \Delta\beta^{PKE} + \Delta\beta^{MLD} = P^{PKE} cos\theta_0 + P^{MLD} sin^2\theta_0 sin[2(\varphi_0 - \beta)]. \tag{6}$$

It is important to note that since PKE is a first-order MO effect, P^{PKE} is directly proportional to magnetization magnitude M_0 (provided that $\boldsymbol{M}$ is oriented along the direction of light propagation). On the other hand, MLD is a second-order MO effect (or quadratic MO, see Chap. 3) and thus the P^{MLD} depends quadratically on M_0, i.e. $P^{MLD} \sim M_0^2$ (provided that $\boldsymbol{M}$ is oriented perpendicular to the direction of light propagation).

4.2.2 Dynamical MO signal in (Ga,Mn)As and its polarization dependence

As mentioned above, the impact of the laser pulse modifies the anisotropy of the sample, which shifts the equilibrium position of the EA, that subsequently leads to the precession of magnetization. The oscillatory motion of magnetization can be detected as a dynamical MO signal δMO that is strongly dependent on the incident light polarization, see Tesařová et *al*. [66] in Appendix 5. To express this explicitly, the analytical formula describing the magnetization dynamics (Eq. 2) can be rewritten in the following form:

$$\delta MO\ (\Delta t, \beta) = A(\beta) cos[2\pi f \Delta t + \Phi(\beta)] e^{-\frac{\Delta t}{t_G}} + C(\beta) e^{-\frac{\Delta t}{t_p}}, \tag{7}$$

where the meaning of the particular components remain the same as in Eq. 2. Moreover, the polarization dependence of the oscillatory and pulse-function amplitude [$A(\beta)$ and $C(\beta)$] enables more thorough insight into the character of the magnetization dynamics and a direct determination of the EA position.

Firstly, the pulse-like function in δMO signal describes the transient non-oscillatory change of the static MO signal MO^{stat}. In fact, in this signal there are two contributions that are reflecting different origin of the magnetization dynamics. The first one reflects the magnetization dynamics due to the *tilt* of the equilibrium EA position, which can be described

as a derivative of Eq. 6 with respect to small change of φ and θ. The second one is connected with the laser-induced change of the magnetization magnitude (*demagnetization*), due to the laser-induced heating of the sample, and can be also obtained from the derivative of Eq. 6 with respect to magnetization change (through the dependence of P^{PKE} and P^{MLD} on the magnetization magnitude). Taking into account that all the samples investigated in this thesis are in-plane magnets, i.e. $\theta_0 = 90^\circ$, we obtain the following expression for the measured pulse-like function amplitude $C(\beta)$:

$$C(\beta) = C_{tilt}(\beta) + C_{demag}(\beta) = \\ -\delta\theta_{qe}P^{PKE} + \delta\varphi_{qe}P^{MLD}2cos\,2(\varphi_0 - \beta) + \frac{\delta M}{M_0}P^{MLD}2sin\,2(\varphi_0 - \beta), \qquad (8)$$

where the first two terms on the right-hand side correspondent to $C_{tilt}(\beta)$ and the last term corresponds to $C_{demag}(\beta)$. $\delta\varphi_{qe}$ and $\delta\theta_{qe}$ describe the transient in-plane and out-of-plane tilt of the EA position and $\delta M/M_0$ describes the reduction of the magnetization magnitude (relative to the equilibrium value M_0). Eqation 8 is of high importance as it directly determines whether the magnetization precession is triggered by the in-plane or out-of-plane tilt of the EA. In the case of the in-plane tilt of the EA, the polarization dependence of C_{tilt} is given by the *cos*-like harmonic function. On the other hand, if the EA is tilted out-of plane, C_{tilt} does not depend on the incident light polarization β. In the case when the EA is tilted in a general direction, C_{tilt} depends harmonically on β, but there is an offset in the polarization dependence. Moreover, fitting the polarization dependence $C(\beta)$ by Eq. 8 enables to quantify the EA tilt, see Tesařová et *al*. [66] in Appendix 5.

The oscillatory function in δMO signal describes the precessional motion of magnetization around the transient EA position and it naturally consists of the in-plane and out-of-plane contributions sensed by MLD and PKE, respectively. The oscillatory function amplitude $A(\beta)$ can be thus written is the form:

$$A(\beta) = \sqrt{[A^{MLD}(\beta)]^2 + [A^{PKE}]^2}, \qquad (9)$$

where $A^{MLD}(\beta)$ describes the β-dependent MO amplitude due to the in-plane motion of magnetization and A^{PKE} is the out-of plane contribution of the precessional amplitude which does not depend on β. The analytical formula for A^{MLD} and A^{PKE} can be obtained from Eq. 6 as its derivative with respect to in-plane and out-of-plane angles φ and θ. Moreover, if we consider that the initial amplitude of the oscillations is approximately equal to the EA tilt $\delta\varphi_{eq}$ and $\delta\theta_{eq}$, the overall oscillatory amplitude is given as:

$$A(\beta) = \sqrt{\left[\delta\varphi_{qe}P^{MLD}2cos\,2(\varphi_0 - \beta)\right]^2 + [-\theta_{qe}P^{PKE}]^2}\,. \qquad (10)$$

The polarization dependence of the oscillatory amplitude is crucial for determining the equilibrium position of the EA in the sample plane, φ_0 (and thus the magnetization position before the impact of the laser pulse). φ_0 corresponds to the polarization orientation where the dependence $A^{MLD}(\beta)$ shows the maximum (see also Fig. 11b below). This conclusion is obvious from the fact, that $A^{MLD}(\beta)$ describes the change of the static MO signal $\Delta\beta^{MLD}$, which

is the strongest when the incident polarization is aligned parallel (or perpendicular) with the magnetization position, i.e. $\beta = \varphi_0$ (or $\beta = \varphi_0 \pm 90^\circ$), see Tesařová et *al*. [66] in Appendix 5.

4.2.3 Reconstruction of magnetization real-space trajectory

The detailed understanding of the time-dependent MO signal enables to perform a quantitative reconstruction of the magnetization real-space trajectory directly from the measured MO signals without assuming any theoretical model or any fitting parameter. As was already mentioned, prior to the impact of the laser pulse, the magnetization is aligned with the EA position (described by φ_0 and θ_0). The impact of the pump pulse disturbs the equilibrium conditions in the sample and leads to the magnetization precession, which is detected by the time-delayed probe pulses. The instantaneous position of the magnetization can be described by the polar and azimuthal angles φ and θ:

$$\varphi(\Delta t) = \varphi_0 + \delta\varphi(\Delta t), \tag{11a}$$

$$\theta(\Delta t) = \theta_0 + \delta\theta(\Delta t), \tag{11b}$$

where $\delta\varphi(\Delta t)$ and $\delta\theta(\Delta t)$ describe the time-dependent in-plane and out-of-plane movement of magnetization, respectively. The magnetization dynamics changes the static MO signal MO^{stat} and the measured MO signal can be thus expressed in terms of the instantaneous magnetization position as a derivative of Eq. 6 with respect to φ, θ and M_0:

$$\delta MO(\Delta t, \beta) = \\ -\delta\theta(\Delta t) P^{PKE} + \delta\varphi(\Delta t) P^{MLD} 2cos\,2(\varphi_0 - \beta) + \frac{\delta M}{M_0} P^{MLD} 2sin\,2(\varphi_0 - \beta), \tag{12}$$

where the first two terms are connected with the oscillatory movement of magnetization and the last term is connected with the demagnetization. We note that Eq. 12 is derived for the in-plane position of the EA, which is the case for all the (Ga,Mn)As samples measured in this thesis. The polarization dependence of the measured MO signal $\delta MO(\Delta t, \beta)$ enables to separate the in-plane and out-of-plane motions of the magnetization, sensed by MLD (which is sensitive to β) and PKE (which is not sensitive to β), respectively. It is apparent from Eq. 12 that the in-plane motion of magnetization can obtained as a linear combination of the MO signals measured for $\beta = \varphi_0$ and $\varphi_0 - 90^\circ$ because the in-plane motion of magnetization is maximal and exactly opposite for $\beta = \varphi_0$ and $\varphi_0 - 90^\circ$ and the demagnetization does not contribute to the measured signal for these angles β. Consequently,

$$\delta\varphi(\Delta t) = [\delta MO(\Delta t, \varphi_0) - \delta MO(\Delta t, \varphi_0 - 90°)]/(4P^{MLD}). \tag{13}$$

Similarly, the out-of-plane motion and the demagnetization can be calculated for $\beta = \varphi_0 - 45^\circ$ and $\varphi_0 - 135^\circ$, where the contribution due to the in-plane motion $\delta\varphi$ does not contribute and the demagnetization terms are exactly opposite:

$$\delta\theta(\Delta t) = -[\delta MO(\Delta t, \varphi_0 - 45°) + \delta MO(\Delta t, \varphi_0 - 135°)]/(2P^{PKE}), \tag{14}$$

$$\frac{\delta M(\Delta t)}{M_0} = [\delta MO(\Delta t, \varphi_0 - 45°) - \delta MO(\Delta t, \varphi_0 - 135°)]/(4P^{MLD}) \quad (15)$$

We note, that also other linear combinations of the $\delta MO(\Delta t, \beta)$ are in principle possible in order to obtain $\delta\varphi(\Delta t)$, $\delta\theta(\Delta t)$ and $\delta M(\Delta t)/M_0$. However, the presented Eqs. 13, 14 and 15 are the most simple and straightforwardly describe the magnetization dynamics after the impact of the laser pulse. In any case, the quantitative reconstruction of the in-plane and the out-of-plane real-space magnetization trajectory depends solely on the signals δMO, which are measured for different probe polarizations β, and on the magnitude of the MO coefficients P^{MLD} and P^{PKE}, which are determined independently in the static MO experiments (see Chap. 4.2.1). The examples of the magnetization dynamics calculated by this procedure can be found in Refs. [66] (see Appendix 5), [21] (see Appendix 6) and [24] (see Appendix 7).

5. Origin of magnetization precession

As pointed out in the previous chapter, the origin of the light-induced precession of magnetization in (Ga,Mn)As is a widely discussed issue, where two distinct mechanism of MA change – the thermal and the non-thermal – are considered to be responsible for this phenomenon [59, 61, 74, 76, 77]. The non-thermal origin was firstly suggested by Oiwa et *al*. [74] and subsequently followed by Hashimoto et *al*. [77]. The authors claimed that the variation of the MA is driven by the generation, cooling and subsequent annihilation of the photo-generated holes. They estimated the relative increase in the hole concentration to be ~ 0.01% for the excitation fluence of ~ 3 μJcm^{-2} [77]. On the other hand, Qi et *al*. [61] observed the magnetization precession for similar light intensities (~ 1 – 10 μJcm^{-2}) but it was ascribed to the transient change of temperature because its relative change was found to be 3 – 4 orders of magnitude larger than the hole concentration change. A new light into this issue is brought by the recent paper of Tesařová et *al*. [24] (see Appendix 7), which represents a thorough study of light-induced magnetization dynamics for a broad range of excitation intensities (~ 7 – 260 μJcm^{-2}). It is shown that, in principle, *both* mechanisms can lead to magnetization dynamics. Moreover, it is possible to separate the thermal and the non-thermal mechanisms by the real-space magnetization trajectory reconstruction (see Chap. 4) and to quantify the experimental conditions for which either of the mechanisms dominates.

In this chapter we discuss the thermal and the non-thermal origin of the oscillatory motion of magnetization in detail. In addition, we describe two distinct non-thermal mechanisms that can lead to magnetization precession.

5.1 Thermal origin

The impact of the laser pulse on (Ga,Mn)As sample (with the photon energy exceeding the energy of the band gap; E_g ~ 1.5 eV) leads to an instant generation of the electron-hole pairs, where the concentration of the photoinduced holes (δp) and electrons (δn_e) is equal. The scattering processes among the carriers build up a hot carrier Fermi-Dirac distribution on the sub-picosecond time scale [61]. Subsequently, the carriers recombine non-radiatively (because of the high concentration of the non-radiative recombination centers caused by the low-temperature growth by MBE; see Chap. 2.3) which increases the density of phonons due to the carrier-phonon interactions. The initial carrier energy is thus transferred to the lattice, resulting into a local increase of the temperature within a few picoseconds [59, 79]. The accumulated heat than diffuses from the illuminated area towards the equilibrium conditions on the time scale of hundreds of picoseconds [24]. The temperature raise time can be obtained directly from the differential reflectivity measurements ($\Delta R/R$) that provide information about the photo-injected carrier concentration and life-time (electrons in particular) [83], see Fig. 6a. The schematic picture of the temperature increase (δT) is depicted in Fig. 6b.

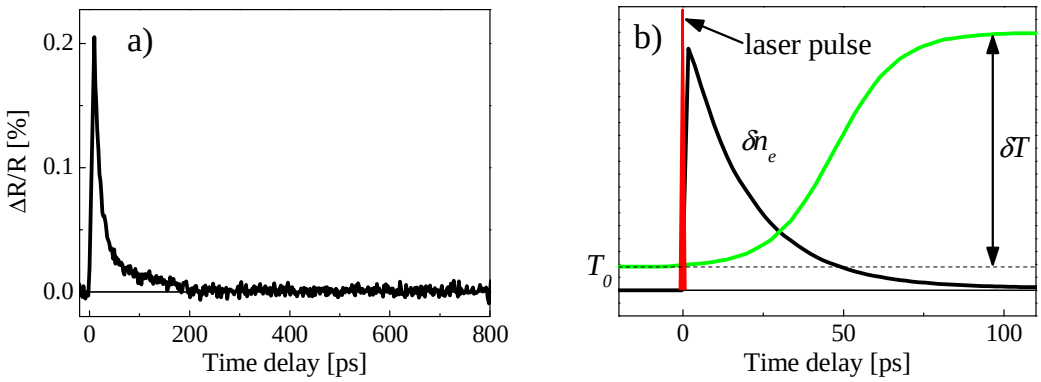

Fig. 6: a) Dynamics of the pump pulse-induced change of the sample reflectivity measured for (Ga,Mn)As sample with 3% Mn doping and the pump intensity I = 42 μJcm^{-2}. The reflectivity dynamics provide the information about the laser-induced carrier concentration (amplitude of the $\Delta R/R$) and lifetime (defined as a time where the reflectivity amplitude decreases to $1/e$). b) Schematic illustration of the laser-induced change of the electron concentration (δn_e) and the subsequent temperature increase (δT) from the equilibrium temperature T_0 after the impact of the femtosecond laser pulse (red peak). The dynamics of δn_e is obtained from the measured transient reflectivity data shown in a) where the corresponding lifetime is ~ 20 ps.

The magnetic anisotropy constants are strongly dependent on the magnetization magnitude - the uniaxial anisotropy scales with magnetization magnitude as M^2 while the biaxial component scales as M^4. Consequently, when the temperature of the sample is increased (i.e., when the magnetization magnitude is decreased), the biaxial anisotropy is reduced more than the uniaxial one, causing the shift of the EA towards the [-110] crystallographic direction [41, 46]. The character of the subsequent magnetization precession around the new quasi-equilibrium EA position is unambiguously described – by the Landau-Lifshitz-Gilbert equation (LLG, see Chap. 6) – enabling the *initial* tilt of the magnetization only towards the [00-1] crystallographic direction. An estimate of the temperature increase δT can be done from the magnetization precession frequencies, as their magnitude reflects the temperature dependent magnetocrystalline anisotropies (see Chap. 6). Figure 7a shows the precession frequency (f) dependence on the sample temperature, measured for low excitation intensity I = 7 μJcm^{-2}, and on the excitation intensity for low sample temperature T = 15 K. The temperature increase δT as a function of the intensity can be deduced from the comparison of these two dependencies ($f(T)$ and $f(I)$) and is shown in Fig. 7b.

It is obvious from Fig. 7b that δT gets saturated around I = 70 μJcm^{-2}, but the character of the magnetization precession does *not* remain the same and changes dramatically for I > 70 μJcm^{-2}. More specifically, the initial tilt of the magnetization reverses towards [001] crystallographic direction for excitation intensities I > 70 μJcm^{-2} (see Tesařová et *al.* [24] in Appendix 7), which is not possible in the case of thermally-induced magnetization precession. Fig. 7b also shows that despite the saturated temperature increase, the hole concentration (δp) increases further with the increasing laser intensity [24]. We note, that δp and its intensity dependence can be calculated from the energy absorbed from the laser light (assuming the absorption coefficient of GaAs) and the intensity dependence of the $\Delta R/R$ amplitude (since δp = δn_e after the impact of the laser pulse). The thermally inaccessible tilts of magnetization for

$I > 70\ \mu\text{Jcm}^{-2}$, together with the increasing carrier concentration points to a distinct, non-thermal mechanism of the magnetization precession.

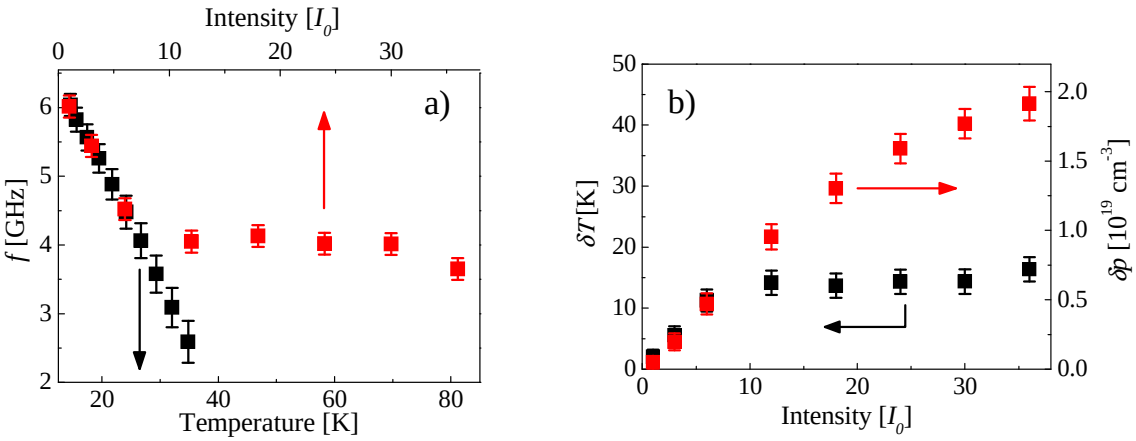

Fig. 7: a) Frequency of the magnetization precession as a function of the temperature (for $I_0 = 7\ \mu\text{Jcm}^{-2}$) and the excitation intensity (at sample temperature $T = 15$ K). b) The intensity dependence of the temperature increase (δT) and the excess hole concentration (δp) after the impact of the laser light. Experimental data were taken for (Ga,Mn)As sample with 3% Mn concentration.

5.2 Non-thermal origin

The non-thermal processes that lead to magnetization precession are caused by the photo-induced carriers and can be divided, regarding the polarization of the excitation light, into two groups – the polarization independent and the polarization dependent ones. In the later ones, the circularly polarized light generates carriers with the defined spin orientation [34] and the subsequent magnetization precession is caused by a transfer of the spin angular momentum from the photo-carriers to the magnetization. This effect, known as the optical spin transfer torque (OSST), was theoretically predicted several years ago [84], but it was experimentally observed only recently (by Němec et *al*. [21], see Appendix 6). On the other hand, the polarization independent processes can be observed for any polarization of light (i.e., also for the linearly polarized light). In this case, the magnetization precession occurs as a result of the carrier spin polarization caused by the relativistic spin-orbit coupling (SOC) among the photo-induced carriers in the spin-split energy band. The effect is called the optical spin-orbit torque (OSOT) and was for the first time ever observed by Tesařová et *al*. in [24] (see Appendix 7). Both of these non-thermal processes are described in more detail in the following sections.

5.2.1 Optical spin-orbit torque

The current induced spin-orbit torques (SOT), that were recently observed in (Ga,Mn)As, opened a new possibilities for further technological development, such as the extension of the operational capabilities in the electronic devices, or the unprecedented

characterizing techniques in material research [23, 85]. The OSOT is its optical analogue and it enables studying the magnetization-related phenomena on the time scales which are orders of magnitudes shorter than in the current induced SOT. This effect is based on the EA reorientation due to the optically induced change of the carrier concentration (holes in particular, since the electrons are weakly spin-orbit coupled) [24]. However, the reorientation of the EA and the subsequent initial tilt of magnetization can be in the opposite direction than in the case of the thermal mechanism, i.e. EA rotates towards the [010] and the magnetization tilts towards [001] crystallographic directions, respectively (compare with the thermal mechanism in Chap. 5.1). We note that the distinct character of magnetization dynamics, which can be determined from the analysis of magnetization real-space trajectory (described in Chap. 4), represents a straightforward method how to distinguish between the thermal and the non-thermal origin of magnetization precession. Such a simplified picture of the non-thermally induced oscillations of magnetization are in agreement with the theoretical calculations (based on the ***k.p*** kinetic exchange Hamiltonian) of the hole-concentration dependent EA position [41], but the detailed understanding of this effect requires more rigorous explanation, based on the SOC in the valance band.

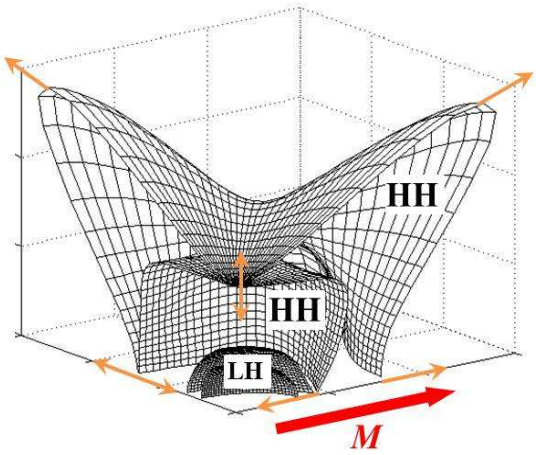

Fig. 8: Schematic illustration of the cross section of the Fermi volume in (Ga,Mn)As in the *k*-space. Non-zero magnetization (red arrow) leads to the anisotropic splitting of the valence bands into four subbands, two heavy (HH) and light (LH) holes bands. The direction of the hole spin orientation in different states on the Fermi surface is indicated by the orange arrows. [25]

Figure 8 shows the (Ga,Mn)As valance band (VB), where the magnetization leads to the anisotropic splitting of the VB into four bands – the spin-split heavy (HH) and light (LH) holes bands, respectively [25]. The SOC causes the change of the expected spin orientation along the top of the Fermi surface, which is essential for the occurrence of the magnetization torque and can be described as following. The impact of the linearly polarized laser light induces a non-equilibrium hole population. Since the angular momentum of light is zero, there is no momentum that could be transferred into the system, so the excited holes are not spin-polarized. However, the subsequent relaxation towards the spin-split Fermi sea of the equilibrium holes produces a non-equilibrium spin polarization, which is misaligned with the magnetization orientation. This photo-hole polarization can be perceived as an effective magnetic field that exerts a torque on the magnetization via the kinetic exchange coupling and leads to magnetization precession. It is important to note that in the case of *no* SOC, the only polarization that the holes could acquire would be parallel with magnetization orientation, which would exclude the existence of the torque. Despite the relatively simple physical origin of the OSOT, its quantitative description, involving the estimate of the hole polarization, is a

rather challenging problem. The exact theoretical treatment is complicated by the vast number of the non-equilibrium processes on the time scale of 10 – 100 femtoseconds after the impact of the laser pulse, that can influence the spin hole polarization before it is determined by the SOC. However, in the first approximation, the spin polarization of holes can be associated with the magnetic anisotropy field H_{an} [24]. In this approximation, the misalignment of the magnetization and the hole polarization has the same physical origin as the dependence of the magnetic EA orientation of the hole density [41].

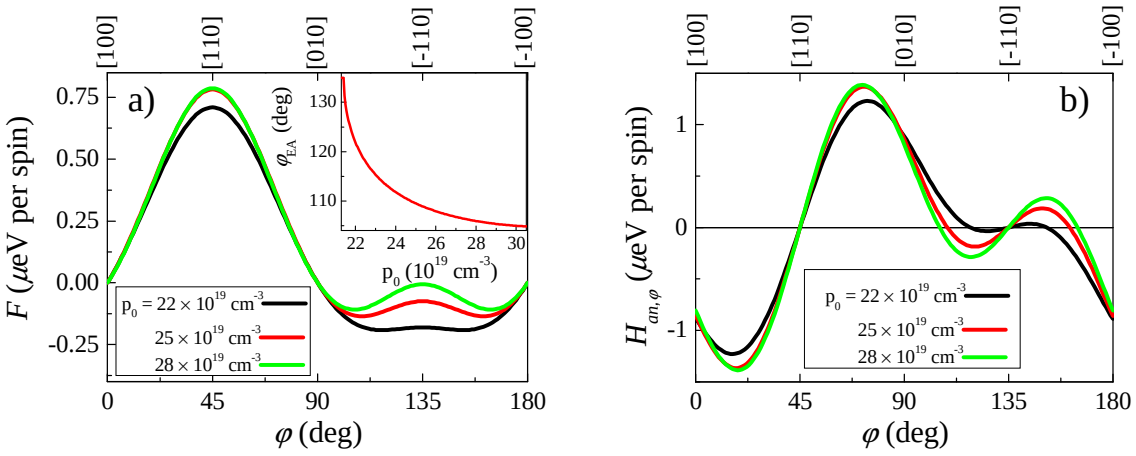

Fig. 9 Computed in-plane angular dependence of the free energy functional F (with respect to the energy along the crystallographic direction [100]) a) and the magnetic anisotropy field $H_{an,\varphi} = -\delta F/\delta\varphi$ b) in (Ga,Mn)As for different hole concentrations p_0. Inset: Dependence of the easy axis position on the concentration of holes. [Supplementary material in 24]

Figure 9a shows the in-plane dependence of the free energy functional F (see Chap. 2.3) in (Ga,Mn)As calculated for the different hole concentrations, where the minimum of F represents the equilibrium EA position (shown in the Inset). The impact of the laser pulse causes an increase of the hole concentration δp (with respect to hole concentration p_0 in dark), which leads to the in-plane movement of the EA and, consequently to the misalignment of the EA position and the magnetization orientation. These changes of the magnetic order give rise to the appearance of H_{an} ($H_{an,\theta} = -\partial F/\partial\theta$ and $H_{an,\varphi} = -\partial F/\partial\varphi$, see Ref. 24), which is non-zero in the plane of the sample (see Fig. 9b). The sign of the calculated H_{an} is consistent with the sense of the initial magnetization tilt observed in the experiments. The detailed derivation of the H_{an}, together with the additional analysis of the magnetization trajectory can be found in Ref. 24 (see Appendix 7).

5.2.2 Optical spin-transfer torque

The optical spin-transfer torque (OSTT) represents another non-thermal effect responsible for the magnetization dynamics after the impact of the laser light. Similarly to the OSOT, the magnetization oscillations are caused by the spin-momentum transfer from the carriers to the magnetization via the exchange coupling. The main difference between these two effects is that in the case of OSTT, the carriers acquire their spin polarization directly

from the circularly polarized light (and thus no SOC is needed for observing this effect). The detailed theoretical description of OSTT is given in Ref. 21 (see Appendix 6) and only a brief summary of this effect will be given here.

The circularly polarized light generates the spin-polarized carriers ($\delta n_e = \delta p < p_0$), where the carrier spin orientation (***n***) is parallel with the direction of the incident light and perpendicular to magnetization orientation (in the case of typical, compressively strained (Ga,Mn)As samples with the in-plane equilibrium position of ***M***), see Fig. 10. The appearance of the OSTT is conditioned by the relatively long spin lifetime of the photo-injected carriers [21] and only the photo-electrons spin lifetime of ~ 10 ps, which is given mainly by the interaction with Mn moments and by the electron recombination time, is sufficient to exert a torque on magnetization. The spin lifetime of holes is dominated by the strong SOC and it is estimated to be ~ 1 - 10 fs [84] which is not enough to cause the OSTT [21], so we will omit holes in further discussion.

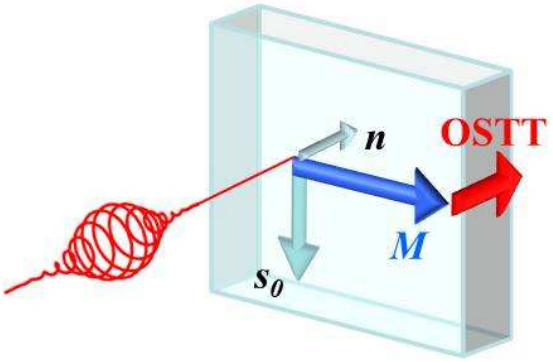

Fig. 10: Schematic illustration of the optical spin transfer torque. The circularly polarized light generates the carrier spin polarization, where the initial orientation of spins (***n***) is parallel with the incident light direction and perpendicular to magnetization (***M***). The steady-state component of the injected spin density ($\boldsymbol{s_0}$) is oriented in the sample plane, perpendicular to ***M***, and exerts a torque on the magnetization vector ***M***.

Right after the impact of the circularly polarized light, the orientation of the generated spins (***n***) is given by the propagation direction and by helicity of the circular polarization. However, the exchange field produced by the Mn moment yields the electron spins precession around the magnetization vector (***M***), with the precessing period ~ 100 fs [84]. As the electron spin lifetime highly exceeds this precession period, the spins precess many times before they relax. In this regime, the steady-state spin density ($\boldsymbol{s_0}$) is oriented in the plane of the sample, but perpendicular to ***M***, and exerts a torque on the magnetization vector, which leads to the subsequent precession of magnetization. It is important to note, that the OSTT starts to act during the laser pulse impact (when the electrons with a concentration δn_e are photoinjected) and fades away within the electron spin lifetime (~ picoseconds). However, the magnetization precession persists up to several nanoseconds. The influence of OSTT is, therefore, most clearly observable in the initial phase of the detected MO signal, see Ref. 21 in Appendix 6 for the measured magnetization trajectories.

6. Determination of micromagnetic parameters

The magnetic properties of any ferromagnetic material are described by the micromagnetic parameters, such as the magnetic anisotropy constants, spin stiffness or the Gilbert damping parameter. There are many different experimental methods that have been developed in order to measure these micromagnetic parameters. In particular, the ferromagnetic resonance (FMR), SQUID magnetometry or the magneto-transport measurements belong among the most commonly used ones [46, 47, 86]. However, it was shown recently by Němec et *al*. [33] (see Appendix 8) that the time-resolved MO spectroscopy can be also exploited in the investigation of the mentioned micromagnetic parameters of the ferromagnet. Moreover, this technique can overcome some of the limitations (e.g., the spatial resolution, the separation of the inhomogeneous contribution to the resonance linewidth, …) of the other experimental techniques [33, 82]. The aim of this chapter is to demonstrate the ability of this powerful technique to deduce all the micromagnetic parameters from a *single* MO pump-and-probe experiment.

Before proceeding to the determination of the anisotropy constants K_i, the Gilbert damping parameter α and the spin stiffness constant D, the analytical description of magnetization dynamics has to be performed as it forms the basis of the whole experimental method. The magnetization dynamics after the impact of the laser pulse can by described by the Landau-Lifshitz-Gilbert (LLG) equation:

$$\frac{d\boldsymbol{M}(t)}{dt} = -\gamma\left[\boldsymbol{M}(t) \times \boldsymbol{H_{eff}}(t)\right] + \frac{\alpha}{M_s}\left[\boldsymbol{M}(t) \times \frac{d\boldsymbol{M}(t)}{dt}\right], \tag{16}$$

where $\gamma = (g\mu_B)/\hbar$ is the gyromagnetic ratio with Landé g-factor $g = 2$ and Bohr magneton μ_B, $\boldsymbol{H_{eff}}$ is the effective magnetic field, α is the Gilbert damping constant and M_s is the saturated magnetization. Since the MO spectroscopy is sensitive both to the in-plane and out-of-plane positions of magnetization, it is convenient to rewrite the LLG equation into the spherical coordinates, characterized by the polar θ and azimuthal φ angles, respectively [43]:

$$\frac{dM_s}{dt} = 0, \tag{17}$$

$$\frac{d\theta}{dt} = -\frac{\gamma}{(1+\alpha^2)M_s}\left(\alpha \cdot A + \frac{B}{sin\theta}\right), \tag{18}$$

$$\frac{d\varphi}{dt} = -\frac{\gamma}{(1+\alpha^2)M_s sin\theta}\left(A - \frac{\alpha \cdot B}{sin\theta}\right), \tag{19}$$

where $A = dF/d\theta$ and $B = dF/d\varphi$ are the derivatives of the free energy functional F (see Eq. 1 in Chap. 2.3) with respect to θ and φ, respectively. For small deviations $\delta\theta$ and $\delta\varphi$ from their equilibrium values θ_0 and φ_0, the solution of Eqs. 18 and 19 can be written in the form $\theta(t) = \theta_0 + \delta\theta(t)$ and $\varphi(t) = \varphi_0 + \delta\varphi(t)$ as [Supplementary in 33, 43]:

$$\theta(t) = \theta_0 + A_\theta e^{-t/t_G} cos(2\pi f t + \Phi_\theta), \tag{20}$$

$$\varphi(t) = \varphi_0 + A_\varphi e^{-t/t_G} cos\big(2\pi f t + \Phi_\varphi\big), \tag{21}$$

where the constants A_θ (A_φ) and Φ_θ (Φ_φ) describe the initial amplitude and phase of θ (φ), respectively. For the typical geometry for the pump-and-probe experiment in (Ga,Mn)As with the in-plane position of magnetization (θ_0 = 90˚) and the external magnetic field applied also in-plane (θ_H = 90˚), the precession frequency and the damping time are given (assuming the relatively slow precession damping; α^2 = 0) [Supplementary in 33]:

$$f = \frac{g\mu_B}{h}\sqrt{\begin{matrix}\left[H_{ext}cos(\varphi-\varphi_H) - 2K_{out} + \frac{K_C(3+\cos 4\varphi)}{2} + 2K_u sin^2\left(\varphi - \frac{\pi}{4}\right)\right]\times \\ \times\left[H_{ext}cos(\varphi-\varphi_H) + 2K_c cos4\varphi - 2K_u sin2\varphi\right]\end{matrix}}, \tag{22}$$

$$\frac{1}{t_G} = \alpha\frac{g\mu_B}{2\hbar}\left(2H_{ext}cos(\varphi-\varphi_H) - 2K_{out} + \frac{K_c}{2}(3+5cos4\varphi) + K_u(1-3sin2\varphi)\right). \tag{23}$$

As seen from Eq. 22, the magnetization oscillation frequency reflects the sensitivity to the magnetic anisotropy of the material (described by the magnetic anisotropy constants K_i). This well-known fact is the basic principle of the FMR technique [47, 48] and will be also exploited in the time-resolved MO method (see Chap. 6.1). Equation 23 shows that the Gilbert damping time, which is measured experimentally (see Chap. 4.1), depends not only on the Gilbert damping parameter α, but also on the anisotropy constants and the mutual orientation of the external magnetic field and the magnetization. We note that the dependence of α on K_i was omitted in the previous publications [76, 77, 78] which may be the reason of the large scatter in the reported values of α.

6.1 Magnetic anisotropy constants

The dependence of the oscillation frequency on the magnetic anisotropy and on the external magnetic field magnitude and orientation enables the direct calculation of the anisotropy constants K_i from the measured time-resolved MO signal. In particular, for a sufficiently strong magnetic field, which aligns the magnetization into its direction (i.e., $\varphi = \varphi_H$), the following equations can be used to fit the obtained precession frequencies:

$$f = \frac{g\mu_B}{h}\sqrt{(H_{ext} - 2K_{out} + K_c)(H_{ext} - 2K_c - 2K_u)} \tag{24}$$

for H_{ext} along the [110] crystallographic direction (i.e. $\varphi_H = \pi/4$), or

$$f = \frac{g\mu_B}{h}\sqrt{(H_{ext} - 2K_{out} + 2K_c + K_u)(H_{ext} + 2K_c)} \tag{25}$$

for H_{ext} along the [010] crystallographic direction (i.e. $\varphi_H = \pi/2$), or

$$f = \frac{g\mu_B}{h}\sqrt{(H_{ext} - 2K_{out} + K_c + 2K_u)(H_{ext} - 2K_c + 2K_u)} \tag{26}$$

for H_{ext} along the [-110] crystallographic direction (i.e. $\varphi_H = 3\pi/4$).

In principle, only three precession frequencies in one magnetic field orientation are needed to obtain all three anisotropy constants K_c, K_u and K_{out}. However, the precision of the magnetic anisotropy determination can be increased when measuring the $f(H_{ext})$ dependence for at least two different orientations of H_{ext} as shown in Fig. 11a.

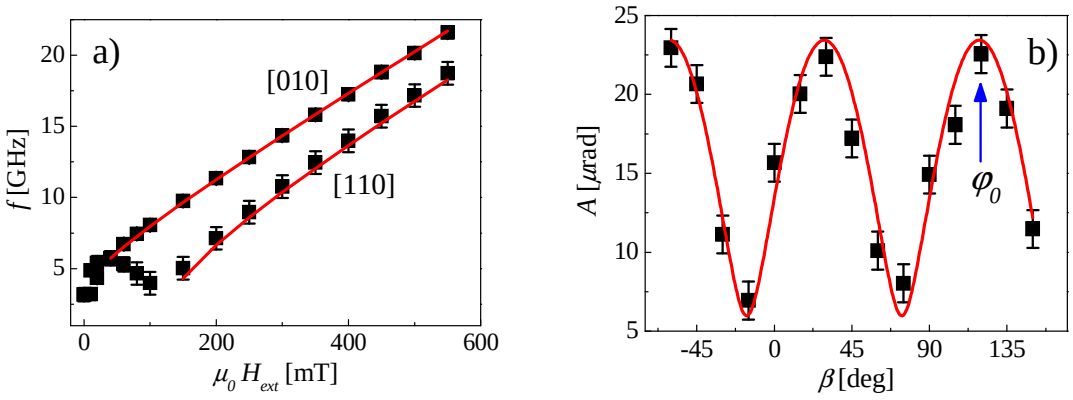

Fig. 11: a) Dependence of the magnetization precession frequency f on the external magnetic field H_{ext} applied along the [010] and [110] crystallographic directions; the red lines are the fits by Eqs. 24 and 25, respectively, with K_c = 31 mT, K_u = 27.5 mT and K_{out} = -190 mT. b) Probe polarization dependence of the oscillatory amplitude A obtained by fitting the measured MO signals by Eq. 7. The red line is the fit by Eq. 10 and the blue vertical arrow depicts the obtained equilibrium easy axis position $\varphi_0 \approx 120^\circ$. The measurements were performed in (Ga,Mn)As sample with 5.2% Mn concentration at the base temperature of 15 K.

The precision can be increased even further when the EA position of magnetization is known. In (Ga,Mn)As samples with the in-plane magnetization orientation, the position of the EA is given by the relative magnitude of K_c and K_u and, therefore, the knowledge of the EA position enables the direct determination of the ratio K_c/K_u. As mention in Chap. 4.2.2, the equilibrium position of the EA can be determined from the amplitude of the time-resolved MO signals when the magnetization dynamics are measured for the different orientations of the linearly polarized probe pulses β, see Fig. 11b.

6.2 Gilbert damping parameter α

The Gilbert damping constant α can be obtained from the numerical modeling of the measured MO data. In the first step, the time-dependent deviations of the spherical angles $[\delta\theta(t), \delta\varphi(t)]$ from their equilibrium values θ_0 and φ_0 are computed by the LLG equation (Eqs. 18 and 19), using the determined anisotropy constants K_i. In the second step it is calculated how such changes of θ and φ modify the static MO response of the sample MO^{stat}, which is the measured signal represented by Eq. 12 in Chap. 4.2.3. The data can be reliably modeled from the time delays ~ 100 ps when the quasi-equilibrium precession of magnetization is established. The only parameters in this modeling procedure are the Gilbert damping coefficient α, the initial deviation of the spherical angles from the corresponding equilibrium positions and the parameters describing the in-plane movement of the easy axis and the

demagnetization signal, which are apparent as the non-oscillatory signal in the measured magnetization dynamics (see Eq. 2 in Chap. 4.1). We note that the magnitude of the initial deviation of the spherical angles, calculated in the model, is strongly dependent on the input value of the static MO coefficients P^{PKE} and P^{MLD}. However, the values of the MO coefficients, which are always measured with some precision, has no influence on the determined value of α. Applying this modeling procedure, the dependence of α on the external magnetic field H_{ext} or on the oscillation frequency f can be obtained, respectively (see Fig. 4 in Appendix 8).

In contrast to the theoretical predictions that α does not depend on the oscillation frequency [87], we observed experimentally that in (Ga,Mn)As α decreases monotonously with increasing oscillation frequency [33] and saturates for $f > 15$ GHz [33], which is in accord with the results reported for other ferromagnetic materials [88, 89]. The most probable explanation of this effect was given by Walowski *et al.* in Ref. 88, where it was assumed that in the low field range (low precession frequency) the small magnetization inhomogeneities can be build, meaning that the magnetization is not fully aligned with H_{ext} but forms ripples. Consequently, the measured MO signal, which detects sample properties averaged over the laser spot size, experiences apparent oscillation damping α, because the magnetic properties (i.e. the precession frequencies) are slightly different within the spot size. On the other hand, for stronger external fields the sample is fully homogeneous and, therefore, the precession damping is not dependent on the applied field. It was found that for (Ga,Mn)As samples the frequency-independent Gilbert damping is strongly dependent on the Mn concentration and it decreases systematically from 0.1 to 0.01 when the nominal Mn concentration increases from 2% to 9% [33] (see Fig. 4b in Appendix 8).

6.3 Spin stiffness

The spin stiffness, which describes the exchange energy associated with the twist of the spins, is one of the most important material parameters that characterize the magnetic properties of a ferromagnet. So far, the spin stiffness in (Ga,Mn)As was typically obtained from the measurements of the spin precession modes by the FMR technique [90, 91]. The precession modes represent the spin wave resonances (SWRs, also known as magnons) that are selectively amplified by fulfilling the boundary conditions of the thin FM film (see e.g. Ref. 43 for detailed discussion). In FMR the SWRs are investigated in the frequency-domain, where they manifest as the multiple absorption peaks in the spectra. However, the SWRs can be also studied in the time-domain by the time-resolved MO spectroscopy [33, 92], where they are apparent as the additional frequencies (f_n) that are larger than that of the uniform magnetization precession (f_0), see Fig. 5 in Appendix 8. For the external magnetic field H_{ext} applied in the sample plane, the angular frequency of the n-th SWR mode f_n is given [33, 92]:

$$f_n = \frac{g\mu_B}{h}\sqrt{\begin{matrix}\left[H_{ext}cos(\varphi-\varphi_H) - 2K_{out} + \frac{K_C(3+\cos 4\varphi)}{2} + 2K_u sin^2\left(\varphi-\frac{\pi}{4}\right)\right]\times \\ \times\left[H_{ext}cos(\varphi-\varphi_H) + 2K_c cos4\varphi - 2K_u sin2\varphi\ +\ \Delta H_n\right]\end{matrix}}, \qquad (27)$$

where $\Delta H_n = H_0 - H_n$ is the shift of the resonant field for the higher index n spin wave modes with respect to the uniform precession mode $n = 0$. For the magnetically homogeneous films, the value of ΔH_n is given by the Kittel relation [90]:

$$\Delta H_n = H_0 - H_n = n^2 \frac{D}{g\mu_B} \frac{\pi^2}{L^2}, \tag{28}$$

where D is the exchange spin stiffness constant, μ_B is the Bohr magneton, g is the Lande g-factor and L is the thickness of the magnetic film. This equation is of high importance as it enables an evaluation of the spin stiffness D from the field differences ΔH_n that can be obtained from the measured frequency spacing of the individual modes (see Eq. 27). It is important to emphasize that Eq. 28 is only valid for the magnetically homogenous films, i.e. for films where the (Ga,Mn)As layer thickness does not exceed ~ 50 nm [32, 33, 43].

Let's now proceed to the exact procedure how the spin stiffness parameter D can be obtained from the time-resolved MO signal. For this purpose, the detection of *at least* one additional SWR, together with the uniform precessional mode $n = 0$, is inevitable, but the more SWRs are detected the more precise determination of D can be performed. We note that multiple SWRs can be observed in thick (Ga,Mn)As samples ($L \geq 50$ nm) [43, 90], but not all of them could be ascribed to Kittel modes, most probably because of the magnetic inhomogeneity of the magnetic layer [43]. Consequently, it is a rather delicate task to evaluate the value of D because the measurement has to be performed on a thick enough film to observe a multiple SWRs but thin enough to prevent its magnetic inhomogeneity. In magnetically homogeneous (Ga,Mn)As samples ($L \leq 50$ nm) we observed three SWRs at most [33, 43]. We note that the most precise procedure how the precession frequencies f_n can be evaluated from the measured MO data is from the Fourier spectra of the oscillatory part of the MO signals. The values H_n can be obtained from the measured dependencies $f_n(H_{ext})$ - for a sufficiently high H_{ext}, the equilibrium position of the EA is aligned with H_{ext} (i.e., $\varphi = \varphi_H$) and the measured $f_n(H_{ext})$ dependencies can be fitted by Eq. 27 for each n, obtaining the only unknown parameter ΔH_n. Finally, the spin stiffness coefficient D can be determined from Eq. 28.

We used this method in the optimized set of (Ga,Mn)As samples and we observed that the spin stiffness parameter D is a weakly increasing function of the Mn doping, with the values of D between 2 and 3 meVnm^2 for the studied samples with the nominal Mn doping from 3.8% to 9%, see Ref. 33 in Appendix 8, where all the results are summarized.

CONCLUSIONS

The ferromagnetic semiconductor (Ga,Mn)As is a very interesting material for the spintronics. Not only it is a material where the proof-of-concept spintronic devices can be realized, but it is also a good model material where new physical phenomena can be discovered and thoroughly studied, and the gained knowledge can be subsequently transferred to conventional room-temperature ferromagnetic metals. The aim of this doctoral thesis was to investigate the magnetic properties of (Ga,Mn)As. We focused mainly on the magnetization dynamics induced by the impact of the ultrashort laser pulses, because the ultrafast manipulation with the magnetic order is of high importance for future envisioned spintronic devices.

We studied an extensive set of high quality (Ga,Mn)As samples with Mn doping ranging from 1.5% to 14%. Using the time-resolved magneto-optical (MO) spectroscopy we observed the laser-induced precession of magnetization in all the samples, except in those with the lowest and the highest Mn concentration, where the magnetic anisotropy was too strong to be significantly influenced by the impact of the laser pulse. We used the magnetic anisotropy-related precession of magnetization as a spectroscopic method for evaluation of all the basic micromagnetic parameters of (Ga,Mn)As – the magnetic anisotropy constants, the Gilbert damping coefficient, and the spin stiffness – from one single set of experimental data. We found a clear monotonous dependence of these parameters on Mn doping, i.e., on the hole concentration and magnetization magnitude, which can be of practical use in the material property engineering.

Moreover, the detailed analysis of the measured MO signals enabled us to establish a new experimental method that can be used for a determination of the real-space magnetization trajectory without any numerical modeling. This real-space magnetization dynamics contributed significantly to our understanding of the mechanism of the laser-induced magnetization dynamics. In particular, we revealed that it can be either of thermal or of non-thermal origin, depending on the light intensity and polarization state. The understanding of these mechanisms enabled us to identify two new physical phenomena – the optical spin transfer torque and the optical spin-orbit torque, which were theoretically predicted but so far experimentally unobserved. Both these effects can have a large impact on the basic research towards the development of the future spintronic applications because they act on a timescale that is several orders of magnitude shorter than in the case of their current-induced counterparts.

BIBLIOGRAPHY

[1] W. M. Chen, I. A. Buyanova: *Handbook of Spintronic Semiconductors*. Pan Stanford Publishing (2010).

[2] D. Awschalom, M. F. Flatté: *Challenges for semiconductor spintronics*. Nat. Phys. **3**, 153 (2007).

[3] I. Žutić, J. Fabian, S. Das Sarma: *Spintronics: Fundamentals and Applications.* Rev. Mod. Phys. **76,** 323 (2004).

[4] Editorial: *More than just room temperature*. Nat. Mater. **9**, 951 (2010).

[5] A.V. Kimel, G.V. Astakhov, A. Kirilyuk, G. M. Schott, G. Karczewski, W. Ossau, G. Schmidt, L.W. Molenkamp, Th. Rasing: *Observation of Giant Magnetic Linear Dichroism in (Ga,Mn)As.* Phys. Rev. Lett. **94**, 227203 (2005).

[6] H. Ohno: *Making Nonmagnetic Semiconductors Ferromagnetic*. Science **281**, 951 (1998).

[7] J. K. Furdyna: *Diluted magnetic semiconductors*. J. Appl. Phys. **64**, R29 (1988).

[8] V. Novák, K. Olejník, J. Wunderlich, M. Cukr, K. Výborný, A. W. Rushforth, K. W. Edmonds, R. P. Campion, B. L. Gallagher, J. Sinova, T. Jungwirth: *Curie point singularity in the temperature derivative of resistivity in (Ga,Mn)As*. Phys. Rev. Lett. **101**, 077201 (2008).

[9] M. Wang, R. P. Campion, A. W. Rushforth, K. W. Edmonds, C. T. Foxon, B. L. Gallagher: *Achieving high Curie temperature in (Ga,Mn)As*. Appl. Phys. Lett. **93**, 132103 (2008).

[10] H. Ohno: *A window on the future of spintronics*. Nat. Mater. **9**, 952 (2010).

[11] H. Ohno, D. Chiba, F. Matsukura, T. Omiya, E. Abe, T. Dietl, Y. Ohno, K. Ohtani: *Electric-field control of ferromagnetism*. Nature **408**, 944 (2000).

[12] N. Samarth: *A model ferromagnetic semiconductor*. Nat. Mater. **9**, 955 (2010).

[13] M. Tanaka, Y. Higo: *Large Tunneling Magnetoresistance in GaMnAs/AlAs/GaMnAs Ferromagnetic Semiconductor Tunnel Junctions*. Phys. Rev. Lett. **87**, 026602 (2001).

[14] H. Saito, S. Yuasa, K. Ando: *Origin of the Tunnel Anisotropic Magnetoresistance in* $Ga_{1-x}Mn_xAs/ZnSe/Ga_{1-x}Mn_xAs$ *Magnetic Tunnel Junction of II-VI/III-V Heterostructures*. Phys. Rev. Lett. **95**, 086604 (2005).

[15] J. Sinova, I. Žutić: *New moves of the spintronics tango*. Mat. Matter. **11**, 368 (2012).

[16] C. Gould, C. Ruster, T. Jungwirth, E. Girgis, G. M. Schott, R. Giraud, K. Brunner, G. Schmidt, L. W. Molenkamp: *Tunneling Anisotropic Magnetoresistance: A Spin-Valve-Like Tunnel Magnetoresistance Using a Single Magnetic Layer*. Phys. Rev. Lett. **93**, 117203 (2004).

[17] B. G. Park, J. Wunderlich, X. Martí, V. Holý, Y. Kurosaki, M. Yamada, H. Yamamoto, A. Nishide, J. Hayakawa, H. Takahashi, A. B. Shick, T. Jungwirth: *A spin-valve-like magnetoresistance of an antiferromagnet-based tunnel junction*. Nat. Matter. **10**, 347 (2011).

[18] J. Wunderlich, T. Jungwirth, B. Kaestner, A. C. Irvine, A. B. Shick, N. Stone, K.-Y. Wang, U. Rana, A. D. Giddings, C. T. Foxon, R. P. Campion, D. A. Williams, B. L. Gallagher: *Coulomb Blockade Anisotropic magnetoresistance Effect in a (Ga,Mn)As Single-Electron Transistor*. Phys. Rev. Lett. **97**, 077201 (2006).

[19] S. Mark, P. Durrenfeld, K. Pappert, L. Ebel, K. Brunner, C. Gould, L. W. Molenkamp: *Fully Electrical Read-Write Device Out of a Ferromagnetic Semiconductor*. Phys. Rev. Lett. **106**, 057204 (2011).

[20] D. C. Ralpha, M. D. Stiles: *Spin transfer torques*. J. Magn. Magn. Matter. **320**, 1190 (2008).

[21] P. Němec, E. Rozkotová, N. Tesařová, F. Trojánek, E. De Ranieri, K. Olejník, J. Zemen, V. Novák, M. Cukr, P. Malý, T. Jungwirth: *Experimental observation of the optical spin transfer torque*. Nat. Phys. **8**, 411 (2012).

[22] A. Brataas, A. D. Kent, H. Ohno*: Current-induced torques in magnetic materials*. Nat. Matter. **11**, 372 (2012).

[23] A. Chernyshov, M. Overby, Y. Lyanda-Geller, L. P. Rokhinson: *Evidence for reversible control of magnetization in a ferromagnetic material via spin-orbit magnetic field*. Nat. Phys. **5**, 656 (2009).

[24] N. Tesařová, P. Němec, E. Rozkotová, J. Zemen, T. Janda, D. Butkovičová, F. Trojánek, K. Olejník, V. Novák, P. Malý, T. Jungwirth: *Experimental observation of the optical spin-orbit torque*. Submitted to Nature Photonics, arXiv: 1207.0307.

[25] T. Dietl, H. Ohno, F. Matsukura, J. Cibert, D. Ferrand: *Zener Model Description of Ferromagnetism in Zinc-Blende Magnetic Semiconductors*. Science **287**, 1019 (2000).

[26] M. Dobrowolska, K. Tivakornsasithorn, X. Liu, J. K. Furdyna, M. Berciu, K. M. Yu, W.Walukiewicz: *Controlling the Curie temperature in (Ga,Mn)As through location of the Fermi level within the impurity band*. Nat. Matter. **11**, 444 (2012).

[27] T. Jungwirth, J. Sinova, A. H. MacDonald, B. L. Gallagher, V. Novák, K. W. Edmonds, A. W. Rushforth, R. P. Campion, C. T. Foxon, L. Eaves, E. Olejník, J. Mašek, S.-R. Eric Yang, J. Wunderlich, C. Gould, L. W. Molenkamp, T. Dietl, H. Ohno: *Character of states near the Fermi level in (Ga,Mn)As: Impurity to valence band crossover*. Phys. Rev. B **76**, 125206 (2007).

[28] T. Jungwirth, J. Sinova, J. Mašek, J. Kučera, A. H. MacDonald: *Theory of ferromagnetic III-V semiconductors.* Rev. Mod. Phys. **78,** 809 (2006).

[29] T. Jungwirth, K. Y. Wang, J. Mašek, K. W. Edmonds, J. König, J. Sinova, M. Polini, N. A. Goncharuk, A. H. MacDonald, M. Sawicki, A. W. Rushforth, R. P. Campion, L. X. Zhao, C. T. Foxon, B. L. Gallagher: *Prospects for high temperature ferromagnetism in (Ga,Mn)As semiconductors*. Phys. Rev. B **72**, 165204 (2005).

[30] Th. Hartmann, S. Ye, P. J. Klar, W. Heimbrodt, M. Lampalzer, W. Stolz, T. Kurz, A. Loidl, H.-A. Krug von Nidda, D. Wolverson, J. J. Davies, H. Overhof: *Tuning of the average p-d exchange in (Ga,Mn)As by modification of the Mn electronic structure*. Phys. Rev. B **70**, 233201 (2004).

[31] K. S. Burch, D. D. Awschalom, D. N. Basov: *Optical properties of III-Mn-V ferromagnetic semiconductors*. J. Magn. Magn. Matter. **320**, 3207 (2008).

[32] T. Jungwirth, P. Horodyská, N. Tesařová, P. Němec, J. Šubrt, P. Malý, P. Kužel, C. Kadlec, J. Mašek, I. Němec, M. Orlita, V. Novák,1 K. Olejník, Z. Šrobáň , P. Vašek, P. Svoboda, J. Sinova: *Systematic Study of Mn-Doping Trends in Optical Properties of (Ga,Mn)As*. Phys. Rev. Lett. **105**, 227201 (2010).

[33] P. Němec, V. Novák, N. Tesařová, E. Rozkotová, H. Reichlová, D. Butkovičová, F. Trojánek, K. Olejník, P. Malý, R. P. Campion, B. I. Gallagher, J. Sinova, T. Jungwirth: *Establishing micromagnetic parameters of ferromagnetic semiconductor (Ga,Mn)As*. Accepted in Nature Communications, arXiv: 1207.0310.

[34] M. I. Dyakonov: *Spin physics in semiconductors.* Springer-Verlag, Berlin - Heidelberg, 2009.

[35] P. Y. Yu, M. Cardona: *Fundametals of Semiconductors*, Springer (1996).

[36] J. Mašek, F. Máca, J. Kudrnovský, O. Makarovsky, L. Eaves, R. P. Campion, K.W. Edmonds, A.W. Rushforth, C. T. Foxon, B. L. Gallagher, V. Novák, J. Sinova, T. Jungwirth: *Microscopic Analysis of the Valence Band and Impurity Band Theories of (Ga,Mn)As*. Phys. Rev. Lett. **105**, 227202 (2010).

[37] K. Ando, H. Saito, K. C. Agarwal, M. C. Debnath, V. Zayets: *Origin of the Anomalous Magnetic Circular Dichroism Spectral Shape in Ferromagnetic $Ga_{1-x}Mn_xAs$: Impurity Bands inside the Band Gap*. Phys. Rev. Lett. **100**, 067204 (2008).

[38] K. S. Burch, D. B. Shrekenhamer, E. J. Singley, J. Stephens, B. L. Sheu, R. K. Kawakami, P. Schiffer, N. Samarth, D. D. Awschalom, D. N. Basov: *Impurity Band Conduction in a High Temperature Ferromagnetic Semiconductor*. Phys. Rev. Lett. **97**, 087208 (2006).

[39] M. J. Tang, M. E. Flatté: *Magnetic Circular Dichroism from the Impurity Band in III-V Diluted Magnetic Semiconductors*. Phys. Rev. Lett. **101**, 157203 (2008).

[40] S. Ohya, K. Takata, M. Tanaka: *Nearly non-magnetic valence band of the ferromagnetic semiconductor GaMnAs*. Nat. Phys. **7**, 342 (2011).

[41] J. Zemen, J. Kučera, K. Olejník, T. Jungwirth: *Magnetocrystalline anisotropies in (Ga,Mn)As: Systematic theoretical study and comparison with experiment.* Phys. Rev. B **80,** 155203 (2009).

[42] M. Birowska, C. Śliwa, J. A. Majewski, T. Dietl: *Origin of bulk uniaxial anisotropy in zinc-blende dilute magnetic semiconductors*. Phys. Rev. Lett. **108**, 237203 (2012).

[43] E. Schmorazerová: *Spin dynamics in GaAs-based semiconductor structures.* Doctoral thesis, Charles University in Prague, Prague (2012).

[44] M. Abolfath, T. Jungwirth, J. Brum, A. H. MacDonald: *Theory of magnetic anisotropy in $III_{1-x}Mn_xV$ ferromagnets*. Phys. Rev. B **63**, 054418 (2001).

[45] K. Hamaya, T. Watanabe, T. Taniyama, A. Oiwa, Y. Kitamoto, Y. Yamazaki: *Magnetic anisotropy switching in (Ga,Mn)As with increasing hole concentration*. Phys. Rev. B **74**, 045201 (2006).

[46] K. Olejník: *Preparation and characterization of ferromagnetic GaMnAs epilayers.* Doctoral thesis, Charles University in Prague, Prague (2009).

[47] X. Liu, J. K. Furdyna: *Ferromagnetic resonance in $Ga_{1-x}Mn_xAs$ dilute magnetic semiconductors*. J. Phys.: Condens. Matter **18**, R245 (2006).

[48] K. Khazen: *Ferromagnetic Resonance Investigation of GaMnAs Nanometric Layers.* Doctoral thesis, Université Paris VI - Pierre et Marie Curie Institut des NanoSiences de Paris, Paris (2008).

[49] C. S. King, J. Zemen, K. Olejník, L. Horák, J. A. Haigh, V. Novák, A. Irvine, J. Kučera, V. Holý: *Strain control of magnetic anisotropy in (Ga,Mn)As microbars*. Phys. Rev. B **83**, 115312 (2011).

[50] B. Beschoten, P. A. Crowell, I. Malajovich, D. D. Awschalom: *Magnetic Circular Dichroism Studies of Carrier-Induced Ferromagnetism in $(Ga_{1-x}Mn_x)As$*. Phys. Rev. Lett. **83**, 3073 (1999).

[51] T. Kuroiwa, T. Yasuda, F. Matsukura, A. Shen, Y. Ohno, Y. Segawa, H. Ohno: *Faraday rotation of ferromagnetic (Ga, Mn)As*. Electron. Lett. **34**, 190 (1998).

[52] A.V. Kimel, G.V. Astakhov, A. Kirilyuk, G. M. Schott, G. Karczewski, W. Ossau, G. Schmidt, L.W. Molenkamp, Th. Rasing: *Observation of Giant Magnetic Linear Dichroism in (Ga,Mn)As*. Phys. Rev. Lett. **94**, 1227203 (2005).

[53] G. Acbas, M.-H. Kim, M. Cukr, V. Novák, M. A. Scarpulla, O. D. Dubon, T. Jungwirth, J. Sinova, J. Cerne: *Electronic Structure of Ferromagnetic Semiconductor $Ga_{1-x}Mn_xAs$ Probed by Subgap Magneto-optical Spectroscopy*. Phys. Rev. Lett. **103**, 137201 (2009).

[54] A. K. Zvezdin, V. A. Kotov: *Moderen Magnetooptics and Magnetooptical Materials.* Institute of Physics, Bristol, Philadelphia (1997).

[55] K. Postava, J. Pištora: *Magneto-optical effects in thin films*. Sborník vědeckých prací Vysoké školy báňské – Technické Univerzity Ostrava, číslo 1, ročník XLV (1999).

[56] R. Lang, A. Winter, H. Pascher, H. Krenn, X. Liu, J. K. Furdyna: *Polar Kerr effect studies of $Ga_{1-x}Mn_xAs$ epitaxial films*. Phys. Rev. B **72**, 024430 (2005).

[57] D. Hrabovsky, E. Vanelle, A. R. Fert, D. S. Yee, J. P. Redoules, J. Sadowski, J. Kanski, L. Ilver: *Magnetization reversal in GaMnAs layers studied by Kerr effect*. Appl. Phys. Lett. **81**, 2806 (2002).

[58] M.-H. Kim, G. Acbas, M.-H. Yang, M. Eginligil, P. Khalifah, I. Ohkubo, H. Christen, D. Mandrus, Z. Fang, J. Cerne: *Infrared anomalous Hall effect in SrRuO3: Exploring evidence for crossover to intrinsic behavior*. Phys. Rev. B **81**, 235218 (2010).

[59] E. Rozkotová, P. Němec, P. Horodyská, D. Sprinzl, F. Trojánek, P. Malý, V. Novák, K. Olejník, M. Cukr, T. Jungwirth: *Light-induced magnetization precession in GaMnAs*. Appl. Phys. Lett. **92**, 122507 (2008).

[60] E. Rozkotová, P. Němec, N. Tesařová, P. Malý, V. Novák, K. Olejník, M. Cukr, T. Jungwirth: *Coherent control of magnetization precession in ferromagnetic semiconductor (Ga,Mn)As*. Appl. Phys. Lett. **93**, 232505 (2008).

[61] J. Qi, Y. Xu, A. Steigerwald, X. Liu, J. K. Furdyna, I. E. Perakis, N. H. Tolk: *Ultrafast laser-induced coherent spin dynamics in ferromagnetic $Ga_{1-x}Mn_xAs/GaAs$ structures*. Phys. Rev. B **79**, 085304 (2009).

[62] R. M. Osgood, S. D. Bader, B. M. Clemens, R. L. White, H. Matsuyama: *Second-order magneto-optic effects in anisotropic thin films*. J. Magn. Magn. Mater. **182**, 297 (1998).

[63] K. Postava, H. Jaffres, A. Schuh, F. Nguyen Van Dau, M. Goiran, A.R. Fert: *Linear and quadratic magneto-optical measurements of the spin reorientation in epitaxial Fe films on MgO*. J. Magn. Magn. Mater. **172**, 199 (1997).

[64] G. P. Moore, J. Ferré, A. Mougin, M. Moreno, L. Daweritz: *Magnetic anisotropy and switching process in diluted $Ga_{1-x}Mn_xAs$ magnetic semiconductor films*. J. Appl. Phys. **94**, 4530 (2003).

[65] N. Tesařová, J. Šubrt, P. Malý, P. Němec, C. T. Ellis, A. Mukherjee, J. Cerne: *High Precision Magnetic Linear Dichroism Measurements in (Ga,Mn)As*. Accepted in Rev. Sci. Intrum., arXiv: 1212.0956.

[66] N. Tesařová, P. Němec, E. Rozkotová, J. Šubrt, H. Reichlová, D. Butkovičová, F. Trojánek, P. Malý, V. Novák, T. Jungwirth: *Direct measurement of the three-dimensional magnetization vector trajectory in GaMnAs by a magneto-optical pump-and-probe method*. Appl. Phys. Lett. **100**, 102403 (2012).

[67] E. De Ranieri, A. W. Rushforth, K. Výborný, U. Rana, E. Ahmad, R. P. Campion, C. T. Foxon, B. L. Gallagher, A. C. Irvine, J. Wunderlich, T. Jungwirth: *Lithographically and electrically controlled strain effects on anisotropic magnetoresistance in (Ga,Mn)As*. New J. Phys. **10**, 065003 (2008).

[68] B. Al-Qadi, N. Nishizawa, K. Nishibayashi, M. Kaneko, H. Munekata: *Thickness dependence of magneto-optical effects in (Ga,Mn)As epitaxial layers*. Appl. Phys. Lett. **100**, 222410 (2012).

[69] A. Kirilyuk, A.V. Kimel, T. Rasing: *Ultrafast optical manipulation of magnetic order*. Rev. Mod. Phys. **80**, 2731 (2010).

[70] G. E. Rowlands, T. Rahman, J. A. Katine, J. Langer, A. Lyle, H. Zhao, J. G. Alzate, A. A. Kovalev, Y. Tserkovnyak, Z. M. Zeng, H. W. Jiang, K. Galatsis, Y. M. Huai, P. Khalili Amiri, K. L. Wang, I. N. Krivorotov, J.-P. Wang: *Deep subnanosecond spin torque switching in magnetic tunnel junctions with combined in-plane and perpendicular polarizers*. Appl. Phys. Lett. **98**, 102509 (2011).

[71] E. Beaurepaire, J.-C. Merle, A. Daunois, J.-Y. Bigot: *Ultrafast Spin Dynamics in Ferromagnetic Nickel*. Phys. Rev. Lett. **76**, 4250 (1996).

[72] J. Wang, Ch. Sun, Y. Hashimoto, J. Kono, G. A. Khodaparast, L. Cywinski, L. J. Sham, G. D. Sanders, Ch. J. Stanton, H. Munekata: *Ultrafast magneto-optics in ferromagnetic III–V semiconductors*. J. Phys. Cond. Matt. **18**, R501 (2006).

[73] E. Kojima, R. Shimano, Y. Hashimoto, S. Katsumoto, Y. Iye, M. Kuwata-Gonokami: *Observation of the spin-charge thermal isolation of ferromagnetic $Ga_{0.94}Mn_{0.06}As$ by time-resolved magneto-optical measurements*. Phys. Rev. B **68**, 193203 (2003).

[74] A. Oiwa, H. Takechi, H. Munekata: *Photoinduced magnetization rotation and precessional motion of magnetization in ferromagnetic (Ga,Mn)As.* J. Supercond. **19**, 9 (2005).

[75] J. Wang, I. Cotoros, K. M. Dani, X. Liu, J. K. Furdyna, D. S. Chemla: *Ultrafast Enhancement of Ferromagnetism via Photoexcited Holes in GaMnAs.* Phys. Rev. Lett. **98**, 217401 (2007).

[76] J. Qi, Y. Xu, N. H. Tolk, X. Liu, J. K. Furdyna, I. E. Perakis*: Coherent magnetization precession in GaMnAs induced by ultrafast optical excitation*. Appl. Phys. Lett. **91**, 112506 (2007).

[77] Y. Hashimoto, S. Kobayashi, H. Munekata: *Photoinduced precession of magnetization in ferromagnetic (Ga,Mn)As*. Phys. Rev. Lett. **100,** 067202 (2008).

[78] S. Kobayashi, Y. Hashimoto, H. Munekata: *Investigation of an eff ective anisotropy field involved in photoinduced precession of magnetization in (Ga,Mn)As.* J. Appl. Phys. **105**, 07C519 (2009).

[79] N. Tesařová, P. Němec, E. Rozkotová, F. Trojánek, P. Malý: *Light-Induced Precession of Magnetization in Ferromagnetic Semiconductor (Ga,Mn)As.* Acta Phys. Polon. A **118**, 1065 (2010).

[80] E. Rozkotová, P. Němec, D. Sprinzl, P. Horodyská, F. Trojánek, P. Malý, V. Novák, K. Olejník, M. Cukr, T. Jungwirth: *Laser-Induced Precession of Magnetization in GaMnAs*. IEEE Trans. Magn. **44**, 2674 (2008).

[81] H. Takechi, A. Oiwa, K. Nomura, T. Kondo, H. Munekata: *Light-induced precession of ferromagnetically coupled Mn spins in ferromagnetic (Ga,Mn)As.* Phys. Stat. Sol. (c) **3**, 4267 (2006).

[82] N. Tesařová, E. Rozkotová, H. Reichlová, P. Malý, V. Novák, M. Cukr,T. Jungwirth, P. Němec*: Influence of Magnetic Anisotropy on Laser-Induced Precession of Magnetization in Ferromagnetic Semiconductor (Ga, Mn)As*. J. Nanosc. Nanotechnol. **12**, 7477 (2012).

[83] Shah J.: *Ultrafast spectroscopy of semiconductors and semiconductor nanostructures*. Springer-Verlag, Berlin, Heidelberg, New York, 1996.

[84] J. Fernandez-Rossier, A. S. Nunez, M. Abolfath, and A. H. MacDonald: *Optical spin transfer torque in ferromagnetic semiconductors.* http://arxiv.org/abs/cond-mat/0304492.

[85] D. Fang, H. Kurebayashi, J. Wunderlich, K. Výborný, L. P. Zarbo, R. P. Campion, A. Casiraghi, B. L. Gallagher, T. Jungwirth, A. J. Ferguson: *Spin-orbit driven ferromagnetic resonance: A nanoscale magnetic characterisation technique*. Nat. Nanotechnol. **6**, 413 (2011).

[86] Kh. Khazen, H. J. von Bardeleben, M. Cubukcu, J. L. Cantin, V. Novak, K. Olejnik, M. Cukr, L. Thevenard, A. Lemaître: *Anisotropic magnetization relaxation in ferromagnetic $Ga_{1-x}Mn_xAs$ thin films*. Phys. Rev. B **78**, 195210 (2008).

[87] J. Sinova, T. Jungwirth, X. Liu, Y. Sasaki, J. K. Furdyna, W. A. Atkinson, A. H. MacDonald: *Magnetization relaxation in (Ga,Mn)As ferromagnetic semiconductors*. Phys. Rev. B **69**, 085209 (2004).

[88] J. Walowski, M. Djordjevic Kaufmann, B. Lenk, C. Hamann, J. McCord, M. Munzenberg: *Intrinsic and non-local Gilbert damping in polycrystalline nickel studied by Ti : sapphire laser fs spectroscopy*. J. Phys. D: Appl. Phys. **41**, 164016 (2008).

[89] A. A. Rzhevsky, B. B. Krichevtsov, D. E. Bürgler, C. M. Schneider: *Magnetization dynamics induced by ultrashort optical pulses in Fe/Cr thin films.* Phys. Rev. B **75**, 224434 (2007).

[90] X. Liu, Y. Y. Zhou, J. K. Furdyna: *Angular dependence of spin-wave resonances and surface spin pinning in ferromagnetic (Ga,Mn)As films*. Phys. Rev. B **75**, 195220 (2007).

[91] C. Bihler, W. Schloch, W. Limmer, S. T. B. Goennenwein, M. S. Brandt: *Spin-wave resonances and surface spin pinning in $Ga_{1-x}Mn_xAs$ thin films*. Phys. Rev. B **79**, 045205 (2009).

[92] D.M. Wang, Y.H. Rena, X. Liu, J.K. Furdyna, M. Grimsditch, R. Merlin: *Ultrafast optical study of magnons in the ferromagnetic semiconductor GaMnAs*. Superlatt. Microstruct. **41**, 372 (2007).

[93] E. Rozkotová: *Dynamika spinově polarizovaných nosičů náboje v polovodičích*. Diplomová práce, Univerzita Karlova v Praze, MFF, Praha (2007).

LIST OF ABBREVIATIONS

DMS	diluted magnetic semiconductor
EA	easy axis
FM	ferromagnetic
FMR	ferromagnetic resonance
IB	impurity band
MA	magnetocrystalline anisotropy
MBE	molecular beam epitaxy
MCD	magnetic circular dichroism
MLD	magnetic linear dichroism
MO	magneto-optical
OSTT	optical spin transfer torque
OSOT	optical spin-orbit torque
PKE	polar Kerr effect
SOC	spin-orbit coupling
SQUID	superconducting quantum interference device
SWR	spin wave resonance
TMR	tunneling magnetoresistance
VB	valance band

LIST OF IMPORTANT SYMBOLS

α	Gilbert damping constant
E_F	Fermi energy
F	free energy functional
g	Lande g-factor
γ	gyromagnetic ratio
H_{ext}	external magnetic field
K_c	cubic anisotropy
K_u	uniaxial anisotropy
K_{out}	out-of-plane anisotropy
μ_B	Bohr magneton
p	hole concentration
T_C	Curie temperature
T	temperature

APPENDICES

Contribution of Naďa Tesařová to attached articles

The results presented in this thesis are a part of an extensive research focused on the ferromagnetic semiconductors, where the (Ga,Mn)As is of the main interest. This research is done in a close collaboration with colleagues from the groups of Tomáš Jungwirth (Institute of Physics, Academy of Sciences in Prague), Václav Holý (Charles University in Prague), Brian Gallagher (University of Nottingham) and John Černe (University at Buffalo). Such a broad collaboration enables a very thorough investigation of the material properties by different experimental techniques, supported by a great theoretical background. This strongly focused research led to a publication of many articles where I am a co-author. However, in this theses I present only those papers where my contribution was major. More specifically, my contribution to the articles, which are presented in the Appendices below, is the following:

Appendix 1: T. Jungwirth, P. Horodyská, N. Tesařová, P. Němec, J. Šubrt, P. Malý, P. Kužel, C. Kadlec, J. Mašek, I. Němec, M. Orlita, V. Novák,1 K. Olejník, Z. Šrobáň , P. Vašek, P. Svoboda, J. Sinova: *Systematic Study of Mn-Doping Trends in Optical Properties of (Ga,Mn)As*. Phys. Rev. Lett. **105**, 227201 (2010).
I constructed the experimental set-up for the static MO measurements and measured all the MO data shown in the paper. I also contributed to the data analysis and to the manuscript writing.

Appendix 2: N. Tesařová, J. Šubrt, P. Malý, P. Němec, C. T. Ellis, A. Mukherjee, J. Cerne: *High Precision Magnetic Linear Dichroism Measurements in (Ga,Mn)As*. Accepted in Review of Scientific Instruments, arXiv:1212.0956.
I constructed the experimental set-up for the static MO measurements both in Prague and in Buffalo and I did all the experiments that are described in the paper. I performed the majority of the data analysis and of the manuscript writing.

Appendix 3: N. Tesařová, P. Němec, E. Rozkotová, F. Trojánek, P. Malý: *Light-Induced Precession of Magnetization in Ferromagnetic Semiconductor (Ga,Mn)As*. Acta Phys. Polon. A **118**, 1065 (2010).
I contributed to the construction of the experimental set-up for the time-resolved MO measurements. I measured all the data, performed their analysis, and wrote the article.

Appendix 4: N. Tesařová, E. Rozkotová, H. Reichlová, P. Malý, V. Novák, M. Cukr,T. Jungwirth, P. Němec: *Influence of Magnetic Anisotropy on Laser-Induced Precession of Magnetization in Ferromagnetic Semiconductor (Ga, Mn)As*. J. Nanosc. Nanotechnol. **12**, 7477 (2012).
I contributed to the construction of the experimental set-up for the time-resolved MO measurements. I measured all the MO data, performed their analysis, and wrote the article.

Appendix 5: N. Tesařová, P. Němec, E. Rozkotová, J. Šubrt, H. Reichlová, D. Butkovičová, F. Trojánek, P. Malý, V. Novák, T. Jungwirth: *Direct measurement of the three-dimensional*

magnetization vector trajectory in GaMnAs by a magneto-optical pump-and-probe method. Appl. Phys. Lett. **100**, 102403 (2012).
I contributed to the construction of the experimental set-up for the time-resolved MO measurements. I measured all the MO data, performed the data analysis and contributed to the analytical derivation of equations that describe the MO response of (Ga,Mn)As, which form the basis of this method for a determination of the real-space magnetization trajectory. I also contributed to the manuscript writing.

Appendix 6: P. Němec, E. Rozkotová, N. Tesařová, F. Trojánek, E. De Ranieri, K. Olejník, J. Zemen, V. Novák, M. Cukr, P. Malý, T. Jungwirth: *Experimental observation of the optical spin transfer torque*. Nat. Phys. **8**, 411 (2012).
I contributed to the construction of the experimental set-up for the time-resolved MO measurements but the time-resolved MO data reported in the main article were measured by Eva Rozkotová. I measured the majority of the experimental data that are shown in the Supplementary material to illustrate the universality of OSTT (Fig. 2 and Fig. 3a in the main article), the magnetic origin of the measured MO signals (Fig. 5 and Fig. 12 in the Supplementary material), and the probe-polarization sensitive measurements (Fig. 9a, Fig. 10, Fig. 11, and Fig. 13 in the Supplementary material). I also contributed to writing of both the main paper and the Supplementary material.

Appendix 7: N. Tesařová, P. Němec, E. Rozkotová, J. Zemen, T. Janda, D. Butkovičová, F. Trojánek, K. Olejník, V. Novák, P. Malý, T. Jungwirth: *Experimental observation of the optical spin-orbit torque*. Submitted to Nature Photonics, arXiv:1207.0307.
I contributed to the construction of the experimental set-up for the time-resolved MO measurements. I measured the MO data shown in Fig. 1, Fig. 2, and Fig. 3, performed their analysis, and contributed to the manuscript writing.
Note: Enclosed is the latest version of the manuscript that is currently in the 2nd round of the referee process in the Nature Photonics. This version is partially different from the version that is located at arXiv:1207.0307. The reason is that due to the Copyright policy of the Nature Publishing Group the revised version of the manuscript cannot be placed at arXiv before it is officially published in the corresponding journal.

Appendix 8: P. Němec, V. Novák, N. Tesařová, E. Rozkotová, H. Reichlová, D. Butkovičová, F. Trojánek, K. Olejník, P. Malý, R. P. Campion, B. I. Gallagher, J. Sinova, T. Jungwirth: *Establishing micromagnetic parameters of ferromagnetic semiconductor (Ga,Mn)As*. Accepted in Nature Communications, arXiv:1207.0310.
I contributed to the construction of the experimental set-up for the time-resolved MO measurements. I measured the MO data and performed the numerical data modeling that are shown in Fig. 1b, c, in Fig. 4 and in Fig. 5. I also contributed to the manuscript writing.
Note: Enclosed is the latest version of the manuscript that was accepted in the Nature Communications. This version is partially different from the version that is located at arXiv: 1207.0310. The reason is that due to the Copyright policy of the Nature Publishing Group the revised version of the manuscript cannot be placed at arXiv before it is officially published in the corresponding journal.

APPENDIX 1

Authors: T. Jungwirth, P. Horodyská, N. Tesařová, P. Němec, J. Šubrt, P. Malý, P. Kužel, C. Kadlec, J. Mašek, I. Němec, M. Orlita, V. Novák,1 K. Olejník, Z. Šrobáň , P. Vašek, P. Svoboda and J. Sinova

Title: Systematic Study of Mn-Doping Trends in Optical Properties of (Ga,Mn)As

Journal: Physical Review Letters

Volume: 105

Article Number: 227201

Year: 2010

Systematic Study of Mn-Doping Trends in Optical Properties of (Ga,Mn)As

T. Jungwirth,[1,2] P. Horodyská,[3] N. Tesařová,[3] P. Němec,[3] J. Šubrt,[3] P. Malý,[3] P. Kužel,[4] C. Kadlec,[4] J. Mašek,[4] I. Němec,[5] M. Orlita,[6,1] V. Novák,[1] K. Olejník,[1,7] Z. Šobáň,[1,8] P. Vašek,[1] P. Svoboda,[1] and Jairo Sinova[9,1]

[1]*Institute of Physics ASCR, v.v.i., Cukrovarnická 10, 162 53 Praha 6, Czech Republic*
[2]*School of Physics and Astronomy, University of Nottingham, Nottingham NG7 2RD, United Kingdom*
[3]*Faculty of Mathematics and Physics, Charles University in Prague, Ke Karlovu 3, 121 16 Prague 2, Czech Republic*
[4]*Institute of Physics ASCR, v.v.i., Na Slovance 2, 182 21 Prague 8, Czech Republic*
[5]*Faculty of Science, Charles University in Prague, Hlavova 2030, 128 40 Prague 2, Czech Republic*
[6]*Laboratoire National des Champs Magnétiques Intenses, CNRS-UJF-UPS-INSA, 25, avenue des Martyrs, 38042 Grenoble, France*
[7]*Hitachi Cambridge Laboratory, Cambridge CB3 0HE, United Kingdom*
[8]*Faculty of Electrical Engineering, Czech Technical University in Prague, Technická 2, 166 27 Prague, Czech Republic*
[9]*Department of Physics, Texas A&M University, College Station, Texas 77843-4242, USA*

(Received 28 July 2010; revised manuscript received 8 October 2010; published 23 November 2010)

We report on a systematic study of optical properties of (Ga,Mn)As epilayers spanning the wide range of accessible Mn_{Ga} dopings. The material synthesis was optimized for each nominal Mn doping in order to obtain films which are as close as possible to uniform uncompensated (Ga,Mn)As mixed crystals. We observe a broad maximum in the mid-infrared absorption spectra whose position exhibits a prevailing blueshift for increasing Mn doping. In the visible range, a peak in the magnetic circular dichroism also shifts with increasing Mn doping. The results are consistent with the description of ferromagnetic (Ga,Mn)As based on the microscopic valence band theory. They also imply that opposite trends seen previously in the optical data on a limited number of samples are not generic and cannot serve as an experimental basis for postulating the impurity band model of ferromagnetic (Ga,Mn)As

DOI: 10.1103/PhysRevLett.105.227201 PACS numbers: 75.50.Pp, 71.55.Eq, 75.30.−m, 75.70.Ak

The discovery of ferromagnetism in (Ga,Mn)As above 100 K [1] opened an attractive prospect for exploring the physics of magnetic phenomena in doped semiconductors and for developing advanced concepts for spintronics. Assessment of a wide range of magnetic and transport properties of the material [2–4] showed that in ferromagnetic (Ga,Mn)As with Mn dopings $x > 1\%$, disorder-broadened and shifted host Bloch bands represent a useful one-particle basis for describing this mixed-crystal degenerate semiconductor. The common kinetic-exchange model implementation of this valence band theory and the more microscopic tight-binding Anderson model or *ab initio* density functional theory can all be shown [5] to be mutually consistent on the level of atomic and orbital resolved band structure. The main utility of valence band theories has been in providing a qualitative and often semiquantitative description of phenomena originating from the exchange split and spin-orbit coupled electronic structure and in assisting the development of prototype spintronic devices [4].

In the insulator nonmagnetic regime ($x \ll 1\%$), the system is readily described by localized Fermi level states residing inside a narrow impurity band separated from the valence band by an energy gap of magnitude close to the isolated Mn_{Ga} impurity binding energy. Recently, a debate has been stirred by proposals, based in particular on optical spectroscopy measurements [6], that the narrow impurity band persists in high-doped (Ga,Mn)As with metallic conduction.

Several phenomenological variants of the impurity band model have been proposed for the high-doped regime [6–10] which are mutually inconsistent from the perspective of the assumed atomic orbital nature of the impurity band states [5]. Further theoretical inconsistencies have arisen from attempts to recreate the phenomenological models microscopically with the constraint of the experimentally determined moderate binding energy of an isolated Mn_{Ga} of $E_a = 0.1$ meV. A detached narrow impurity band does not persist in any of the variants of the model to dopings $x > 1\%$ at which (Ga,Mn)As has metallic conduction [5]. Since to date no framework has been introduced which would allow us to test the validity of the impurity band model by comparing microscopic theory calculations to experiment, it is only the experimental evidence alone which can serve as a basis for postulating the impurity band picture. In particular, the redshift of the infrared absorption peak and the rigidity of the near band-gap spectral features in the magnetic circular dichroism with increasing doping [6,7,9] have been regarded as the key experimental signatures of the impurity band. The goal of this Letter is to assess whether these signatures are generic in ferromagnetic (Ga,Mn)As materials to represent a valid experimental foundation of the impurity band model. Simultaneously we inspect the consistency of the valence band theory of (Ga,Mn)As with the measured data.

We study doping trends in the optical spectra over a wide Mn concentration range in a consistently and controllably prepared set of materials. We have optimized the growth

and postgrowth annealing procedures individually for each nominal doping in order to minimize the density of compensating defects and other unintentional impurities and to achieve high uniformity of the epilayers in the growth and lateral directions, as detailed in the supplementary material [11]. Nominal dopings of our set of (Ga,Mn)As epilayers grown on GaAs substrates span a range from paramagnetic insulating materials with $x < 1\%$ to materials with x up to $\approx 14\%$, corresponding to $\approx 8\%$ of uncompensated Mn_{Ga}, and ferromagnetic transition temperatures reaching 190 K [11]. Samples with $x \leq 1\%$ have thickness of 100 nm. All epilayers with $x \geq 1.5\%$ are 20 nm thick. In these materials with large Mn doping, high quality epilayers are obtained only for thicknesses larger than ~10 nm and lower than ~50 nm. All samples within the series have reproducible characteristics with the overall trend of increasing Curie temperature (in the ferromagnetic films), increasing hole concentration, and increasing magnetic moment density with increasing x. The samples have a high degree of uniformity on a macroscopic scale as inferred from their sharp magnetic and transport singularities at the Curie point (see supplementary material for more details [11]).

Samples used in transmission measurements have a polished back side of the wafers to minimize diffusive light scattering. The unpolarized transmission experiments [11] on the (Ga, Mn)As/GaAs samples and on the control bare GaAs substrate were performed at 300 K in the range 25–11 000 cm^{-1} (3–1360 meV) using the Fourier transform infrared spectroscopy. The range between 120–600 cm^{-1} (15–75 meV) with strong phonon response in GaAs substrate is excluded from the data. Control low-temperature measurements which confirm the doping trends observed at 300 K are included in the supplementary material [11]. Measurements of the complex conductivity in the low-frequency range 8–80 cm^{-1} (1–10 meV) of the (Ga, Mn)As/GaAs wafers (with measurement of the bare GaAs substrate as a reference) were performed by means of terahertz time-domain transmission spectroscopy [11]. Magneto-optical experiments [11] at 15 K in the near infrared to visible range 970–20160 cm^{-1} (1.2–2.5 eV) were performed primarily in the reflection geometry because of the small epilayer thickness of the optimized materials and increasing growth strain in the (Ga, Mn)As/GaAs epilayers reaching 0.5% in the high-doped materials. Control magneto-optical measurements in transmission were done on a 230 nm thick (Ga,Mn)As epilayer with the GaAs substrate removed after growth by wet etching.

First we discuss the observed broad maximum in the unpolarized infrared absorption near 200 meV. In Fig. 1(a) we plot experimental data obtained directly from the measured infrared transmissivities. The real part of the ac conductivity curves shown in Fig. 1(b) represent the best fit to the measured transmission in the THz and infrared ranges [11]. The fit is anchored at low frequencies by the directly measured THz conductivity. (The scatter in the measured THz conductivity reflects the precision of these measurements which is limited primarily by the quality of sample surfaces [11].) The position of the midinfrared absorption peak in both representations of the measured data has a prevailing blueshift tendency with increasing doping. This is reminiscent of the blueshift of this spectral feature seen in our (and previously studied [12]) control GaAs:C materials, shown in Fig. 1(c). We recall that for the nonmagnetic hydrogenic acceptors it is established that the peak originates from transitions inside the semiconductor valence band. Based on microscopic valence band theory calculations, these transitions have also been predicted to

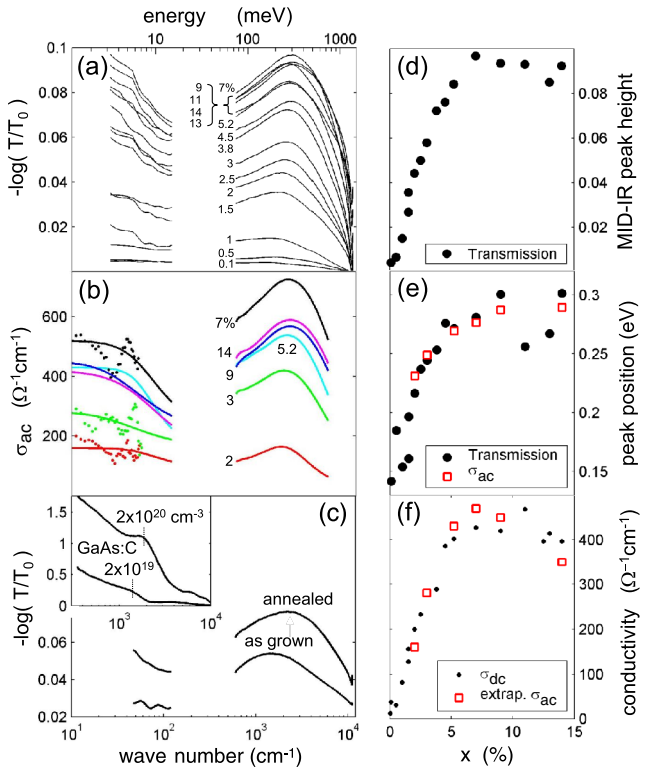

FIG. 1 (color online). (a) Infrared absorption of a series of optimized (Ga, Mn)As/GaAs epilayers with nominal Mn doping $x = 0.1\%$–14% plotted from the measured optical transmissions of the samples (T) and of the reference bare GaAs substrate (T_0). Spectra of the 100 nm thick samples with $x \leq 1\%$ were divided by 5 for consistency with those measured for the 20 nm thick higher doped samples. (b) Real part of the ac conductivity (lines) obtained from the measured complex conductivity in the terahertz range (points) and from fitting the complex conductivity in the infrared range to the measured transmissions. (c) Comparison of the infrared absorption in as-grown and annealed 4.5% doped sample. Inset: Comparison to GaAs:C samples with carbon doping densities 2×10^{19} and 2×10^{20} cm^{-3}. (d) Height of the (Ga,Mn)As midinfrared absorption peak as a function of Mn doping. (e) Position of the peak inferred from the transmission measurements and from the fitted ac conductivities. (f) Zero frequency conductivities obtained from dc-transport measurements and from extrapolated optical ac conductivities measured in the terahertz range.

yield the broad maximum in the midinfrared spectra of (Ga,Mn)As which is rather insensitive to the exchange splitting of the valence band [13,14]. Apart from the predicted prevailing blueshift, the peak position in (Ga,Mn)As can have a nonmonotonic dependence on doping as a consequence of momentum nonconserving transitions allowed by the strong disorder in (Ga,Mn)As [15].

A redshift of the measured midinfrared peak reported in Ref. [7] in as-grown and annealed samples arranged by expected increasing hole concentrations has been presented as the key evidence of the failure of the valence band theories. The data were phenomenologically interpreted in terms of impurity band conduction persisting to the high-doped metallic (Ga,Mn)As. In the subsequent analysis it has been pointed out [15], however, that the association of this peak to an impurity band is implausible (i) because of the absence of the thermally activated dc-transport counterpart in the high-doped samples, (ii) because of the initial blueshift of this midinfrared feature with respect to the impurity band transition peak in the very dilute insulating samples, and (iii) because of the appearance of the peak at frequencies above $2E_a$, which is the expected upper bound for impurity band transitions. Our data in Fig. 1 corroborate the conclusions of Ref. [15] by demonstrating that the redshift of the midinfrared peak with increasing Mn_{Ga} doping is not the general and not even the prevailing trend in (Ga,Mn)As materials prepared with the minimized number of compensating and other unintentional impurities.

In Figs. 1(a) and 1(b) we have not included measurements in the as-grown epilayers because their characteristics are not fully reproducible, are more ambiguous, and the materials are less uniform [11]. Nevertheless, to make a connection to previous studies we have measured the midinfrared peak in a nominally 4.5% Mn-doped sample before and after annealing. As shown in Fig. 1(c), we observe a blueshift of the midinfrared peak after annealing; i.e., the redshift is not observed in our materials even if we use annealing to increase the effective doping. The same trend was confirmed in our as-grown and annealed samples with 12% nominal Mn doping. In Figs. 1(d)–1(f) we highlight the observed correlation between the peak position and its height, as well as the expected correlation from the valence band theories between the amplitude of the peak and the dc conductivity. We also point out the close correspondence shown in Fig. 1(f) between the dc conductivities obtained from extrapolated THz data and from dc longitudinal and Hall transport measurements, which confirms the consistency of our optical data.

Unlike the unpolarized optical spectroscopy, the magneto-optical effects are very sensitive to the magnetic state of the system, their interpretation is more microscopically constrained, and they yield sharper spectral features. This is particularly valid for the infrared magneto-optical spectroscopy for which previous study [16] has shown that the disordered valence band theory with kinetic-exchange-split bands of ferromagnetic (Ga,Mn)As accounts semiquantitatively for the overall characteristics of the measured data. We now extend the analysis to higher energies including transitions across the semiconductor band gap.

The magnetic circular dichroism in the reflection geometry is given by $\mathrm{MCD(deg)} = 90/\pi(R^+ - R^-)/(R^+ + R^-)$, where $R^{+(-)}$ is the reflected intensity of the light with the angular momentum $+1$ (-1). The main result of MCD measurements in our (Ga,Mn)As materials, shown in Figs. 2(a) and 2(b), is the observed large blueshift of the MCD peak (the peak is negative in the above sign convention). Our data contradict the conclusion based on experiments in Ref. [9] which stated that the position of the MCD peak was independent of doping and that this was a signature of the pinning of the Fermi level in a rigid narrow impurity band [9,10]. We have also performed additional MCD experiments in pairs of as-grown and annealed (Ga,Mn)As materials. Upon annealing, we again observe a blueshift of the MCD peak, as illustrated in Fig. 2(c).

Theoretical modeling of the MCD spectra within the valence band theory, described in detail in Ref. [11], is shown in Fig. 2(d). The magnitude of the peak and its absolute position depend on the detailed implementation of the model, e.g., on the way disorder or band-gap renormalization effects are treated [11]. On a qualitative level and independent of these specific implementations of the model, the valence band theory with the antiferromagnetic

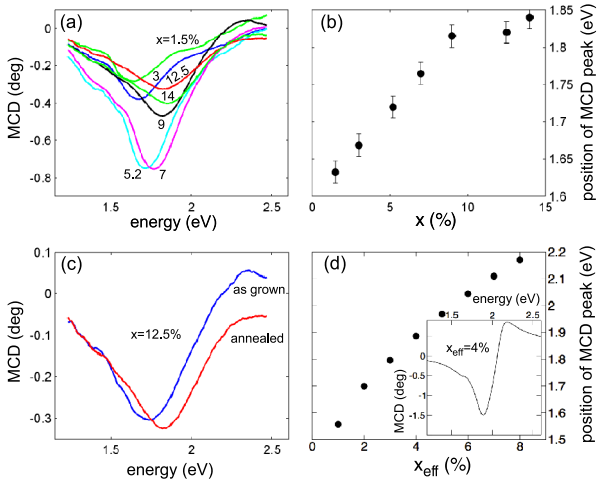

FIG. 2 (color online). (a) Reflection MCD measurements in samples from the optimized series of 20 nm thick epilayers spanning the whole studied range of Mn dopings of ferromagnetic (Ga,Mn)As. (b) Experimental position of the MCD peak (negative in the considered sign convention) as a function of nominal doping. (c) Comparison of the MCD measurements in the 12.5% doped as-grown and annealed epilayer. (d) Theoretical position of the MCD peak as a function of effective doping of uncompensated Mn_{Ga} impurities (see Ref. [11]); inset shows theoretical MCD spectrum for 4% effective doping.

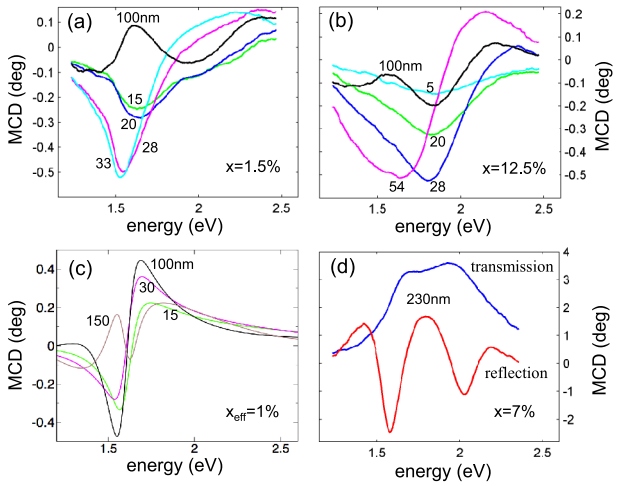

FIG. 3 (color online). Measured reflection MCD data in samples with different (Ga,Mn)As epilayer thickness and nominal Mn doping 1.5% (a), 12.5% (b). (c) Theoretical thickness dependence of the MCD spectra at 1% effective doping. (d) Transmission and reflection MCD measurements in a 7% nominally doped 230 nm thick freestanding (Ga,Mn)As epilayer.

p-d kinetic exchange [3] reproduces the overall experimental shape of the MCD spectrum, the sign of the MCD peak, and the blueshift of the peak with increasing doping.

Because our experiments were performed in the reflection geometry we have prepared several control samples to assess the role of multiple reflections. In Figs. 3(a) and 3(b) we show a comparison of MCD spectra in (Ga,Mn)As epilayers of different thicknesses controlled during growth or postgrowth by etching [11]. In the control thicker (Ga,Mn)As samples, the MCD peak is superimposed on oscillations caused by the multiple reflections. The oscillations are completely suppressed in the 20 nm thick films, and the reflection MCD peak position is therefore not affected by the film thickness in our series of optimized 20 nm thick (Ga,Mn)As epilayers. The transition from a thin film to a film where multiple reflections are important is captured qualitatively by the valence band theory calculations, as shown in Fig. 3(c).

As an additional consistency check of the sign of our MCD signals with respect to previous MCD experiments in (Ga,Mn)As we have also measured the freestanding 230 nm thick 7% Mn-doped (Ga,Mn)As epilayer in both reflection and transmission MCD geometry. In the latter case the dichroism is given by $\mathrm{MCD(deg)} = 90/\pi(T^+ - T^-)/(T^+ + T^-)$, where $T^{+(-)}$ is the transmitted intensity of the light with the angular momentum $+1$ (-1). Our transmission MCD data shown in Fig. 3(d) are very similar to measurements in samples with comparable doping and film thickness reported in Ref. [17].

To conclude, our optical spectroscopy measurements in a large set of systematically prepared (Ga,Mn)As epilayers show that doping trends reported previously in a limited number of samples and regarded as the key experimental evidence of the impurity band nature of Fermi level states are not generic and not even prevailing in ferromagnetic (Ga,Mn)As materials. The experimental foundation of the impurity band model based on these optical spectroscopies is therefore invalid, which corroborates the absence of a microscopic theory foundation of this model. In contrast, the valence band model, which is readily established from microscopic theory and from numerous previous comparisons to experiments, accounts qualitatively or semiquantitatively for the measured optical data.

We acknowledge experimental support from Duncan K. Maude and EU Grants FP7-215368 SemiSpinNet and FP7-214499 NAMASTE, Czech Republic Grants KAN400100652, LC510, MEB020928, Preamium Academiae, AV0Z10100521, MSM0021620834, MSM0021620857, GACR 202/09/H041, SVV-2010-261306 of the Charles University, and U.S. Grants NSF-MRSEC DMR-0820414, ONR-N000140610122, DMR-0547875, and SWAN-NRI. J. S. acknowledges financial support through a Cottrell Scholar Award from the Research Corporation.

[1] H. Ohno, Science **281**, 951 (1998).
[2] F. Matsukura, H. Ohno, and T. Dietl, in *Handbook of Magnetic Materials*, edited by K. H. J. Buschow (Elsevier, Amsterdam, 2002), Vol. 14, p. 1.
[3] T. Jungwirth, J. Sinova, J. Mašek, J. Kučera, and A. H. MacDonald, Rev. Mod. Phys. **78**, 809 (2006).
[4] *Spintronics*, edited by T. Dietl, D. D. Awschalom, M. Kaminska, and H. Ohmo, Semiconductors and Semimetals, Vol. 82 (Elsevier, New York, 2008).
[5] J. Mašek *et al.*, following Letter, Phys. Rev. Lett. **105**, 227202 (2010).
[6] K. S. Burch, D. D. Awschalom, and D. N. Basov, J. Magn. Magn. Mater. **320**, 3207 (2008).
[7] K. S. Burch *et al.*, Phys. Rev. Lett. **97**, 087208 (2006).
[8] P. R. Stone *et al.*, Phys. Rev. Lett. **101**, 087203 (2008).
[9] K. Ando *et al.*, Phys. Rev. Lett. **100**, 067204 (2008).
[10] J.-M. Tang and M. E. Flatté, Phys. Rev. Lett. **101**, 157203 (2008).
[11] See supplementary material at http://link.aps.org/supplemental/10.1103/PhysRevLett.105.227201 for additional information on material growth and characterization, optical experiments, and theory.
[12] W. Songprakob, R. Zallen, D. V. Tsu, and W. K. Liu, J. Appl. Phys. **91**, 171 (2002).
[13] J. Sinova *et al.*, Phys. Rev. B **66**, 041202 (2002).
[14] S. R. E. Yang *et al.*, Phys. Rev. B **67**, 045205 (2003).
[15] T. Jungwirth *et al.*, Phys. Rev. B **76**, 125206 (2007).
[16] G. Acbas *et al.*, Phys. Rev. Lett. **103**, 137201 (2009).
[17] B. Beschoten *et al.*, Phys. Rev. Lett. **83**, 3073 (1999).

APPENDIX 2

Authors: N. Tesařová, J. Šubrt, P. Malý, P. Němec, C. T. Ellis, A. Mukherjee and J. Cerne

Title: High Precision Magnetic Linear Dichroism Measurements in (Ga,Mn)As

Journal: accepted in Review of Scientific Instruments

Preprint server: http://arxiv.org/abs/1212.0956

High Precision Magnetic Linear Dichroism Measurements in (Ga,Mn)As

N. Tesařová[a)], J. Šubrt, P. Malý and P. Němec
Faculty of Mathematics and Physics, Charles University in Prague, Ke Karlovu 3, 121 16 Prague 2, Czech Republic

C. T. Ellis, A. Mukherjee and J. Cerne
Department of Physics, University at Buffalo, The State University of New York, Buffalo, New York 14260, USA

Investigation of magnetic materials using the first-order magneto-optical Kerr effects (MOKE) is well established and is frequently used in the literature. On the other hand, the utilization of the second-order (or quadratic) magneto-optical (MO) effects for the material research is rather rare. This is due to the small magnitude of quadratic MO signals and the fact that the signals are even in magnetization (i.e., they do not change a sign when the magnetization orientation is flipped), which makes it difficult to separate second-order MO signals from various experimental artifacts. In 2005 a giant quadratic MO effect - magnetic linear dichroism (MLD) - was observed in the ferromagnetic semiconductor (Ga,Mn)As. This discovery not only provided a new experimental tool for the investigation of in-plane magnetization dynamics in (Ga,Mn)As using light at normal incidence, but it also motivated the development of experimental techniques for the measurement of second-order MO effects in general. In this paper we compare four different experimental techniques that can be used to measure MLD and to separate it from experimental artifacts. We show that the most reliable results are obtained when the harmonic dependence of MLD on a mutual orientation of magnetization and light polarization plane is used together with the in-situ rotation of the sample followed by the magnetic field-induced rotation of magnetization. Using this technique we measure the MLD spectra of (Ga,Mn)As in a broad spectral range from 0.1 eV to 2.7 eV and we observe that MLD has a comparable magnitude as polar MOKE signals in this material.

I. INTRODUCTION

Magneto-optical (MO) spectroscopy is a powerful tool for investigating basic properties of various magnetic and non-magnetic materials such as the electronic structure, magnetic anisotropy, spin population and magnetic excitations.[1-7] The first-order magneto-optical Kerr effect (MOKE) is usually used for this purpose due to the relatively large signals that it produces and its sensitivity to both in-plane (longitudinal and transverse Kerr effect) and out-of-plane (polar Kerr effect) positions of magnetization, respectively.[8-11] Although second-order (or quadratic) MO effects were investigated thoroughly by the magneto-optical community,[3,9,12-15] they were usually disregarded in materials research because they are observable only in materials with in-plane magnetization and usually lead to much smaller signals compared to the first-order MOKE.[3,9,13,14,16] In 2005 a giant quadratic MOKE effect - magnetic linear dichroism (MLD) - was observed in ferromagnetic (FM) semiconductor (Ga,Mn)As.[5] The discovery of a quadratic magneto-optical effect with a magnitude comparable to the first-order polar Kerr effect (PKE),[4,5,17] established MLD as a legitimate tool for investigating different material properties and interesting physical phenomena.[4,5] For example, for the normal incidence of light, PKE and MLD are sensitive to the out-of-plane and in-plane projections of the magnetization, respectively.[4] Consequently, the simultaneous measurement of the polarization rotation due to PKE and MLD enabled a reconstruction of the real space magnetization trajectory induced by the impact of a laser pump pulse in (Ga,Mn)As.[4,17,18] MLD can also be perceived as anisotropic magnetoresistance (AMR) at

[a)]Electronic mail: nada.tesarova@mff.cuni.cz.

finite frequencies, as both the DC and AC phenomena are even in magnetization, as was shown for photon energies near 1 eV.[19] This is analogous to PKE, which can be viewed as the AC anomalous Hall effect[20] that is odd in magnetization. Moreover, the sensitivity of MLD to the energy states that are responsible for magnetic order in FM semiconductors[5] makes MLD spectroscopy a very promising tool for providing new insights into these materials.

The reliable experimental measurement of the polarization change due to MLD is, however, a challenging task. While the experimental techniques for measurements of first-order MOKE are well-established and relatively easy to use, their direct application to MLD is not possible. For example, the magnitude of PKE is determined by measuring the light polarization rotation induced by the out-of plane oriented magnetization *M*. Since PKE is odd in magnetization (as it is proportional to *M*), the MO signals measured for parallel and antiparallel orientations of *M* with respect to the direction of the incident beam, which are set by the direction of a saturating magnetic field, should have a same magnitude but opposite sign. All the possible non-magnetic artifacts, which are typically present in the measured signals, can thus be readily removed by determining the difference between the signals measured at $+M$ and $-M$. On the contrary, MLD is an even function of the magnetization (as it is proportional to M^2, [Ref. 12, Ref. 3]). This means that the 180˚ magnetization reorientation leads to the same MO signal[4] and, consequently, it is not an easy task to separate the real MO signal from polarization artifacts. In this paper we compare several experimental procedures that enable polarization artifact removal and show that the most reliable results are obtained by our novel experimental technique that employs the polarization dependence of MLD. Using this technique we measured the MLD spectra of the archetypical FM semiconductor (Ga,Mn)As in a broad spectral range (0.1 – 2.7 eV), which covers all the optical transitions from states that could be responsible for the FM order in this semiconductor.[2,5]

This paper is divided into six parts. In Sec. II, we first introduce the phenomenological description of MLD and derive its dependence on the polarization of the incident light. In Secs. III and IV we describe the different experimental techniques that we use to measure MLD in (Ga,Mn)As samples together with some interesting technical details of our apparatus. Finally, in Sec. V we present and discuss the achieved results. A detailed mathematical description of the methods is shown in the Appendix.

II. PHENOMENOLOGICAL DESCRIPTION OF MLD

In general, MLD is a second-order MO effect which is caused by a different (complex) index of refraction for light polarized parallel and perpendicular to magnetization orientation. MLD was originally observed in transmission, as a dichroism of linearly polarized light induced by the presence of a magnetic field or magnetization.[12] The difference in absorption for light polarized parallel and perpendicular to the magnetization orientation leads to a rotation of the polarization plane of linearly polarized light.[12] The same name was subsequently adopted also for the MO effect in the near-normal reflection geometry[4,5,15,21-23] where the rotation of linearly polarized light (or the change of its ellipticity) is caused by the different refraction indices for two orthogonal linear polarization components of light. We note that MLD is analogous to magnetic linear birefringence (MLB) - or Cotton-Mouton or Voigt effects, which are observed in the transmission geometry.[12,13,24]

In this article we will concentrate on the rotation of light polarization induced by MLD for light reflected at normal incidence from a sample with in-plane magnetization. The definition of the MLD signal in this context is the following:

$$MLD\ [\mathrm{rad}] = \frac{1}{2}\frac{I_R^{\parallel} - I_R^{\perp}}{I_R^{\parallel} + I_R^{\perp}}, \qquad (1)$$

where $I_R^{||}$ and $I_R^{\perp}$ are the intensities of the reflected light polarized parallel and perpendicular to the magnetization, respectively. Equation (1) can be written equivalently in terms of the reflection coefficients $r_{||}$ and $r_{\perp}$:

$$MLD\ [\text{rad}] = \frac{1}{2}\frac{r_{\parallel}^2 - r_{\perp}^2}{r_{\parallel}^2 + r_{\perp}^2}. \quad (2)$$

The sign as well as the magnitude of the MLD signal are sensitive to the polarization orientation of the incident light. The polarization dependence of the MLD can be analytically calculated using the trigonometric relation between the magnetization orientation in the sample plane, given by the angle φ_M, and the incident and reflected light polarizations, given by the angles β and β' [see Fig. 1(a) for the angle definition]. The polarization rotation $\Delta\beta$ ($\Delta\beta \equiv \beta' - \beta$) due to MLD can be expressed as (see Ref. 4 for more details):

$$tan(\Delta\beta) = \frac{(r_{\parallel} - r_{\perp})tan(\varphi_M - \beta)}{r_{\parallel} + r_{\perp}tan^2(\varphi_M - \beta)}, \quad (3)$$

Assuming a small rotation of light polarization, i.e., $r_{||}/r_{\perp} \approx 1$, we obtain:

$$\Delta\beta = P^{MLD} sin[2(\varphi_M - \beta)], \quad (4)$$

where $P^{MLD} = 0.5(r_{||}/\ r_{\perp} - 1)$ is the MLD magneto-optical coefficient. Equation (4) shows that the MLD is zero when the incident polarization is parallel or perpendicular to magnetization orientation (i.e., $\varphi_M - \beta = 0^{\circ}$ or 90°, respectively). On the other hand, the rotation of light polarization is maximized when the angle between the magnetization and the incident polarization is $\pm 45^{\circ}$. In this case, the magnitude of the polarization rotation is given solely by the MLD magneto-optical coefficient P^{MLD} and Eqs. (4) and (2) are equivalent if we again assume $r_{||}/\ r_{\perp} \approx 1$:

$$P^{MLD} = \frac{1}{2}\left(\frac{r_{\parallel}}{r_{\perp}} - 1\right) = \frac{1}{2}\frac{r_{\parallel} - r_{\perp}}{r_{\perp}}\frac{(r_{\parallel} + r_{\perp})}{(r_{\parallel} + r_{\perp})} \approx \frac{1}{2}\frac{r_{\parallel}^2 - r_{\perp}^2}{r_{\parallel}^2 + r_{\perp}^2}. \quad (5)$$

III. EXPERIMENTAL TECHNIQUES

We use several different experimental configurations to measure the MLD in (Ga,Mn)As. The near normal reflection geometry is employed in all configurations – the angle between the incident beam direction and the sample normal, ψ, did not exceed 6° (see Fig. 1).

The polarization rotation due to MLD can be measured directly from its definition using Eq. (1). As a first step, the magnetization is oriented by applying a saturating external magnetic field in the sample plane. The reflected light intensity is then measured for the incident light polarization parallel and perpendicular to the magnetization orientation, respectively, and the magnitude of MLD is computed from Eq. (1). Although this method works in principle, it is usually necessary to use other experimental techniques that enable more sensitive measurements of the small polarization rotations – especially in (Ga,Mn)As where the MLD magnitude typically does not exceed 1 mrad.

The most common method for determining the MLD-related MO signal is the measurement of the hysteresis loops for magnetic field sweeps in the sample plane.[3,5,9,14,15] In Fig. 1(b) we show the typical setup used for this kind of experiment. As mentioned in the introduction and as can be also seen from Eq. (4), the MLD signals are the same for two opposite orientations of magnetization, making the hysteresis loop measurement impossible for 180° reorientation of magnetization. However, MLD hysteresis can be measured in

samples with fourfold magnetocrystaline anisotropy.[3,9,14-16] In (Ga,Mn)As the fourfold symmetry is a consequence of the competing uniaxial and cubic magnetic anisotropies, resulting in four equivalent magnetization easy axes (instead of two, as in conventional ferromagnets).[5,23,25] Magnetic field sweeps in the sample plane thus result in the M-shaped MO signal reflecting the magnetization jumps among these four easy axes.[5,23,25] In order to measure such hysteretic signals, the incident polarization of light is set by the polarizer (P_1) to an "appropriate" orientation (the best orientation choice will be discussed in detail below) and the magnetization induced polarization rotation is detected by a polarization-sensitive optical bridge, which consists of a half wave plate ($\lambda/2$), polarizing beam splitter (P_2) and two detectors (D_1 and D_2). We note that although this setup is very sensitive to small rotations of the light polarization plane, a quantitative determination of the MLD magnitude from such measurements is not straightforward and will be discussed together with the obtained results later in the text.

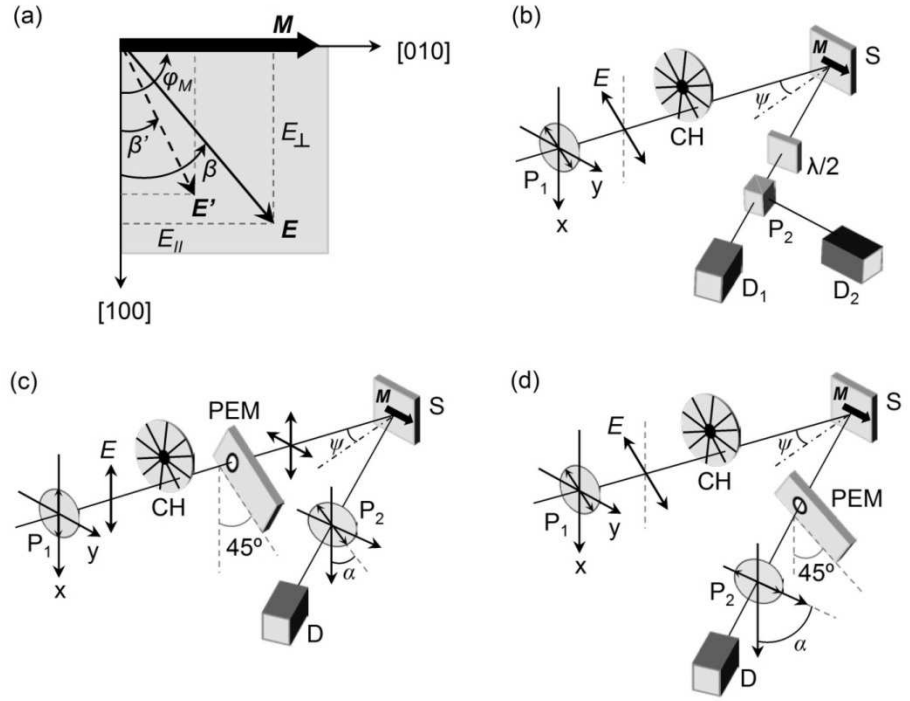

Fig. 1. Magnetization-induced rotation of light due to MLD and schematic illustrations of several experimental configurations used to detect MLD. (a) Different reflection coefficients for light polarized parallel ($E_{\parallel}$) and perpendicular ($E_{\perp}$) relative to magnetization orientation (M), at an angle φ_M, lead to a rotation of the polarization plane of linearly polarized light. The orientations of the incident E and reflected E' polarization planes are described by angles β and β', respectively. (b) The rotation of light polarization, which is set by polarizer (P_1), after reflection from sample (S) can be measured in a setup with a polarization-sensitive optical bridge that consists of half wave plate ($\lambda/2$), polarizing beam splitter (P_2) and two detectors (D_1, D_2). (c) and (d) Experimental configurations using a photoelastic modulator (PEM). During the measurement, polarizer (P_2) is oriented at α = 45° and 90° in part (c) and (d), respectively. The incident beam is modulated by mechanical chopper (CH), ψ is the angle between the incident beam direction and the normal to the sample surface.

Another approach for MLD measurement is to use highly sensitive experimental techniques that modulate the light polarization.[12] Two experimental configurations using polarization modulation are shown in Fig. 1(c) and (d). This technique is based on modulating the relative phase of two orthogonal linear polarizations that pass through a photoelastic modulator (PEM). In Fig. 1(c), the polarization of incident light is set perpendicular (or parallel) to the fixed position of the magnetization. The optical axis of the PEM is oriented

45˚ with respect to the incident polarization, so it modulates the phase difference δ between the *x* and *y* components of the polarization periodically: $\delta = \delta_0 \sin(\omega_{\mathrm{PEM}} t)$, where δ_0 is the dynamic retardance amplitude and ω_{PEM} is the natural resonant frequency of the PEM.[26] When $\delta_0 = \pi$, the polarization of the light transmitted through the PEM is changed from vertical to horizontal at a frequency $2\omega_{\mathrm{PEM}} = 2\pi \times 100$ kHz.[26] These two perpendicular polarizations are reflected from the sample with different (complex) amplitudes, producing different projections on the optical axis of the subsequent linear polarizer (P_2). The intensity of light I_D at the detector [D in Fig. 1(d)] is derived in the Appendix and can be expressed as:

$$I_D = \frac{I_0}{2}(1 + \cos\delta cos2(\alpha + \Delta\beta) + sin\delta sin2(\alpha + \Delta\beta) sin\Delta\eta), \tag{6}$$

where I_0 is the intensity of the incident light, $\Delta\beta$ represents the polarization rotation due to MLD, α is the angle that describes the rotation of the P_2 optical axis from the *x*-axis, and $\Delta\eta = \eta_y - \eta_x$ is the magnetization induced phase shift of the two reflected orthogonal polarizations, which causes the ellipticity of light.[12] In order to detect and subsequently unambiguously separate the MLD induced rotation and ellipticity, we set $\alpha = 45^{\circ}$. We can now rewrite Eq. (6) as a series of harmonic terms with Bessel function coefficients, focusing on the first four terms in the expansion to obtain:

$$I_D \approx \frac{I_0}{2}(1 - J_0(\delta_0) sin(2\Delta\beta) + 2J_1(\delta_0)\, cos(2\Delta\beta) sin(\Delta\eta)\, sin(\omega_{PEM} t) - 2J_2(\delta_0)\, sin(2\Delta\beta)\, cos(2\omega_{PEM} t)), \tag{7}$$

where $J_n(\delta)$ is an *n*-th order of the Bessel function. The overall intensity of the light is modulated by a mechanical chopper at approximately 1 kHz, and provides the average or dc[26] intensity of the radiation. The output of the detector consists of three frequency components that are processed by lock-in amplifiers; a $I(0)$-component which is detected at the chopper frequency, and the odd and even frequency components of ω_{PEM} – $I(\omega_{PEM})$ and $I(2\omega_{PEM})$, respectively (see Appendix for complete analysis). We note that Eq. (7) is only approximate, as each of the components has its own sensitivity given by the detection-amplification system, caused mainly by the detector/amplifier rolloff,[26] which is calibrated for all our measurements. Although this equation clearly shows that in principle we are able to detect not only the rotation of light polarization (term containing $sin(2\Delta\beta)$ at frequency $2\omega_{\mathrm{PEM}}$), but also its ellipticity (term containing $sin(\Delta\eta)$ at frequency ω_{PEM}), we will concentrate only on the MLD induced rotation of light in the following analysis. Assuming small rotation angles (i.e., $sin2(\Delta\beta) \approx 2\Delta\beta$ and $J_0(\delta_0) sin2(\Delta\beta) \ll 1$), we can write the expression for the magnetization induced polarization rotation as:

$$\Delta\beta = -\frac{I(2\omega_{PEM})}{I(0)} \frac{1}{4C_2 J_2(\delta_0)}, \tag{8}$$

where C_2 is a constant given by the frequency-dependent sensitivity of the detection system. In order to obtain the magnitude of $\Delta\beta$, i.e., the MLD coefficient P^{MLD}, one needs to perform a calibration procedure that sets the value of $C_2 J_2(\delta_0)$ (see the Appendix for a detailed description of the calibration procedure).

A modification of the experimental setup shown in Fig. 1(c) is obtained when the PEM is placed after the sample, as in Fig. 1(d). In this case, light is polarized at 45˚ with respect to vertical after passing through polarizer (P_1) so that the angle between the magnetization and the incident polarization is 45˚. Analogously to the previous case, the light acquires ellipticity and rotation after being reflected from the sample. The polarization state of light is subsequently analyzed by the PEM, which modulates the relative phase between the two orthogonal polarizations – the unaltered incident polarization, which is parallel to the PEM

optical axis, and the magneto-optically induced polarization, which is perpendicular to the PEM optical axis. The linear polarizer (P_2), which is placed after the PEM, is oriented at $\alpha = 90^\circ$ (i.e., 45° with respect to the PEM optical axis) and mixes the two orthogonal polarization components exiting the PEM. Applying a similar analysis as for the previous setup (see the Appendix), we obtain the same mathematical expression for MLD, given by Eq. (8). In order to calibrate the measured signal we perform an in-situ calibration technique developed in Ref. 1. Here the PEM and P_2 are rotated as a single unit by a known angle, producing a well-defined signal at the $2\omega_{PEM}$ frequency. This signal is then used to calibrate the polarimetry system.[1] It is worth noting that this experimental setup is extremely sensitive to the orientation of the reflected polarization with respect to the PEM, and that even miniscule changes in the alignment due to non-magnetic artifacts can lead to spurious signals. In order to circumvent such experimental artifacts, one needs to measure the *relative* change of the signal due to the sample's magnetization. This can be done either by hysteresis loop measurements, i.e., by changing the magnetization position in the sample plane by an application of the in-plane external magnetic field, or by a physical rotation of the sample, i.e., by changing the magnetization position without an external magnetic field. In this paper we describe a technique where both these approaches are combined to get the most reliable MLD-related signals. A detailed experimental procedure is discussed later in the text.

IV. EXPERIMENTAL DETAILS

The experiments are performed on two 20 nm thick (Ga,Mn)As samples with a nominal Mn concentration of 3% and 7%. The samples are grown on the GaAs(001) substrates by low temperature molecular beam epitaxy. The growth conditions and post-growth annealing are optimized for both samples in order to get as close as possible to the intrinsic properties of idealized, uniform and uncompensated (Ga,Mn)As epilayers (see Ref. 6 for more information). The Curie temperature (T_C) of the 3% and 7% Mn samples are 77 K and 159 K, respectively. The magnetic anisotropy of the samples was studied by the superconductive quantum interference device (SQUID), showing the four equivalent, non-perpendicular easy axis orientations of the magnetization in the sample plane.[27]

In order to probe these samples over a broad energy range, the MLD measurements are done in two collaborating laboratories at Charles University in Prague and University at Buffalo, with the former using visible photon energies above 1.2 eV and the latter concentrating on lower, infrared photon energies below 1.2 eV. The MLD is measured using discrete spectral lines from CO_2 (115 – 133 meV), CO (215 – 232 meV) and Ti-sapphire (1.63 eV) lasers and two distinct broadband light sources: a halogen lamp with a diffraction grating monochromator (Jobin Yvon Spex Model HR250) and the Xe lamp (Perkin-Elmer Cermax) with a double-pass CaF_2 prism monochromator (Perkin-Elmer Model 99).[28] The main advantage of the prism monochromator is that each wavelength is dispersed into a unique angle, which is not the case for the diffraction grating monochromator where a cut-off filter is used to remove the higher order diffraction peaks. Unlike typical arc lamps, which are housed in glass (limiting their usage to below 2.5 μm), our Xe lamp is equipped with a sapphire window that enables access to longer wavelengths. Depending on the light wavelength, different sets of optics are used. In the 10.6 – 2 μm wavelength range (115 – 620 meV), we use a ZnSe PEM (II/ZS50, Hinds Instruments) and BaF_2 holographic wire-grid polarizers. A fused silica PEM (I/FS50, Hinds Instruments) and calcite Glan-Taylor polarizers are used in the 2 – 0.46 μm wavelength range (620 – 2 700 meV). To avoid interference effects caused by multiple reflections within the PEM when coherent laser light is used, the ZnSe PEM is tilted forward 25° and the fused silica PEM crystal is wedged. Two different cryostats are used: a superconducting magneto-optical cryostat (Cryo Industries), reaching

temperatures down to 6 K and magnetic fields up to 7 T and an optical cryostat (Janis Reasearch) reaching temperatures down to 8 K with a separate electromagnet (HV – 4H, Walker Scientific) producing a magnetic field up to 2 T. In order to rotate the sample at low temperatures (T ~ 15 K), a special copper sample holder is constructed for the 7 T magneto-optical cryostat, enabling a complete (360˚) rotation of the sample around an axis parallel to the incident radiation direction. The sample rotation is achieved by two kevlar threads wrapped around the sample holder and around two brass cylinders that are placed at the top of the sample stick. The kevlar threads pass through separate vacuum feed-throughs inside the cryostat. The actual rotation of the sample holder is done by rotating the brass cylinders, which increases the tension on one thread while decreasing it on the other. A schematic illustration and the photograph of the sample holder are shown in Fig. 2.

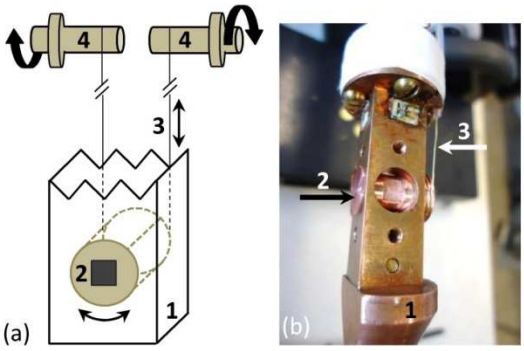

Fig. 2. (Color online) Rotating sample holder. (a) Schematic illustration of the coldfinger (1), from the front side, with the sample holder (2) and sample (black square). The arrows indicate how the sample holder is rotated when kevlar threads (3), which are wrapped around two brass cylinders (4), are pulled/loosened. (b) Photograph of the rotating sample holder. The sample is glued on the front side of the holder.

V. RESULTS AND DISCUSSION

In Fig. 3 we show the measurement of MLD using the definition described by Eq. (1). In this experiment, the magnetization is oriented by a strong external magnetic field of 500 mT (that is well-above the saturation field) along the [010] crystallographic direction (see Fig. 1(a) for a definition of the coordinate system). The intensity of the reflected light with the polarization parallel ($I_R^{||}$) and perpendicular ($I_R^{\perp}$) to magnetization direction is measured [see Fig. 3(a)]. The most important aspect of this measurement is to keep the incoming intensity the same for both polarizations of light. In order to meet this condition we use a linear polarizer with a fixed orientation and a λ/2 Fresnel rhomb to rotate the incident light polarization. The $I_R^{||}$ and $I_R^{\perp}$ spectra, measured at 15 K, are shown in Fig. 3(a) for GaMnAs sample with 3% of Mn. The overall shape of the intensity spectra is dominated by the emission spectrum of the halogen lamp, and no apparent difference can be seen between the curves. The difference between $I_R^{||}$ and $I_R^{\perp}$ is more pronounced in Fig. 3(b), where we show the signal that is calculated from the measured data using Eq. (1). The same procedure is also performed at temperature T = 150 K, which is high above the sample Curie temperature, with no magnetic field applied. Despite the zero magnetic moment in the sample, our measurements show a nonzero difference signal also at T = 150 K which can be attributed to experimental artifacts in our system (e.g., a birefringence of the cryostat windows, a polarization-sensitive response of the photodetector, etc.). By subtracting the curves in Fig. 3(b) we obtain the MLD spectrum of the sample without the artifacts [see Fig. 3(c)]. The relatively large experimental error comes from the poor reproducibility of the MLD spectrum, caused mainly by the fact that a relatively small MLD signal is obtained by subtracting two

large signals. In order to confirm the MLD-related origin of the measured spectrum, we probe the polarization dependence of the signal around its peak (~ 1.6 eV). The results that are shown in Fig. 3(d) are in a good agreement with the polarization dependence of MLD described by Eq. (4). It is worth noting that since there are two orthogonal polarizations used in order to measure the MLD signal, the incident light polarization $\beta = 45^{\circ}$ corresponds to Eq. (1). The measured data are fitted by the Eq. (4), obtaining the MLD coefficient P^{MLD} = 0.9987.

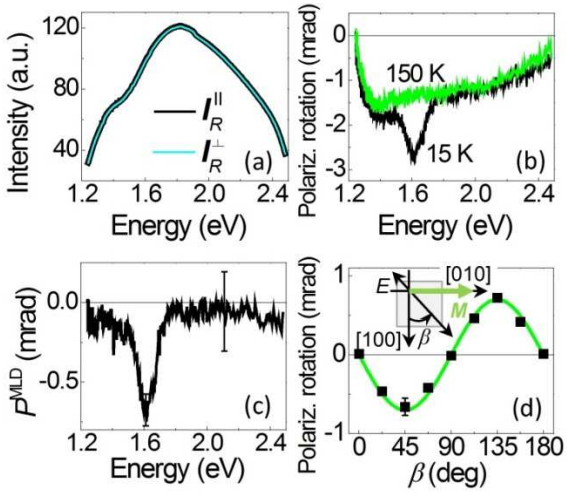

Fig. 3. (Color online) Measurement of MLD from the definition described by Eq. 1 in a $Ga_{1-x}Mn_xAs$ epilayer with nominal Mn doping x = 3% with the Curie temperature T_C = 77 K. (a) Spectral profile of reflected light intensity with polarization parallel ($I_R^{\parallel}$) and perpendicular ($I_R^{\perp}$) to the magnetization at T = 15 K. (b) Polarization rotation determined from the data shown in (a) using Eq. (1) for T = 15 K. The same measurements were performed for a temperature above the Curie temperature with no external magnetic field. The data obtained for 150 K should not have any MLD features since $|M| = 0$, so any structure in these data are reproducible experimental artifacts. (c) MLD spectrum obtained by subtracting the curves shown in (b). (d) Polarization dependence of the MLD (black points) measured at photon energy 1.6 eV in the geometry shown in the inset, where the polarization rotation for $\beta = 45^{\circ}$ corresponds to Eq. (1). The solid line is a fit by Eq. 4 with an MLD coefficient P^{MLD} = 0.9987 mrad. As expected, the polarization rotation signal is maximal at $\beta = 45^{\circ}$, where $E_{\parallel} = E_{\perp}$ and zero when the incident polarization is perfectly perpendicular ($\beta = 0^{\circ}$) or parallel ($\beta = 90^{\circ}$) to M.

In Fig. 4(a) we show the hysteresis loops measured in the experimental setup depicted in Fig. 1(b) for the 3% Mn sample. A Ti-sapphire laser tuned to a photon energy of 1.62 eV is used to obtain a large MLD-related signal [see Fig. 3(c)]. The M-shaped hysteresis loops are a typical signature of four energetically equivalent magnetization easy axes in the sample plane [labeled "M_1" – "M_4" in Fig. 4(c)].[5,15,23,25] For a detailed understanding of the measured MO data, it is illustrative to perform the following analysis. Let us assume that by the application of a magnetic field the magnetization jumps from the easy axis (EA) M_4 to M_1. The orientation of magnetization in the sample plane is described by angles $\varphi_{M1} = \gamma - \xi/2$ and $\varphi_{M4} = \gamma + \xi/2$, respectively, where γ is the position of the easy axes bisector and ξ is their mutual angle [see Fig. 4(d) for a definition of the angles γ and ξ]. According to Eq. (4), we can write the polarization rotation signals $\Delta\beta_1$ and $\Delta\beta_4$ for magnetization in M_1 and M_4, respectively, as:

$$\Delta\beta_1 = P^{MLD} sin2((\gamma - \frac{\xi}{2}) - \beta) \quad (9)$$

$$\Delta\beta_4 = P^{MLD} sin2((\gamma + \frac{\xi}{2}) - \beta). \quad (10)$$

The amplitude of the measured MO signal in the hysteresis loop is thus equal to $\Delta\beta = \Delta\beta_4 - \Delta\beta_1$:

$$\Delta\beta = 2P^{MLD} cos\, 2(\gamma - \beta) sin(\xi). \quad (11)$$

Equation (11) shows that the hysteresis loop amplitude is not only proportional to the MLD coefficient P^{MLD} but also depends on the angle between two adjacent easy axes. The orientations of the EA are given by the overall magnetic anisotropy of the sample, which is quite complex in (Ga,Mn)As.[29,30] It consists of two competing contributions. The first one is the biaxial anisotropy along the [100] and [010] crystallographic directions, which originates from the cubic symmetry of the GaAs host lattice, and the second one is the uniaxial anisotropy along the [-110] crystallographic direction.[29,30] It is the uniaxial anisotropy that causes γ = 135° in all (Ga,Mn)As samples and the maximum magnitude of the hysteresis loops is thus measured for β = 45° or 135°. We note that Eq. (11) shows the same periodicity as the "static" MLD-related signal [see Eq. (4)] - cf. Fig. 3(d) and Fig. 4(b).

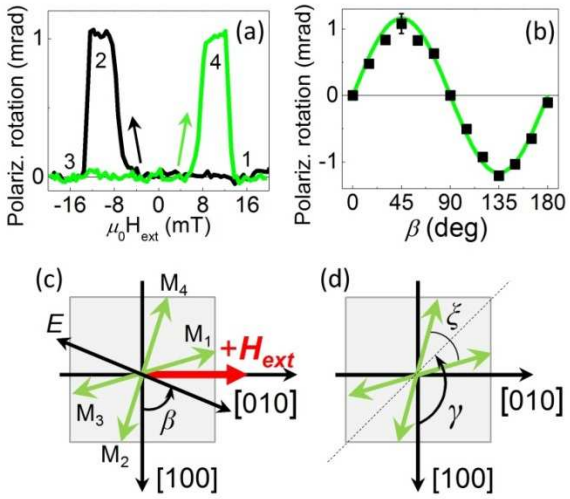

Fig. 4. (Color online) Rotation of light polarization measured at 15 K using the polarization-sensitive optical bridge. (a) *M*-shaped hysteresis loops are a signature of four energetically equivalent magnetization easy axes, which are schematically labeled M_1 - M_4 in (c). The number adjacent to the measured MO signal indicate the orientation of the magnetization along a particular easy axis. The photon energy is 1.62 eV and the incident orientation of linear light polarization β = 45˚, where β is depicted in (c). The measurement begins with a positive applied magnetic field causing the sample to be magnetized along M_1. As the external magnetic field is reduced and becomes negative (black curve), the magnetization jumps to M_2, producing a new rotation signal. When the applied magnetic field becomes more negative, the magnetization jumps into M_3, which leads to the same MO signal as in the case of magnetization in M_1. The green curve in (a) shows the polarization rotation signal when the applied magnetic field is swept from negative to positive values. Note that this techniques measures relative changes in the reflected light polarization as the magnetization switches from one EA to another; the absolute polarization rotation in (a) is arbitrary. (b) Hysteresis loop amplitude as a function of the light polarization orientation β (black points) together with the fit by Eq. 11 (solid line) with parameters P^{MLD} = 0.9987 mrad and ξ = 60˚, where ξ is the angle between adjacent easy axes, as shown in (d).

The major difference, however, is that the magnetization orientation (φ_M) and the corresponding MO coefficient (P^{MLD}) can be directly determined from the data shown in Fig. 3(d). On the contrary, the polarization dependence of the hysteresis loops [data in Fig. 4(b)] has to be supplemented by some additional independent measurement to obtain the information about the EA positions or P^{MLD}. For example, we can take the value P^{MLD} = 0.9987 from the fit of the data in Fig. 3(d) as the independent input and by fitting the data in Fig. 4(b) using Eq. (11) we can obtain the angle between the EA, ξ = 60˚ and in turn the

absolute orientation of EA in the sample plane: $\varphi_{M1} = 135^\circ - \xi/2 = 105^\circ$, $\varphi_{M4} = 135^\circ + \xi/2 = 165^\circ$, $\varphi_{M3} = \varphi_{M1} + 180^\circ$, and $\varphi_{M2} = \varphi_{M4} + 180^\circ$. We note that these results are in excellent agreement with the EA orientations obtained in this sample by independent time-resolved magneto-optical and SQUID measurements.[4,18,31,32]

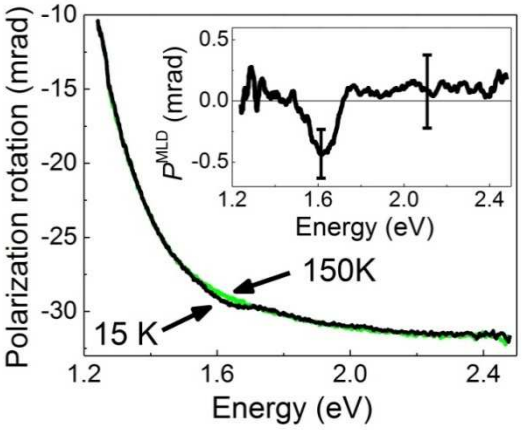

Fig. 5. (Color online) MLD measurement by the "temperature-corrected" PEM technique. The polarization rotation detected at temperatures below (15 K) and above (150 K) the sample Curie temperature are shown. Inset: Spectral dependence of MLD determined from the difference between the data depicted in the main panel.

In Fig. 5 we show the MLD measurement in the 3% Mn sample using the PEM experimental setup described in Fig. 1(c). We observe that the measured signal contains not only the MLD-related signal but also a strong background that is still present at temperatures above T_C. To remove it, we subtract the signals measured at 15 K and 150 K. The MLD spectrum obtained by this "temperature-corrected" PEM technique is shown in the inset of Fig. 5. The experimental error of this MLD signal is quite large due to the fact that we are subtracting two large signals with a magnitude of tens of miliradians in order to get a signal that is at least fifty times smaller. We note that, in principle, the background signal can be removed not only by heating up the ferromagnetic sample above its T_C but also from a comparison of the signals measured at the same temperature in "similar" magnetic and non-magnetic samples (GaMnAs and GaAs in our case). We have verified that MLD spectra obtained by both approaches are similar, but the latter procedure provides less reproducible results. This is a consequence of small movements of the reflected beam within the experimental setup which cannot be avoided when the samples are interchanged. The "temperature-corrected" PEM technique could be also used to measure the MLD-related change of reflected light ellipticity [see Eq. (7)]. However, we observe that the detected signal at ω_{PEM}, which is connected with the ellipticity, is not stable enough in time to enable a reliable comparison of the signals measured below and above T_C. This time instability of the signals, which is much more pronounced at ω_{PEM} (ellipticity) than at $2\omega_{PEM}$ (rotation), seems to be induced by slight variations of the PEM retardance, which is highly sensitive to temperature, due to drift in the laboratory ambient temperature.

Finally, we describe the measurement of MLD by our new experimental technique [Fig. 1(d)] where we combine the sensitivity of light polarization modulation using a PEM with the reduced background signal of hysteresis loop measurements [Fig. 1(b)]. The major advantage of the hysteresis measurements is that they reflect the *change* of the MO signal that is induced by the magnetization jump from one EA to another, and therefore "automatically" separate the measured signal from experimental artifacts. However, the common implementation of this technique can be applied only in samples with a sufficiently large angular separation ξ between the adjacent magnetic easy axes – see inset in Fig. 4(c) and Eq. (11). We show below

how this limitation can be eliminated if a rotation of the magnetization by an external magnetic field is supplemented by a rotation of the whole sample. Moreover, the analysis of the polarization state of the reflected light by the PEM can be performed in a much broader spectral range than in the case of the polarization-sensitive optical bridge employing a half wave plate. In the latter case, the wavelength range is extremely limited unless many different wave plates are used. Finally, both the magnetization-related change of light rotation and ellipticity can be measured simultaneously by detecting the signals at $2\omega_{PEM}$ and ω_{PEM}, respectively. The limitation of this technique is that it can only be applied to samples with an in-plane magnetic anisotropy, where the positions of the magnetization EA are known from independent SQUID or pump-probe MO measurements.[4,32]

The measurement procedure itself consists of several steps which are schematically shown in Fig. 6(a). In the first step, we rotate the sample so that one of the EA is as close as possible to the direction of the external magnetic field (H_{ext}), which is horizontal in our case. By subsequent application of a strong magnetic field (H_{ext} ~ 600 mT) we "force" the magnetization to be aligned with this EA (as in case of four equivalent EA, the magnetization can be oriented in any of them). In the second step, we set H_{ext} to zero and rotate the sample so that the magnetization is 45˚ away from horizontal. The position of the sample is now fixed and it is not changed during the actual measurement of the MLD. Next, we shine a light on the sample with a polarization plane along the magnetization orientation. Consequently, the reflected light should not experience any polarization rotation [see Eq. 4] and, therefore, any signal measured at the reference frequency and its harmonics are just background artifacts that can be set to zero (e.g., by a small simultaneous rotation of the PEM and P_2). In the third step, we apply H_{ext} that tilts the magnetization position until it is aligned with the direction of H_{ext}, which for the sample with 3% Mn is $\mu_0 H_{ext} > 20$ mT [see Fig. 6(b)]. Note that since H_{ext} is large in this case, the orientation of M along H_{ext} does not need to be along an EA. The 45˚ rotation of the magnetization within the sample plane causes one polarization component of the incident light to be aligned with M and the other, equal amplitude component to be perpendicular to M. As a result the rotation and ellipticity magnitudes change from minimal to a maximal values, with the changes being caused solely by MLD. We emphasize that the measured MO-signal is obtained without moving/rotating the sample, changing its temperature, or moving/rotating any optical elements. We find that unlike other changes, applying an external magnetic field is minimally disruptive to the reflected polarization. The 45˚ reorientation of the magnetization by the application of H_{ext} yields a measured polarization rotation $\Delta\beta$ that is directly equal to P^{MLD} [see Eq. 4]. We note that in a control experiment above the sample T_C we did not observe any MLD-related MO signal [see Fig. 6(b)], in accordance with the negligibly small overall magnetic moment in the sample. The measured spectral dependence of P^{MLD}, where each data point is determined at a discrete photon energy using the procedure described above, is shown in Fig. 6(c). The error bars in the polarization rotation (~ 45 μrad) are mainly due to the uncertainty in the sample position, i.e., the EA position with respect to the magnetic field direction. The error bars in the ellipticity (~ 100 μrad) are larger due to more noise in the signal at ω_{PEM}. It is worth noting, that some signal at ω_{PEM} is always present and cannot be zeroed as in the case of the rotation signal, and we refer to it as the background signal, which is not connected with the magnetization reorientation. The observed background ellipticity signal arises from optical components placed after the sample, e.g. cryostat windows, lenses, PEM etc. The ellipticity changes induced by the magnetization reorientation are typically on the order of the background signal noise, making the determination of MLD ellipticity less precise. In order to increase the sensitivity of the MLD measurements, one can rotate the sample 90˚ instead of 45˚ after the initial orientation of magnetization along an EA. In this case, the magnetization position is oriented 45˚ with respect to the incident polarization, causing a non-zero magneto-

optical signal in rotation (and ellipticity) before the horizontal magnetic field is applied. This signal in rotation is zeroed deliberately by small rotation of the PEM and P_2 (as discussed above, some background ellipticity signal is always present and cannot be zeroed). The application of the external magnetic field will induce a 90˚ reorientation of the magnetization position, and now the polarization component of the incident light that was parallel with M becomes perpendicular to it and the other, equal amplitude component that was perpendicular to M becomes parallel to it. This results in a sign change of the MO signals, effectively *doubling* the measured step-like magneto-optical signal compared to the 45˚ rotation case, in accordance with Eq. (11).

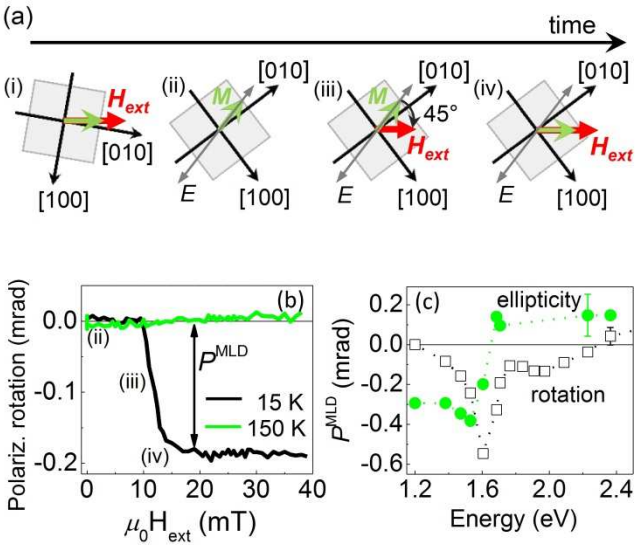

Fig. 6. (Color online) MLD measurement by the "rotation-corrected" PEM technique. (a) Schematic illustration of the individual steps performed in the measurement procedure. (i) Before the actual measurement of MLD, the sample easy axis (green arrow) is oriented along the saturating external magnetic field H_{ext} (red arrow). (ii) In the next step, the magnetic field is turned off and the sample is rotated for 45˚ so that the magnetization M and the incident light polarization plane E are parallel, i.e., there is no polarization rotation due to MLD. (iii) and (iv) The position of the sample is fixed and the application of H_{ext} leads to the magnetization reorientation and, consequently, to the light polarization rotation. (b) MLD signal produced by the change of the magnetization orientation relative to *E*, as indicated in (a), at temperatures below (15 K) and above (150 K) the sample Curie temperature, at a photon energy of 1.7 eV. (c) Spectral dependence of the light polarization rotation and ellipticity measured at T = 15 K.

We can now compare the MLD spectra measured in one sample using three different techniques: the determination of MLD using two separate measurements with orthogonal probing light polarizations [Fig. 3(c)]; "temperature-corrected" PEM technique (inset in Fig. 5); and the "rotation-corrected" PEM technique [Fig. 6(c)]. We see that the main characteristic feature of the MLD spectrum – the peak at ~ 1.62 eV – is present at the same position and with a similar magnitude in all the spectra. However, the major difference is in the spectral regions where only weak MLD-related signals are detected and, therefore, where in the first two methods a subtraction of two similar signals leads to a large uncertainty in the magnitude, and even in the sign, of the MLD signal [see the spectral ranges around 1.3 eV and 2.4 eV in Fig. 3(c) and in the inset in Fig. 5]. This uncertainty is, in principle, not present in the "rotation-corrected" PEM technique. To further illustrate the differences in the sensitivity of the experimental techniques, we show in Fig. 7 the MLD spectra measured in (Ga,Mn)As epilayers with 3% and 7% Mn content by the "temperature-corrected" (solid line) and the "rotation-corrected" (points) PEM techniques, respectively. We see that for the 7% Mn sample the subtraction of the measured data in the "temperature-corrected" technique

appears to distort the measured spectral profile of MLD. We note that the magnitude of the MLD peaks in the visible and mid-infrared spectral regions is comparable with the magnitude of PKE measured in the identical samples.[4,17,18,31]

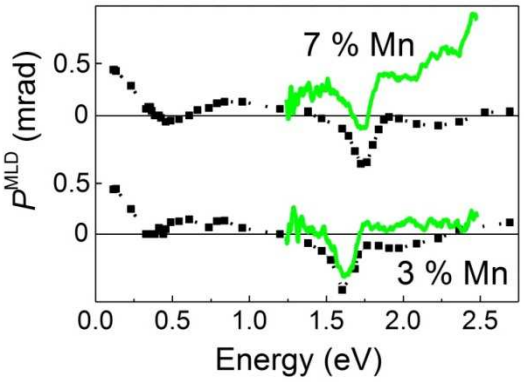

Fig.7. (Color online) Comparison of the spectral dependence of MLD measured in samples with 3% and 7% Mn concentration by two different experimental techniques. The solid line corresponds to MLD spectra measured by the "temperature-corrected" PEM technique, where rather strong experimental artifacts are present, and the points correspond to MLD spectra measured by the "rotation-corrected" PEM technique.

VI. CONCLUSION

We present an overview of four different experimental techniques that can be used to measure the magnetic linear dichroism (MLD) in the ferromagnetic semiconductor (Ga,Mn)As. We show that the most reliable results are obtained using a new experimental technique that controls the angle between the sample magnetization and the polarization of probing light by rotating the sample and applying an external magnetic field. The main advantage of this technique is that it probes the magneto-optical signal that is directly connected with the ferromagnetic order in the sample while reducing artifacts from the experimental setup. In addition, this technique enables MLD measurements in samples with a strong uniaxial anisotropy, where only two EA, with 180˚ symmetry, are present. Using this technique we measure the MLD spectrum in a broad energy range from 0.1 eV to 2.7 eV in (Ga,Mn)As samples with 3% and 7% concentration of Mn atoms. We observe that the MLD is enhanced in the visible and the mid-infrared spectral regions, which is due to electronic interband transitions between the valence and conduction bands and intraband transitions within the valence band, respectively. The strong spectral features in the MLD spectrum might also bring light into the long lasting discussion about the character of the band structure in (Ga,Mn)As.

In conclusion, we would like to note that the experimental technique presented in this paper is not limited to ferromagnetic semiconductors such as (Ga,Mn)As, but it can be used to measure second-order magneto-optical effects in other ferromagnetic materials.

VII. ACKNOWLEGEMENT

We wish to thank V. Novák, K. Olejník and M. Cukr for sample growth and characterization. We also thank T.J. Gruenauer and K.M. Cullinan for their work on designing and machining the rotating sample holder system that is used in the magneto-optical cryostat. We are grateful to K. Výborný for his helpful discussions about MLD from a theoretical point of view and A. Markelz for providing additional optical components.

This work was supported by the Grant Agency of the Czech Republic Grant No. 202/09/H041 and P204/12/0853 and the Grant Agency of the Charles University in Prague

Grant No. SVV-2012-265306 and No. 443011. We also acknowledge the financial support provided by the School of Physics, Faculty of Mathematics and Physics at the Charles University in Prague. Work done at University at Buffalo is supported by NSF-DMR1006078.

APPENDIX

In Fig. 1(c), the electric field is polarized along the *x*-axis when it is transmitted through the polarizer P_1. Taking advantage of the Jones matrix formalism, the electric field can be simply expressed in the linear basis as:

$$E_0 \begin{pmatrix} 1 \\ 0 \end{pmatrix}, \tag{A1}$$

where E_0 denotes the amplitude of the electric field. When passing through the PEM, with the optical axis tilted 45˚ from the *x*-axis towards the *y*-axis, we can write the electric field in the following form:

$$\tfrac{1}{2} E_0 \begin{pmatrix} 1 & -1 \\ 1 & 1 \end{pmatrix} \begin{pmatrix} 1 & 0 \\ 0 & e^{i\delta} \end{pmatrix} \begin{pmatrix} 1 & 1 \\ -1 & 1 \end{pmatrix} \begin{pmatrix} 1 \\ 0 \end{pmatrix}, \tag{A2}$$

where the periodic retardation of the PEM, δ, is defined in the main text. The magnetized sample induces a rotation and a change in the ellipticity of the reflected light polarization, because of the different complex reflection coefficients for light polarized along the *x* and *y* axes. We can describe the magnetization-induced ellipticity by Jones matrix for a general phase retarder. The polarization rotation $\Delta\beta$ can be included in the projection of light polarization into the optical axis of the polarizer P_2, where the optical axis is oriented at the angle α with respect to the *x*-axis. The amplitude of the electric field vector $\boldsymbol{E}$ which is transmitted through P_2 is given:

$$\tfrac{1}{2} E_0 \begin{pmatrix} 1 + e^{i\delta} \\ 1 - e^{i\delta} \end{pmatrix} \begin{pmatrix} 1 & 0 \\ 0 & e^{i\Delta\eta} \end{pmatrix} \begin{pmatrix} cos(\alpha + \Delta\beta) \\ sin(\alpha + \Delta\beta) \end{pmatrix}, \tag{A3}$$

where $\Delta\eta = \eta_y - \eta_x$ is the polarization phase shift between the *x* and *y* polarization components producing the ellipticity. The overall intensity of light reaching the detector $I_D \sim |\boldsymbol{E}|^2 = \boldsymbol{EE^*}$ is given by Eq. (6) in the main text. The lock-in amplifiers demodulate the signal from the detector, which (in the first approximation) consists of three components:

$$I_D = q_0 I(0) + q_1 I(\omega_{PEM}) sin(\omega_{PEM} t) + q_2 I(2\omega_{PEM}) cos(2\omega_{PEM} t)\,, \tag{A4}$$

where $I(0)$ is the intensity of the light modulated at the chopper frequency and $I(\omega_{PEM})$ and $I(2\omega_{PEM})$ are the light intensities modulated at ω_{PEM} and $2\omega_{PEM}$, respectively. q_0, q_1 and q_2 represent the sensitivities of the detection-amplification system for $I(0)$, $I(\omega_{PEM})$ and $I(2\omega_{PEM})$, respectively. Employing the Bessel functions, the detected signal components $I(0)$, $I(\omega_{PEM})$ and $I(2\omega_{PEM})$ can be written:

$$I(0) = \tfrac{I_0}{2}(1 + J_0(\delta_0) cos2(\Delta\beta + \alpha))\,, \tag{A5a}$$

$$I(\omega_{PEM}) = \tfrac{I_0}{2}(2J_1(\delta_0) sin2(\Delta\beta + \alpha) sin(\Delta\eta))\,, \tag{A5b}$$

$$I(2\omega_{PEM}) = \tfrac{I_0}{2}(2J_2(\delta_0) cos2(\Delta\beta + \alpha))\,. \tag{A5c}$$

We note that the Eq. (7) in the main text was derived from Eq. (A4), (A5a), (A5b) and (A5c), respectively, assuming $\alpha = \pi/4$.

The polarization rotation $\Delta\beta$ can be determined as the ratio of $I(2\omega_{PEM})/I(0)$:

$$\frac{I(2\omega_{PEM})}{I(0)} = -C_2 \frac{2J_2(\delta_0)cos2(\Delta\beta+\alpha)}{1-J_0(\delta_0)cos2(\Delta\beta+\alpha)}, \quad \text{(A6)}$$

where the coefficient $C_2 = q_0/q_2$. In the small angle approximation and with the assumption that $\alpha = \pi/4$, Eq. (A6) leads to Eq. (8) in the main text.

The calibration of the experimental setup is needed in order to estimate the value of $C_2J_2(\delta_0)$ in Eq. (8), thus obtaining P^{MLD} from the measured rotation signal $\Delta\beta$. For this purpose, we replace the (Ga,Mn)As sample by a silver mirror and we first measure the signal for $\alpha = 0$ and subsequently for $\alpha = \pi/2$. The mirror does not induce any rotation of light polarization plane ($\Delta\beta = 0$), so the Eq. (A6) can be rewritten as:

$$\frac{I(2\omega_{PEM})}{I(0)} = \pm\frac{2C_2J_2(\delta_0)}{1\pm J_0(\delta_0)}, \quad \text{(A7)}$$

where the "+"sign corresponds to $\alpha = 0$ and "–" sign corresponds to $\alpha = \pi/2$. $J_0(\delta_0)$ can be determined by taking the ratio of $(I(2\omega_{PEM})/I(0))_{\alpha=0}$ and $(I(2\omega_{PEM})/I(0))_{\alpha=\pi/2}$. The value $C_2J_2(\delta_0)$ can be obtained from Eq. (A7), using the calculated value of $J_0(\delta_0)$.

The similar mathematical analysis can be applied in case of PEM placed after the sample as shown in Fig. 1(d). In this case, the incident polarization of light is at 45° with respect to *x*:

$$\frac{E_0}{\sqrt{2}}\begin{pmatrix}1\\1\end{pmatrix}. \quad \text{(A8)}$$

After the reflection from the magnetized sample, the electric field vector can be written in the form:

$$\frac{E_0}{\sqrt{2}}\begin{pmatrix} cos(\frac{\pi}{4}+\Delta\beta) \\ e^{i\Delta\eta}sin(\frac{\pi}{4}+\Delta\beta)\end{pmatrix}. \quad \text{(A9)}$$

The PEM modulates the phase difference between the components parallel and perpendicular to its optical axis and P_2, oriented at the angle $\alpha = 90^{\circ}$, mixes them subsequently. The magnitude of the electric field vector after P_2 is given by a multiplication of Jones matrices of all the optical components:

$$\frac{E_0}{\sqrt{2}}\begin{pmatrix} cos(\frac{\pi}{4}+\Delta\beta) \\ e^{i\Delta\eta}sin(\frac{\pi}{4}+\Delta\beta)\end{pmatrix}\begin{pmatrix}1+e^{i\delta} & 1-e^{i\delta}\\ 1-e^{i\delta} & 1+e^{i\delta}\end{pmatrix}\begin{pmatrix}0\\1\end{pmatrix}. \quad \text{(A10)}$$

The overall intensity calculations lead to the same expression for MLD as in Eq. (8).

REFERENCES

[1] M. H. Kim, G. Acbas, M. H. Yang, I. Ohkubo, H. Christen, D. Mandrus, M. A. Scarpulla, O. D. Dubon, Z. Schlesinger, P. Khalifah, J. Cerne, Phys. Rev. B **75**, 214416 (2007).

[2] G. Acbas, M. H. Kim, M. Cukr, V. Novak, M. A. Scarpulla, O. D. Dubon, T. Jungwirth, J. Sinova, J. Cerne, Phys. Rev. Lett. **103**, 137201 (2009).

[3] R. M. Osgood III, S. D. Bader, B. M. Clemens, R. L. White, H. Matsuyama, J. Magn. Magn. Mater. **182**, 297 (1998).

[4] N. Tesařová, P. Němec, E. Rozkotová, J. Šubrt, H. Reichlová, D. Butkovičová, F. Trojánek, P. Malý, V. Novák, T. Jungwirth, Appl. Phys. Lett. **100**, 102403 (2012) and its Supplementary material.

[5] A. V. Kimel, G. V. Astakhov, A. Kirilyuk, G. M. Schott, G. Karczewski, W. Ossau, G. Schmidt, L. W. Molenkamp, Th. Rasing, Phys. Rev. Lett. **94**, 227203 (2005).

[6] T. Jungwirth, P. Horodyská, N. Tesařová, P. Němec, J. Šubrt, P. Malý, P. Kužel, C. Kadlec, J. Mašek, I. Němec, M. Orlita, V. Novák, K. Olejník, Z. Šobáň, P. Vašek, P. Svoboda, J. Sinova, Phys. Rev. Lett. **105**, 227201 (2010).

[7] J. Cerne, M. Grayson, D. C. Schmadel, G. S. Jenkins, H. D. Drew, R. Hughes, A. Dabkowski, J. S. Preston,P. J. Kung, Phys. Rev. Lett. **84**, 3418 (2000).

[8] A. K. Zvezdin, V. A Kotov, Modern Magnetooptics and Magnetooptical Materials (Institute of Physics Publishing, Bristol and Philadelphia, ISBN 075030362X, 1997).

[9] R. P. Cowburn, S. J. Gray, J. Ferré, J. A. C. Bland, J. Miltat, J. Appl. Phys. **78**, 7210 (1995).

[10] G. Y. Guo, H. Ebert, Phys. Rev. B **51**, 12633 (1995).

[11] S.D. Bader, J. Magn. Magn. Mater. **100**, 440 (1991).

[12] J. Ferre, G. A. Gehring, Rep. Prog. Phys. **47**, 513 (1984).

[13] R. Carey, B. W. Thomas, J. Phys. D **7**, 2362 (1974).

[14] K. Postava, D. Hrabovský, J. Pištora, A. R. Fert, Š. Višnovský, T. Yamaguchi, J. Appl. Phys. **91**, 7293 (2002).

[15] B. Al-Qadi, N. Nishizawa, K. Nishibayashi, M. Kaneko, H. Munekata, Appl. Phys. Lett. **100**, 222410 (2012).

[16] K. Postava, H. Jaffres, A. Schuhl, F. Nguyen Van Dau, M. Gorian, A. R. Fert, J. Magn. Magn. Mater. **172**, 199 (1997).

[17] P. Němec, E. Rozkotová, N. Tesařová, F. Trojánek, E. De Ranieri, K. Olejník, J. Zemen, V. Novák, M. Cukr, P. Malý, T. Jungwirth, Nature Phys. **8**, 411 (2012).

[18] N. Tesařová, P. Němec, E. Rozkotová, J. Zemen, F. Trojánek, K. Olejník, V. Novák, P. Malý, T. Jungwirth, submitted, arXiv: 1207.0307

[19] E. De Ranieri, A. W. Rushforth, K. Výborný, U. Rana, E. Ahmad, R. P. Campion, C. T. Foxon, B. L. Gallagher, A. C. Irvine, J. Wunderlich, T. Jungwirth, New J. Phys. **10**, 065003 (2008).

[20] N. Nagaosa, J. Sinova, S. Onoda, A. H. MacDonald, N. P. Ong, Rev. Mod. Phys. **82**, 1539 (2010).

[21] Y. Zhu, X. Zhang, T. L. X. Huang, L. Han, J. Zhao, Appl. Phys. Lett. **95**, 052108 (2009).

[22] Y. Hashimoto, S. Kobayashi, H. Munekata, Phys. Rev. Lett. **100,** 067202 (2008).

[23] G. P. Moore, J. Ferré, A. Mougi, M. Moreno, L. Daweritz, J. Appl. Phys. **94**, 4530 (2003).

[24] Eunsoon Oh, D. U. Bartholomew, A. K. Ramdas, J. K. Furdyna, U. Debska, Phys. Rev. B **44**, 10551 (1991).

[25] J. Aoyama, Y. Hashimoto, S. Kobayashi, H. Munekata, J. Appl. Phys. **105**, 07C518 (2009).

[26] K. Sato, Jap. J. Appl. Phys. **20**, 2403 (1981).

[27] N. Tesařová, E. Rozkotová, H. Reichlová, P. Malý, V. Novák, M. Cukr, T. Jungwirth, P. Němec, J. Nanosci. Nanotechnol. **12**, 7477 (2012).

[28] M. H. Kim, V. Kurz, G. Acbas, C. T. Ellis, J. Cerne, J. Opt. Soc. Am. B **28**, 199 (2011).

[29]M. Kopecký, J. Kub, F. Máca, J. Mašek, O. Pacherová, A. W. Rushforth, B. L. Gallagher, R. P. Campion, V. Novák,T. Jungwirth, Phys. Rev. B **83**, 235324 (2011).
[30]A. W. Rushforth, E. De Ranieri, J. Zemen, J. Wunderlich, K. W. Edmonds, C. S. King, E. Ahmad, R. P. Campion, C. T. Foxon, B. L. Gallagher, K. Výborný, J. Kučera, T. Jungwirth, Phys. Rev. B, **78**, 085314 (2008).
[31]P. Němec, V. Novák, N. Tesařová, E. Rozkotová, H. Reichlová, D. Butkovičová, F. Trojánek, K. Olejník, P. Malý, R. P. Campion, B. L. Gallagher, J. Sinova, T. Jungwirth, submitted, arXiv: 1207.0310.
[32]E. Rozkotová, P. Němec, P. Horodyská, D. Sprinzl, F. Trojánek, P. Malý, V. Novák, K. Olejník, M. Cukr, T. Jungwirth, Appl. Phys. Lett **92**, 122507 (2008).

APPENDIX 3

Authors: N. Tesařová, P. Němec, E. Rozkotová, F. Trojánek and P. Malý

Title: Light-Induced Precession of Magnetization in Ferromagnetic Semiconductor (Ga,Mn)As

Journal: Acta Physica Polonica A

Volume: 118

Article Number: 1065

Year: 2010

14th Czech and Slovak Conference on Magnetism, July 6–9, 2010, Košice, Slovakia

Light-Induced Precession of Magnetization in Ferromagnetic Semiconductor (Ga,Mn)As

N. Tesařová, P. Němec*, E. Rozkotová, F. Trojánek and P. Malý

Charles University, Faculty of Mathematics and Physics, Ke Karlovu 3, 121 06 Prague, Czech Republic

Precession of magnetization induced by laser pulses in (Ga,Mn)As was studied by the pump-and-probe technique. We concentrated on various experimental aspects that can be used to identify a part of the measured magneto-optical signals that provides information about the dynamics of magnetization. We also revealed that the fact that it takes about 80 ps before the quasi-equilibrium precession of magnetization is initiated by the impact of laser pulse.

PACS numbers: 75.50.Pp, 75.78.−n, 78.47.J−, 78.47.D−

1. Introduction

Diluted magnetic semiconductors, with (Ga,Mn)As as the most studied representative, have attracted a significant attention in recent years mainly due to the carrier mediated ferromagnetism [1]. The impact of a laser pulse on (Ga,Mn)As leads to the photo-injection of carriers and to the temperature transient increase that in turn induce a precession of magnetization, which can be detected by a time-resolved magneto-optical (MO) spectroscopy [2–4]. However, we have observed recently that the measured MO signal contains not only the information about the ferromagnetically coupled Mn spins, but it is affected also by the laser-induced change of the complex index of refraction [5]. In this paper we concentrate on the identification of a part of the measured MO signal that provides information about the dynamics of magnetization.

2. Experimental

The experiments were performed on the 20 nm thick ferromagnetic layer of $Ga_{1-x}Mn_xAs$ grown on a GaAs (001) substrate by the low-temperature molecular beam epitaxy. Content of Mn, Curie temperature, and hole concentration in the sample are $x \approx 0.03$, $T_C \approx 77$ K, and $p \approx 4.7 \times 10^{20}$ cm^{-3}, respectively. The easy axis of magnetization lies in the sample plane; the magnetization is oriented close to [010] direction during the experiment. The polarization of the pump pulses was circular (with the helicity controlled by the quarter-wave plate) and the probe pulses were linearly polarized (along the direction of magnetization). The angles of incidence (measured from the normal of the sample surface) for pump and probe beams were 3° and 9°, respectively. All experiments were done at 15 K with no external magnetic field applied ($\mu_0 H_{ext} < 50$ μT) with a time resolution of about 200 fs.

* corresponding author; e-mail: nemec@karlov.mff.cuni.cz

3. Results and discussion

The impact of pump laser pulses on the sample modifies its magnetic and optical properties and these changes are detected by time-delayed probe pulses. We used the experimental setup where the pump-induced changes of rotation of probe polarization ($\Delta\theta$) or ellipticity ($\Delta\eta$) are measured simultaneously with the transient change of the sample reflectivity $\Delta R/R$ [3].

Typical data of $\Delta\theta$ measured for circularly polarized pump pulses are shown in Fig. 1. The data clearly reveal that after ≈ 100 ps the dynamics of $\Delta\theta$ does not depend on the helicity of the circular polarization. On the other hand, the signal at shorter time delays is strongly polarization dependent. This polarization-sensitive $\Delta\theta$ signal does not depend significantly on temperature (i.e., it is present even above T_C), orientation of linear polarization of the probe pulses or external magnetic field (not shown here). The absorption of circularly polarized light leads to a photogeneration of spin-polarized carriers [3]. Therefore, we attribute the polarization-sensitive $\Delta\theta$ signal to the dynamics of spin-polarized electrons. The very similar decay of the polarization-sensitive $\Delta\theta$ signal and the sample reflectivity $\Delta R/R$, which is not sensitive to the pump polarization, shows that the dynamics of spin-polarized electrons is dominated by their lifetime (see the inset of Fig. 1). The most important conclusion for the investigation of magnetization dynamics is that this polarization-sensitive signal does not provide direct information about the ferromagnetic order in the sample.

In the following, we will concentrate on the polarization-independent part of the signal, which is de-

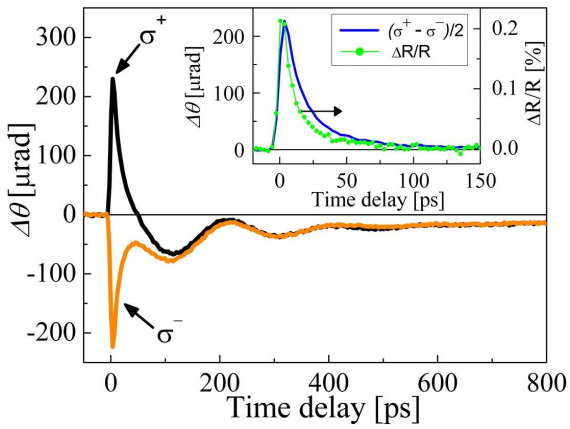

Fig. 1. Dynamics of probe polarization rotation ($\Delta\theta$) measured for circularly polarized pump pulses (σ^+ and σ^-) at 15 K with no external magnetic field applied; 80 fs pulses tuned to 1.63 eV with fluence of 46 μJ cm^{-2} were used. Inset: polarization-sensitive part, $(\sigma^+ - \sigma^-)/2$, of the measured $\Delta\theta$ signal (solid line) and the dynamics of transient reflectivity (line with points).

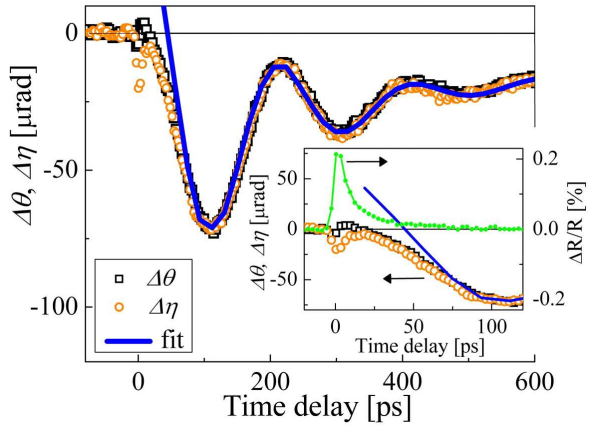

Fig. 2. Polarization-independent part, $(\sigma^+ + \sigma^-)/2$, of the rotation ($\Delta\theta$) and ellipticity ($\Delta\eta$) (points) measured under identical conditions (we note that no normalization was applied). The solid line is the fit by a sum of the exponentially damped sine harmonic function and the pulse-like function [4]; the parameters of the fit are: $A = 82$ μrad, $\tau_D = 145$ ps, $\omega = 31.3$ GHz, $\varphi = 59°$, $B = -42$ μrad, $\tau_1 = 1$ ps, $\tau_2 = 700$ ps. Inset: detail of the MO data and the transient reflectivity (line with points).

fined as an average of the signals measured with σ^+ and σ^- polarized pump pulses. In Fig. 2 we show the dynamics of $\Delta\theta$ and $\Delta\eta$. The curves are very similar except for short time delays. This implies that in the measured MO signal the "optical part" of the signal [6] has a sizable contribution only in a time range where the reflectivity (i.e., the complex index of refraction) is modified considerably by pump pulses (see the inset of Fig. 2). For time delays larger than $\approx$ 80 ps the polarization-independent MO data can be fitted well by a phenomenological model [3, 5] where the signal is decomposed into a damped precession of the magnetization around its quasi-equilibrium easy axis position (the oscillatory signal with amplitude A, angular frequency ω, initial phase φ and damping time τ_D) and into a tilt of the easy axis in the sample plane (the pulse-like function with amplitude B and rise and decay times τ_1 and τ_2, respectively). The strong deviation of the fit and the data for shorter time delays (see the inset of Fig. 2) illustrates that it takes about 80 ps to establish a quasi-equilibrium precession of the magnetization. Our observation that the magnetization precession is not fully developed immediately after an impact of the laser pulse is in accord with the results reported also for other magnetic materials. For example, in a very recent experiment in GdFeCo films a time delay of $\approx$ 90 ps was necessary before the laser pulse-induced switching of magnetization was completed [7].

4. Conclusions

We identified a part of the measured MO signal that provides information about the collective oscillations of ferromagnetically coupled Mn spins. We also revealed that the quasi-equilibrium precession of magnetization is initiated as late as 80 ps after the impact of the pump pulse.

Acknowledgments

We acknowledge V. Novák for sample preparation and characterization and T. Jungwirth for many discussions. This work was supported by Ministry of Education of the Czech Republic (research centre LC510 and the research plan MSM0021620834), Grant Agency of the Czech Republic (grant no. 202/09/H041) and by grant no. SVV-2010-261306 of the Charles University in Prague.

References

[1] T. Jungwirth, J. Sinova, J. Mašek, A.H. MacDonald, *Rev. Mod. Phys.* **78**, 809 (2006).

[2] A. Oiwa, H. Takechi, H. Munekata, *J. Supercond.* **18**, 9 (2005).

[3] E. Rozkotová, P. Němec, P. Horodyská, D. Sprinzl, F. Trojánek, P. Malý, V. Novák, K. Olejník, M. Cukr, T. Jungwirth, *Appl. Phys. Lett.* **92**, 122507 (2008).

[4] Y. Hashimoto, S. Kabayashi, H. Munekata, *Phys. Rev. Lett.* **100**, 067202 (2008).

[5] E. Rozkotová, P. Němec, N. Tesařová, P. Malý, V. Novák, K. Olejník, M. Cukr, T. Jungwirth, *Appl. Phys. Lett.* **93**, 232505 (2008).

[6] E. Kojima, R. Shimano, Y. Hashimoto, S. Katsumoto, M. Kuwata-Gonokami, *Phys. Rev. B* **68**, 193203 (2003).

[7] K. Vahaplar, A.M. Kalashnikova, A.V. Kimel, D. Hinzke, U. Nowak, R. Chantrell, A. Tsukamoto, A. Itoh, A. Kirilyuk, Th. Rasing, *Phys. Rev. Lett.* **103**, 117201 (2009).

APPENDIX 4

Authors: N. Tesařová, E. Rozkotová, H. Reichlová, P. Malý, V. Novák, M. Cukr,T. Jungwirth and P. Němec

Title: Influence of Magnetic Anisotropy on Laser-Induced Precession of Magnetization in Ferromagnetic Semiconductor (Ga, Mn)As

Journal: Journal of Nanoscience and Nanotechnology

Volume: 12

Article Number: 7477

Year: 2012

Journal of
Nanoscience and Nanotechnology
Vol. 12, 7477–7481, 2012

Influence of Magnetic Anisotropy on Laser-Induced Precession of Magnetization in Ferromagnetic Semiconductor (Ga, Mn)As

Tesařová Nad'a[1], Rozkotová Eva[1], Reichlová Helena[1], Malý Petr[1], Novák Vít[2], Cukr Miroslav[2], Jungwirth Tomáš[2,3], and Němec Petr[1,*]

[1] *Faculty of Mathematics and Physics, Charles University in Prague, Ke Karlovu 3, 121 06, Prague, Czech Republic*
[2] *Institute of Physics ASCR v.v.i., Cukrovarnická 10, 162 53 Prague, Czech Republic*
[3] *School of Physics and Astronomy, University of Nottingham, Nottingham NG7 2RD, United Kingdom*

The laser-induced precession of magnetization in (Ga, Mn)As samples with different magnetic anisotropy was studied by the time-resolved magneto-optical method. We observed that the dependence of the precession amplitude on the external magnetic field depends strongly on the magnetic anisotropy of (Ga, Mn)As and we explain this phenomenon in terms of competing cubic and uniaxial anisotropies. We also show that the corresponding anisotropy fields can be deduced from the magnetic field dependence of the precession frequency.

Keywords: Magnetic Anisotropy, Magnetic Semiconductors, Time-Resolved Spectroscopy.

RESEARCH ARTICLE

1. INTRODUCTION

In the last decade, the diluted magnetic semiconductor (Ga, Mn)As attracted significant attention due to the fact that in this material the ferromagnetic order originates from the interaction between itinerant holes and localized Mn moments.[1,2] The magnetic properties are, therefore, sensitive to the carrier concentration that make this material a rather interesting model system for the basic research.[3] In particular, the magnitude and/or the orientation of magnetization can be modified on the picosecond time scale.[4,5]

In 2005, it was revealed that the optical excitation of (Ga, Mn)As by femtosecond laser pulses triggers a precession of ferromagnetically coupled Mn spins.[5] Since then, the photo-induced precession of magnetization has been investigated by several groups.[6–10] It was concluded that the precession of magnetization is a consequence of the laser pulse-induced change of the magnetic anisotropy. But the exact mechanism is still under debate.[6–12] Recently, we have shown that the magnetic anisotropy can be modified by laser pulses not only due to the temperature increase but also due to the increase of holes concentration.[11] The precession of magnetization was studied in various (Ga, Mn)As samples and the influence of the Mn doping[9,10] and of the thermal annealing[8,9] was investigated. Nevertheless, the role of a magnetic anisotropy on the precession amplitude was not addressed in detail up to now.

The interpretation of the experimental results reported by different groups is significantly complicated by the fact that (Ga, Mn)As is, in principle, a disordered material. Therefore, a special care has to be taken when generalizing any phenomenon obtained in one particular sample to the universal behavior of this material system. Recently, we have reported on a systematic study of optical and magneto-optical properties of optimized set of (Ga, Mn)As epilayers spanning the wide range of accessible substitutional Mn_{Ga} dopings.[13] The optimization of the materials in the series, which is performed individually for each nominal doping, minimizes the uncertainties in the sample parameters and produces high quality epilayers which are as close as possible to uniform uncompensated (Ga, Mn)As mixed crystals. For each nominal Mn doping x, the growth and post-growth annealing conditions were separately optimized in order to achieve the highest Curie temperature T_C attainable at the particular x.[13] In this paper we report on a detailed study of the laser induced-precession of magnetization in two optimized (Ga, Mn)As samples that have a markedly different magnetic anisotropy. In particular, we show that the dependence of the precession amplitude on the external magnetic field depends strongly on the magnetic anisotropy and we

*Author to whom correspondence should be addressed.

explain this phenomenon in terms of competing cubic and uniaxial anisotropies in the samples.

2. EXPERIMENTAL DETAILS

The experiments were performed using two optimized 20 nm thick $Ga_{1-x}Mn_xAs$ epilayers with a distinct Mn content. The samples were grown on a GaAs(001) substrate by low-temperature molecular beam epitaxy and annealed in air. The nominal Mn doping (x), Curie temperature (T_C) and equilibrium hole concentration (p_0) are 3%, 77 K and 6.6×10^{20} cm^{-3} for sample A, and 7%, 159 K and 1.4×10^{21} cm^{-3} for sample B, respectively.[13] The magnetic anisotropy of the samples was studied by the superconducting quantum interference device (SQUID). The laser pulse-induced dynamics of magnetization was studied by the standard time-resolved magneto-optical (MO) technique.[8] As a light source, we used the Ti:sapphire laser that was tuned above the material bandgap ($h\upsilon = 1.64$ eV) and that produced laser pulses with a repetition rate of 82 MHz and a pulse width ≈200 fs. The polarization of the pump pulses was circular (with a helicity controlled by the wave plate) and the probe pulses were linearly polarized along the [100] crystallographic direction. The energy fluence of the pump pulse was ∼28 μJ cm^{-2}, with the pump to probe intensity ratio 20:1. The time-resolved MO data reported here correspond to the polarization-independent part of the pump-induced rotation of probe polarization, which was computed from the as-measured data by averaging the signals obtained for the opposite helicities of circularly polarized pump pulses.[11] The measured magneto-optical signals are due to the polar Kerr effect (PKE), which is sensitive to the out-of-plane component of magnetization, and magnetic linear dichroism (MLD), which is sensitive to the in-plane component of magnetization.[11] The samples were placed in a cryostat at the temperature of about 15 K. The external magnetic field H_{ext} ranging from ≈0 mT (i.e., smaller than 50 μT) to 550 mT was applied in the [010] crystallographic direction. In all time-resolved experiments we first applied $H_{ext} = 550$ mT and then we reduced the field to the required value. This initialization procedure was used to set the magnetization in the easy axis position that is the closest to the [010] crystallographic direction.

3. RESULTS AND DISCUSSION

In order to investigate the influence of the magnetic anisotropy on the magnetization precession in $Ga_{1-x}Mn_xAs$ we focused on two samples with a different Mn content because the concentration of Mn atoms is one of the crucial parameters that determine the magnetic anisotropy in this material. Under equilibrium conditions, the magnetization is oriented in the easy axis direction, i.e., in the crystallographic direction that corresponds to the minimal energy of the system if no external magnetic field is applied. The position of the easy axis is given by the overall magnetic anisotropy that is quite complex in (Ga, Mn)As. It consists of two competing contributions. The first one is the biaxial [100]/[010] anisotropy which originates from the cubic symmetry of the GaAs host lattice. The second one is the growth-induced uniaxial anisotropy.[14] These anisotropies are strongly dependent on the carrier concentration and on the lattice temperature.[15] The investigated samples were grown on GaAs substrate and, consequently, they are compressively strained that resulted in the in-plane position of the easy axis.[2, 15]

In Figure 1(a) we show the measured temperature dependent magnetization projections to [100], [−110] and [110] in-plane crystallographic directions in sample A. From the data it is clearly apparent that in the low temperature region (from 5 to ≈20 K) the cubic anisotropy dominates, because the magnetization exhibits a maximal projection along the [100] direction. However, the contribution of the uniaxial anisotropy is not negligible as can be seen from the non-equal projections along the directions [−110] and [110]. This shows that at low temperatures the easy axis position is slightly tilted from the [100] direction towards the [−110] direction. With the increasing temperature, the cubic anisotropy is quenched faster than the uniaxial one[15] and, consequently, above ≈30 K the uniaxial anisotropy prevails. On the other hand, in sample B the uniaxial anisotropy dominates even at low temperatures that is clearly apparent from the small magnetization projection along the [110] direction. (We note that in sample B the temperature-induced quenching of magnetic anisotropies was so strong that above ≈100 K the measured data were strongly influenced by the magnetic field of 2 mT that was present in the SQUID during the measurement. Consequently, above ≈100 K the data could

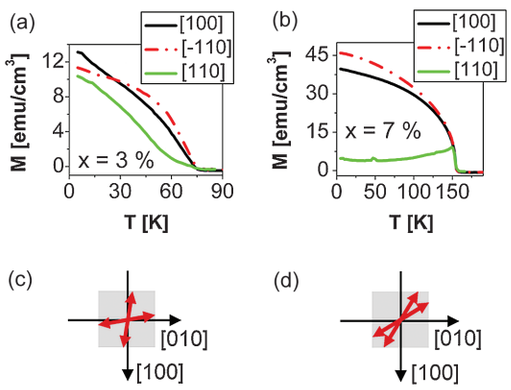

Fig. 1. Temperature dependence of magnetization projections to different crystallographic directions measured by SQUID in $Ga_{1-x}Mn_xAs$ samples with (a) $x = 0.03$ and (b) $x = 0.07$. (c) and (d) Schematic illustrations of four equivalent magnetization easy axis positions (red arrows) with respect to the main crystallographic directions [100] and [010] at 15 K for samples with $x = 0.03$ and $x = 0.07$, respectively.

not be used for a reliable determination of the magnetic anisotropy in this sample.) In Figures 1(c) and (d) we show the schematic illustrations of the four equivalent easy axis positions with respect to the main crystallographic directions in the investigated (Ga, Mn)As samples at 15 K. The observed magnetic anisotropies are fully consistent with the reported experimental[16] and theoretical[15] results and confirm the expected relative enhancement of the uniaxial anisotropy with the increasing Mn doping.

In Figure 2 we show the measured MO signal that is induced by the impact of pump pulses in sample *A*—the oscillatory signal is a signature of the laser-induced precession of magnetization.[6–10] The data can be fitted well by the exponentially damped harmonic function (see Fig. 2(b)) that is superimposed on a pulse-like background (see Fig. 2(c)):[8, 12]

$$\mathrm{MO}(t) = A\cos(\omega t + \Delta)e^{-t/t_G} + Ce^{-t/t_p} \qquad (1)$$

where A and C are the amplitudes of the oscillatory and pulse-like function, respectively, ω is the angular frequency of precessing Mn spins, Δ is a phase factor, τ_G is the Gilbert damping time, and τ_p is the damping time of the pulse-like background. This analytical formula describes the phenomenological model,[11] where the signal is decomposed into a precession of magnetization around the quasi-equilibrium easy axis and into the laser-induced tilt of the easy axis. The oscillatory signal is strongly dependent on the external magnetic field H_{ext}. In Figure 2 we show the data measured in sample *A* for two different magnetic fields applied along the [010] direction. In this sample, the external magnetic field suppresses the precession amplitude—see Figure 2(b). On the contrary, as illustrated in Figure 3, the precession amplitude can be strongly enhanced by H_{ext} in sample *B*. The markedly different response of the precession amplitude to H_{ext} in samples *A* and *B* is clearly apparent also from Figure 4(a). We should note here, that the application of H_{ext} influences also the equilibrium position of magnetization in the sample plane. Consequently, the magneto-optical response of the material can be changed due to the modification of the MLD magneto-optical coefficient, which depends on the angle between the magnetization and the linear polarization of the probe pulses.[11] This effect is negligible in sample *A* because H_{ext} is applied rather close to the easy axis and thus the equilibrium position of magnetization does not change much with H_{ext}. In sample *B*, the equilibrium position of magnetization is shifted monotonously from the easy axis towards the [010] direction [see Fig. 1(d)] with increasing H_{ext}. And even though this effect alters the MO response of the sample *B* it could not be the origin of the observed non-monotonous dependence of the precession amplitude on H_{ext}.

For the interpretation of the measured phenomena it is necessary to analyze the origin of the laser-induced precession of magnetization in detail. Absorption of a strong laser pulse in (Ga, Mn)As leads to a photogeneration of electron–hole pairs and to an increase of the sample temperature.[7, 9, 11] As already described above, both the

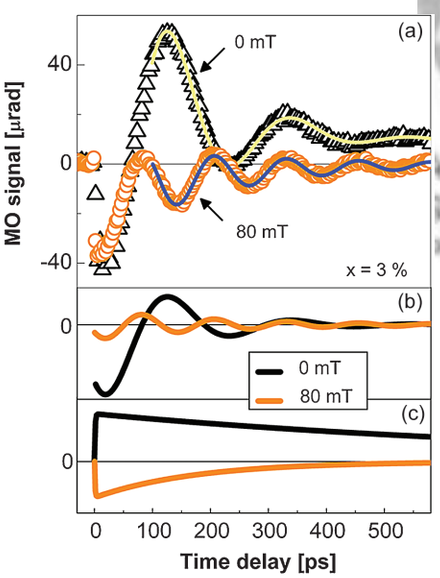

Fig. 2. (a) Time-resolved magneto-optical (MO) signal measured at 15 K in $Ga_{1-x}Mn_xAs$ sample with $x = 0.03$ for 0 mT and 80 mT external magnetic field applied along the [010] crystallographic direction (points). Solid lines are the fits by Eq. (1)—i.e., by a sum of the exponentially damped harmonic function and the pulse-like function, which are plotted separately in (b) and (c), respectively. The parameters of the fits are: $A = 114$ μrad, $\tau_G = 117$ ps, $\omega = 29.4$ GHz, $\Delta = 222°$, $C = 18.5$ μrad, $\tau_p = 880$ ps and $A = 20$ μrad, $\tau_G = 213$ ps, $\omega = 50.3$ GHz, $\Delta = 211°$, $C = -14$ μrad, $\tau_p = 175$ ps for 0 mT and 80 mT, respectively.

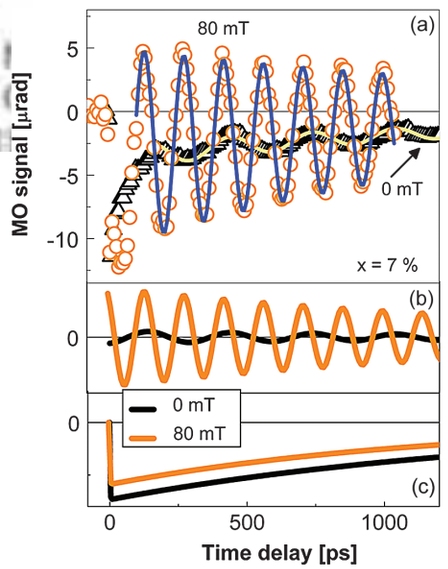

Fig. 3. Same as Figure 2 for $Ga_{1-x}Mn_xAs$ sample with $x = 0.07$. The parameters of the fit are: $A = 1.0$ μrad, $\tau_G = 1560$ ps, $\omega = 21.0$ GHz, $\Delta = 280°$, $C = -3.6$ μrad, $\tau_p = 1500$ ps and $A = 8.0$ μrad, $\tau_G = 1580$ ps, $\omega = 43.6$ GHz, $\Delta = 130°$, $C = -2.9$ μrad, $\tau_p = 1180$ ps for 0 mT and 80 mT, respectively.

RESEARCH ARTICLE

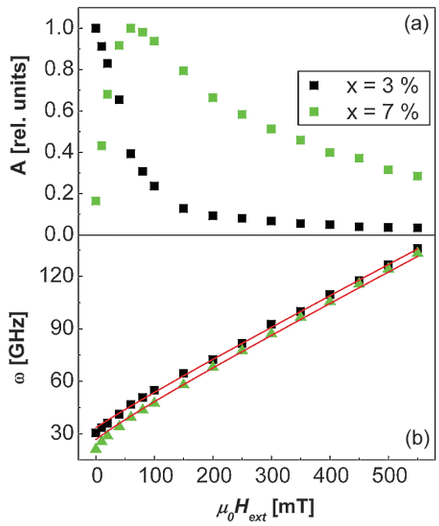

Fig. 4. Magnetic field dependence of (a) normalized precession amplitude A and (b) precession frequency ω (points). The lines in (b) are fits by Eq. (2) with parameters described in the main text.

cubic and the uniaxial anisotropies depend strongly on the concentration of holes and on the sample temperature but the dependences are rather different for them.[15] The impact of the pump pulse can modify the relative strength of these anisotropies and, therefore, it can change the position of the easy axis in the sample. This, in turn, triggers the precessional motion of magnetization which aims at pointing to this new quasi-equilibrium position where the energy of the system is minimal.[11] Nevertheless, the increase of the holes concentration and/or of the sample temperature does not always lead to the reorientation of the easy axis. For example, if the uniaxial anisotropy were far much stronger than the cubic anisotropy, the easy axis would be always located at [−110] crystallographic orientation. This shows that the laser-induced change of the easy axis position, which is triggering the precession of magnetization, can be observed only if the contribution of the cubic and the uniaxial anisotropies to the overall magnetic anisotropy in the sample are "comparable" (i.e., when the corresponding anisotropy fields contribute "similarly" to the free energy density F in the sample[14]). The external magnetic field H_{ext} appears as another uniaxial anisotropy in the sample (Zeeman term in F).[14] In our particular case, H_{ext} is applied along the [010] crystallographic direction. Therefore, an increase of H_{ext} modifies F in such a way that it deepens the energy minimum connected with the cubic anisotropy which is located along the [010] direction. We also recall that prior to the time-resolved experiments we always performed the initialization procedure that prepared the magnetization in a state that was the closest to the [010] crystallographic direction. In the case of sample A, the position of the easy axis—i.e., the position of the minimum of F without the external field—is given mainly by the cubic anisotropy [see Fig. 1(c)]. Consequently, the application of H_{ext} deepens even more this energy minimum and, therefore, reduces the precession amplitude [see Fig. 4(a)]. The precession amplitude for the highest values of H_{ext} is nearly zero in this sample because at these field levels the position of the energy minimum is given solely by the direction of H_{ext}, which does not depend at all on any change induced in the sample by the laser pulses. In sample B the uniaxial anisotropy dominates [see Fig. 1(d)] and the magnetic field again deepens the energy minimum due to the cubic anisotropy along the [010] direction. The measured non-monotonous dependence of the precession amplitude on H_{ext} [see Fig. 4(a)] is a signature that for weak magnetic fields (up to ≈80 mT) the sensitivity of the energy minimum position to the laser-induced changes of the cubic and uniaxial anisotropies is increasing. For larger H_{ext} the precession amplitude is decreasing for the same reason as in the sample A.

The application of H_{ext} leads to the monotonous increase of the precession frequency ω—see Figure 4(b)—that is in accord with the predictions of the classical gyromagnetic theory.[14] The measured data can be fitted by the equation[12]

$$\omega = \gamma\sqrt{(H_{ext} + H_{4\parallel} + 4\pi M_{eff} + H_{2\parallel}/2)(H_{ext} + H_{4\parallel})} \quad (2)$$

where $4\pi M_{eff} = 4\pi M - H_{2\perp}$ and $H_{4\parallel}$, $H_{2\parallel}$ and $H_{2\perp}$ are the in-plane cubic, in-plane uniaxial and perpendicular uniaxial anisotropy fields, respectively, and $4\pi M$ represents the demagnetization term.[14] Due to the high number of parameters, the fitting of the measured data by Eq. (2) determines the corresponding anisotropy constants ambiguously. In order to get the correct value of the anisotropy constants, we had to take into account also the magnetization easy axis position that was determined by SQUID (see Figs. 1(c) and (d)). In the fitting, we used the gyromagnetic ratio $\gamma = 2.2 \times 10^5$ mA^{-1} s^{-1}, which corresponds to Mn g-factor of 2, and we obtained $4\pi M_{eff} =$ 236 mT, $H_{2\parallel} = 65$ mT, $H_{4\parallel} = 98$ mT for sample A and $4\pi M_{eff} = 266$ mT, $H_{2\parallel} = 60$ mT, $H_{4\parallel} = 64$ mT for sample B. Equation (2) also explains why the precession frequency in samples A and B is quite distinct at 0 mT (where the corresponding frequency difference is ≈30%) but nearly the same at 550 mT (where the frequency difference is ≈1%). Without external magnetic field, ω is given solely by the anisotropy constants, which are quite distinct in these two samples, but for higher values of H_{ext} the influence of the samples magnetic anisotropy on ω is strongly suppressed.

In conclusion, we studied the laser-induced magnetization precession in (Ga, Mn)As. We concentrated on two samples with a different Mn doping that have quite distinct magnetic anisotropy. We showed that the external magnetic field strongly influences the precession of magnetization. If the magnetic field is applied close to the magnetically easy direction, the precession amplitude is quenched by the field. On the other hand, if the field is applied in the

RESEARCH ARTICLE

magnetically hard direction, the precession amplitude can be strongly enhanced. The anisotropy fields of the material can be deduced from the magnetic field dependence of the precession frequency.

Acknowledgment: This work was supported by Grant Agency of the Czech Republic (grant nos. P204/12/0853 and 202/09/H041), Grant Agency of the Charles University in Prague (grant nos. 443011 and SVV-2012-265306), EU ERC Advanced Grant No. 268066 and FP7-215368 SemiSpinNet, and by Preamium Academiae from the Academy of Sciences of the Czech Republic.

References and Notes

1. T. Dietl, H. Ohno, and F. Matsukura, *Phys. Rev. B* 63, 195205 (**2001**).
2. T. Jungwirth, J. Sinova, J. Mašek, J. Kučera, and A. H. MacDonald, *Rev. Mod. Phys.* 78, 809 (**2006**).
3. N. Samarth, *Nat. Mater.* 9, 955 (**2010**).
4. J. Wang, I. Cotoros, K. M. Dani, X. Liu, J. K. Furdyna, and D. S. Chemla, *Phys. Rev. Lett.* 98, 217401 (**2007**).
5. A. Oiwa, H. Takechi, and H. Munekata, *J. Supercond. Novel Mag.* 18, 9 (**2005**).
6. J. Qi, Y. Xu, N. H. Tolk, X. Liu, J. K. Furdyna, and I. E. Perakis, *Appl. Phys. Lett.* 91, 112506 (**2007**).
7. Y. Hashimoto, S. Kobayashi, and H. Munekata, *Phys. Rev. Lett.* 100, 067202 (**2008**).
8. E. Rozkotová, P. Nìmec, P. Horodyská, D. Sprinzl, F. Trojánek, P. Malý, V. Novák, K. Olejník, M. Cukr, and T. Jungwirth, *Appl. Phys. Lett.* 92, 122507 (**2008**), arXiv: 0802.2043.
9. J. Qi, Y. Xu, A. Steigerwald, X. Liu, J. K. Furdyna, I. E. Perakis, and N. H. Tolk, *Phys. Rev. B* 79, 085304 (**2009**).
10. S. Kobayashi, Y. Hashimoto, and H. Munekata, *J. Appl. Phys.* 105, 07C519 (**2009**).
11. P. Němec, E. Rozkotová, N. Tesařová, F. Trojánek, E. De Ranieri, K. Olejník, J. Zemen, V. Novák, M. Cukr, P. Malý, and T. Jungwirth, *Nature Phys.* 8, 411 (**2012**).
12. E. Rozkotová, P. Němec, N. Tesařová, P. Malý, V. Novák, K. Olejník, M. Cukr, and T. Jungwirth, *Appl. Phys. Lett.* 93, 232505 (**2008**), arXiv: 0808.3738.
13. T. Jungwirth, P. Horodyská, N. Tesařová, P. Němec, J. Šubrt, P. Malý, P. Kužel, C. Kadlec, J. Mašek, I. Němec, M. Orlita, V. Novák, K. Olejník, Z. Šobáň, P. Vašek, P. Svoboda, and J. Sinova, *Phys. Rev. Lett.* 105, 227201 (**2010**), and the Supplementary material, arXiv: 1007.4708.
14. X. Liu, and J. Furdyna, *J. Phys.: Condens. Matter* 18, R245 (**2006**).
15. J. Zemen, J. Kučera, K. Olejník, and T. Jungwirth, *Phys. Rev. B* 80, 155203 (**2009**).
16. K. Hamaya, T. Watanbe, T. Taniyama, A. Oiwa, Y. Kitamoto, and Y. Yamazaki, *Phys. Rev. B* 74, 045201 (**2006**).

Received: 29 April 2011. Accepted: 9 November 2011.

APPENDIX 5

Authors: N. Tesařová, P. Němec, E. Rozkotová, J. Šubrt, H. Reichlová, D. Butkovičová, F. Trojánek, P. Malý, V. Novák and T. Jungwirth

Title: Direct measurement of the three-dimensional magnetization vector trajectory in GaMnAs by a magneto-optical pump-and-probe method

Journal: Applied Physical Letters

Volume: 100

Article Number: 102403

Year: 2012

Direct measurement of the three-dimensional magnetization vector trajectory in GaMnAs by a magneto-optical pump-and-probe method

N. Tesařová,[1] P. Němec,[1,a)] E. Rozkotová,[1] J. Šubrt,[1] H. Reichlová,[1] D. Butkovičová,[1] F. Trojánek,[1] P. Malý,[1] V. Novák,[2] and T. Jungwirth[2,3]
[1]*Faculty of Mathematics and Physics, Charles University in Prague, Ke Karlovu 3, 121 16 Prague 2, Czech Republic*
[2]*Institute of Physics ASCR v.v.i., Cukrovarnická 10, 162 53 Prague, Czech Republic*
[3]*School of Physics and Astronomy, University of Nottingham, Nottingham NG7 2RD, United Kingdom*

(Received 5 January 2012; accepted 19 February 2012; published online 7 March 2012)

We report on a quantitative experimental determination of the three-dimensional magnetization vector trajectory in GaMnAs by means of the static and time-resolved pump-and-probe magneto-optical measurements. The experiments are performed in a normal incidence geometry and the time evolution of the magnetization vector is obtained without any numerical modeling of magnetization dynamics. Our experimental method utilizes different polarization dependences of the polar Kerr effect and magnetic linear dichroism to disentangle the pump-induced out-of-plane and in-plane motions of magnetization, respectively. We demonstrate that the method is sensitive enough to allow for the determination of small angle excitations of the magnetization in GaMnAs. The method is readily applicable to other magnetic materials with sufficiently strong circular and linear magneto-optical effects. © *2012 American Institute of Physics*. [http://dx.doi.org/10.1063/1.3692599]

The magnetic data storage relies on setting the magnetization orientation along a certain direction in a ferromagnetic material. The speed of data storage is connected with the dynamical response of magnetization to external stimuli. A direct experimental determination of the time-dependent non-equilibrium magnetization vector is therefore desirable because of the basic understanding of magnetization dynamics as well as for practical applications of the magnetization switching phenomena. In the last decade, several variants of experimental stroboscopic magneto-optical (MO) methods have been reported, which enable to measure the real-time trajectory of non-equilibrium magnetization.[1–5] In particular, the out-of-plane component of magnetization is well accessible due to the polar magneto-optical Kerr effect (MOKE). Here a linearly polarized light experiences a change of polarization after the reflection on a magnetized medium and the magnitude of this polarization change is proportional to the projection of the magnetization along the light propagation. The availability of femtosecond lasers together with a relative simplicity of the corresponding experimental setup made a time-resolved MOKE the most effective experimental tool for the measurement of the ultrafast magnetization dynamics.[6] However, in a typical experimental setup—with a rather small angle between the light propagation direction and the normal to the sample surface (angle of incidence, θ_i, in the following), only the out-of-plane component of the magnetization is detected.[7] To measure the in-plane components of the time dependent magnetization, it is necessary to employ another magneto-optical phenomenon than the polar MOKE. The most common techniques utilize the change of light polarization due to the longitudinal MOKE,[2,3,8] the change of light intensity due to transversal MOKE,[1] the interpretation of reflected light intensity at different polarizations by the Fresnel matrix formalism,[5] or the second-harmonic MOKE technique[4] (see the supplementary material for a detailed discussion of the corresponding experimental methods and their limitations[9]). With these methods, it is however a significant experimental challenge to perform a quantitative, high-sensitivity measurement of the time dependence of the full three-dimensional magnetization vector.[9] In this paper we introduce an experimental technique which utilizes a different MO effect—the magnetic linear dichroism—for measuring of the in-plane component of the time dependent magnetization. Importantly, this MO effect can be observed in exactly the same sample orientation and experimental setup as the polar MOKE which enables to perform direct quantitative measurements of the full three-dimensional magnetization vector evolutions.

Diluted ferromagnetic semiconductors, with (Ga,Mn)As as the most thoroughly investigated example, are magnetic materials that are prepared by a partial replacement of non-magnetic atoms by the magnetic ones.[10,11] Even though the achieved Curie temperature is still well below room temperature,[10,11] their research can provide fundamental insight into physical phenomena that are also present in other types of magnetic materials—like ferromagnetic metals—where they can be exploited in realistic spintronic applications.[10–12] In 2005, a giant magnetic linear dichroism (MLD) was reported in (Ga,Mn)As.[13] As pointed out above, the outstanding feature of this MO effect is that it provides an access to the in-plane component of the magnetization even at normal incidence and that it can be unambiguously separated from the polar Kerr effect (PKE) by its dependence on the orientation of probe beam polarization plane.[9,13] In Fig. 1 we schematically illustrate the origin of PKE and MLD. In PKE the rotation of light polarization (or the change of its ellipticity) occurs due to the different index of refraction for σ^+ and σ^- circularly polarized light propagating parallel to the direction of magnetization **M**. This polarization rotation depends linearly on the magnitude of the out-of-plane component of **M**

a)Electronic mail: nemec@karlov.mff.cuni.cz.

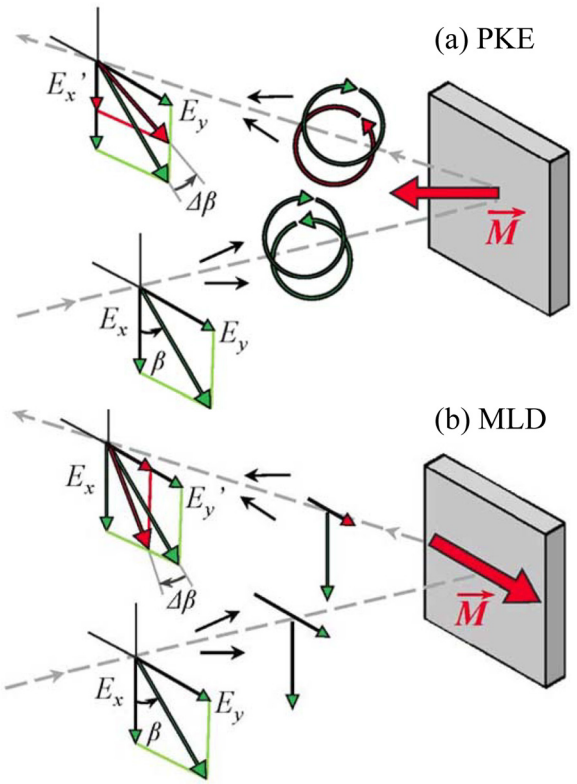

FIG. 1. (Color online) Schematic illustration of two magneto-optical effects in (Ga,Mn)As, which are responsible for a rotation of the polarization plane $\Delta\beta$ of reflected light at normal incidence. (a) Polar Kerr effect (PKE) that is due to the different index of refraction for σ^+ and σ^- circularly polarized light propagating parallel to the direction of magnetization **M**. (b) Magnetic linear dichroism (MLD) that is due to the different absorption (reflection) coefficient for light linearly polarized parallel and perpendicular to **M** if the light propagates perpendicular to the direction of **M**. E_x and E_y are the projections of the light amplitude to the crystallographic directions [100] and [010], respectively.

and is independent of the orientation of the light polarization plane β.[9] On the other hand, MLD originates from the different absorption (reflection) coefficient for the light with a polarization plane oriented parallel and perpendicular to **M**.[9] This effect scales quadratically with the in-plane magnetization component and varies as $\sin(2\beta)$.[9]

We investigated the laser-pulse induced dynamics of magnetization by the well known pump-and-probe MO technique where the output of a femtosecond laser is divided into a strong pump pulse and a weak probe pulse which are focused to a same spot on the sample.[6,7] Laser pulses, with the time width of 200 fs and the repetition rate of 82 MHz, were tuned to 1.64 eV (i.e., above the semiconductor band gap). The fluence of the pump pulses is 30 μJ cm^{-2}, which corresponds to the photoinjected carrier density of about 1.7×10^{18} cm^{-3}, and probe pulses were twenty times weaker. The experiment was performed close to the normal incidence ($\theta_i = 2°$ and 8° for pump and probe pulses, respectively) with a sample placed in a cryostat and cooled down to the temperature of about 15 K. The time-resolved data reported here were obtained without any external magnetic field applied. However, prior to this time-resolved experiment, the magnetization was oriented in a well defined position (so-called easy axis) by an application of 500 mT along the [010] crystallographic direction in the sample plane (see Fig. 1 and its figure caption for a definition of the coordinate system). The dynamical MO data shown here correspond to the pump-hellicity-independent part of the measured signals.[14] We also confirmed that the measured dynamical MO signal reflects the magnetization dynamics by comparing the signal corresponding to the probe rotation and elipticity change.[15] The orientation of polarization plane of linearly polarized probe pulses β, which is measured from the [100] crystallographic direction, was changed by a wave plate. The magnitudes of MO coefficients of PKE (P^{PKE}) and MLD (P^{MLD}) were measured in separate static magneto-optical experiments where an external magnetic field of 500 mT was used to align the magnetization in the out-of-plane and in-plane orientations, respectively. All the reported experiments were performed in several samples with a different Mn content from our set of high-quality epilayers which are as close as possible to uniform uncompensated $Ga_{1-x}Mn_xAs$ mixed crystals.[16] The obtained results are rather similar for all the samples and, therefore, we report here only the results measured in a sample with nominal doping $x = 5.2\%$ and Curie temperature $T_c = 132$ K. Magnetic anisotropy constants and easy-axis orientation were independently determined by SQUID magnetization measurements.[16]

In Fig. 2(a), we show measured time-resolved MO signals. The observed oscillatory signal is a signature that an impact of the pump pulse induces a precession of magnetization in the sample.[17–20] Recall that no external magnetic field was applied during this experiment and, therefore, the precession frequency is solely given by the internal magnetic

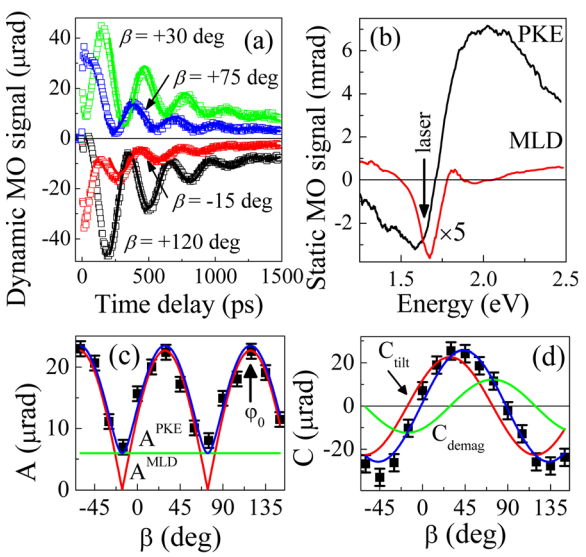

FIG. 2. (Color online) Magneto-optical signals (polarization rotations) measured in (Ga,Mn)As. (a) Dynamics of the MO signal induced by an impact of pump pulse on the sample that was measured by probe pulses with different polarization orientations β (points); lines are fit by Eq. (1) with parameters $\omega_{Mn} = 20.2$ GHz, $\tau_G = 360$ ps, and $\tau_p = 1050$ ps. (b) Spectral dependence of static PKE and MLD, the arrow indicates the spectral position of the laser pulses used in the time-resolved experiment shown in part (a); note that the data for MLD are multiplied by 5 for clarity. (c) and (d) Polarization dependence of the oscillation amplitude A (c) and of the pulse function amplitude C (d) at time delay of 200 ps that was obtained by fitting the dynamics shown in (a) (points). Lines are results of simultaneous fits of $A(\beta)$ by Eq. (2) and $C(\beta)$ by Eq. (3) with parameters: $\delta\varphi_{qe} = +1.1°$, $\delta\theta_{qe} = 0°$, $\delta M_s/M_0 = -1\%$ (Ref. 9). The deduced position of the easy axis in the sample without the pump pulse $\varphi_0 = 119°$ is depicted by the vertical arrow in (c).

anisotropy fields. The most striking feature apparent from Fig. 2(a) is that—at identical pumping conditions—the measured dynamical MO data are strongly dependent on the probe polarization orientation β. This behavior was already reported in Ref. 18 where it was assigned to the contribution of MLD to the measured MO signal. However, as the MO coefficients of the sample used in Ref. 18 were not known to the authors, the numerical analysis of the data by the Landau-Lifshitz-Gilbert (LLG) equation was only qualitative.[18]

In Fig. 2(b) we show the spectral dependence of magneto-optical coefficients, obtained from the static magneto-optical measurements, describing the magnitude of PKE and MLD in the studied sample. It reveals that at the spectral position where the experiment was performed, MLD is merely five-times smaller than PKE which explains the strong dependence of the dynamical MO signal on β [see Fig. 2(a)]. To disentangle the various contributions in the measured time dependent data, it is quite illustrative to perform the following analysis. The measured dynamical MO signal δMO, which is a function of the time delay between pump and probe pulses Δt and of β, can be fitted well by the phenomenological equation,

$$\delta MO(\Delta t,\beta) = A(\beta)\cos[\omega_{Mn}\Delta t + \Phi(\beta)]e^{-\frac{\Delta t}{\tau_G}} + C(\beta)e^{-\frac{\Delta t}{\tau_p}} \quad (1)$$

where A and C are the amplitudes of the oscillatory and pulse function, respectively, ω_{Mn} is the ferromagnetic moment precession frequency, Φ is the phase factor, τ_G is the Gilbert damping time, and τ_p is the pulse function decay time. All the measured data in Fig. 2(a) can be fitted reasonably well by Eq. (1) with a one set of parameters ω_{Mn}, τ_G, and τ_p. The dependences $A(\beta)$ and $C(\beta)$ obtained by this fitting procedure are displayed in Figs. 2(c) and 2(d), respectively. The magnetization orientation can be characterized by polar (φ) and azimuthal (θ) angles—see inset in Fig. 3(a) for their definition. Before an impact of the pump pulse the magnetization points along the easy axis direction (characterized by angles φ_0 and θ_0), which is determined by the magnetic anisotropy of the sample. From the SQUID measurement we know that $\theta_0 = 90°$ but the precise value of φ_0 is difficult to obtain from these data.[16] Absorption of the pump laser pulse leads to a photo-injection of electron-hole pairs and to a transient increase of the lattice temperature.[17–19] This in turn leads to a quasi-equilibrium change of the easy axis position with maximal in-plane and out-of-plane tilts $\delta\varphi_{qe}$ and $\delta\theta_{qe}$, respectively. Consequently, the magnetization starts to precess around the modified, quasi-equilibrium easy axis position. The measured oscillatory MO signal contains a component due to the out-of-plane motion of the magnetization, which is sensed by PKE, and a signal due to the in-plane movement of magnetization, which is sensed by MLD. The first one (with an amplitude A^{PKE}) does not depend on β but the second one (with an amplitude A^{MLD}) is a harmonic function of β.[9] Due to the precessional motion of magnetization these signals are phase shifted by 90° and the total amplitude of the oscillatory MO signal $A(\beta)$ is given by[9]

$$A(\beta) = \sqrt{[\delta\varphi_{qe}P^{MLD}2\cos 2(\varphi_0-\beta)]^2 + [A^{PKE}]^2}. \quad (2)$$

Equation (2) can be used to fit the measured dependence of $A(\beta)$ that enables to deduce the equilibrium position of the easy axis in the sample plane $\varphi_0 = 119 \pm 2°$ [see Fig. 2(c)]. We recall that prior to this experiment we oriented the magnetization along the easy axis that is the closest to the [010] crystallographic direction, which corresponds to $\beta = 90°$.

The obtained detailed understanding of the measured MO signals enables us to perform the full quantitative reconstruction of the real-time trajectory of magnetization from the measured dynamical MO signals *without any numerical modeling*. The measured dynamical MO signal can be expressed as[9]

$$\delta MO(\Delta t,\beta) = -\delta\theta(\Delta t)P^{PKE} + \delta\varphi(\Delta t)P^{MLD}2\cos 2(\varphi_0-\beta) + \frac{\delta M_s(\Delta t)}{M_0}P^{MLD}2\sin 2(\varphi_0-\beta), \quad (3)$$

where the first two terms in Eq. (3) describe the influence of magnetization movement perpendicular to the sample plane and in the sample plane, respectively; $\delta\varphi(\Delta t)$ and $\delta\theta(\Delta t)$ are the corresponding transient tilts relative to the equilibrium values φ_0 and θ_0. The last term in Eq. (3) describes the MO signal change due to the pump-induced demagnetization.[21] The pulse function in δMO signal is a transient non-oscillatory change of the MO signal.[9] Therefore, Eq. (3) can be used to fit the experimentally observed dependence $C(\beta)$ if the functions $\delta\varphi(\Delta t)$ and $\delta\theta(\Delta t)$ are replaced by the corresponding quasi-equilibrium tilts of the easy axis $\delta\theta_{qe}$ and $\delta\varphi_{qe}$ along which the magnetization precesses.[9] In fact, the analysis of $C(\beta)$ is of fundamental importance for the interpretation of the measured MO signals because it enables to determine experimentally whether the precession of magnetization is triggered by the out-of-plane or by the in-plane movement of the easy axis. If the out-of-plane movement were dominant in C_{tilt} [i.e., in the first two terms in Eq. (3)], it would not depend on β. On contrary, the observed harmonic dependence of C_{tilt} on β [see Fig. 2(d)] clearly shows that in the investigated sample the easy axis is tilted in the in-plane direction. Moreover, also the demagnetization contribution to the measured pulse function in δMO signal

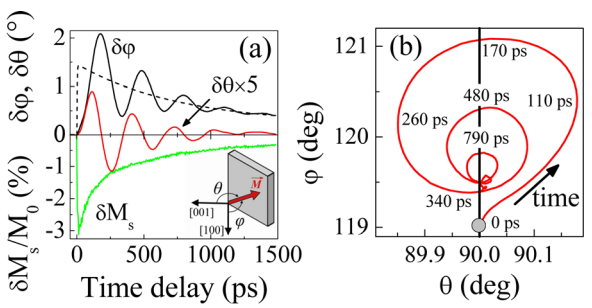

FIG. 3. (Color online) Direct experimental reconstruction of the magnetization real-space trajectory. An impact of the pump pulse induces a change of the magnetization magnitude and orientation relative to the corresponding equilibrium values (see inset in part (a) for a definition of the polar, φ, and azimuthal, θ, angles). (a) Time evolution of $\delta\varphi(t)$, $\delta\theta(t)$, and $\delta M_s(t)/M_0$; the dotted line depicts the in-plane evolution of the easy axis position around which the magnetization precesses. (b) Orientation of magnetization at different times after the impact of the pump pulse; the sample plane is represented by the vertical line and the equilibrium position of the easy axis is depicted by the grey spot.

(C_{demag}) can be separated by this fitting procedure [see Fig. 2(d)].

The actual orientation of the magnetization at any time delay Δt is given by $\varphi(\Delta t) = \varphi_0 + \delta\varphi(\Delta t)$, $\theta(\Delta t) = \theta_0 + \delta\theta(\Delta t)$ and its magnitude is given by $M_s(\Delta t) = M_0 + \delta M_s(\Delta t)$. It is apparent from Eq. (3) [see also Fig. 2(d)] that for β equal to φ_0 and $\varphi_0 - 90°$ the demagnetization does not contribute to the measured dynamical MO signal. Moreover, contributions to δMO due to $\delta\varphi$(t) are maximal and exactly opposite for $\beta = \varphi_0$ and $\beta = \varphi_0 - 90°$. Consequently,

$$\delta\varphi(\Delta t) = [\delta MO(\Delta t, \varphi_0) - \delta MO(\Delta t, \varphi_0 - 90°)]/(4P^{MLD}). \quad (4)$$

Similarly, for β equal to $\varphi_0 - 45°$ and $\varphi_0 - 135°$ the contributions due to $\delta\varphi(t)$ are not present in δMO and the signal due to the demagnetization is exactly opposite for these two angles that leads to

$$\delta\theta(\Delta t) = -[\delta MO(\Delta t, \varphi_0 - 45°) + \delta MO(\Delta t, \varphi_0 - 135°)]/(2P^{PKE}), \quad (5)$$

$$\frac{\delta M_s(\Delta t)}{M_0} = [\delta MO(\Delta t, \varphi_0 - 45°) - \delta MO(\Delta t, \varphi_0 - 135°)]/(4P^{MLD}). \quad (6)$$

In Fig. 3 we show the dynamics of magnetization that was deduced from the data depicted in Fig. 2(a). We note that the time-evolution of the magnetization determined by this direct experimental procedure is very similar to the one that we obtained by a numerical fitting of the measured data by LLG equation.[9] Moreover, the experimental procedure described above enables to deduce directly also the demagnetization dynamics [see Fig. 3(a)] which is not involved in LLG equation.[9]

Finally we point out that the applicability of our technique is not limited to the ferromagnetic semiconductor GaMnAs. As the heart of the technique is the simultaneous presence of PKE and MLD in one material, it should be possible to use it in any magnetic material where these two or other similar MO effects (like Faraday and Cotton-Mouton MO effects[22,23]) are comparable in a certain spectral range. This suggests that other promising candidates for implementation of this technique are, for example, $FeBO_3$ (Ref. 22) and $DyFeO_3$.[23]

In conclusion, we have demonstrated a magneto-optical, normal incidence pump-and-probe method that enables to perform a quantitative measurement of the real-time trajectory of the full three-dimensional magnetization vector without a need to change the sample position or detection geometry. This method is well suited for detecting small angle magnetization excitations in ferromagnetic semiconductors or other magnetic materials with sufficiently strong circular and linear magneto-optical effects.

This work was supported by the Grant Agency of the Czech Republic grant no. P204/12/0853 and 202/09/H041, by the Grant Agency of Charles University in Prague grant no. 443011 and SVV-2011-263306, by EU grant ERC Advanced Grant 268066 - 0MSPIN, and by Preamium Academiae of the Academy of Sciences of the Czech Republic.

[1]Y. Acremann, C. H. Back, M. Buess, O. Portmann, A. Vaterlaus, D. Pescia, and H. Melchior, Science **290**, 492 (2000).
[2]M. R. Freeman and W. K. Hiebert, in *Spin Dynamics in Confined Magnetic Structures I*, edited by B. Hillebrands and K. Ounadjela (Springer, Berlin, 2002), Chap. 4.
[3]J. Fassbender, in *Spin Dynamics in Confined Magnetic Structures I*, edited by B. Hillebrands and K. Ounadjela (Springer, Berlin, 2003), Chap. 3.
[4]Th. Gerrits, H. A. M. van den Berg, J. Hohlfeld, L. Bär, and Th. Rasing, Nature **418**, 509 (2002).
[5]E. Carpene, E. Mancini, D. Dazzi, C. Dallera, E. Puppin, and S. De Silvestri, Phys. Rev. B **81**, 060415(R) (2010).
[6]A. Kirilyuk, A. V. Kimel, and T. Rasing, Rev. Mod. Phys. **82**, 2731 (2010).
[7]M. van Kampen, C. Jozsa, J. T. Kohlhepp, P. LeClair, L. Lagae, W. J. M. de Jonge, and B. Koopmans, Phys. Rev. Lett. **88**, 227201 (2002).
[8]W. K. Hiebert, L. Lagae, and J. De Boeck, Phys. Rev. B **68**, 020402(R) (2003).
[9]See supplementary material at http://dx.doi.org/10.1063/1.3692599 for a discussion of existing experimental methods, which enable to visualize the real-space trajectory of magnetization, for a detailed description of a magneto-optical response of (Ga,Mn)As, for a derivation of the equations used in this article, and for a comparison of the magnetization dynamics deduced by the proposed direct experimental procedure with that obtained by a numerical fitting of the measured data by LLG equation.
[10]T. Jungwirth, J. Sinova, J. Mašek, and A. H. MacDonald, Rev. Mod. Phys. **78**, 809 (2006).
[11]T. Dietl, Nature Mater. **9**, 965 (2010).
[12]Editorial, Nature Mater. **9**, 951 (2010).
[13]A. V. Kimel, G. V. Astakhov, A. Kirilyuk, G. M. Schott, G. Karczewski, W. Ossau, G. Schmidt, L. W. Molenkamp, and T. Rasing, Phys. Rev. Lett. **94**, 227203 (2005).
[14]P. Němec, E. Rozkotová, N. Tesařová, F. Trojánek, E. De Ranieri, K. Olejník, J. Zemen, V. Novák, M. Cukr, P. Malý, and T. Jungwirth, "Experimental observation of the optical spin transfer torque," Nature Phys. (in press).
[15]E. Rozkotová, P. Němec, D. Sprinzl, P. Horodyská, F. Trojánek, P. Malý, V. Novák, K. Olejník, M. Cukr, and T. Jungwirth, IEEE Trans. Mag. **44**, 2674 (2008).
[16]T. Jungwirth, P. Horodyská, N. Tesařová, P. Němec, J. Šubrt, P. Malý, P. Kužel, C. Kadlec, J. Mašek, I. Němec *et al.*, Phys. Rev. Lett. **105**, 227201 (2010) and its supplementary material.
[17]J. Qi, Y. Xu, N. H. Tolk, X. Liu, J. K. Furdyna, and I. E. Perakis, Appl. Phys. Lett. **91**, 112506 (2007).
[18]Y. Hashimoto, S. Kobayashi, and H. Munekata, Phys. Rev. Lett. **100**, 067202 (2008).
[19]E. Rozkotová, P. Němec, P. Horodyská, D. Sprinzl, F. Trojánek, P. Malý, V. Novák, K. Olejník, M. Cukr, and T. Jungwirth, Appl. Phys. Lett. **92**, 122507 (2008).
[20]E. Rozkotová, P. Němec, N. Tesařová, P. Malý, V. Novák, K. Olejník, M. Cukr, and T. Jungwirth, Appl. Phys. Lett. **93**, 232505 (2008).
[21]J. Wang, I. Cotoros, K. M. Dani, X. Liu, J. K. Furdyna, and D. S. Chemla, Phys. Rev. Lett. **98**, 217401 (2007).
[22]A. M. Kalashikova, A. V. Kimel, R. V. Pisarev, V. N. Gridnev, P. A. Usachev, A. Kirilyuk, and T. Rasing, Phys. Rev. B **78**, 104301 (2008).
[23]R. Iida, T. Satoh, T. Shimura, K. Kuroda, B. A. Ivanov, Y. Tokunaga, and Y. Tokura, Phys. Rev. B **84**, 064402 (2011).

APPENDIX 6

Authors: P. Němec, E. Rozkotová, N. Tesařová, F. Trojánek, E. De Ranieri, K. Olejník, J. Zemen, V. Novák, M. Cukr, P. Malý and T. Jungwirth

Title: Experimental observation of the optical spin transfer torque

Journal: Nature Physics

Volume: 8

Article Number: 411

Year: 2012

nature physics

ARTICLES

PUBLISHED ONLINE: 1 APRIL 2012 | DOI: 10.1038/NPHYS2279

Experimental observation of the optical spin transfer torque

P. Němec[1]*, E. Rozkotová[1], N. Tesařová[1], F. Trojánek[1], E. De Ranieri[2], K. Olejník[3], J. Zemen[3,4], V. Novák[3], M. Cukr[3], P. Malý[1] and T. Jungwirth[3,4]

The spin transfer torque is a phenomenon in which angular momentum of a spin polarized electrical current entering a ferromagnet is transferred to the magnetization. The effect has opened a new research field of electrically driven magnetization dynamics in magnetic nanostructures and plays an important role in the development of a new generation of memory devices and tunable oscillators. Optical excitations of magnetic systems by laser pulses have been a separate research field the aim of which is to explore magnetization dynamics at short timescales and enable ultrafast spintronic devices. We report the experimental observation of the optical spin transfer torque, predicted theoretically several years ago, building the bridge between these two fields of spintronics research. In a pump-and-probe optical experiment we measure coherent spin precession in a (Ga, Mn)As ferromagnetic semiconductor excited by circularly polarized laser pulses. During the pump pulse, the spin angular momentum of photo-carriers generated by the absorbed light is transferred to the collective magnetization of the ferromagnet. We analyse quantitatively the observed magnetization dynamics triggered by the optical spin transfer torque using independently determined micromagnetic parameters and magneto-optical coefficients of the studied (Ga, Mn)As.

The (Ga, Mn)As ferromagnetic semiconductors used in our work are favourable candidates for observing the optical spin transfer torque[1,2]. The direct-gap GaAs host allows the generation of a high density of photo-carriers, optical selection rules for circularly polarized light then yield a high degree of spin-polarization of photo-carriers in the direction of the light propagation, and these carrier spins interact with ferromagnetic moments on Mn via exchange coupling. When the ferromagnetic Mn moments are excited, this can be sensitively detected by probe laser pulses owing to the strong magneto-optical signals in (Ga, Mn)As (refs 3–12).

The coupled precession dynamics of the magnetization orientation $\hat{\mathbf{M}}$ and the photo-carrier spin density $\mathbf{s}$ is governed by the equations

$$\frac{\mathrm{d}\hat{\mathbf{M}}}{\mathrm{d}t} = \frac{J}{\hbar}\hat{\mathbf{M}} \times \mathbf{s}$$

$$\frac{\mathrm{d}\mathbf{s}}{\mathrm{d}t} = \frac{JS_{\mathrm{Mn}}c_{\mathrm{Mn}}}{\hbar}\mathbf{s} \times \hat{\mathbf{M}} + P\hat{\mathbf{n}} - \frac{\mathbf{s}}{\tau} \qquad (1)$$

where J is the carrier–Mn moment exchange coupling constant ($\approx$50 meV nm^3 for holes and $\approx$10 meV nm^3 for electrons in (Ga, Mn)As) , $S_{\mathrm{Mn}} = 5/2$ is the Mn local moment, $c_{\mathrm{Mn}} \sim 1\,\mathrm{nm}^{-3}$ is the typical Mn moment density, $\hat{\mathbf{M}}$ is the unit vector of the magnetization orientation, P is the rate per unit volume at which carrier spins with orientation $\hat{\mathbf{n}}$ are optically injected into the ferromagnet, and τ is the photo-carrier spin lifetime. In the geometry of our experiments, with normal incidence of the laser pulse and the in-plane easy axis of (Ga, Mn)As, the equilibrium $\hat{\mathbf{M}}$ is perpendicular to $\hat{\mathbf{n}}$. The orientation of $\hat{\mathbf{n}}$ is given by the helicity of the circularly polarized laser pulse. In equation (1) we omitted gradient terms[13] of the photo-carrier spin polarization. This is justified by the small thickness (20 nm) of the (Ga, Mn)As epilayers studied, through which the light attenuation is only a few per cent, and by the similar absorption coefficients of the (Ga, Mn)As epilayer and the GaAs substrate near the bandgap[14].

The timescale of photo-electron precession due to the exchange field produced by the high-density ferromagnetic Mn moments is $\sim 2\pi\hbar/JS_{\mathrm{Mn}}c_{\mathrm{Mn}} \sim 100$ fs. The major source of spin decoherence of the photo-electrons in (Ga, Mn)As is the exchange interaction with fluctuating Mn moments. Microscopic calculations of the corresponding relaxation time give a typical scale of tens of picoseconds (ref. 1). The other factor that limits τ introduced in equation (1) is the photo-electron decay time, which is also approximately tens of picoseconds, as inferred from reflectivity measurements of the (Ga, Mn)As samples (see Supplementary Information). Within the spin lifetime, the photo-electron spins therefore precess many times around the exchange field of ferromagnetic Mn moments before they relax. In the corresponding regime of $\tau JS_{\mathrm{Mn}}c_{\mathrm{Mn}}/\hbar \gg 1$, the steady-state spin density of photo-electrons obtained from equation (1), by neglecting the last term, is

$$\mathbf{s}_0 \approx \frac{\hbar P}{JS_{\mathrm{Mn}}c_{\mathrm{Mn}}}(\hat{\mathbf{n}} \times \hat{\mathbf{M}}) \qquad (2)$$

The steady-state spin density given by equation (2) is oriented in the plane of the ferromagnetic film and perpendicular to the magnetization vector. The physical interpretation of this result is that the rate of the out-of-plane tilt of $\mathbf{s}_0$ due to precession around the exchange field produced by the ferromagnetic moments is precisely compensated by the rate of photo-injection of out-of-plane oriented electron spins. From equation (1) we see that $\mathbf{s}_0$ exerts a torque on the Mn magnetization vector, given by

$$\frac{\mathrm{d}S_{\mathrm{Mn}}c_{\mathrm{Mn}}\hat{\mathbf{M}}}{\mathrm{d}t} \approx P\hat{\mathbf{M}} \times (\hat{\mathbf{n}} \times \hat{\mathbf{M}}) \qquad (3)$$

[1]Charles University in Prague, Faculty of Mathematics and Physics, Ke Karlovu 3, 121 16 Prague 2, Czech Republic, [2]Hitachi Cambridge Laboratory, Cambridge CB3 0HE, UK, [3]Institute of Physics ASCR, v.v.i., Cukrovarnická 10, 162 53 Praha 6, Czech Republic, [4]School of Physics and Astronomy, University of Nottingham, Nottingham NG7 2RD, UK. *e-mail: nemec@karlov.mff.cuni.cz.

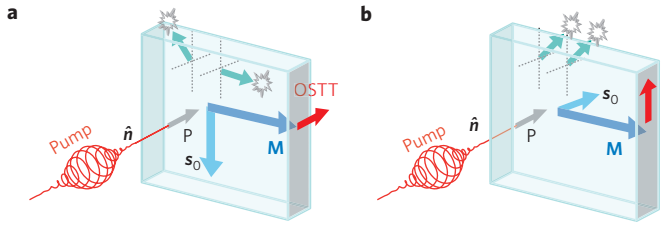

Figure 1 | Schematic illustration of the optical spin transfer torque. **a**, Schematic illustration of the optical spin transfer torque in the large spin lifetime limit. The rate P of the photo-carrier spin injection along the light propagation axis $\hat{\mathbf{n}}$ (normal to the sample plane) is completely transferred to the optical spin transfer torque (OSTT) acting along the normal to the sample plane on the magnetization $\mathbf{M}$ of the ferromagnet. The steady-state component of the injected spin density $\mathbf{s}_0$ is oriented in the plane of the sample and perpendicular to the in-plane equilibrium magnetization vector. The fast precessing component of the spin of a photo-carrier (small upper arrows) relaxes to the environment at a random orientation, producing a zero net momentum transfer to the environment. This picture applies to photo-electrons in (Ga, Mn)As. **b**, A weak torque acting on $\mathbf{M}$ (red arrow) produced by photo-carriers with a short spin lifetime. Most of the spin angular moment is transferred to the environment in this limit. For photo-holes in (Ga, Mn)As this picture is more relevant than the picture of the strong optical spin transfer torque shown in **a**.

Equation (3) describes the optical spin transfer torque, shown schematically in Fig. 1a. The fast precessing component of the spin of a photo-carrier relaxes to the environment with a random orientation, producing a zero net momentum transfer to the environment. Viewed from the perspective of total angular momentum conservation, the steady state $\mathbf{s}_0$ mediates a transfer of the entire electron spin injection rate to the rate of change of $\hat{\mathbf{M}}$ and no spin angular momentum is lost by the photo-electrons to the environment. We note that there is a correspondence between the form of the torque described by equation (3) and the adiabatic spin transfer torque discussed in the context of current-induced domain wall motion[1,15].

The solution of equation (1) in the opposite limit of $\tau JS_{\mathrm{Mn}}c_{\mathrm{Mn}}/\hbar \ll 1$, obtained by neglecting the first term, is illustrated in Fig. 1b. Here the steady-state spin density of photo-carriers is out-of-plane and its magnitude scales with τ. The amplitude of the corresponding torque

$$\frac{\mathrm{d}S_{\mathrm{Mn}}c_{\mathrm{Mn}}\hat{\mathbf{M}}}{\mathrm{d}t} \approx \frac{\tau JS_{\mathrm{Mn}}c_{\mathrm{Mn}}}{\hbar}P(\hat{\mathbf{M}}\times\hat{\mathbf{n}}) \qquad (4)$$

is then much smaller than the optical spin transfer torque in equation (3). The photo-carrier spins tilt only slightly before relaxing, that is, most of the angular momentum of the photo-carriers is transferred to the environment and not to the magnetization vector $\hat{\mathbf{M}}$ in this small spin lifetime limit. The precession time of holes in (Ga, Mn)As is roughly tens of femtoseconds and the spin lifetime of holes, dominated by the strong spin–orbit coupling, is estimated to ~1–10 fs (ref. 1). As $\tau JS_{\mathrm{Mn}}c_{\mathrm{Mn}}/\hbar \lesssim 1$ for holes, their contribution is better approximated by the weaker torque of equation (4) and we will therefore omit holes in further discussions. (Note that there is a correspondence between the form of the torque described by equation (4) and the non-adiabatic spin transfer torque discussed in the context of current-induced domain wall motion[1,15]).

The experimental observation of the magnetization precession in (Ga, Mn)As excited by the optical spin transfer, with the characteristic opposite phases of the oscillations excited by pump pulses of opposite helicities, is presented in Fig. 2a. In the experiment, the output of a femtosecond laser is divided into a strong ($70\,\mu\mathrm{J\,cm^{-2}}$), 300-fs-long pump pulse and a weak, delayed

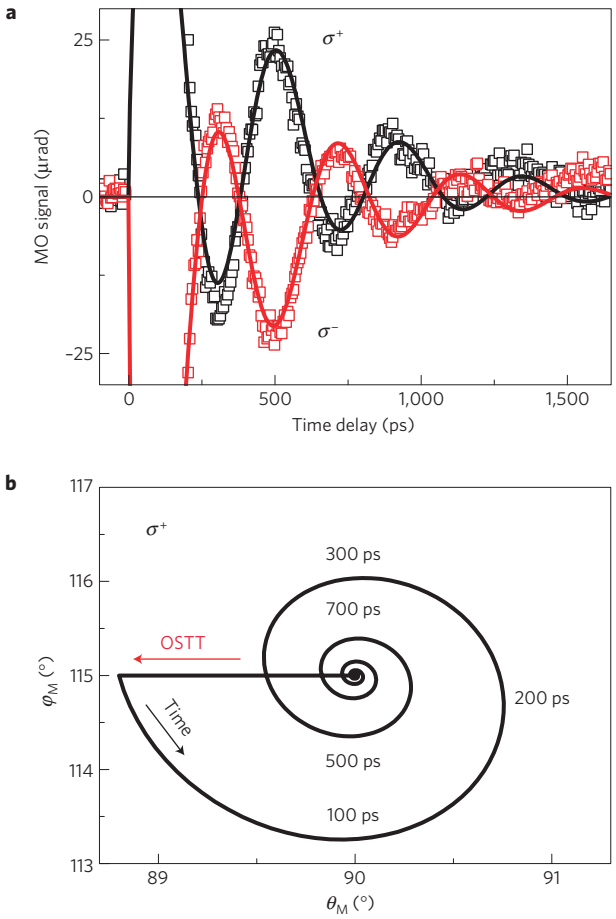

Figure 2 | Experimental observation of the optical spin transfer torque. **a**, Precession of the magnetization induced in (Ga, Mn)As by σ^+ and σ^- circularly polarized pump pulses. Points are the measured rotations of the polarization plane of the reflected linearly polarized probe pulse as a function of the time delay between pump and probe pulses. Lines are the theoretically calculated time-dependent magneto-optical signals. **b**, The calculated time evolution of the orientation of the magnetization in the sample, described by the polar angle φ_M measured from the [100] axis and the azimuthal angle θ_M measured from the sample normal [001], induced by the σ^+ circularly polarized pulse. The orientation of the optical spin transfer torque for the σ^+ polarization is shown in the figure by red arrow (OSTT). For the σ^- polarization of the pump pulse, the torque points in the opposite direction. The experiment was performed on the (Ga, Mn)As sample attached to a piezo-stressor at an applied bias $U = -150$ V. The probe input polarization orientation is 25°, the temperature of the measurement 35 K, the excitation laser intensity 70 μJ cm^2, and the photon energy 1.64 eV.

probe pulse, both of which are focused to the same spot on the measured sample. The photon energy of 1.64 eV is tuned above the semiconductor bandgap to excite magnetization dynamics by photon absorption. To observe the optical spin transfer torque we use a circularly polarized pump laser beam. The pump-induced change of the magneto-optical response of the sample is measured by a time-delayed linearly polarized probe pulse. The magneto-optical signals shown in Fig. 2 represent the rotation of the polarization plane of the reflected probe beam. It is a combination of the signal due to the out-of-plane motion of the magnetization, which is sensed by the polar Kerr effect (PKE), and the signal due to the in-plane component of the ferromagnetic moment, which is sensed by the magnetic linear dichroism (MLD; ref. 16). These two contributions can be experimentally separated by their

polarization dependence; PKE does not depend on the probe input polarization angle whereas MLD is a harmonic function of the input polarization angle. See Supplementary Information for details on sample preparation, experimental techniques, and extensive data on a series of (Ga, Mn)As samples with a Mn doping range of 1–14% .

As the period of the oscillations (0.4 ns) seen in Fig. 2a is much larger than the pump pulse duration, the action of the optical spin transfer torque is reflected only in the initial phase and amplitude of the free precession of the magnetization. The free dynamics of the magnetization is governed by the Landau–Lifshitz–Gilbert torque $\gamma(\hat{\mathbf{M}} \times \mathbf{H}_{\mathrm{eff}})$, with $\mathbf{H}_{\mathrm{eff}}$ a combination of the internal magnetic anisotropy fields and external magnetic field, and by the damping term $\gamma\alpha\hat{\mathbf{M}}/|\mathbf{M}| \times (\hat{\mathbf{M}} \times \mathbf{H}_{\mathrm{eff}})$. Here γ is the gyromagnetic ratio and α is the Gilbert damping constant. The micromagnetic parameters were determined from independent magnetization measurements using both a superconducting quantum interference device and magneto-optical ferromagnetic resonance (see Supplementary Information). As the PKE and MLD coefficients were also determined for our (Ga, Mn)As materials from independent static magneto-optical measurements (see Supplementary Information), we can transform the calculated time-dependent magnetization into magneto-optical signals and directly compare them with the measured data, as shown in Fig. 2a.

In Fig. 2b we show the calculated time evolution of the polar angle φ_{M} and the azimuthal angle θ_{M} of the magnetization. The corresponding theoretical magneto-optical signals are shown in Fig. 2a (solid lines) . In the calculations we set $P \approx 1 \times 10^{-2}\,\mathrm{nm}^{-3}$ per 300 fs. For the intensity of the pump laser pulse applied, this value is comparable to the corresponding photo-carrier injection rate in GaAs. We point out that the agreement between theory and experiment is on the level of the individual PKE and MLD components of the total magneto-optical signal and that the initial tilt of the magnetization is in the out-of-plane direction (see Supplementary Information). From the analysis we conclude that the excitation of magnetization dynamics shown in Fig. 2a can be fully ascribed to the optical spin transfer torque.

In Fig. 3a we demonstrate that the previously reported inverse magneto-optical mechanism for exciting magnetization precession by circularly polarized light is not contributing in our experiments in (Ga, Mn)As. The inverse magneto-optical effect does not require photon absorption, and the corresponding theory was derived and its effects observed in transparent magnetic dielectrics[17]. To test whether the inverse magneto-optical effect contributes in our (Ga, Mn)As samples we tuned the energy of the pump laser beam below the semiconductor bandgap, to 1.44 eV. Here the optical spin transfer torque is not effective because of the negligible absorption. On the other hand, an excitation energy below the bandgap is favourable for the inverse magneto-optical effect. The direct PKE at 1.44 eV is comparable to, or even larger than, that at 1.64 eV, as shown in Fig. 3a. Therefore, if active above the bandgap at 1.64 eV, the inverse magneto-optical effect should be clearly detectable at 1.44 eV. No magnetization dynamics is, however, excited using an energy at 1.44 eV, from which we conclude that the inverse magneto-optical effect is not contributing in our experiments.

Pump pulses with opposite helicities trigger magneto-optical signals with opposite phases, as shown in Fig. 2a, suggesting that the optical spin transfer torque is also not accompanied by any polarization-independent excitation mechanism. Indeed, a linearly polarized pump pulse with any orientation of the polarization does not excite the magnetization precession, as illustrated in Fig. 3b. The polarization-independent data obtained by summing the signals for the two opposite helicities are almost identical to the data corresponding to a linearly polarized pump pulse. They show a non-oscillatory signal that decays on the timescale at which the photo-carrier-induced change of the sample reflectivity decays. The

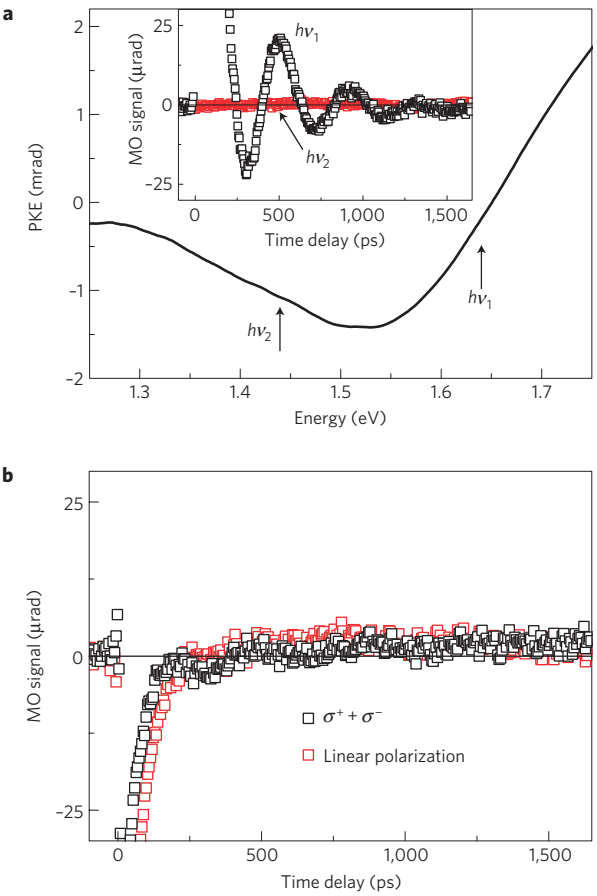

Figure 3 | Absence of inverse magneto-optical effect and polarization-independent excitations. a, Energy dependence of the PKE magneto-optical coefficient. The vertical arrows indicate the photon energies $h\nu_1 = 1.64$ eV (above the semiconductor bandgap) and $h\nu_2 = 1.44$ eV (below the semiconductor bandgap) of the circularly polarized pump pulse that were used in the pump-and-probe measurements shown in the inset. Except for the variation of the photon energy of the pump pulse, the experimental conditions of the measurements shown in the inset are the same as in Fig. 2a. **b**, Helicity-independent part ($(\sigma^+ + \sigma^-)/2$) of the signal measured at the pump pulse photon energy 1.64 eV and the pump-and-probe measurement with a linearly polarized pump pulse of energy 1.64 eV; all other experimental conditions are the same as in Fig. 2a.

signal is therefore of optical rather than magnetic origin (for more details see Supplementary Information).

Polarization-independent excitations of magnetization precession in (Ga, Mn)As have been reported previously by several groups, including ourselves[3–12]. The experiments were interpreted in terms of changes of the magnetocrystalline anisotropy induced by the laser pulse[3–12]. Two mechanisms have been proposed as contributing to the transient tilt of the magnetization easy axis due to photon absorption: an increase in the temperature[6,7] and an increase in the hole-density[3,11,12]. The samples we study in this work can also be excited by a mechanism related to magnetic anisotropy. In the measurements shown in Figs 2–4 we have intentionally suppressed this mechanism to highlight our observation of the optical spin transfer torque. We have done this by attaching a lead zirconate titanate (PZT) piezostressor to the 3.8% Mn-doped (Ga, Mn)As sample, which modifies the magnetic anisotropy of the ferromagnetic film owing to the differential thermal contraction and allows for an additional *in situ* electrical control of the in-plane magnetocrystalline anisotropy. (More detailed descriptions of the preparation

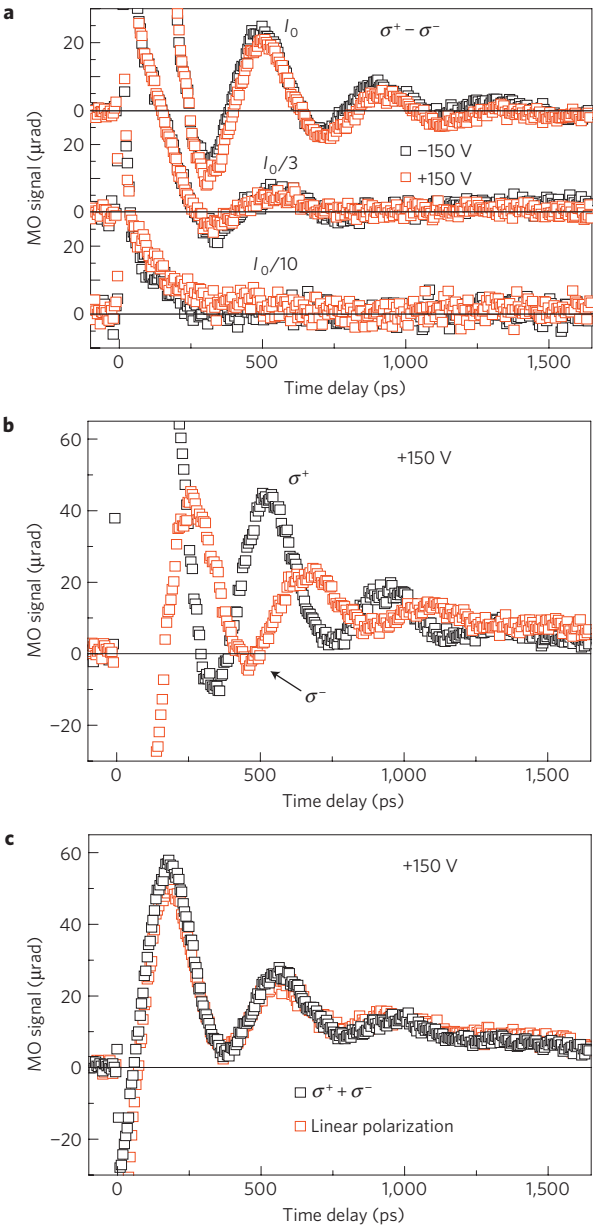

Figure 4 | Helicity-dependent and polarization-independent signals at different piezovoltages. a, Intensity dependence ($I_0 = 70\,\mu J\,cm^2$) of the helicity-dependent signal for the piezo-voltages $U = \pm 150$ V. **b**, Magneto-optical signal measured with σ^+ and σ^- circularly polarized pump pulses and piezo-voltage $U = +150$ V. **c**, Polarization-independent part of the signal shown in **b** together with data measured with linearly polarized pump pulses.

and characterization of the PZT/(Ga, Mn)As hybrid structures are given in refs 18–20 and in the Supplementary Information.)

The strain induced by the differential thermal contraction is $\sim 10^{-3}$. This strain significantly reduces the out-of-plane magnetic anisotropy of the (Ga, Mn)As, which leads to an approximate factor of three enhancement over the bare sample in the helicity-dependent signal induced by the out-of-plane optical spin transfer torque (see Supplementary Information). The additional piezovoltage strain, proportional to the applied bias, reaches $\sim 1 \times 10^{-4}$ for $|U| = 150$ V. These strains have a negligible effect on the out-of-plane anisotropy field and should not, therefore, affect the helicity-dependent signal induced by the out-of-plane optical spin transfer torque. In Fig. 4a we show, by comparing the measurements at large positive and negative piezovoltages, that the helicity-dependent excitation is indeed not sensitive to the piezovoltage. Also consistent with the optical spin transfer torque phenomenology, the figure shows that the amplitude of the magnetization oscillations scales with the intensity of the circularly polarized laser pulse.

Unlike the out-of-plane anisotropy, biasing the piezostressor can significantly affect the more subtle balance of the weaker in-plane anisotropy fields. We aligned the axis of the stressor at an angle 115° from the [100] crystal direction. This is close to the easy axis of the bare sample, where the orientation is a result of the competition of the biaxial and uniaxial in-plane anisotropies in (Ga, Mn)As (see Supplementary Information). Application of a large negative piezovoltage of −150 V, with the measurements shown in Figs 2, 3 and 4a, deepens the minimum in the in-plane magnetic anisotropy energy such that the applied laser intensities do not produce a measurable in-plane tilt of the easy axis and, therefore, a measurable magnetization precession. As shown in Fig. 4b and c, the application of a positive piezovoltage allows us to observe the polarization-independent excitation in the same sample. Consistently, the ratio of the helicity-dependent and polarization-independent signals is proportional to the applied piezovoltage, as shown in the Supplementary Information. The helicity-dependent signal is observed throughout the series of (Ga, Mn)As materials with different Mn dopings, as we also show in the Supplementary Information. Without the attached PZT stressor, that is, with the stronger out-of-plane magnetic anisotropy field in the bare samples, the helicity-dependent signal is typically 5–20× weaker than the polarization-independent signal and was omitted in previous studies of optically excited magnetization precession in (Ga, Mn)As.

The measured oscillation frequencies and Gilbert damping constants for the polarization-independent and helicity-dependent excitations are identical. Independent of whether the excitation is due to the in-plane shift of the magnetic easy axis or due to the out-of-plane optical spin transfer torque, the precessing moments are the same in both cases. From studies of the dependence of the precession frequency on internal anisotropy and external magnetic fields, it is established that these are the precessing ferromagnetic Mn moments (see Supplementary Information and refs 3,5–11). We conclude by pointing out that bringing the spin transfer physics into optics introduces a fundamentally distinct mechanism from the previously reported thermal and non-thermal laser excitations of magnets. Using optics in the field of spin transfer torques decreases, by several orders of magnitude, the timescales at which these phenomena are observed.

Received 5 August 2011; accepted 24 February 2012; published online 1 April 2012

References

1. Fernández-Rossier, J., Núñez, A. S., Abolfath, M. & MacDonald, A. H. Optical spin transfer in ferromagnetic semiconductors. Preprint at http://arXiv.org/abs/cond-mat/0304492 (2003).
2. Núñez, A. S., Fernández-Rossier, J., Abolfath, M. & MacDonald, A. H. Optical control of the magnetization damping in ferromagnetic semiconductors. *J. Magn. Magn. Mater.* **272–276,** 1913–1914 (2004).
3. Oiwa, A., Takechi, H. & Munekata, H. Photoinduced magnetization rotation and precessional motion of magnetization in ferromagnetic (Ga, Mn)As. *J. Supercond.* **18,** 9–13 (2005).
4. Wang, D. M. Light-induced magnetic precession in (Ga, Mn)As slabs: Hybrid standing-wave Damon-Eshbach modes. *Phys. Rev. B* **75,** 233308 (2007).
5. Takechi, H., Oiwa, A., Nomura, K., Kondo, T. & Munekata, H. Light-induced precession of ferromagnetically coupled Mn spins in ferromagnetic (Ga, Mn)As. *Phys. Status Solidi C* **3,** 4267–4270 (2007).
6. Qi, J. *et al.* Coherent magnetization precession in GaMnAs induced by ultrafast optical excitation. *Appl. Phys. Lett.* **91,** 112506 (2007).
7. Qi, J. *et al.* Ultrafast laser-induced coherent spin dynamics in ferromagnetic $Ga_{1-x}Mn_xAs$/GaAs structures. *Phys. Rev. B* **79,** 085304 (2009).

8. Rozkotová, E. *et al.* Light-induced magnetization precession in GaMnAs. *Appl. Phys. Lett.* **92,** 122507 (2008).
9. Rozkotová, E. *et al.* Coherent control of magnetization precession in ferromagnetic semiconductor (Ga, Mn)As. *Appl. Phys. Lett.* **93,** 232505 (2008).
10. Hashimoto, Y. & Munekata, H. Coherent manipulation of magnetization precession in ferromagnetic semiconductor (Ga, Mn)As with successive optical pumping. *Appl. Phys. Lett.* **93,** 202506 (2008).
11. Hashimoto, Y., Kobayashi, S. & Munekata, H. Photoinduced precession of magnetization in ferromagnetic (Ga, Mn)As. *Phys. Rev. Lett.* **100,** 067202 (2008).
12. Kobayashi, S., Suda, K., Aoyama, J., Nakahara, D. & Munekata, H. Photo-induced precession of magnetization in metal/(Ga, Mn)As systems. *IEEE Trans. Magn.* **46,** 2470–2473 (2010).
13. Zutic, I., Fabian, J. & Erwin, S. C. Spin injection and detection in silicon. *Phys. Rev. Lett.* **97,** 026602 (2006).
14. Burch, K. S., Stephens, J., Kawakami, R. K., Awschalom, D. D. & Basov, D. N. Ellipsometric study of the electronic structure of GaMnAs and low-temperature GaAs. *Phys. Rev. B* **70,** 205208 (2004).
15. Vanhaverbeke, A. & Viret, M. Simple model of current-induced spin torque in domain walls. *Phys. Rev. B* **75,** 024411 (2007).
16. Kimel, A. V. *et al.* Observation of giant magnetic linear dichroism in (Ga, Mn)As. *Phys. Rev. Lett.* **94,** 227203 (2005).
17. Kirilyuk, A., Kimel, A. V. & Rasing, T. Ultrafast optical manipulation of magnetic order. *Rev. Mod. Phys.* **82,** 2731–2784 (2010).
18. Jungwirth, T. *et al.* Systematic study of Mn-doping trends in optical properties of (Ga, Mn)As. *Phys. Rev. Lett.* **105,** 227201 (2010).
19. Rushforth, A. W. *et al.* Voltage control of magnetocrystalline anisotropy in ferromagnetic–semiconductor/piezoelectric hybrid structures. *Phys. Rev. B* **78,** 085314 (2008).
20. De Ranieri, E. *et al.* Lithographically and electrically controlled strain effects on anisotropic magnetoresistance in (Ga, Mn)As. *New J. Phys.* **10,** 065003 (2008).

Acknowledgements

We acknowledge fruitful discussions with A. V. Kimel, J. Sinova, J. Wunderlich, J. Fernández-Rossier and A. H. MacDonald, and support from the European Union European Research Council (ERC) Advanced Grant No. 268066 and FP7-215368 SemiSpinNet, from the Ministry of Education of the Czech Republic Grants No. LC510 and MSM0021620834, from the Grant Agency of the Czech Republic Grant No. 202/09/H041 and P204/12/0853, from the Charles University in Prague Grant No. SVV-2012-265306 and 443011, and from the Academy of Sciences of the Czech Republic No. AV0Z10100521 and Preamium Academiae.

Author contributions

Sample preparation: V.N., M.C., E.R. and E.D.R.; experiments and data analysis: E.R., N.T., P.N., P.M., K.O and T.J.; data modelling: P.N. and F.T.; theory: J.Z. and T.J.; writing: T.J. and P.N.; project planning: P.N. and T.J.

Additional information

The authors declare no competing financial interests. Supplementary information accompanies this paper on www.nature.com/naturephysics. Reprints and permissions information is available online at www.nature.com/reprints. Correspondence and requests for materials should be addressed to P.N.

nature physics

SUPPLEMENTARY INFORMATION

DOI: 10.1038/NPHYS2279

Experimental observation of the optical spin transfer torque: Supplementary material

P. Němec,[1] E. Rozkotová,[1] N. Tesařová,[1] F. Trojánek,[1] E. De Ranieri,[2] K. Olejník,[3,2]
J. Zemen,[3] V. Novák,[3] M. Cukr,[3] P. Malý,[1] and T. Jungwirth[3,4]

[1] *Charles University in Prague, Faculty of Mathematics and Physics, Ke Karlovu 3, 121 16 Prague 2, Czech Republic*

[2] *Hitachi Cambridge Laboratory, Cambridge CB3 0HE, UK*

[3] *Institute of Physics ASCR, v.v.i., Cukrovarnická 10, 16253 Praha 6, Czech Republic*

[4] *School of Physics and Astronomy, University of Nottingham, Nottingham NG72RD, United Kingdom*

PACS numbers: 75.50.Pp, 76.50.+g, 78.20.Ls, 78.47.-p

INTRODUCTION

This supplementary material describes a detailed information about the time-resolved magneto-optical experiments performed in a large set of high-quality (Ga,Mn)As epilayers and hybrid structures piezo-stressor/(Ga,Mn)As where *in situ* electrical control of magnetic anisotropy can be achieved. Diluted magnetic semiconductors, with (Ga,Mn)As as the most thoroughly investigated example, are in principle disordered materials. Therefore, a special care has to be taken when generalizing the experimental results obtained in one particular sample to the universal behavior of this material system. Very recently we reported on a systematic study of optical and magneto-optical properties of optimized set of (Ga,Mn)As epilayers spanning the wide range of accessible substitutional Mn_{Ga} dopings [1]. The optimization of the materials in the series, which is performed individually for each nominal doping, minimizes the uncertainties in the experimental sample parameters and produces high quality epilayers which are as close as possible to uniform uncompensated (Ga,Mn)As mixed crystals. For each nominal Mn doping x, the growth and post-growth annealing conditions were separately optimized in order to achieve the highest Curie temperature T_c attainable at the particular x. The highest T_c criterion was found to lead simultaneously to layers with maximized uniformity and minimized compensation by unintentional impurities and defects [1].

SAMPLES

The time-resolved magneto-optical experiments were performed in an optimized set of high-quality (Ga,Mn)As epilayers whose selected characteristics are summarized in Tab. I. All samples are in-plane magnets in which the cubic anisotropy competes with an additional uniaxial anisotropy. At very low dopings, the cubic anisotropy dominates and the easy axis align with the main crystal axis [100] or [010]. At intermediate dopings, the uniaxial anisotropy is still weaker but comparable in magnitude to the cubic anisotropy. At very high dopings, the uniaxial anisotropy dominates and the system has one strong easy-axis along the [1-10] in-plane diagonal.

TABLE I: Table summarizing the basic characteristics of selected samples from the series of optimized materials: x is nominal doping, d is film thickness, T_C is Curie temperature, M_s is saturated magnetic moment.

sample	x (%)	d (nm)	T_C (K)	M_s (emu/cm^3)
F010	1.5	20	29	8.9
F008	2	20	47	11.6
F007	2.5	20	60	11.5
F002	3	20	77	16.2
F016	3.8	20	96	24.7
E101	4.5	19	111	27.8
F020	5.2	20	132	33.3
D071	7	50	150	47.4
E115	7	20	159	51.0
E122	9	20	179	63.7
F056	14	20	182	78.1

HELICITY-DEPENDENT AND HELICITY-INDEPENDENT PRECESSION OF MAGNETIZATION

Laser-pulse induced dynamics of magnetization is investigated by the pump-and-probe magneto-optical technique [2]. A schematic diagram of our experimental set-up is shown in Fig. 1. The output of a femtosecond laser is divided into a strong pump pulse and a weak probe pulse that are focused to the same spot on the measured sample. The photon energy 1.64 eV is tuned above the semiconductor band gap in order to excite magnetization dynamics

by photon absorption. The circular polarization of pump beam results in the spin-polarization of the photo-generated carriers [3].

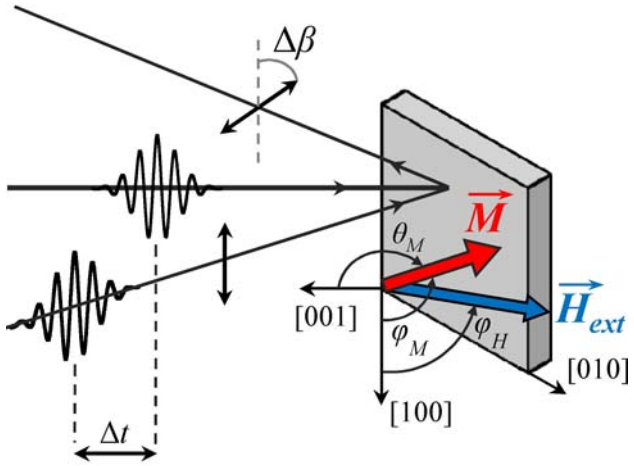

FIG. 1 Schematic diagram of the experimental set-up. The orientation of magnetization in the sample is described by the polar angle φ_M and azimuthal angle θ_M. The external magnetic field H_{ext} is applied in the sample plane at an angle φ_H. The rotation of the polarization plane $\Delta\beta$ of the reflected linearly polarized probe pulse is measured as a function of the time delay Δt between pump and probe pulses.

The helicity-independent precession of magnetization is connected with a transfer of energy from laser pulses to the material. In particular, this signal is induced by the modification of the sample magnetic anisotropy due to the transient increase of the sample temperature δT and/or of the hole concentration δp [4]. The observed precession frequencies are given by the magneto-crystalline anisotropy fields in the samples. This is clearly apparent from the fact that the dependence of the precession frequency on the magnitude of the external magnetic field agrees perfectly with that predicted by the classical gyromagnetic theory for ferromagnetically coupled Mn spins with the g-factor of 2 (see Inset in Fig. 1 in Ref. 5 and Fig. 12 in this Supplementary material). Moreover, the precession signal can be successfully modeled by the Landau-Lifshitz-Gilbert equation with the magnetic anisotropy constants that were independently determined for each (Ga,Mn)As sample from magnetization measurements by the superconducting quantum interference device (SQUID) – see below. The helicity-independent precession of magnetization was reported for the first time in 2005 by A. Oiwa *et al* [6] and after that several groups investigated this phenomenon systematically [4-12]. Nevertheless, the helicity-dependent mechanism of magnetization precession was not reported prior to this work.

The thickness and the Mn concentration in the sample used for the experiments reported in the main paper are not markedly different from those used in previous reports about the laser-induced precession in magnetization in (Ga,Mn)As [4-12]. The key difference,

however, is in the modified magnetic anisotropy of the sample. In particular, the possibility to tune the sample anisotropy *in situ* by the piezo-stressor enabled us to suppress completely the anisotropy-related mechanism of magnetization precession. Nevertheless, it should be stressed that the helicity-dependent mechanism of magnetization precession could be observed also in ordinary samples without the attached piezo-stressor. In Fig. 2 we show the helicity-dependent $[(\sigma^+ - \sigma^-)/2]$ and helicity-independent $[(\sigma^+ + \sigma^-)/2]$ signals, which were computed from the signals measured after excitation by σ^+ and σ^- circularly polarized pump pulses, for several samples with different Mn concentration x. In fact, we were able to detect the helicity-dependent signal in the vast majority of the investigated samples. The relative strength of the helicity-dependent signal with respect to that of the helicity-independent signal depends strongly on the applied magnetic field and on the light intensity – the helicity-dependent signal is typically from 5 to 20-times smaller than the helicity-independent signal.

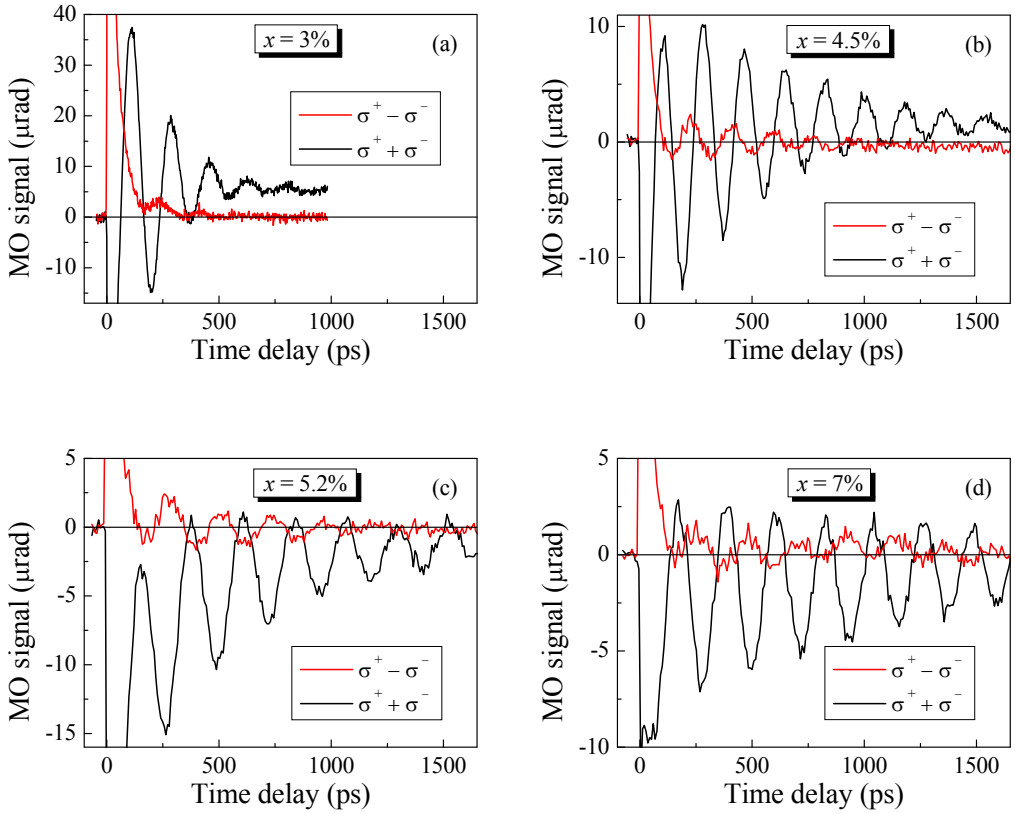

Fig. 2. Helicity-dependent $[(\sigma^+ - \sigma^-)/2]$ and helicity-independent $[(\sigma^+ + \sigma^-)/2]$ signals measured in various $Ga_{1-x}Mn_xAs$ samples; photon energy $h\upsilon$=1.64 eV, excitation intensity I = 46 μJ.cm^{-2}, sample temperature T = 15 K, probe input polarization orientation (from the [100] crystal direction) β = 0°, $\mu_0 H_{ext}$ = 20 mT, φ_H = 90°.

From the bare epilayers, the relative magnitude of the helicity-dependent signal was the largest in sample with x = 3.8% where it was only about 2.5-times smaller than the helicity-independent one – see Fig. 3(a). Therefore, we selected this particular sample for the

experiment with the attached piezo-stressor that was aiming at *in situ* modification of the sample magnetic anisotropy by the applied strain. We glued the commercial piezo-stressor to the sample at room temperature but the actual experiment was performed at low temperature. Consequently, due to the considerably smaller thermal contraction of the piezo-stressor compared to that of (Ga,Mn)As, the temperature decrease by itself induced a rather strong tensile strain ~ 10^{-3} even with no voltage U applied to the piezo-stressor [13, 14]. This strain reduces significantly the out-of-plane magnetic anisotropy of the (Ga,Mn)As that leads to a considerable smaller precession frequency in the sample with the attached piezo-stressor [Fig. 3(b) and (c)] compared to that in the bare epilayer [Fig. 3(a)]. Moreover, this leads also to a very strong enhancement of the helicity-dependent signal which is 2.8-times *larger* than the helicity-independent one even for U = 0 V [see Fig. 3(d)]. Further application of U = -150 V to the piezo-stressor, which induces a compressive strain of (-1.5 ± 0.5) × 10^{-4} along the piezo-stressor main axis and a tensile strain of (0.3 ± 0.1) ×10^{-4} along its minor axis, is then sufficient for a complete quenching of the anisotropy-related helicity-independent mechanism

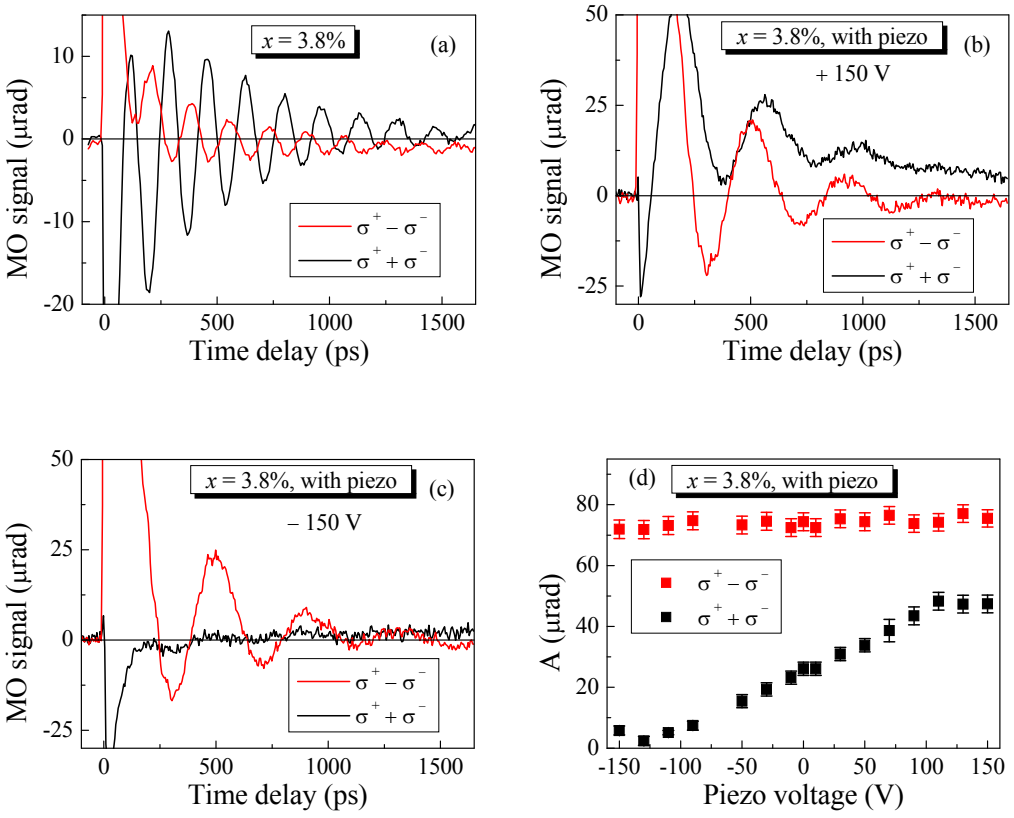

Fig. 3. Helicity-dependent and helicity-independent signals measured in $Ga_{1-x}Mn_xAs$ sample with x = 3.8% (a) and in the same sample attached to the piezo-stressor for the applied voltages U = +150 V (b) and U = –150 V (c). Dependence of the precession signal amplitudes, which were obtained by fitting the measured data by Eq. (11), on the voltage applied to the piezo-stressor is shown in (d); I = 70 μJ.cm^{-2}, $\mu_0 H_{ext}$ = 30 mT, φ_H = 115°, β = 25°.

of magnetization precession [see Fig. 3(c)]. In Fig. 4 we show the magnetic field dependence of the amplitude A of the helicity-independent oscillations for positive and negative piezo-voltages. At U = +150 V, the amplitude shows the expected gradual decrease with increasing magnetic field [7]. At U = −150 V, on the other hand, the decrease is much more rapid and the polarization-independent oscillations are effectively quenched at 20 mT. This is because at large negative piezo-voltages the internal anisotropy field forcing magnetization to align with the stressor axis (which is set close to the easy-axis of the unstressed epilayer) is significantly strengthened. With only a relatively weak additional external magnetic field, the changes in the magnetic anisotropy induced by the laser pulse are then not sufficient to trigger measurable spin precession.

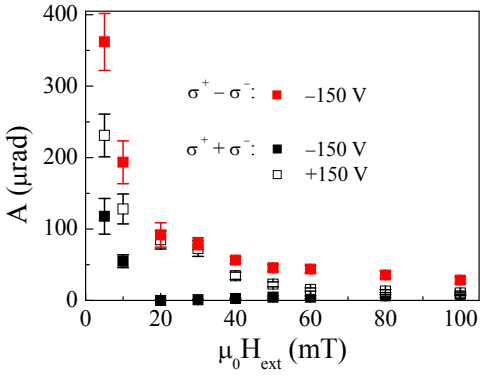

FIG. 4 Influence of external magnetic field H_{ext} on amplitude of the precession signal A for helicity-dependent ($\sigma^+ - \sigma^-$) and helicity-independent ($\sigma^+ + \sigma^-$) MO signals measured in $Ga_{1-x}Mn_xAs$ sample with x = 3.8% attached to the piezo-stressor for U = –150 V and U = +150 V; the helicity-dependent values of A are almost identical for –150 V and +150 V and, therefore, the data for +150 V are not shown for clarity; I = 70 μJ.cm^{-2}, $\mu_0 H_{ext}$ = 30 mT, φ_H = 115°, β = 25°.

In the following, we describe in detail the optical, magneto-optical and magnetic properties of (Ga,Mn)As samples. In particular, we illustrate that the magneto-optical coefficients and the micromagnetic parameters of the samples were determined independently by separate experiments that enabled us to model the magnetization dynamics by Landau-Lifshitz-Gilbert equation with a very restricted set of fitting parameters.

DYNAMICS OF MAGNETIZATION VS. DYNAMICS OF MAGNETO-OPTICAL SIGNAL

Magneto-optics deals with phenomena induced by interaction between light and a matter exposed to a magnetic field (external or internal). Reflection of linearly polarized light from the magnetic medium leads to the rotation of light polarization ψ' and to the change of its ellipticity ψ'' [15]. For the polar Kerr effect (where a magnetization is along the light propagation) they can be expressed in the following form [12]:

$$\psi' = f_{\psi'} \cdot M \,, \tag{1a}$$

$$\psi'' = f_{\psi''} \cdot M \,, \tag{1b}$$

where M is the magnetization, $f_{\psi'}$ and $f_{\psi''}$ are functions that depend on the electronic properties of the material and that can be expressed in terms of the refractive index and the absorption coefficient. Correspondingly, the light-induced dynamical change of ψ' and ψ'' consists of two components

$$\Delta\psi'(t) \approx f_{\psi'} \cdot \Delta M(t) + \Delta f_{\psi'}(t) \cdot M \,, \tag{2a}$$

$$\Delta\psi''(t) \approx f_{\psi''} \cdot \Delta M(t) + \Delta f_{\psi''}(t) \cdot M \,, \tag{2b}$$

where only the first term (the so-called "magnetic part" of the signal) reflects the magnetization dynamics while the second term (the so-called "optical part" of the signal) is a consequence of the pump pulse-induced change of the complex index of refraction of the sample. Consequently, the dynamics of both the rotation and ellipticity has to be measured and compared before the obtained magneto-optical signal is attributed to the magnetization dynamics [15]. In the case of (Ga,Mn)As, the situation is further complicated by the fact that not only the polar Kerr effect but also the magnetic linear dichroism contribute to the measured magneto-optical signal (see below). Nevertheless, the above discussion remains qualitatively valid also in this case. The laser pulse-induced change of the rotation and ellipticity measured in a (Ga,Mn)As epilayer with nominal doping x = 3% is shown in Fig. 5. The curves are very similar except for short time delays. This implies that the "optical part" of the signal has a sizable contribution only in a time range up to ≈ 30 ps where the reflectivity

(i.e., the complex index of refraction) is modified considerably by the pump pulse (see the inset of Fig 5).

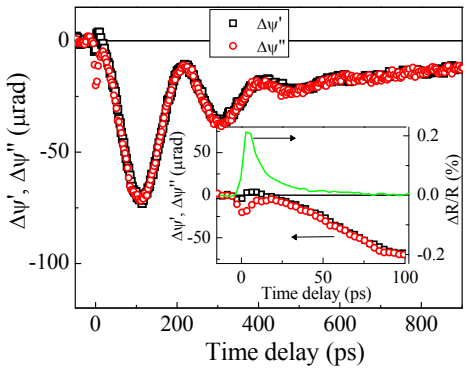

Fig. 5. Comparison of the laser pulse-induced change of the rotation ψ' and ellipticity ψ'' measured in a (Ga,Mn)As epilayer with nominal doping x = 3%; T = 15 K, I = 70 μJ.cm^{-2}, $\mu_0 H_{ext} \approx 0$ mT, β = 105°. Inset: Detail of the measured dynamics of $\Delta\psi'$ and $\Delta\psi''$ (points) together with the pulse-induced reflectivity change $\Delta R/R$ (line).

The measured dynamics of the reflectivity change $\Delta R/R$ provides us information also about the characteristic relaxation and recombination times of electrons in the investigated samples [16]. From the measured data we can conclude that the majority of photo-generated free electrons decays within ≈ 30 ps after the photo-injection. This rather short lifetime of the free electrons is similar to that reported for the low temperature grown GaAs (LT-GaAs), which is generally interpreted as a result of a high concentration of nonradiative recombination centers induced by the low temperature growth mode of the MBE [17]. The nonradiative recombination of the photo-injected electrons is accompanied by an emission of phonons (i.e., by a heating of the sample). Consequently, the measured decay time of $\Delta R/R$ corresponds to a rise time of the laser-induced transient change of the sample temperature δT, which is about 2 K (10 K) for the pump intensity 12 μJ.cm^{-2} (70 μJ.cm^{-2}) at the equilibrium sample temperature 15 K. We also point out that the photo-electron decay time is much larger than the photo-electron spin precession time in the exchange field of Mn local moments which allows us to omit the recombination terms (Ref. 16 from the main text) from the LLG equations (1) in the man text.

OPTICAL RESPONSE OF (GA,MN)AS FILMS

Absorption of laser photons leads to a photogeneration of electrons and holes with identical concentrations. However, because the density of states is considerably higher for holes (due to their larger mass), the pump-induced change of the distribution function is much

larger for electrons and, consequently, the measured change of complex index of refraction is dominated by electrons [16]. Therefore, the initial value of the reflectivity change can be regarded as a measure of the relative number of the photo-generated electrons (and thus also of the holes). In Fig. 6 we show that the pump-induced change of the complex index of refraction is linear in pump-pulse intensity at least up to 210 μJ.cm^{-2}.

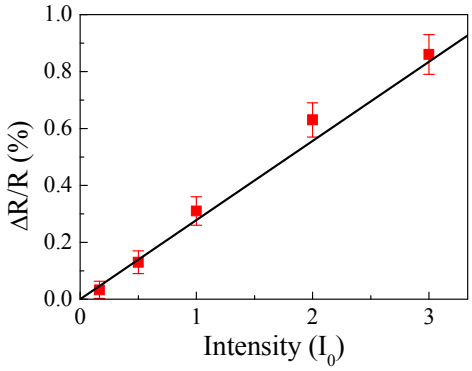

Fig. 6. Intensity dependence of the initial value of the pulse-induced reflectivity change $\Delta R/R$ measured in a (Ga,Mn)As epilayer with nominal doping $x = 3\%$ at $T = 15$ K; $I_0 = 70$ μJ.cm^{-2}.

The thickness of the investigated (Ga,Mn)As film (20 nm) is considerably smaller than the penetration depth of the laser at the corresponding photon energy (≈ 600 nm). Consequently, the absorption of photons leads to a rather constant concentration of photo-injected carriers in (Ga,Mn)As along the growth direction, which can be estimated from the laser spot size on the sample, photon energy, and absorption and reflection coefficients of GaAs. On the other hand, also the carriers photo-injected in the substrate could, in principle, contribute to the measured signals. To address this, we performed and extensive set of control experiments for (Ga,Mn)As layers on the GaAs substrate and for the GaAs substrate alone. The experiments showed that the oscillatory signal reported in the main paper comes solely from the (Ga,Mn)As epilayer. In addition to this signal, however, there is a rather weak magneto-optical signal that is connected with electrons photo-excited in the substrate. Nevertheless, due to the rather low g-factor of electrons in GaAs of about 0.4, for the magnetic field of 30 mT, which is the only one that is used in the experiments reported in the main paper, this magneto-optical signal from the substrate is apparent just as a weak non-oscillatory background. Therefore, this signal from the substrate can be safely neglected in the qualitative analysis of the oscillatory signal that is connected with the precession of magnetization in (Ga,Mn)As. In our case, the small thickness of the (Ga,Mn)As films disable a reliable separation of the magneto-optical signals connected with the carriers that are photo-

injected in (Ga,Mn)As epilayers and GaAs substrate, respectively [20]. In the very low doping limit, the incorporation of Mn was reported to lead to a strong suppression of the electron spin relaxation [21, 22]. However, higher doping levels (above $x \approx 0.01\%$) lead to a reduction of the electron spin lifetime [23] that reaches a typical scale of 10´s ps for ferromagnetic materials [24], which is in a very good agreement with the theoretical predictions [25].

STATIC MAGNETO-OPTICAL SIGNALS IN (GA,MN)AS

In (Ga,Mn)As there are two magneto-optical (MO) effects that are responsible for the measured signal. In the following we will concentrate on the rotation of the polarization plane of the reflected linearly polarized light but the same applies also for the change of the light ellipticity. We will also limit the discussion to the case when the light beam is close to the normal incidence (in our experiment the angle of incidence is 2° and 8° for pump and probe pulses, respectively). The first of the effects is the well-known polar Kerr effect (PKE), which is sometimes called magneto-optical Kerr effect (MOKE), where the rotation of polarization occurs due to the different index of refraction for σ^+ and σ^- circularly polarized light propagating *parallel to the direction of magnetization* - see Fig. 7(a). We note that the angle

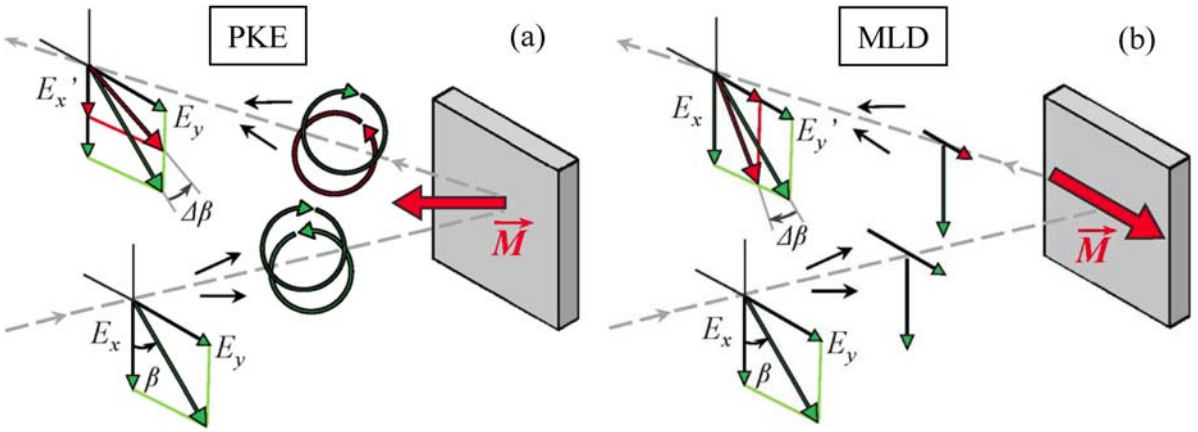

Fig. 7. Schematic illustration of the two magneto-optical effects in (Ga,Mn)As that are responsible for a rotation of the polarization plane $\Delta\beta$ of reflected light at normal incidence. (a) Polar Kerr effect (PKE) that is due to the different index of refraction for σ^+ and σ^- circularly polarized light propagating parallel to the direction of magnetization M. (b) Magnetic linear dichroism (MLD) that is due to the different absorption (reflection) coefficient for light linearly polarized parallel and perpendicular to M if the light propagates perpendicular to the direction of M.

of incidence of the probe beam is rather close to the normal incidence. Consequently, the influence of the longitudinal and transverse Kerr effects is strongly suppressed. Moreover, in GaMnAs the polar Kerr effect is typically the strongest effect from the family of magneto-

optical Kerr effects [26]. The rotation of light polarization $\Delta\beta$ due to PKE is proportional to the projection of magnetization to the direction of light propagation (see Fig. 1 for the definition of the coordinate system)

$$MO^{PKE} \equiv \Delta\beta^{PKE} \equiv \beta' - \beta = P^{PKE}\frac{M_z}{M_s} = P^{PKE}\cos\theta_M , \qquad (3)$$

where β and β' describes the orientation of the input and output linear polarization [see Fig. 8(a)], P^{PKE} is the corresponding magneto-optical coefficient of the sample, M_s and M_z are magnitude and z component of magnetization, and θ_M describes the out-of-plane orientation of magnetization, respectively. Here we adopted the following sign convention: If light is reflected along the direction of magnetization, the value $P^{PKE} > 0$ corresponds to a counterclockwise rotation of incident polarization (i.e., $\Delta\beta > 0$) when viewed by an observer facing the sample – see Fig. 8(a). We note that this MO effect is linear in magnetization (i.e., the sign of $\Delta\beta$ is changed when the direction of magnetization is reversed) and that the value of $\Delta\beta^{PKE}$ does not dependent on β.

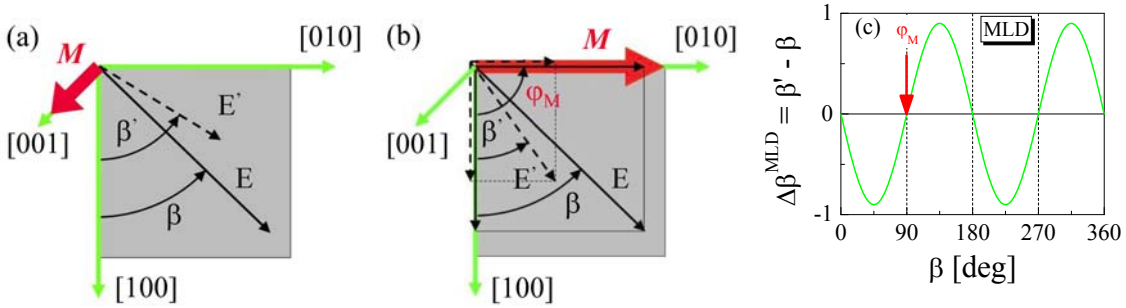

Fig. 8. Polarization dependence of magneto-optical effects. (a) PKE is proportional to the out-of-plane projection of magnetization; for $P^{PKE} > 0$ and $M_z > 0$ this MO effect leads to $\Delta\beta > 0$ for any β. (b) MLD is sensitive to the in-plane projection of magnetization; the magnitude and sign of $\Delta\beta$ is a harmonic function of β as described by Eq. (7) and schematically illustrated in (c) where the vertical red arrow depicts the assumed position of the magnetization.

The second MO effect is the magnetic linear dichroism (MLD) [18], which originates from to the different absorption (reflection) coefficient for light linearly polarized parallel and perpendicular to M. This effect occurs if the light propagates *perpendicular to the direction of magnetization M* - see Fig. 7(b). To derive the rotation of light polarization due to MLD we first suppose that the magnetization is located in the sample plane with a position characterized by an azimuthal angle φ_M. We can express the projections of the incident

electric field amplitude E parallel to magnetization ($E^{\parallel}$) and perpendicular to magnetization ($E^{\perp}$) using φ_M and the input polarization orientation β

$$E^{\parallel} = E\cos(\varphi_M - \beta), \tag{4a}$$

$$E^{\perp} = E\sin(\varphi_M - \beta). \tag{4b}$$

The same can be done for the reflected electric field amplitude E'. If we now consider that $E^{\parallel}$ ($E^{\perp}$) is reflected from (Ga,Mn)As with the amplitude reflection coefficient a (b), we obtain

$$tg(\varphi_M - \beta) = \frac{E^{\perp}}{E^{\parallel}}, \tag{5a}$$

$$tg(\varphi_M - \beta') = \frac{bE^{\perp}}{aE^{\parallel}}, \tag{5b}$$

from which the rotation of light polarization $\Delta\beta \equiv \beta' - \beta$ can be easily derived

$$tg\Delta\beta = \frac{(a-b)\,tg(\varphi_M - \beta)}{a + b\left[tg(\varphi_M - \beta)\right]^2}. \tag{6}$$

If we now assume that $a/b \approx 1$ (i.e., that $\Delta\beta$ is small) we obtain

$$\Delta\beta = P^{MLD}\sin 2(\varphi_M - \beta), \tag{7}$$

where the magneto-optical coefficient P^{MLD} is defined as

$$P^{MLD} = 0.5\left(\frac{a}{b} - 1\right). \tag{8}$$

In a more general case, when magnetization has an arbitrary orientation characterized by φ_M and θ_M, the rotation of light polarization by MLD is given by

$$MO^{MLD} \equiv \Delta\beta^{MLD} \equiv \beta' - \beta = P^{MLD}\sin\theta_M \sin 2(\varphi_M - \beta). \tag{9}$$

The total MO response of any (Ga,Mn)As sample is given by a sum of contributions due to PKE and MLD:

$$MO^{stat} = MO^{PKE} + MO^{MLD} = P^{PKE}\cos\theta_M + P^{MLD}\sin\theta_M \sin 2(\varphi_M - \beta) \qquad (10)$$

The magnitude of P^{PKE} and P^{MLD} can be directly measured if the magnetization is oriented by a strong external magnetic field to the out-of-plane (θ_M = 0°) and in-plane (θ_M = 90°) positions, respectively. As an example, we show in Fig. 9(a) the spectral dependence of P^{PKE} and P^{MLD} measured in a (Ga,Mn)As epilayer with nominal doping x = 7%. We note that even though the magnitude of P^{PKE} is typically larger than that of P^{MLD}, there exists a relatively broad spectral region around 1.6 eV where they are comparable. In Fig. 9(b) the measured temperature dependence of P^{MLD} is compared with M^2, which was measured by SQUID, that confirms the expected [18] quadratic dependence of P^{MLD} on M.

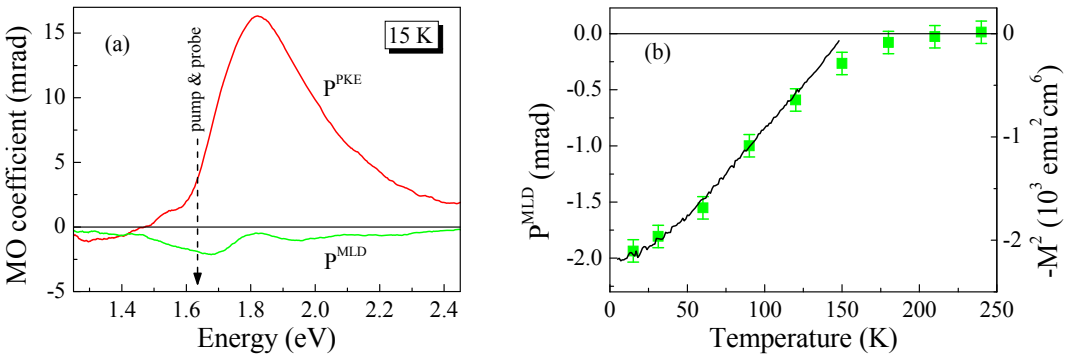

Fig. 9. (a) Spectral dependence of magneto-optical coefficients P^{PKE} and P^{MLD} measured in a (Ga,Mn)As epilayer with nominal doping x = 7% (Curie temperature T_c = 150 K) at temperature 15 K; the vertical arrow shows schematically the spectral position of laser pulses used for the pump & probe experiment. (b) Temperature dependence of P^{MLD} measured at 1.64 eV (points) and temperature dependence of (-1)×M^2 (line).

PROBE-POLARIZATION DEPENDENCE IN HELICITY-INDEPENDENT DYNAMIC MAGNETO-OPTICAL SIGNAL

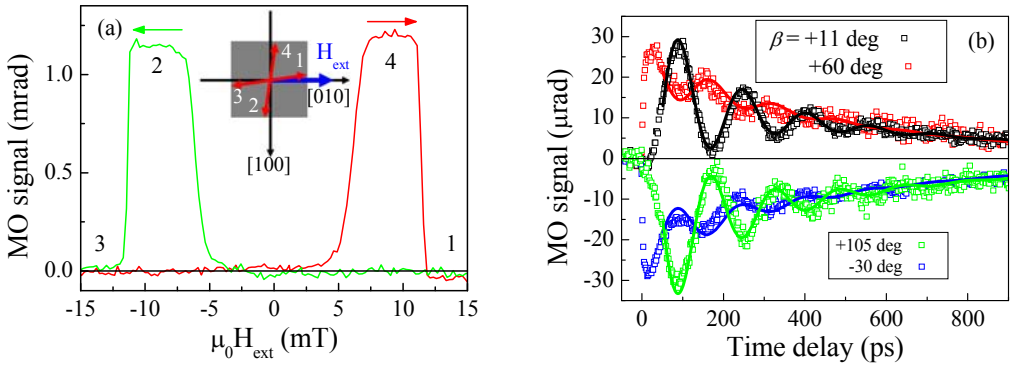

Fig. 10. Magneto-optical signal measured at temperature 15 K in a (Ga,Mn)As epilayer with nominal doping x = 3%. (a) M-shaped hysteresis loop that is a signature of the existence of four energetically equivalent easy axis positions of magnetization [10], which are schematically labeled "1" to "4" in the inset. (b) Dynamics of the helicity-independent MO signal induced by an impact of pump pulse on the sample with a magnetization in the position "1" that was measured by probe pulses with different β (points). Lines are fits by Eq. (11). I = 12 μJ.cm^{-2}.

In Fig. 10 we show, as an example, the data measured in a (Ga,Mn)As epilayer with nominal doping x = 3%. Prior to the time-resolved experiment, we prepared the magnetization in a state close to the [010] crystallographic direction [easy axis position labeled "1" in Fig. 10(a)]. An impact of the pump laser pulse changes the easy axis position and, consequently, triggers the precession of magnetization around this new quasi-equilibrium position. The resulting precessional MO signal strongly depends on the orientation of linear polarization of probe pulses β as shown in Fig. 10(b), where the helicity-independent part of the MO signal is depicted.

The measured pump-induced dynamical change of the magneto-optical signal, δMO, can be fitted well by the phenomenological equation,

$$\delta MO(t) = A\cos(\omega_{Mn}t + \Delta)e^{-t/\tau_G} + Ce^{-t/\tau_p}, \qquad (11)$$

where A and C are the amplitudes of the oscillatory and pulse function, respectively, ω_{Mn} is the ferromagnetic moment precession frequency, Δ is the phase factor, τ_G is the Gilbert damping time, and τ_p is the pulse function decay time. All the measured data in Fig. 10(b) can be fitted well by Eq. (11) with a one set of parameters ω_{Mn}, τ_G and τ_p. The dependence $A(\beta)$ obtained by this fitting procedure is displayed in Fig. 11. The position of the maximum in the dependence $A(\beta)$ at $\beta \approx 100°$ corresponds to the equilibrium position φ_M of the easy axis in

the sample (i.e., its position without the pump pulse). This conclusion immediately follows from the fact that the β dependence of A comes from the MO signal induced by a change of the in-plane projection of magnetization, which is detected by MLD. And from Fig. 8(c) it is clearly apparent that the strongest change of the MO signal due to an in-plane movement of magnetization is observed when the probe pulses are polarized along the magnetization or perpendicular to it (i.e., when the derivative of Eq. (7) with respect to φ_M is the largest). We recall that prior to this measurement we prepared the magnetization in a state close to [010] crystallographic direction.

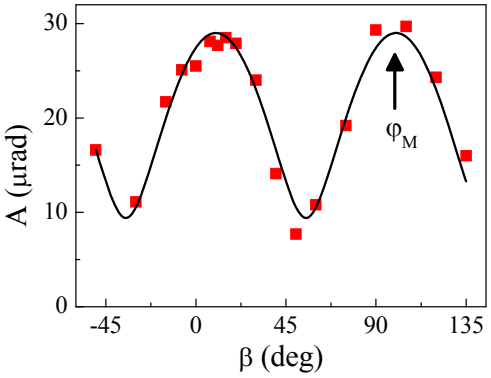

Fig. 11. Polarization dependence of the amplitude of the oscillatory part A that was obtained by fitting the dynamics shown in Fig. 10(b) by Eq. (11) with a fixed values ω_{Mn} = 33.9 GHz, τ_G = 165 ps, and τ_p = 880 ps (points). The vertical arrow depicts the derived easy axis position in the sample without the pump pulse.

NUMERICAL MODELLING OF DYNAMIC MAGNETO-OPTICAL SIGNAL BY LLG EQUATION

We performed an extensive numerical modeling of the measured precessional MO signal by the Landau-Lifshitz-Gilbert (LLG) equation. We used LLG equation in spherical coordinates where the time evolution of magnetization magnitude M_s and orientation, which is characterized by the polar θ and azimuthal φ angles, is given by:

$$\frac{dM_s}{dt} = 0 \ , \tag{12}$$

$$\frac{d\theta}{dt} = -\frac{\gamma}{\left(1+\alpha^2\right)M_s}\left(\alpha \cdot A + \frac{B}{\sin\theta}\right), \tag{13}$$

$$\frac{d\varphi}{dt} = \frac{\gamma}{\left(1+\alpha^2\right)M_s \sin\theta}\left(A - \frac{\alpha \cdot B}{\sin\theta}\right), \tag{14}$$

where α is the Gilbert damping parameter and γ is the gyromagnetic ratio. Functions $A = dF/d\theta$ and $B = dF/d\varphi$ are the derivatives of the energy density functional F with respect to θ and φ, respectively. We expressed F in a form:

$$F = M\left[\begin{array}{l} H_c \sin^2\theta\left(\frac{1}{4}\sin^2 2\varphi \sin^2\theta + \cos^2\theta\right) - H_{[001]}\cos^2\theta - \frac{H_{[110]}}{2}\sin^2\theta(1-\sin 2\varphi) - \\ - H_{ext}\left[\cos\theta\cos\theta_H + \sin\theta\sin\theta_H\cos(\varphi-\varphi_H)\right] \end{array}\right], \tag{15}$$

where H_c, $H_{[001]}$ and $H_{[110]}$ are constants that characterize the magnetic anisotropy in (Ga,Mn)As [19] and H_{ext} is the external magnetic field whose orientation is given by the angles θ_H and φ_H. We would like to stress that our approach is considerably distinct from that used up to now for a modeling of the laser pulse-induced precession of magnetization in (Ga,Mn)As [9, 11] where the magnetic anisotropy of the material was characterized by *one effective magnetic field*, *which was a fitting parameter*. Instead, we used a realistic model of the magnetic anisotropy in (Ga,Mn)As [19] and we determined *independently* the corresponding anisotropy constants in the sample. The anisotropy constants can be either measured by SQUID or FMR or, as we show below, they can be evaluated directly from the laser-induced precession of magnetization – and we have verified that all these methods provide the same results.

For all the investigated samples, we used the following procedure for the magnetic anisotropy determination which is demonstrated using the results obtained for (Ga,Mn)As epilayer with nominal doping x = 3%. We first measured the probe-polarization dependence of the precession signal. From the position of the peak in the measured polarization dependence of the precession amplitude we determined the position of the easy axis in the sample plane, which is $\varphi_M \approx 100°$ for this particular sample (see Fig. 11). The position of the easy axis in the sample plane is given by the ratio of the cubic (H_c) and uniaxial ($H_{[110]}$) anisotropy constants, therefore, in this particular sample we have $H_{[110]} / H_c \approx 0.5$. Next, we measured the dependence of the precession frequency on the magnitude of the external

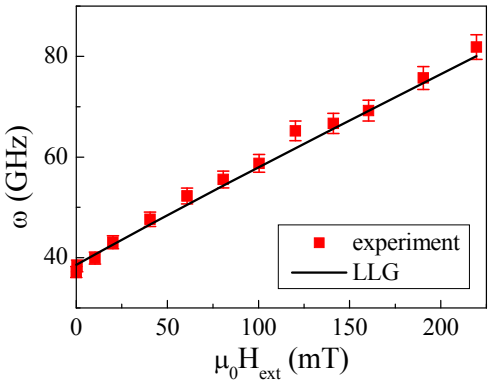

Fig. 12. Dependence of the precession frequency ω on the magnitude of magnetic field H_{ext} applied along the [010] crystallographic direction ($\varphi_H = 90°$) in (Ga,Mn)As epilayer with nominal doping $x = 3\%$ (points); $T = 15$ K; $I = 12$ μJ.cm^{-2}. The line was computed by our numerical model based on LLG equation with the following parameters: g = 2; $\mu_0 H_c = 64$ mT, $\mu_0 H_{[110]} = 32$ mT and $\mu_0 H_{[001]} = -108$ mT.

magnetic field (points in Fig. 12). Finally, we adjusted the magnitude of the anisotropy constants in the model to obtain the best match between the computed and measured frequencies (see Fig. 12).

A. Helicity-independent signal

As a consistency check of our model, we performed a numerical modeling of the probe-polarization dependence of the hellicity-independent precession of magnetization. To model the measured data, we first computed from LLG equation the time-dependent deviations of the spherical angles [$\delta\theta(t)$ and $\delta\varphi(t)$] from the corresponding equilibrium values ($\theta_M = 90°$, $\varphi_M \approx 100°$). Then we calculated how such changes of θ and φ modify the magneto-optical response of the sample, which is the signal that we detect experimentally. In Fig. 13(a) we show the precession data measured by probe pulses with different polarization angle β in a (Ga,Mn)As epilayer with nominal doping $x = 3\%$ (points) – we note that this is the same data set that was already shown in Fig. 10(b). The lines in Fig. 13(a) are fits by our numerical model and the corresponding dynamics of $\delta\theta(t)$ and $\delta\varphi(t)$, which are the same for all the curves in Fig. 13(a), are shown in Fig. 13(b). And we stress that also the magneto-optical constants ($P^{PKE} = -0.24$ mrad, $P^{MLD} = -0.9$ mrad) of the sample were not fitted – they were measured in independent static magneto-optical experiments. Overall, we find the agreement between this rather complex data set and the computed results very good.

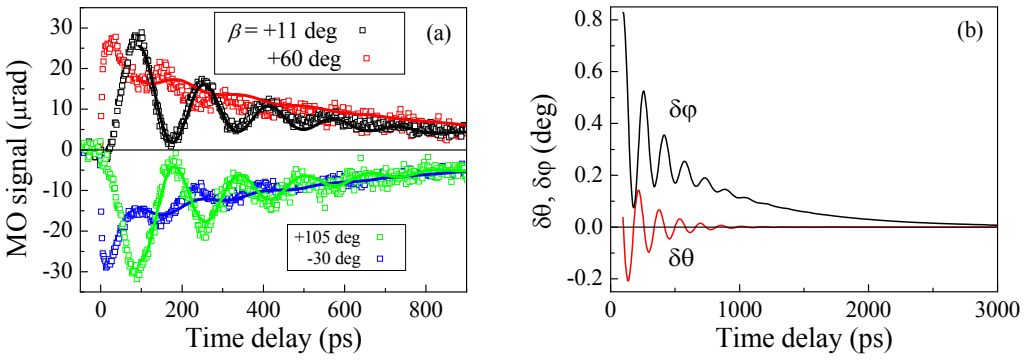

Fig. 13. Modeling of the helicity-independent magneto-optical signal measured at temperature 15 K in a (Ga,Mn)As epilayer with nominal doping x = 3% (Curie temperature T_c = 77 K) using LLG equation. (a) Dynamics of the helicity-independent MO signal measured by probe pulses with different β (points). Lines are fits by the numerical model described in the text. (b) Time evolution of $\delta\theta(t)$ and $\delta\varphi(t)$ that were used to model the data shown in (a).

B. Helicity-dependent signal

Having established the reliability of our numerical model for the well-known polarization-independent signal (and the correct incorporation of the magneto-optical response of GaMnAs in particular), we now proceed to the modeling of the helicity-dependent signal. In Fig. 14(a) we show the precession data measured by probe pulses with different polarization angle β in a (Ga,Mn)As epilayer with nominal doping x = 3.8% attached to a piezo-stressor (points) – we note that this is the sample described in detail in the main paper. The lines in Fig. 14(a) are fits by our numerical model and the corresponding dynamics of magnetization, which is the same for all the curves in Fig. 14(a), is shown in Fig. 14(b). We would like to stress that our numerical model correctly describes not only the magnitude but also the phase of the measured magneto-optical signal. In particular, the phase shift of π and $\pi/2$ is clearly apparent for probe polarization rotated by 90° and 45°, respectively.

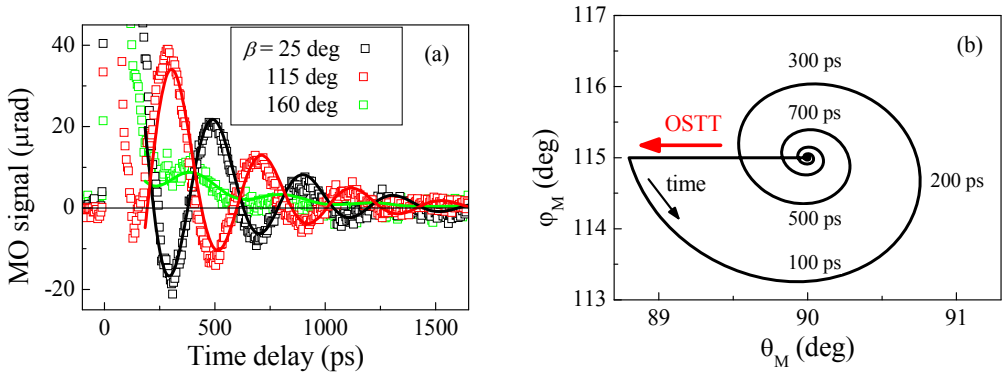

Fig. 14. Modeling of the probe-polarization dependence of the helicity-dependent magneto-optical signal using LLG equation. (a) Dynamics of the helicity-dependent MO signal measured by probe pulses with different β in (Ga,Mn)As epilayer with nominal doping x = 3.8% attached to a piezo-stressor (points); temperature 35 K, I = 70 μJ.cm^{-2}, $\mu_0 H_{ext}$ = 30 mT, φ_H = 115°. Lines are fits by the numerical model for the out-of-plane tilt of the

magnetization due to the optical spin transfer torque (OSST). (b) Calculated time evolution of the orientation of the magnetization in the sample, described by the polar angle φ_M and the azimuthal angle θ_M, that was used to model the data shown in (a).

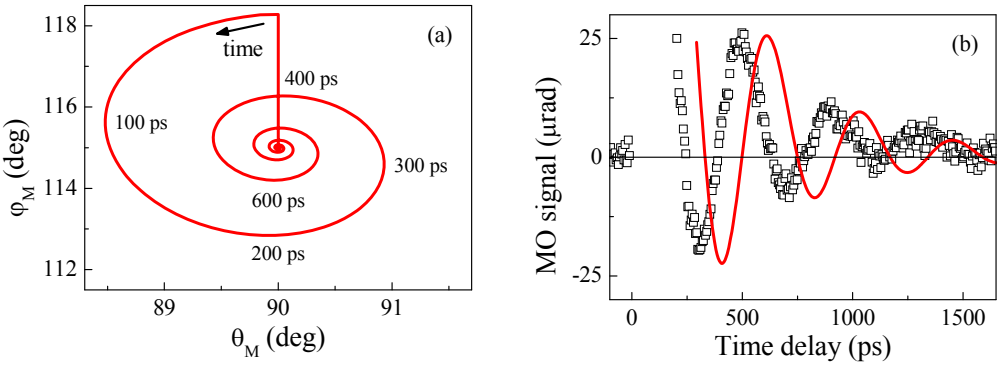

Fig. 15. Confirmation of the out-of-plane tilt of the magnetization due to the optical spin transfer torque. If the in-plane tilt of the magnetization is assumed (a) the computed MO signal is phase shifted for $\pi/2$ with respect to the measured data (b). Experimental conditions are identical to that in Fig. 14; results for $\beta = 25°$ only are shown for simplicity.

The measured phase of the oscillatory signal is in fact a direct experimental proof that the helicity-dependent signal is initiated by the *out-of-plane* tilt of magnetization (see Fig. 14(b) and Fig. 1 in the main paper). In Fig. 15 we show that if the in-plane shift of magnetization were assumed the computed magneto-optical signal would be strongly phase-shifted with respect to the measured one.

REFERENCES

[1] Jungwirth, T. *et al.* Systematic study of Mn-doping trends in optical properties of (Ga,Mn)As. *Phys. Rev. Lett.* **105**, 227201 (2010) *and its Supplementary material*, arXiv: 1007.4708.

[2] Kirilyuk, A., Kimel, A. V. & Rasing, T. Ultrafast optical manipulation of magnetic order. *Rev. Mod. Phys*. **82**, 2731 (2010).

[3] Dyakonov, M.I. and Perel V.I. *in* Optical orientation, *edited by Meier F. and Zakharchenya B. (North-Holland, Amsterdam, 1984), Vol. 8 of Modern problems in condensed matter sciences, Chap. 2*.

[4] Rozkotová, E. *et al.* Light-induced magnetization precession in GaMnAs. *Appl. Phys. Let.* **92**, 122507 (2008), arXiv: 0802.2043.

[5] Rozkotová, E. *et al.* Coherent control of magnetization precession in ferromagnetic semiconductor (Ga,Mn)As. *Appl. Phys. Lett.* **93**, 232505 (2008), arXiv: 0808.3738.

[6] Oiwa, A., Takechi, H. & Munekata, H. Photoinduced magnetization rotation and precessional motion of magnetization in ferromagnetic (Ga,Mn)As.
J. Supercond **18**, 9 (2005).
[7] Takechi, H., Oiwa, A., Nomura, K., Kondo, T. & Munekata, H. Light-induced precession of ferromagnetically coupled Mn spins in ferromagnetic (Ga,Mn)As.
phys. stat. sol. (c) **3**, 4267 (2006).
[8] Qi, J. *et al.* Coherent magnetization precession in GaMnAs induced by ultrafast optical excitation. *Appl. Phys. Lett.* **91**, 112506 (2007).
[9] Qi, J. *et al.* Ultrafast laser-induced coherent spin dynamics in ferromagnetic $Ga_{1-x}Mn_xAs$/GaAs structures. *Phys. Rev. B* **79**, 085304 (2009).
[10] Hashimoto, Y. & Munekata, H. Coherent manipulation of magnetization precession in ferromagnetic semiconductor (Ga,Mn)As with successive optical pumping.
Appl. Phys. Lett. **93**, 202506 (2008).
[11] Hashimoto, Y., Kobayashi, S. & Munekata, H. Photoinduced precession of magnetization in ferromagnetic (Ga,Mn)As. *Phys. Rev. Lett.* **100**, 067202 (2008).
[12] Rozkotová, E. *et al.* Laser-induced precession of magnetization in GaMnAs.
IEEE Trans. Mag. **44**, 2674 -2677 (2008).
[13] Rushforth, A. W. *et al.* Voltage control of magnetocrystalline anisotropy in ferromagnetic-semiconductor/piezoelectric hybrid structures. *Phys. Rev. B* **78**, 085314 (2008).
[14] de Ranieri, E. *et al.* Lithographically and electrically controlled strain effects on anisotropic magnetoresistance in (Ga,Mn)As. *New J. Phys.* **10**, 065003 (2008).
[15] Koopmans, B. *et al.* Ultrafast magneto-optics in nickel: magnetism or optics? *Phys. Rev. Lett.* **85**, 844-847 (2000).
[16] Shah J.: Ultrafast spectroscopy of semiconductors and semiconductor nanostructures. *Springer Series in Solid-State Sciences vol. 115, Springer-Verlag, Berlin, Heidelberg, New York*, 1996.
[17] Stellmacher M. *et al.* Dependence of the carier lifetime on acceptor concentration in GaAs grown at low-temperature under different growth and annealing condiitions.
J. Appl. Phys. **88**, 6026 (2000).
[18] Kimel, A. V. *et al.* Observation of giant magnetic linear dichroism in (Ga,Mn)As.
Phys. Rev. Lett. 94, 227203 (2005).
[19] Zemen, J. *et al.* Magnetocrystalline anisotropies in (Ga,Mn)As: Systematic theoretical study and comparison with experiment. *Phys. Rev. B* **80**, 155203 (2009).

[20] Zhou, R. *et al.* Temperature dependence of the effective g factor in diluted magnetic semiconductor (Ga,Mn)As. *J. Appl. Phys.* **103**, 053901 (2008).

[21] Astakhov, G.V. *et al.* Suppression of electron spin relaxation in Mn-doped GaAs. *Phys. Rev. Lett.* **101**, 076602 (2008).

[22] Akimov, I.A. *et al.* Electron-spin dynamics in Mn-doped GaAs using time-resolved magneto-optical techniques. *Phys. Rev. B* **80**, 081203(R) (2009).

[23] Poggio, M. *et al.* Structural, electrical and magneto-optical characterization of paramagnetic GaMnAs quantum wells. *Phys. Rev. B* **72**, 235313 (2005).

[24] Kimel A.V. *et al.* Picosecond dynamics of the photoinduced spin polarization in epitaxial (Ga,Mn)As films. *Phys. Rev. Lett.* **92**, 237203 (2004).

[25] Fernández-Rossier, J. *et al.* Optical spin transfer in ferromagnetic semiconductors. *http://arXiv.org/abs/cond-mat/0304492.*

[26] Moore G.P. *et al.* Magnetic anisotropy and switching process in diluted $Ga_{1-x}Mn_xAs$ magnetic semiconductor films. *J. Appl. Phys.* **94**, 4530 (2003).

APPENDIX 7

Authors: N. Tesařová, P. Němec, E. Rozkotová, J. Zemen, T. Janda, D. Butkovičová, F. Trojánek, K. Olejník, V. Novák, P. Malý and T. Jungwirth

Title: Experimental observation of the optical spin-orbit torque

Journal: submitted to Nature Photonics

Preprint server: http://arxiv.org/abs/1207.0307

Experimental observation of the optical spin-orbit torque

N. Tesařová,[1] P. Němec,[1] E. Rozkotová,[1] J. Zemen,[2,3] T. Janda,[1] D. Butkovičová,[1]
F. Trojánek,[1] K. Olejník,[3] V. Novák,[3] P. Malý,[1] and T. Jungwirth[3,2]

[1]*Faculty of Mathematics and Physics, Charles University in Prague, Ke Karlovu 3, 121 16 Prague 2, Czech Republic*

[2]*School of Physics and Astronomy, University of Nottingham, Nottingham NG7 2RD, United Kingdom*

[3]*Institute of Physics ASCR, v.v.i., Cukrovarnická 10, 162 53 Praha 6, Czech Republic*

(Dated: November 22, 2012)

PACS numbers: 75.50.Pp, 76.50.+g, 78.20.Ls, 78.47.-p

Spin polarized carriers electrically injected into a magnet from an external polarizer can exert a spin transfer torque (STT)[1,2] whose physical origin is a non-relativistic angular momentum transfer. The phenomenon belongs to a leading area of spintronics research focusing on the manipulation of magnetic moments by electric fields. A current induced spin-orbit torque (SOT)[3–8] is a distinct relativistic phenomenon in which magnetization dynamics is induced in a uniform spin-orbit coupled ferromagnet in the absence of the external polarizer. In the ferromagnetic semiconductor (Ga,Mn)As, an optical counterpart of the non-relativistic STT (OSTT)[9,10] has been recently observed[11] in which a circularly polarized pump laser pulse acts as the external polarizer. In this paper we report the observation of the optical counterpart of the relativistic SOT (OSOT) in (Ga,Mn)As. The absence of an external polarizer in our OSOT corresponds to photo-carrier excitations by helicity independent pump laser pulses which do not impart angular momentum. The OSOT relies on spin-orbit coupling of non-equilibrium carriers, in a direct analogy to the current induced SOT. In our measurements of the time-dependent magnetization trajectories, the signatures of the OSOT are clearly distinct from the competing thermal excitation mechanism, and the OSOT can even dominate in (Ga,Mn)As materials with properly controlled micromagnetic parameters.

The seminal works on the current induced STT date back decades[12–14] and the effect already plays a key role in commercially developed spintronic technologies.[15] In the current induced STT, spin-polarized carriers are electrically injected into a magnetic object (ferromagnetic layer, domain wall, etc.) from an external polarizer which is represented by another part of the non-uniform magnetic structure. The basic origin of the STT is in the non-relativistic physics of the angular momentum transfer from the external polarizer to the magnetic object. The OSTT[11] is the optical counterpart of the STT as the direction and magnitude of the non-equilibrium carrier spin-density is governed again by the properties of an external polarizer which in the OSTT case is represented by the intensity, propagation axis, and helicity of the circularly polarized pump laser pulse. In a direct analogy to the (adiabatic) STT, the coupled dynamics of the magnetization $\vec{M}$ and the non-equilibrium

carrier spin density $\vec{s}$ can be written as,[9–11]

$$\begin{aligned} \frac{d\vec{M}}{dt} &= \frac{J}{\hbar}\vec{M}\times\vec{s} \\ \frac{d\vec{s}}{dt} &= \frac{J}{\hbar}\vec{s}\times\vec{M} + P\hat{n}\,, \end{aligned} \tag{1}$$

where J is the carrier - magnetic moment exchange coupling constant and P is the rate at which carrier spins with orientation $\hat{n}$ are injected into the ferromagnet by the external polarizer. From the steady-state, non-equilibrium carrier spin density solution ($d\vec{s}/dt = 0$) we obtain explicitly the angular momentum transfer relation between the OSTT($\equiv d\vec{M}/dt$) and the carrier spin injection rate P.

In the SOT, the term corresponding to the injection form the external polarizer is not present and the quantum-mechanical dynamics of the carrier spins is given by,[4] $d\langle\hat{s}\rangle/dt = \frac{1}{i\hbar}\langle[\hat{s}, H]\rangle$, where $\hat{s}$ is the carrier spin operator and $\langle ...\rangle$ denotes quantum mechanical averaging. The carrier Hamiltonian, $H = H_0 + H_{ex} + H_{so}$, can be written as a sum of the non-relativistic non-magnetic term H_0, the carrier spin - magnetic moment exchange coupling $H_{ex} = J\vec{M}\hat{s}$, and the spin-orbit term H_{so}. This implies that,

$$\frac{d\vec{s}}{dt} = \frac{J}{\hbar}\vec{s}\times\vec{M} + \frac{1}{i\hbar}\langle[\hat{s}, H_{so}]\rangle \tag{2}$$

where $\vec{s} = \langle\hat{s}\rangle$. The steady-state carrier spin density solution of Eq. (2) shows explicitly the spin-orbit coupling origin of SOT$\equiv d\vec{M}/dt = \frac{J}{\hbar}\vec{M}\times\vec{s} = \frac{1}{i\hbar}\langle[\hat{s}, H_{so}]\rangle$. Apart from the spin-orbit coupling, the SOT obtained form Eq. (2) also requires the exchange coupling of the carrier spins to the magnetic moments, i.e., requires broken time reversal symmetry of the exchange-split carrier bands. All these features of the SOT are common to both the previously discussed current induced SOT[3–8] and our OSOT reported in this paper.

We point out that the electrical and optical SOTs may differ in the specific contributions to H_{so} which dominate the effect. In the Boltzmann linear-response transport theory, $\langle ...\rangle$ represents quantum-mechanical averaging constructed from the equilibrium eigenstates of H and with the non-equilibrium steady state entering through an asymmetric redistribution of the occupation numbers of these eigenstates on the Fermi surface due the applied electrical drift and relaxation. Because of this specific form of the asymmetric non-equilibrium charge redistribution with a conserved total number of carriers, the current induced SOT requires broken inversion symmetry terms in H_{so}.[3–8] The OSOT is caused by optical generation and relaxation of photo-carriers without an applied drift (without a defined direction of the

carrier flow) and without conserving the equilibrium number of carriers in dark. Therefore, the broken inversion symmetry in the crystal is not required, and inversion symmetric H_{so} terms plus the time-reversal symmetry breaking exchange-coupling terms are sufficient for observing the OSOT. Note that there is a direct analogy between, on one hand, the broken microscopic inversion symmetry being required in the current induced SOT and not required in the OSOT and, on the other hand, the macroscopic non-uniform magnetic structure being required in the current induced STT and not required in the OSTT.[11]

Ferromagnetic semiconductor (Ga,Mn)As utilized in our experiments is a favorable candidate material for observing the optical spin torque phenomena. The direct-gap GaAs host allows the generation of high density non-equilibrium photo-carriers and the carrier spins interact with ferromagnetic moments on Mn via strong exchange coupling.[16] When the ferromagnetic Mn moments are excited, this can be sensitively detected by probe laser pulses due to large magneto-optical (MO) signals in (Ga,Mn)As. Several groups have reported MO studies of fast laser induced magnetization dynamics in (Ga,Mn)As (see Supplementary information).[17–26] However, the direct search and observation of the optical counterparts of STT and SOT have not been the subject of these studies until the work in Ref. 11 and the work presented in this paper.

The OSTT generated by the circularly polarized light requires large spin lifetime of the injected carriers and, therefore, the weakly spin-orbit coupled photo-electrons in the (Ga,Mn)As conduction band play the key role in this case.[9–11] The OSOT is a fundamentally distinct photomagnetic phenomenon from the OSTT since the helicity-independent excitation does not impart angular momentum. The effect relies on the spin-orbit coupling and, therefore, the non-equilibrium photo-holes generated in (Ga,Mn)As are essential for the OSOT. Our physical picture of the OSOT in (Ga,Mn)As is based on the SOT formalism of Eq. (2) and on the following representation of the non-equilibrium steady state spin-polarization of the photo-holes: The optically injected photo-holes relax towards the hole Fermi energy of the p-type (Ga,Mn)As on a short ($\sim$ 100 fs) timescale[27] and the excitation/relaxation processes create a non-equilibrium excess hole density in the spin-orbit coupled, exchange-split valence band. The increased number of occupied hole states, as compared to the equilibrium state in dark, can generate a non-equilibrium hole spin polarization which is misaligned with the equilibrium orientation of Mn moments. This non-equilibrium photo-hole polarization persists over the timescale of the hole recombination ($\sim$ps) during

which it exerts a torque on the Mn local moments.

The schematic illustration and our experimental observation of the OSOT are shown in Fig. 1. The experimental identification of the OSOT requires to separate this non-thermal photomagnetic effect from the competing thermal excitation mechanism of magnetization dynamics (see Refs. 28,29 and Supplementary information). The absorption of the pump laser pulse leads to photo-injection of electron-hole pairs. The non-radiative recombination of photo-electrons produces a transient increase of the lattice temperature which builds up on the time scale of $\sim$ 10 ps and persists over $\sim$ 1000 ps. This results in a quasi-equilibrium easy-axis (EA) orientation which is tilted from the equilibrium EA. Consequently, Mn moments in (Ga,Mn)As will precess around the quasi-equilibrium EA, as illustrated in Fig. 1a, with a typical precession time of $\sim$ 100 ps given by the magnetic anisotropy fields in (Ga,Mn)As. As discussed in detail below, the EA stays in-plane and the sense of rotation within the plane of the (Ga,Mn)As film with increasing temperature is uniquely defined. In the notation introduced in Fig. 1c, the change of the in-plane angle $\delta\varphi$ of the magnetization during the thermally excited precession can be only positive. The OSOT, illustrated in Fig. 1b, acts during the laser pulse (with a duration of 200 fs) and fades away within the hole recombination time ($\sim$ ps). It causes an impulse tilt of the magnetization which allows us to clearly distinguish the OSOT from the considerably slower thermal excitation mechanism. Moreover, the initial OSOT induced tilt of magnetization can yield precession angles that are inaccessible in the thermally induced magnetization dynamics. This provides another evidence for the OSOT.

Examples of the direct observation of the thermally governed excitation of magnetization at a lower pump pulse intensity of $6I_0$ ($I_0 = 7$ μJcm^{-2}) and of the excitation at a higher intensity of $12I_0$ with a strong contribution from the OSOT are shown in Fig. 1d for a 3% doped (Ga,Mn)As sample (with the Curie temperature $T_c = 77$ K). Note that these dynamical MO signals are independent of the polarization of pump pulses, i.e., they are the same for any orientation of the polarization plane of linearly polarized pump laser pulses and they also correspond to the polarization-independent part of the MO signals extracted by summing the signals induced by σ^+ and σ^- circularly polarized pump pulses (see Supplementary information). The distinct features of the OSOT, described in the previous paragraph, are clearly visible when comparing the two measured trajectories of magnetization angles. This key demonstration has been enabled by the technique which we developed in Ref. 30 and

which translates the measured dynamical MO signals in our pump-and-probe experiments to the time-dependent magnetization vector trajectory. This is done without assuming any theoretical model for the magnetization dynamics and without using any fitting parameter. Our experimental method utilizes different dependences of the polar Kerr effect (PKE) and magnetic linear dichroism (MLD) on the orientation of linear polarization of the probe laser pulses to disentangle the contributions to the MO signal from the out-of-plane and in-plane components of the magnetization motion, respectively. The magnitudes of PKE and MLD coefficients in a particular (Ga,Mn)As sample are determined from static MO experiments in which an external magnetic field is used to align the magnetization in a defined orientation (see Supplementary information). To obtain each point on the trajectory of the magnetization vector excited in the pump-and-probe experiment, we performed a set of measurements of the MO signal as a function of the orientation of the polarization plane of the linearly polarized probe pulse. The dynamical MO measurements in Fig. 1 and below in Fig. 2 were performed at zero magnetic field; prior to the experiment, the magnetization was aligned with the EA. (For more details on the experimental technique see Refs. 11,30 and Supplementary information.)

Detailed measurements for several intensities of the pump pulses are shown in Fig. 2. The key characteristics of the magnetization dynamics at low intensities I_0 and $6I_0$ reflect the strong thermal excitation mechanism described in Fig. 1a. In equilibrium, the EA in the 3% Mn doped sample is tilted by approximately 10° from the [010] ($\varphi = 90°$) crystal axis towards the [$\bar{1}$10] ($\varphi = 135°$) in-plane diagonal direction as a result of the competing biaxial and in-plane uniaxial anisotropy fields.[31] With increasing temperature, the easy-axis rotates further towards the [$\bar{1}$10] direction. This is because the uniaxial anisotropy component scales with magnetization as $\sim M^2$ while the biaxial component scales as $\sim M^4$ and, therefore, the uniaxial anisotropy gets enhanced relative to the biaxial anisotropy with increasing temperatures. This expected EA rotation is confirmed by independent SQUID measurements and microscopic calculations based on the exchange-split, Kohn-Luttinger representation of the Hamiltonian H for (Ga,Mn)As,[16,32] shown in Fig. 3a,b. (Note that the model Hamiltonian we use is consistent with ab initio density functional calculations and X-ray photoemission measurements[33] showing that the spectral weight of Mn d-states has a maximum around 3-4 eV below the Fermi energy, the Mn d-states are hybridized with the host valence band orbitals continuously up to the Fermi energy, and no detached impurity band[34] from the

valence band is observed.) The amplitude of the precession angles for the intensity $6I_0$ (Fig. 2b) is larger than for the intensity I_0 (Fig. 2a). This is consistent with a larger increase of the transient temperature (and corresponding larger tilt of the quasi-equilibrium EA) for the larger pump pulse intensity. We have deduced the temperature increase due to pump pulses from the measured precession frequencies which reflect the temperature dependent magnetocrystalline anisotropy energies. In Fig. 3c we plot the dependence of the precession frequency on the base sample temperature at low excitation intensity I_0 and on the laser intensity at low base temperature of 15 K. From the comparison of these two measurements we infer the magnitude of the transient temperature change as a function of the laser intensity. (Note that consistent temperature vs. intensity calibration is obtained from the comparison of the intensity dependence of the pump-induced demagnetization and the temperature dependence of the remanent magnetization measured by SQUID.)

Fig. 3c confirms a sizable difference in transient temperatures for intensities I_0 and $6I_0$. Remarkably, the heating of the sample by the laser pulses saturates at approximately $10I_0$, as seen from Fig. 3c (see also Supplementary information for more details). The measured trajectories of the dynamical magnetization vector, however, show dramatic differences below and above $10I_0$. The impulse tilt and precession angles inaccessible by the thermal excitations, seen in Figs. 2c,d for intensities $12I_0$ and $30I_0$, were already pointed out in Fig. 1 as key signatures of the OSOT. The complete saturation of the transient temperature increase at $10I_0$ provides another confirmation that a distinct non-thermal mechanism must strongly contribute to the magnetization dynamics at higher pump pulse intensities. Note that the thermal mechanism, albeit saturated above $10I_0$, is still visible together with the OSOT signatures in the high pump intensity data. The magnetization does not relax to the original state on the timescale of the measurements shown in Fig. 2 but to the quasi-equilibrium EA which is tilted from the equilibrium EA due to the transient increase of temperature. This quasi-equilibrium thermal tilt strongly increases from I_0 to $6I_0$, however, no further increase is detected at $12I_0$ and $30I_0$. This is consistent with the independently inferred saturation of the thermal mechanism around $10I_0$.

The connection between the OSOT and photo-carrier generation is evidenced in Fig. 3d. Here we show the observed change in the measured reflectivity of the (Ga,Mn)As film which correlates with the number of generated photo-carriers (see Supplementary information). The pump-induced change of the index of refraction is linear in pump-pulse intensity up to

$\approx 25I_0$ after which it starts to saturate. It means that, unlike the transient temperature, the number of generated photo-carriers keeps increasing with increasing pump pulse intensity above $10I_0$. The concentration of photo-injected carriers can be estimated from the laser spot size, photon energy, and absorption and reflection coefficients of the sample. For the higher intensity measurements, the obtained photo-carrier density is of the order of $\sim 10^{19}$ cm^{-3}.

In Fig. 3b we show that the equilibrium EA is sensitive to the hole density variations[35,36] and that the sense of the tilt of the EA with increasing hole density can be opposite than in the case of the temperature increase. As explained in detail below, Fig. 3b provides the clue why the instantaneous out-of-plane component of the tilt of the magnetization due to the OSOT is opposite than the initial out-of-plane component of the precessing magnetization around the thermally excited quasi-equilibrium EA at lower pump intensities. The relation between the OSOT and the magnetocrystalline anisotropy field can be microscopically demonstrated using the OSOT formalism of Eq. (2) and, similar to the theory of the current induced SOT, assuming in $\vec{s} = \langle \hat{s} \rangle$ the quantum-mechanical averaging constructed from the equilibrium eigenstates of H. The non-equilibrium steady state differs from the equilibrium state in dark in that the distribution function has a shifted Fermi level corresponding to the extra density of the photo-holes. In this approximation, the OSOT is determined by the hole density dependent magnetocrystalline anisotropy field $\vec{H}_{an}$ since,[5]

$$\begin{aligned} \vec{H}_{an} &= -\frac{\partial}{\partial \vec{M}} \sum_a \int d\mathbf{k} \epsilon_{a,\vec{k}} f_{a,\vec{k}} = -\sum_a \int d\vec{k} \langle a, \vec{k}| \frac{\partial H}{\partial \vec{M}} |a, \vec{k}\rangle f_{a,\vec{k}} \\ &= -\sum_a \int d\vec{k} \langle a, \vec{k}| J\hat{s} |a, \vec{k}\rangle f_{a,\vec{k}} = -J\vec{s}. \end{aligned} \tag{3}$$

Here $\epsilon_{a,\vec{k}}$ and $f_{a,\vec{k}}$ are the eigenenergy of H and Fermi distribution function, respectively, labeled by the band and wavevector index. Consistent with the in-plane orientation of the EA, we obtain that the out-of-plane transverse component of the anisotropy field, $\vec{H}_{an,\theta} = -J\vec{s}_\theta = 0$ for any in-plane $\vec{M}$ and any considered hole density. The in-plane transverse component, $\vec{H}_{an,\varphi} = -J\vec{s}_\varphi$, is zero when $\vec{M}$ is aligned with the EA at a given hole density and non-zero for other orientations of $\vec{M}$ at the same hole density. Since the EA orientation is sensitive to the hole density, as shown in Fig. 3b, $\vec{H}_{an,\varphi}$ for a given orientation of $\vec{M}$ can change when the hole density is increased by the photo-excitation (see Supplementary information). The sign of the calculated $\vec{H}_{an,\varphi}$ is consistent with the sense of the initial magnetization tilt observed in experiments governed by the OSOT. The amplitudes of $J\vec{s}_\varphi$,

obtained from the calculated hole density dependent anisotropy fields, are $\sim \mu$eV which is about 10 times smaller than the experimental strength of OSOT fields inferred form the measured out-of-plane tilts of the magnetization. The exchange-split, Kohn-Luttinger model is known to underestimate the anisotropy fields in the lower doped ferromagnetic (Ga,Mn)As samples.[32] Considering this general limitation of the model Hamiltonian theory we can conclude that the calculations confirm our experimental observation of the OSOT.

In the OSOT calculations we have considered the exchange-split Kohn-Luttinger Hamiltonian of (Ga,Mn)As which has been consistently used in numerous previous studies to model the magnetocrystalline anisotropy and a variety of other relativistic magnetic, magneto-transport, and magneto-optical effects in (Ga,Mn)As.[16] Note that we have neglected effects of photo-carrier excitations by linearly-polarized light that are associated with broken inversion symmetry.[37,38] Corresponding additional terms in H_{so} may occur in bulk III-V semiconductors due to lattice strains. However, we observe the largest OSOT in our annealed 3% Mn-doped (Ga,Mn)As grown on a GaAs substrate which has a relatively small lattice-matching strain of 10^{-3}. The strain is enhanced in higher doped samples, reaching 0.005 in the 9% Mn-doped sample, however, the OSOT decreases with increasing doping, as shown below. It confirms that the strain related broken inversion terms in H_{so} do not play a significant role in the OSOT in our (Ga,Mn)As samples.

In the remaining paragraphs we discuss the effects of controlling micromagnetic parameters of (Ga,Mn)As on the observed magnetization dynamics. In particular we demonstrate, that controlling the micromagnetic parameters allows us to eliminate the thermal mechanism while still detecting the OSOT. One of the pronounced features of the measurements in Fig. 2, omitted in the previous discussion, is the enhanced damping of the magnetization precession at higher pump pulse intensities. The higher excitation intensity causes higher demagnetization and, correspondingly, a stronger inhomogeneous ferromagnetic resonance damping. In Fig. 4 we demonstrate that the damping due to magnetic inhomogeneities is suppressed at applied magnetic fields along the easy-axis (at higher precession frequencies), as previously established in the systematic MO study of micromagnetic parameters of (Ga,Mn)As[31] and as is typical for MO ferromagnetic resonance measurements in high crystal quality ferromagnets (see Supplementary information for more details). Apart from confirming that weaker damping of the precession is recovered when performing our experiments at non-zero external magnetic fields, the experiments have another direct implication

for our OSOT study. Applied fields of the order of 10's mT, which is comparable to the in-plane anisotropy fields,[31] not only reduce the damping but also gradually suppress the quasi-equilibrium tilt of the EA induced by the transient temperature increase (see Figs. 4a-c). The dominantly out-of-plane OSOT is, however, much less affected by the applied field since the out-of-plane anisotropy field is an order of magnitude larger than the in-plane anisotropies.[31] At 100 mT applied field, we then still observe the impulse tilt of the magnetization due to the OSOT while the thermal effect is already diminished (see Figs. 4d).

Controlling the rich doping dependence of the micromagnetic parameters of our high quality (Ga,Mn)As materials[31] allows us to eliminate the thermal mechanism even at zero applied field, as demonstrated in Fig. 5. The idea of these measurements is as follows: Increasing the temperature always tilts the EA towards the in-plane diagonal ($\varphi = 135°$ in our notation). Consistent with the systematic measurements of the anisotropy fields in our series of GaMnAs materials,[31] we found that the base temperature EA of the 3% Mn doped sample (with $T_c = 77$ K) is at 100° and of a 5% sample (with $T_c = 132$ K) at 121°, while for a 7% Mn-doped sample (with $T_c = 159$ K) and a 9% Mn-doped sample (with $T_c = 179$ K) the base temperature zero-field EA is already aligned with the $\varphi = 135°$ in-plane diagonal. As shown in Fig. 5a, we indeed again observe a clear thermal effect in the 5% sample. The precession trajectory is less damped and more elliptic, as compared to the 3% Mn-doped samples (see Fig. 2b). This is consistent with the systematic doping trends in the (Ga,Mn)As micromagnetic parameters, namely with the reduction of the Gilbert damping and the enhancement of the out-of-plane anisotropy field in the higher doped samples.[31] In the 7% and 9% Mn-doped samples the thermal effect is completely suppressed (see Figs. 5b-d) since higher temperature can only strengthen the uniaxial anisotropy along the diagonal and, therefore, the EA does not tilt from the 135° angle when the temperature is increased by the pump pulse. Remarkably, we still observe the impulse out-of-plane tilts in the 7% and 9% samples, i.e., we observe magnetization excitation which we can ascribe entirely to the OSOT. Also consistent with expectations, the amplitude of OSOT increases with increasing pump intensity (see Figs. 5c,d), while the thermal mechanism is absent independent of the pump intensity, and the OSOT in these highly doped materials is significantly weaker than in the low doped 3% sample.

To conclude, we have reported an experimental study of magnetization dynamics in (Ga,Mn)As induced by helicity-independent laser excitations. We have performed several

complementary experiments which identified the presence of a non-thermal mechanism of the photo-carriers exerting a torque on the magnetization. Since the helicity-independent excitations do not impart angular momentum and since thermal effects have been separated out, the observed non-thermal photomagnetic torque originates from spin-orbit coupling effects of the photo-carriers. This makes the OSOT fundamentally distinct from the previously reported non-relativistic OSTT in which angular momentum of the circularly polarized light is transferred via photo-carrier spins to the magnetization. Our work demonstrates the possibility to study SOTs on the short time-scales achievable by the optical pump-and-probe experimental technique. The relativistic OSOT effects should be observable in other systems including, e.g., antiferromagnetic semiconductors which unlike their ferromagnetic counterparts can have magnetic transition temperatures well above room temperature.[39] It is well established that magnetocrystalline anisotropies are equally present in spin-orbit coupled antiferromagnets as in ferromagnets and recently it has been demonstrated that the spin-orbit coupling induced anisotropic magnetotransport effects can be also strong in antiferromagnets.[40] OSOT belongs to this family of relativistic effects and its exploration in antiferromagnets may open another novel avenue of optical spin torque research beyond (Ga,Mn)As.

---

[1] D. Ralph and M. Stiles and S. Bader (editors). Current perspectives: Spin transfer torques. *J. Magn. Magn. Mater.* **320**, 1189 (2008).

[2] Brataas, A., Kent, A. D. & Ohno, H. Current-induced torques in magnetic materials. *Nature Mater.* **11**, 372 (2012).

[3] Manchon, A. & Zhang, S. Theory of nonequilibrium intrinsic spin torque in a single nanomagnet. *Phys. Rev.* **B 78**, 212405 (2008).

[4] Manchon, A. & Zhang, S. Theory of spin torque due to spin-orbit coupling. *Phys. Rev.* **B 79**, 094422 (2009).

[5] Garate, I. & MacDonald, A. H. Influence of a transport current on magnetic anisotropy in gyrotropic ferromagnets. *Phys. Rev.* **B 80**, 134403 (2010). arXiv:0905.3856.

[6] Chernyshov, A. *et al.* Evidence for reversible control of magnetization in a ferromagnetic material by means of spin-orbit magnetic field. *Nature Phys.* **5**, 656 (2009). arXiv:0812.3160.

[7] Miron, I. M. *et al.* Current-driven spin torque induced by the Rashba effect in a ferromagnetic metal layer. *Nature Mat.* **9**, 230 (2010).

[8] Fang, D. *et al.* Spin-orbit driven ferromagnetic resonance: A nanoscale magnetic characterisation technique. *Nature Nanotech.* **6**, 413 (2011). arXiv:1012.2397.

[9] Fernández-Rossier, J., Núñez, A. S., Abolfath, M. & MacDonald, A. H. Optical spin transfer in ferromagnetic semiconductors (2003). arXiv:cond-mat/0304492.

[10] Núñez, A. S., Fernández-Rossier, J., Abolfath, M. & MacDonald, A. H. Optical control of the magnetization damping in ferromagnetic semiconductors. *J. Magn. Magn. Mater.* **272-276**, 1913 (2004).

[11] Nemec, P. *et al.* Experimental observation of the optical spin transfer torque. *Nature Phys.* **8**, 414 (2012). arXiv:1201.1436.

[12] Berger, L. Exchange interaction between ferromagnetic domain wall and electric current in very thin metallic films. *J. Appl. Phys.* **55**, 1954 (1984).

[13] Slonczewski, J. C. Current-driven excitation of magnetic multilayers. *J. Magn. Magn. Mater.* **159**, L1 (1996).

[14] Berger, L. Emission of spin waves by a magnetic multilayer traversed by a current. *Phys. Rev.* **B 54**, 9353 (1996).

[15] Chappert, C., Fert, A. & Dau, F. N. V. The emergence of spin electronics in data storage. *Nature Mat.* **6**, 813 (2007).

[16] Jungwirth, T., Sinova, J., Mašek, J., Kučera, J. & MacDonald, A. H. Theory of ferromagnetic (III,Mn)V semiconductors. *Rev. Mod. Phys.* **78**, 809 (2006). arXiv:cond-mat/0603380.

[17] Oiwa, A., Takechi, H. & Munekata, H. Photoinduced magnetization rotation and precessional motion of magnetization in ferromagnetic (Ga,Mn)As. *J. Supercond. Nov. Magn.* **18**, 9 (2005).

[18] Wang, D. M. *et al.* Light-induced magnetic precession in (Ga,Mn)As slabs: Hybrid standing-wave damon-eshbach modes. *Phys. Rev.* **B 75**, 233308 (2007). arXiv:cond-mat/0609646.

[19] Takechi, H., Oiwa, A., Nomura, K., Kondo, T. & Munekata, H. Light-induced precession of ferromagnetically coupled Mn spins in ferromagnetic (Ga,Mn)As. *Phys. Status Solidi C* **3**, 4267 (2007).

[20] Qi, J. *et al.* Coherent magnetization precession in GaMnAs induced by ultrafast optical excitation. *Appl. Phys. Lett.* **91**, 112506 (2007). arXiv:0706.4270.

[21] Qi, J. *et al.* Ultrafast laser-induced coherent spin dynamics in ferromagnetic $Ga_{1-x}Mn_xAs$/GaAs

structures. *Phys. Rev.* **B 79**, 085304 (2009).

[22] Rozkotova, E. *et al.* Light-induced magnetization precession in GaMnAs. *Appl. Phys. Lett.* **92**, 122507 (2008). arXiv:0802.2043.

[23] Rozkotová, E. *et al.* Coherent control of magnetization precession in ferromagnetic semiconductor (Ga,Mn)As. *Appl. Phys. Lett.* **93**, 232505 (2008). arXiv:0808.3738.

[24] Hashimoto, Y. & Munekata, H. Coherent manipulation of magnetization precession in ferromagnetic semiconductor (Ga,Mn)As with successive optical pumping. *Appl. Phys. Lett.* **93**, 202506 (2008). arXiv:0810.3728.

[25] Hashimoto, Y., Kobayashi, S. & Munekata, H. Photoinduced precession of magnetization in ferromagnetic (Ga,Mn)As. *Phys. Rev. Lett.* **100**, 067202 (2008).

[26] Kobayashi, S., Suda, K., Aoyama, J., Nakahara, D. & Munekata, H. Photo-induced precession of magnetization in metal/(Ga,Mn)As systems. *IEEE Trans. Magn.* **46**, 2470 (2010).

[27] Yildirim, M. *et al.* Interband dephasing and photon echo response in gamnas. *Appl. Phys. Lett.* **101**, 062403 (2012).

[28] Wang, J. *et al.* Ultrafast magneto-optics in ferromagnetic III-V semiconductors. *J. Phys.: Condens. Matter* **18**, R501 (2006).

[29] Kirilyuk, A., Kimel, A. V. & Rasing, T. Ultrafast optical manipulation of magnetic order. *Rev. Mod. Phys.* **82**, 2731 (2010).

[30] Tesarova, N. *et al.* Direct measurement of the three dimensional magnetization vector trajectory in GaMnAs by a magneto-optical pump-and-probe method. *Appl. Phys. Lett.* **102403**, 100 (2012). arXiv:1201.1213.

[31] Nemec, P. *et al.* Establishing micromagnetic parameters of ferromagnetic semiconductor (Ga,Mn)As (2012). arXiv:1207.0310.

[32] Zemen, J., Kucera, J., Olejnik, K. & Jungwirth, T. Magneto crystalline anisotropies in (Ga,Mn)As: a systematic theoretical study and comparison with experiment. *Phys. Rev.* **B 80**, 155203 (2009). arXiv:0904.0993.

[33] Gray, A. X. *et al.* Bulk electronic structure of the dilute magnetic semiconductor GaMnAs through hard x-ray angle-resolved photoemission. *Nature Mater.* **11**, 957 (2012).

[34] Ohya, S., Takata, K. & Tanaka, M. Nearly non-magnetic valence band of the ferromagnetic semiconductor GaMnAs. *Nature Phys.* **7**, 342 (2011).

[35] Chiba, D. *et al.* Magnetization vector manipulation by electric fields. *Nature* **455**, 515 (2008).

[36] Owen, M. H. S. *et al.* Low voltage control of ferromagnetism in a semiconductor p-n junction. *New J. Phys.* **11** (2009). arXiv:0807.0906.

[37] Ganichev, S. D. *et al.* Zero-bias spin separation. *Nature Phys.* **2**, 609 (2006). arXiv:cond-mat/0605556.

[38] Tarasenko, S. A. Optical orientation of electron spins by linearly polarized light. *Phys. Rev.* **B 72**, 113302 (2005).

[39] Jungwirth, T. *et al.* Demonstration of molecular beam epitaxy and a semiconducting band structure for I-Mn-V compounds. *Phys. Rev.* **B 83**, 035321 (2011). arXiv:1007.0177.

[40] Park, B. G. *et al.* A spin-valve-like magnetoresistance of an antiferromagnet-based tunnel junction. *Nature Mat.* **10**, 347 (2011). arXiv:1011.3188.

Corresponding author

Correspondence and requests for materials should be addressed to Petr Němec, nemec@karlov.mff.cuni.cz, Charles University in Prague, Faculty of Mathematics and Physics, Ke Karlovu 3, 121 16 Prague 2, Czech Republic.

Acknowledgment

We acknowledge fruitful discussions with Allan H. MacDonald, Jairo Sinova, and Jorg Wunderlich, and support from the EU ERC Advanced Grant No. 268066 and FP7-215368 SemiSpinNet, from the EPSRC Grant No. EP/H029257/1, from the Grant Agency of the Czech Republic Grant No. 202/09/H041 and P204/12/0853, from the Charles University in Prague Grant No. SVV-2012-265306 and No. 443011, and from the Academy of Sciences of the Czech Republic Preamium Academiae.

Author contributions

Sample preparation: V.N., K.O.; experiments and data analysis: N.T., P.N., E.R., T.Ja., D.B., P. M., K.O, T.Ju.; data modeling: P.N., F.T.; theory: J.Z., T.Ju.; writing: T.Ju., P.N.; project planning: P.N., T.Ju.

Additional information

Supplementary information accompanies this paper on www.nature.com/naturephysics. Reprints and permissions information is available online at http://npg.nature.com/reprintsandpermissions. Correspondence and requests for materials should be addressed to P.N.

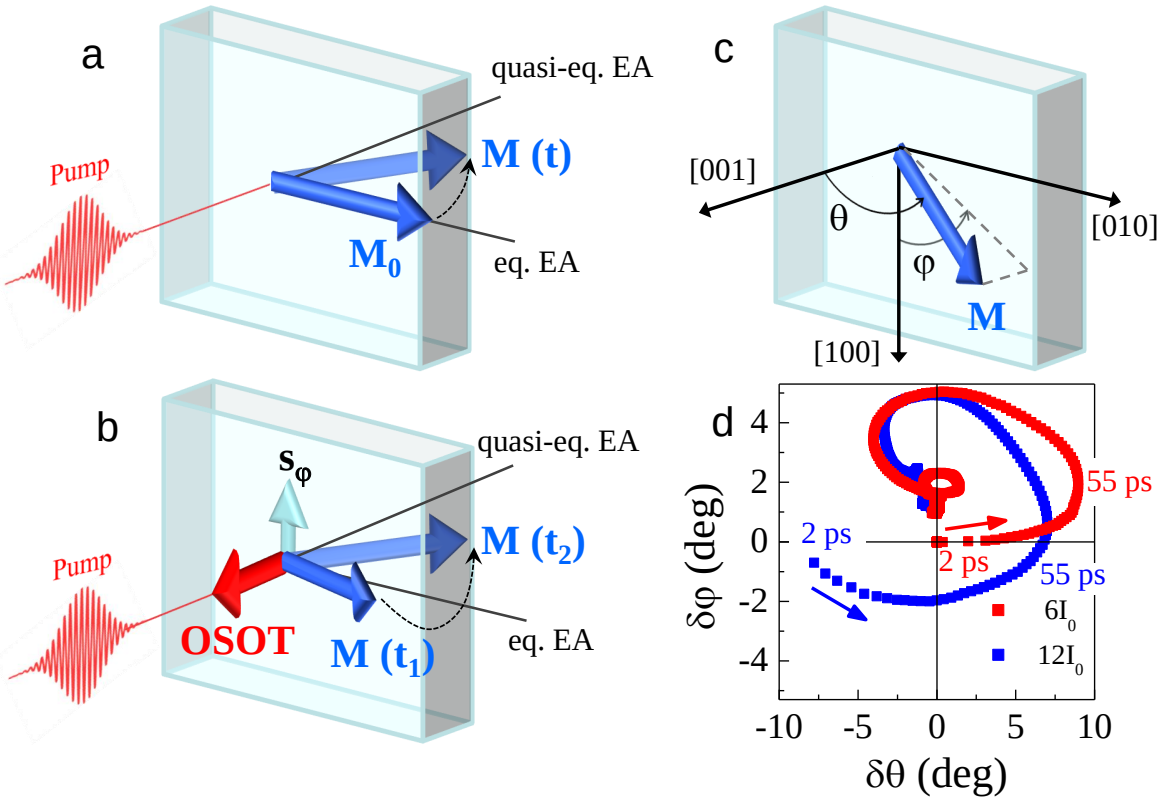

FIG. 1: **Schematic illustration and experimental observation of the optical spin-orbit torque. a,** Schematic illustration of the thermally excited precession of magnetization $\mathbf{M}(t)$ around the transient quasi-equilibrium easy axis (EA). $\mathbf{M}_0$ is the magnetization vector aligned with the in-plane equilibrium EA before the pump pulse. **b,** Schematic illustration of the OSOT induced by the in-plane transverse component $\mathbf{s}_\varphi$ of the non-equilibrium hole spin polarization. On the time-scale of magnetization precession, OSOT causes an instantaneous tilt of the magnetization $\mathbf{M}(t_1)$ which allows us to clearly distinguish OSOT from the considerably slower thermal excitation mechanism. The initial OSOT induced tilt of magnetization can yield precession angles that are inaccessible in the thermally induced magnetization dynamics. **c,** Definition of the coordinate system. **d,** Time evolution of the magnetization vector measured in a (Ga,Mn)As material with nominal Mn-doping $x = 3\%$. The direction of the time increase is depicted by arrows. Magnetization tilt angles $\delta\varphi$ and $\delta\theta$ are measured with respect to the equilibrium EA. Sample base temperature before pump pulse was 15 K and experiments were performed at zero magnetic field. At lower pump intensity $6I_0$ ($I_0 = 7$ μJcm^{-2}) the precession is induced thermally while at $12I_0$ the OSOT induced initial tilt is observed.

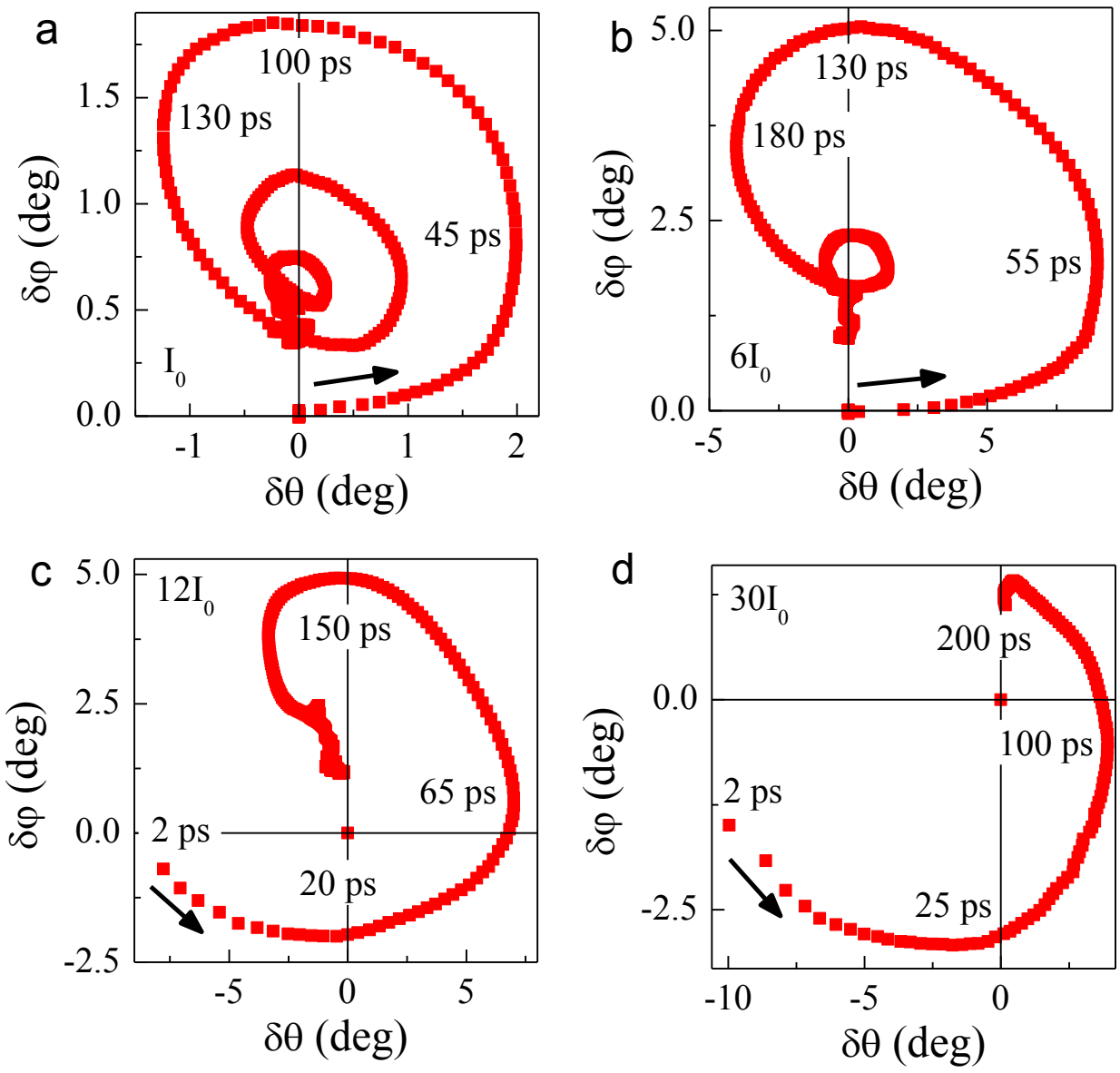

FIG. 2: **Direct experimental reconstruction of the magnetization trajectory from MO signals. a-d,** Time evolution of the magnetization vector measured in the 3% Mn-doped (Ga,Mn)As at pump intensities $I_0 - 30I_0$. The plotted data correspond to time delays between pump and probe pulses in steps of 2 ps. Sample base temperature before pump pulse was 15 K and experiments were performed at zero magnetic field.

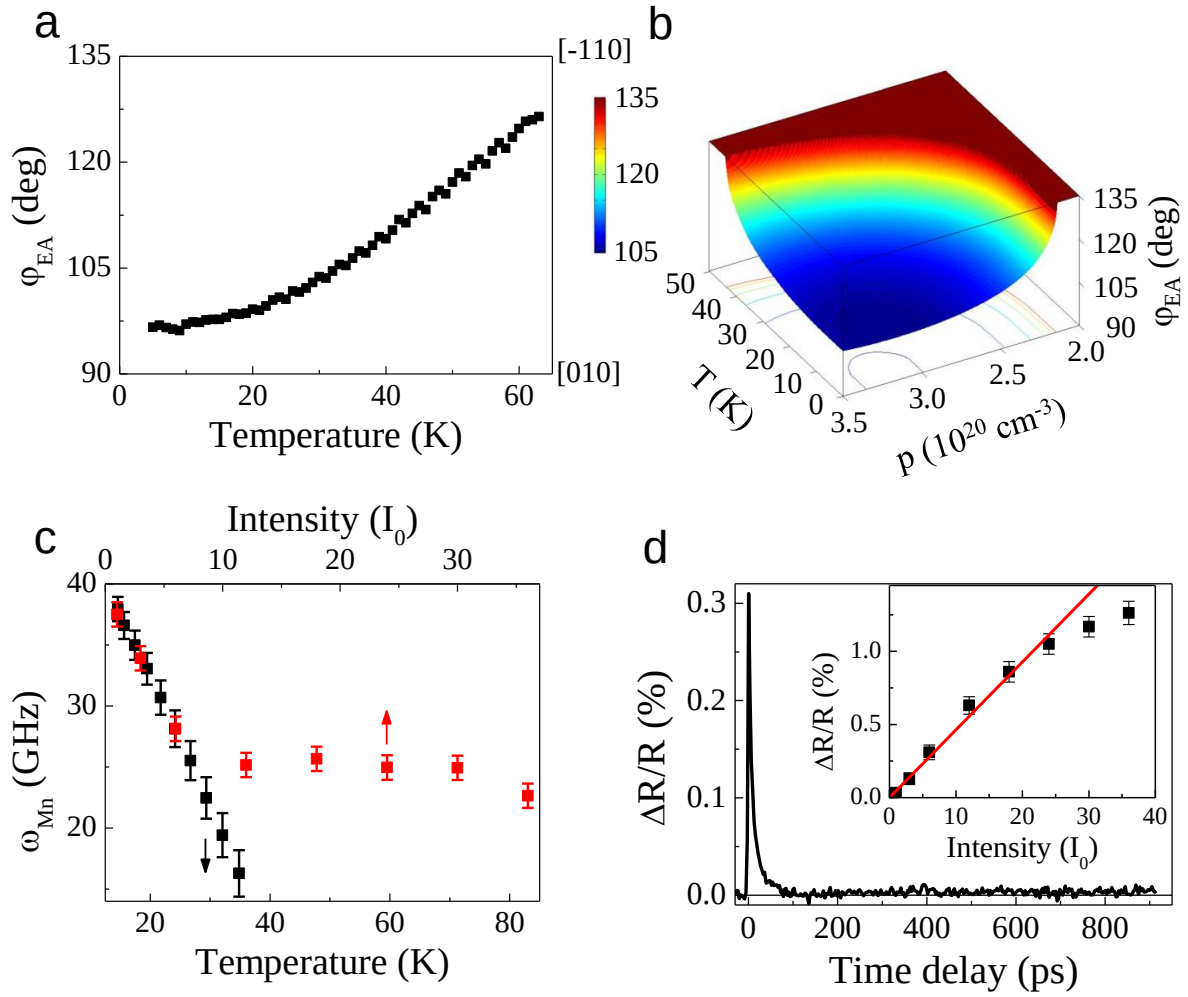

FIG. 3: **Characterization of the 3% Mn-doped (Ga,Mn)As. a,** Temperature dependence of the equilibrium EA orientation determined from SQUID magnetization measurements. Consistent EA orientations are inferred from the MO experiments. **b,** Microscopic calculations of the temperature and hole density dependent EA orientation. **c,** Frequency of precessing Mn moments measured at zero magnetic field as a function of the base temperature at low excitation intensity I_0, and as a function of the pump intensity at low base temperature of 15 K. **d,** Dynamics of pump-induced reflectivity change at intensity $6I_0$. Inset shows the intensity dependence of the initial reflectivity change at base temperature of 15 K (line depicts a linear dependence).

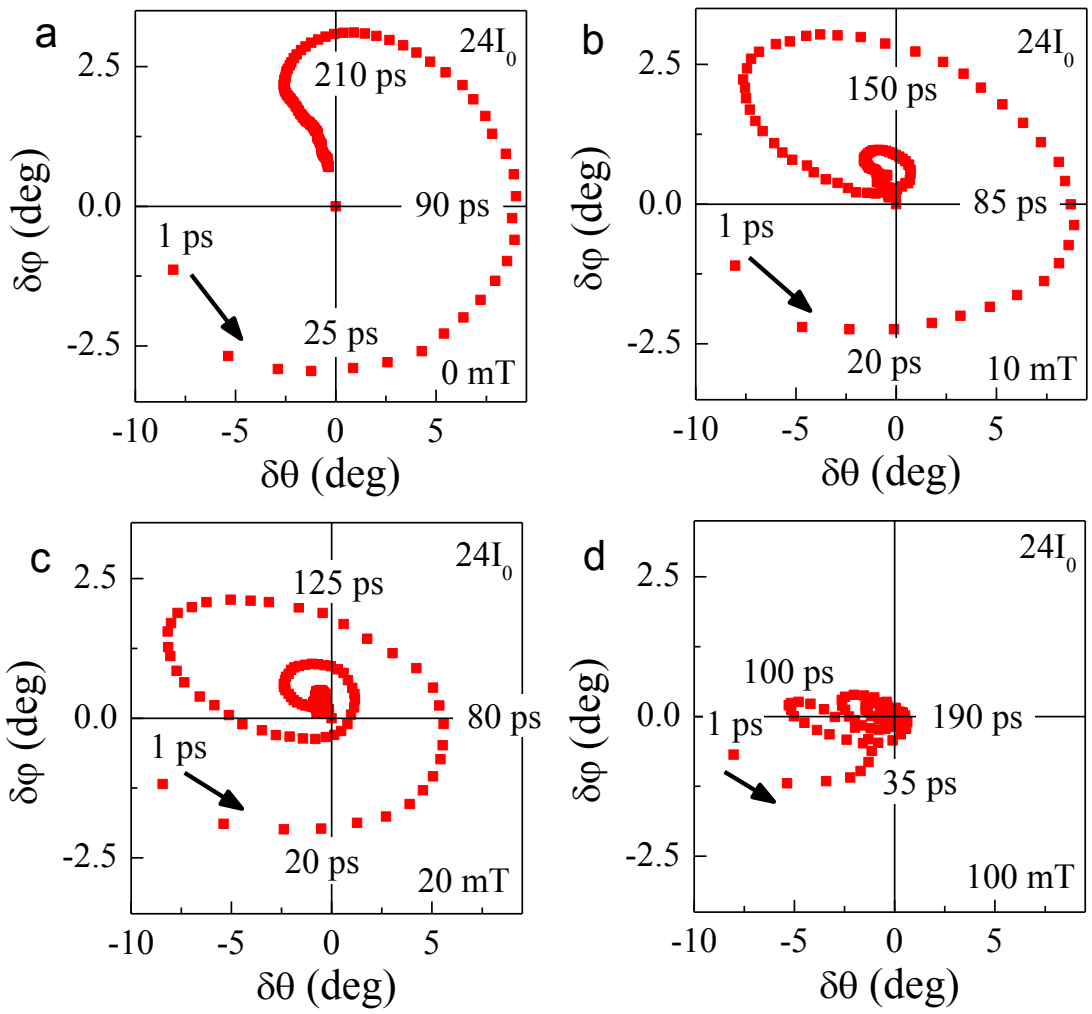

FIG. 4: **Suppression of the damping and of the thermal excitation mechanism by magnetic field a-d,** Influence of the external magnetic field of amplitude 0-100 mT applied along the easy axis in the 3% Mn-doped (Ga,Mn)As on the magnetization trajectory at pump intensity of $24I_0$ and sample base temperature 15 K.

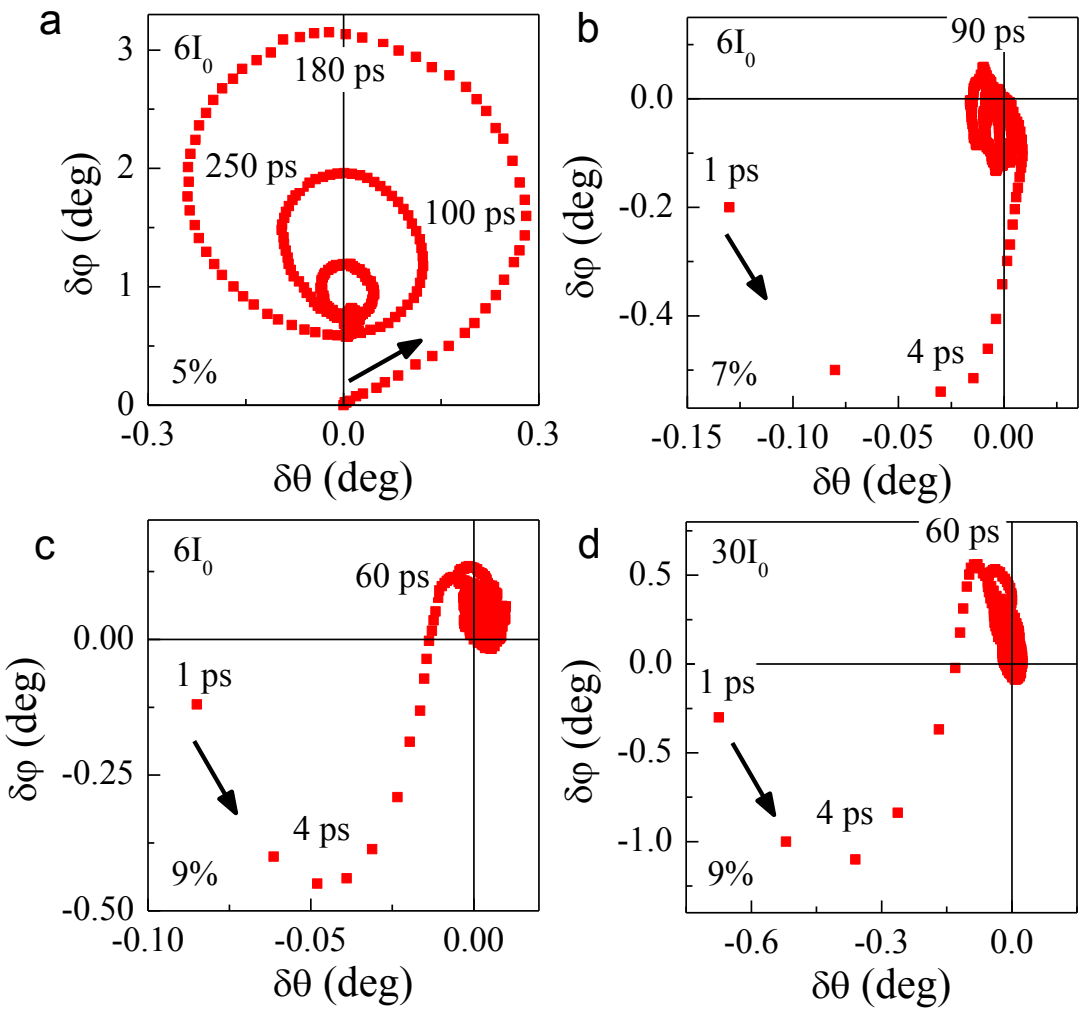

FIG. 5: **Suppression of the thermal excitation mechanism at higher Mn-dopings a-c,** Magnetization trajectory in (Ga,Mn)As with 5, 7, and 9% Mn-doping at pump intensity of $6I_0$. **d,** Magnetization trajectory in the 9% doped (Ga,Mn)As at pump intensity of $30I_0$. Sample base temperature before pump pulse was 15 K and experiments were performed at zero magnetic field.

APPENDIX 8

Authors: P. Němec, V. Novák, N. Tesařová, E. Rozkotová, H. Reichlová, D. Butkovičová, F. Trojánek, K. Olejník, P. Malý, R. P. Campion, B. I. Gallagher, J. Sinova and T. Jungwirth

Title: Establishing micromagnetic parameters of ferromagnetic semiconductor (Ga,Mn)As

Journal: accepted in Nature Communications

Preprint server: http://arxiv.org/abs/1207.0310

The essential role of carefully optimized synthesis for elucidating intrinsic material properties of (Ga,Mn)As

P. Němec,[1] V. Novák,[2] N. Tesařová,[1] E. Rozkotová,[1] H. Reichlová,[2,1]
D. Butkovičová,[1] F. Trojánek,[1] K. Olejník,[2] P. Malý,[1] R. P. Campion,[3]
B. L. Gallagher,[3] Jairo Sinova,[4,2] and T. Jungwirth[2,3]

[1]*Faculty of Mathematics and Physics, Charles University in Prague, Ke Karlovu 3, 121 16 Prague 2, Czech Republic*

[2]*Institute of Physics ASCR, v.v.i., Cukrovarnická 10, 162 53 Praha 6, Czech Republic*

[3]*School of Physics and Astronomy, University of Nottingham, Nottingham NG7 2RD, United Kingdom*

[4]*Department of Physics, Texas A&M University, College Station, TX 77843-4242, USA*

(Dated: December 11, 2012)

Abstract

(Ga,Mn)As is at the forefront of spintronics research exploring the synergy of ferromagnetism with the physics and the technology of semiconductors. However, the electronic structure of this model spintronics material has been debated and the systematic and reproducible control of the basic micromagnetic parameters and semiconducting doping trends has not been established. In this paper we show that seemingly small departures from the individually optimized synthesis protocols yield non-systematic doping trends, extrinsic charge and moment compensation, and inhomogeneities which conceal intrinsic properties of (Ga,Mn)As. On the other hand, we demonstrate reproducible, well controlled, and microscopically understood semiconducting doping trends and micromagnetic parameters in our series of carefully optimized epilayers. Hand-in-hand with the optimization of the material synthesis we have developed experimental capabilities based on the magneto-optical pump-and-probe method which allowed us to simultaneously determine the magnetic anisotropy, Gilbert damping, and spin stiffness constants from one consistent set of measured data.

PACS numbers: 75.50.Pp,75.30.-m,75.70.Ak

Under equilibrium growth conditions the incorporation of magnetic Mn ions into GaAs is limited to approximately 0.1%. To circumvent the solubility problem a non-equilibrium, low-temperature molecular-beam-epitaxy (LT-MBE) technique was employed which led to first successful growths of (Ga,Mn)As ternary alloys with more than 1% Mn and to the discovery of ferromagnetism in these materials.[1–4] The compounds qualify as ferromagnetic semiconductors to the extent that their magnetic and other properties can be altered by the usual semiconductor electronics engineering variables, such as doping, electric fields, or light. (Ga,Mn)As has become a test-bed material for spintronic research, in particular for exploring known and discovering new magneto-transport and magneto-optical phenomena. (For more details on (Ga,Mn)As spintronics research see Supplementary Discussion.)

In ferromagnetic (Ga,Mn)As, the theory of spin-orbit coupled GaAs bands modified by the exchange splitting and alloying effects of randomly distributed Mn_{Ga} acceptors/local-moments represents a common basis for describing its semiconducting and ferromagnetic properties.[5] The kinetic-exchange model implementation of this valence band theory and the microscopic tight-binding Anderson approach or *ab-initio* density functional theory can all be shown to be mutually consistent on the level of atomic and orbital resolved band structure.[6] (For more details on the theory of (Ga,Mn)As see Supplementary Figures S1-S3, and Supplementary Discussion.)

In a recurring alternative proposal, the Fermi level in ferromagnetic materials with $\sim 10^{20} - 10^{21}$ cm^{-3} Mn-acceptor densities is assumed to still reside in a narrow impurity band detached from the valence band, i.e., the band structure keeps the form closely reminiscent of a single isolated Mn_{Ga} impurity level.[7–9] Several phenomenological variants of the impurity band model have been proposed whose assumed spectroscopic characteristics are, however, mutually inconsistent and have not been recreated from microscopic band structure theories.[6] Since to date no framework has been introduced which would allow to test the validity of the impurity band model by comparing microscopic atomic orbital based theory calculations to experiment it is primarily the experimental findings which have served as a basis for postulating the impurity band picture. A common feature of these experimental reports is the limited attention paid to the details of the synthesis of this highly non-equilibrium alloy.[7,9] As we show in this paper, careful material optimization is, however, of central importance. Small departures from optimized sample synthesis obscure the doping trends and experimental determination of intrinsic micromagnetic parameters of the

material. The justification of the impurity band picture by the experiments in unoptimized materials is therefore unreliable. This leaves the impurity band models without an adequate microscopic theory or experimental support. On the other hand, the valence band model is linked in a transparent way to density functional or tight-binding-Anderson microscopic theories, as pointed out above. Simultaneously, the microscopically justified theory provides consistent predictions for the broad range of semiconducting doping trends and micromagnetic parameters we report below on the entire series of the optimized (Ga,Mn)As materials. Our work, therefore, leads to the conclusion that there is no physics grounds for the "battle of the bands"[10] in (Ga,Mn)As.

Results

Optimized synthesis of (Ga,Mn)As epilayers. The essential importance of the optimization of the (Ga,Mn)As synthesis is illustrated in Fig. 1 where we plot, side by side, basic electrical and magnetic characteristics of two medium, 7% nominally Mn-doped epilayers. (The determination of the nominal Mn concentration in the as-grown epilayers is detailed in the Supplementary Discussion.) The left column figures (Figs. 1a-c) show data measured on a material which we prepared under carefully optimized conditions for the given nominal Mn-doping. The sample has sharp Curie point singularities in magnetization and electrical transport typical of uniform, high-quality itinerant ferromagnets (Fig. 1a).[11] Magnetization precession damping factor and spin-wave resonances (SWRs) obtained from magneto-optical (MO) measurements (Figs. 1b,c) confirm the high magnetic quality of the material. As we discuss in detail below, the initial decrease of the damping factor with frequency followed by a frequency independent part (Fig. 1b) is typical of uniform ferromagnets and allows us to accurately infer the intrinsic Gilbert damping constant.[12] Similarly, the observed Kittel SWR modes of a uniform ferromagnet (Fig. 1c) allow us to measure accurately the magnetic anisotropy and spin stiffness parameters of (Ga,Mn)As, as detailed below.

The right column data (Figs. 1d-f) were measured on a 7% Mn-doped epilayer differing from the sample of the left column in only one of the synthesis parameters not being optimized. As we discuss below, the stoichiometry, substrate growth temperature, postgrowth annealing temperature and time, and epilayer thickness are among the key synthesis parameters. (For more details on our materials synthesis see Methods.) All these parameters were equally carefully optimized in the two samples except for the epilayer thickness. In

the medium and high Mn-doped samples, full material optimization is possible only for film thicknesses $\lesssim$ 50 nm. The epilayer whose measurements are shown in the right panels of Fig. 1 is 500 nm thick. Its magnetization and transport Curie point singularities are largely smeared out, the damping factor is strongly frequency dependent,[13] and alternating number of SWRs is observed with increasing applied field whose spacings are inconsistent with Kittel modes. Clearly, the material is non-uniform, the magnetization and transport data indicate strong moment and charge compensation by extrinsic impurities, and for this material it is impossible to reliably extract any of the intrinsic micromagnetic parameters of (Ga,Mn)As.

In Fig. 2 we illustrate that even in films thinner than 50 nm, apparently small changes in the remaining key synthesis parameters can dramatically affect the material quality. It is broadly accepted that staying near the 1:1 stoichiometric As:(Ga+Mn) ratio is favorable for the LT-MBE growth of (Ga,Mn)As.[14,15] In Fig. 2a we plot our optimal growth temperature T_G for the stoichiometric growth as a function of the nominal Mn-doping x. (We used the GaAs band-edge spectrometer to measure the substrate temperature and the predictive substrate heater control to stabilize the T_G during the growth.) Note that the optimal T_G remains near (from the lower temperature side) the 2D/3D growth-mode boundary which implies its strong dependence on x. In Fig. 2b we plot the Curie temperature T_C as a function of the annealing time for the optimal $T_G = 190°C$ for the 13% Mn doped sample and for two annealing temperatures. One is the optimal annealing temperature $T_A = 160°C$ and the other one is 20°C lower. Clearly, the record $T_C = 188$ K sample is obtained by optimizing simultaneously the annealing time and T_A. Figs. 2c,d illustrate how the increasing T_C is accompanied by the improving material quality (reduction of extrinsic compensation and sample inhomogeneity) over the annealing time for optimal T_G and T_A. To highlight the crucial importance of the optimal T_G during the growth, we show in Figs. 2e,f the same annealing sequence measurements as in Figs. 2c,d on a 13% doped sample grown at a temperature of only 10° below the optimal T_G. In striking contrast to the material grown at the optimal T_G, the sample is insulating and paramagnetic in the as-grown state. Ferromagnetism and metallic conduction can be recovered by annealing, however, the compensation and inhomogeneity cannot be removed and the ferromagnetic transition temperature remains tens of degrees below the T_C of the sample grown at the optimal T_G. Similarly low quality samples are obtained by growing at higher than the optimal T_G.

Figs. 1 and 2 illustrate the following general conclusions we can draw from our exten-

sive material optimization studies. Inferring doping trends in basic material properties of (Ga,Mn)As from sample series mixing as-grown and annealed materials, as has been often the case in the literature,[7,9] is unsuitable as the quality of the samples may vastly vary in such a series. Chosing one *a priori* fixed T_G, T_A, and annealing time for a range of Mn-dopings, as is also common in the literature,[7,9,16,17] is unlikely to produce a high-quality, uniform and uncompensated (Ga,Mn)As material even for one of the considered dopings and is bound to produce lower-quality samples for most of the studied Mn-dopings. Finally, reliable measurements of intrinsic semiconducting and magnetic properties on optimized (Ga,Mn)As samples require exceedingly long annealing times for film thicknesses $\gtrsim 50$ nm and are unachievable in ~ 100 nm and thicker films by the known approaches to the (Ga,Mn)As epilayer synthesis.

Doping trends in the series of optimized (Ga,Mn)As epilayers. After finding the optimal growth and post-growth conditions for each individual nominal doping we obtained a series of comparably high-quality samples spanning a wide range of Mn dopings. At nominal dopings below $\sim 0.1\%$ the materials from the series are paramagnetic, strongly insulating, showing signatures of the activated transport corresponding to valence band – impurity band transitions at intermediate temperatures, and valence band – conduction band transitions at high temperatures (see Fig. 3a). For higher nominal dopings, $0.5 \lesssim x \lesssim 1.5\%$, no clear signatures of activation from the valence band to the impurity band are seen in the transport, confirming that the bands start to overlap and mix, yet the materials remain insulating. At $x \approx 1.5\%$, the low-temperature conductivity of the film increases abruptly by several orders of magnitude (see Fig. 3b), and the system turns into a degenerate semiconductor. The onset of ferromagnetism occurs already on the insulating side of the insulator-to-metal transition at $x \approx 1\%$. All metallic samples within the series have sharp Curie point singularities (see Fig. 3c).

The hole density p measured from the high-field Hall effect (see Supplementary Figure S4, Equation S1, and Discussion for more details) increases with increasing doping in the optimized materials (see Fig. 3d). Similarly, the magnetization and T_C steadily increase with x (see Figs. 3e,f). Assuming 4.5 μ_B per Mn atom[18] (μ_B is the Bohr magneton) we can estimate the density N_{Mn} of uncompesated Mn_{Ga} moments from the magnetization data (see left y-axis in Fig. 3e). Since there is no apparent deficit of p compared to N_{Mn} and since the interstitial Mn impurity, which is the main extrinsic defect, compensates one local moment

but two holes we conclude that interstitial Mn is completely (within the experimental error) removed in our optimally synthesized epilayers. Hence, our series of (Ga,Mn)As materials have well controlled characteristics, showing a systematic trend of increasing magnetization with increasing x, increasing T_C (reaching 188 K), and increasing hole density. The materials have no measurable charge or moment compensation of the substitutional Mn_{Ga} impurities and have a large degree of uniformity reflected by sharp Curie point singularities. (See Supplementary Discussion for more details on theoretical and experimental doping trends in (Ga,Mn)As.). We point out that this phenomenology is in striking contrast to the non-systematic doping trends in semiconducting and magnetic properties reported, e.g., in Ref. 9 on the mixed series of as-grown and annealed, ~ 100 nm thick (Ga,Mn)As epilayers prepared without individually optimizing T_G, T_A, and the annealing time.

Micromagnetic parameters of (Ga,Mn)As. Fig. 4 demonstrates that the intrinsic micromagnetic parameters of (Ga,Mn)As measured on our carefully optimized materials show also a smooth monotonous doping dependence. As detailed below, their values are characteristic of common band ferromagnets and all the semiconducting and magnetic properties summarized in Figs. 3 and 4 are consistent with the microscopically established electronic structure of (Ga,Mn)As.[5,6] We point out that we have confirmed the control and reproducibility of the above material properties of (Ga,Mn)As on the individually optimized films by multiple material synthesis experiments at a given Mn doping in two distinct MBE laboratories in Prague and in Nottingham. This is a positive observation, highly non-trivial for the heavily doped non-equilibrium grown semiconductor, which is essential for the reliable understanding and utilizing the material. Not surprisingly for the highly non-equilibrium synthesis, the growth parameters quoted in this paper should not be taken as a universal recipe for (Ga,Mn)As. The optimal growth and postgrowth annealing conditions may vary from one to the other experimental system to an extent which for our two MBE laboratories is not large but may be beyond the straightforward cross-calibration error bars.

A more than an order of magnitude experimental scatter and a lack of any clear trend as a function of Mn-doping can be found in the previous literature for the Gilbert damping and spin-stiffness constants (see Supplementary Discussion).[19–28] Significant variations can be also found in the experimental magnetic anisotropy constants of (Ga,Mn)As.[29] The disarray of the previously measured micromagnetic parameters reflects partly the lack of careful

materials optimization but also the limitations of common magnetic characterization techniques when applied to the thin-film dilute-moment (Ga,Mn)As samples. In the remaining part of the paper we therefore describe in more detail our experimental determination of the micromagnetic parameters of (Ga,Mn)As. Hand-in-hand with the optimization of the material synthesis we have developed experimental capabilities based on the MO pump-and-probe method which allow us to simultaneously determine the magnetic anisotropy, Gilbert damping, and spin stiffness constants from one consistent set of measured data. The possibility to excite and detect precession of ferromagnetic Mn moments in (Ga,Mn)As by this method has been extensively discussed in previous MO studies (see Methods for the detailed description of the method).[30–41] All experiments presented below were performed at 15 K.

The anisotropy constants, shown in Fig. 4a, were obtained combining three complementary measurements. In the first experiment we measured the external magnetic field $H_{\rm ext}$ dependence of the precession frequency f of the time resolved MO signal. In the studied (Ga,Mn)As/GaAs epilayers, the internal magnetic anisotropy fields are dominated by three components. The out-of-plane component $K_{\rm out}$ is a sum of the thin-film shape anisotropy and the magnetocrystalline anisotropy due to the compressive growth strain in (Ga,Mn)As. The cubic magnetocrystalline anisotropy $K_{\rm c}$ reflects the zinc-blende crystal structure of the host semiconductor. The additional uniaxial anisotropy component along the in-plane diagonal $K_{\rm u}$ is not associated with any measurable macroscopic strain in the epilayer. The precession frequency is given by,

$$f = \frac{g\mu_{\rm B}}{h}\sqrt{\left(H_{\rm ext}\cos(\varphi-\varphi_{\rm H}) - 2K_{\rm out} + K_{\rm c}(3+\cos 4\varphi)/2 + 2K_{\rm u}\sin^2(\varphi-\pi/4) + \Delta H_n\right)} \times \sqrt{\left(H_{\rm ext}\cos(\varphi-\varphi_{\rm H}) + 2K_{\rm c}\cos 4\varphi - 2K_{\rm u}\sin 2\varphi + \Delta H_n\right)}, \quad (1)$$

where g is the Landé g-factor of Mn moments, φ and $\varphi_{\rm H}$ are the in-plane magnetization and external magnetic field angles measured from the [100] crystal axis, and ΔH_n is the shift of the resonant field for the higher index n spin wave modes with respect to the $n = 0$ uniform precession mode. In order to uniquely determine the anisotropy constants, the field-dependent precession frequency measurements were complemented by MO experiments with variable polarization angle of the probe beam. The latter measurements allow us to precisely determine the angle of the equilibrium easy axis of the magnetization (see Supplementary Discussion).[40,41] Finally, we confirmed the consistency of the obtained anisotropy constants by performing static measurements of magnetization hysteresis loops by the super-

conducting quantum interference device (SQUID). The sign of $K_{\rm out}$ implies that all studied (Ga,Mn)As/GaAs materials are in-plane ferromagnets. Note that in the low-doped and high-doped samples with very stable in-plane easy-axes aligned with one of the main crystal directions the dynamical MO experiments become unfeasible. The overall magnitudes of the anisotropy constants, as well as of the magnetization and $T_{\rm C}$, are consistently described by the microscopically established band theories of (Ga,Mn)As.[5]

The magnetization precession damping factor, shown in Fig. 4b, is obtained by fitting the measured dynamical MO signal to Landau-Lifshitz-Gilbert (LLG) equations using the experimentally obtained magnetic anisotropy constants. The high accuracy of the LLG fits is demonstrated in Figs. 5a,b on data measured on the 5.2% doped sample. The obtained dependence of the damping factor on the external magnetic field applied along the [010] and [110] directions is shown in Fig. 5c. At smaller fields, the damping factor is not constant and shows a strong anisotropy with respect to the field angle. When plotted as a function of frequency, however, the dependence on the field-angle disappears, as shown in Fig. 5d. We can therefore conclude that the apparent anisotropy of the damping factor can in our materials be ascribed fully to the field-angle dependence via the precession frequency. In all our studied materials, the frequency-independent Gilbert damping constant α is isotropic and can be accurately determined from MO data with precession frequencies $f \gtrsim 15$ GHz. The MO damping factor phenomenology observed in Fig. 5 (and Fig. 1b) is consistent with corresponding MO measurements in uniform metal ferromagnets.[12]

We point out that in ferromagnetic resonance (FMR) experiments, the measurement frequency was limited typically to two values, $f = 9$ and 35 GHz which even in the optimized (Ga,Mn)As materials is not sufficient to reliably separate the intrinsic Gilbert damping constant from the inhomogeneous broadening of the FMR line-width. The dynamical MO measurements, on the other hand, span a large enough range of frequencies and allow us to extract a consistent set of frequency-independent values of α for our series of optimized ferromagnetic (Ga,Mn)As materials. We find a systematic doping trend across the series in which the Gilbert constant decreases from ~ 0.1 to 0.01 when the nominal Mn doping increases from $\sim 2\%$ to 5% and then remains nearly constant (see Fig. 4b). The magnitudes of α and the doping dependence are consistent with Gilbert damping constants in conventional transition metal ferromagnets. In metals, α typically increases with increasing resistivity and is enhanced in alloys with enhanced spin-orbit coupling.[42–44] Similarly, in our measure-

ments in (Ga,Mn)As, the increase of α correlates with a sizable increase of the resistivity in the lower Mn-doped samples. Also, the spin-orbit coupling effects tend to be stronger in the lower doped samples with lower filling of the valence bands and with the carriers closer to the metal-insulator transition.[5] Theory ascribing magnetization relaxation to the kinetic-exchange coupling of Mn moments with holes residing in the disordered, exchange-split, and spin-orbit-coupled valence band of (Ga,Mn)As yields a comparable range of values of α as observed in our measurements.[19]

The MO pump-and-probe technique utilized in our work allows us in principle also for the direct measurement of the spin stiffness. However, one has to find the rather delicate balance between thin enough epilayers whose material quality can be optimized and thick enough films allowing the observation of the higher-index Kittel spin-wave modes[45] of a uniform ferromagnet. For these modes, the spin-stiffness parameter D is directly obtained from the measured resonant fields,

$$\Delta H_n \equiv H_0 - H_n = D\frac{n^2}{L^2}\frac{\pi^2}{g\mu_{\rm B}}\,, \tag{2}$$

where L is the thickness of the ferromagnetic film. The MO pump-and-probe technique has the key advantage here that, unlike FMR, it is not limited to odd index spin wave modes.[45] The ability to excite and detect the $n = 0$, 1, and 2 resonances is essential for the observation of the Kittel modes in our optimized (Ga,Mn)As epilayers whose thickness is limited to ~ 50 nm.

In Fig. 6a we show an example of the time dependent MO signal measured in a 48 nm thick optimized epilayer with 7% nominal Mn doping. Three SWRs are identified in the sample with frequencies f_0, f_1, and f_2, as shown in Figs. 6b,c. The association of these SWRs with the Kittel modes, described by Eq. (2), is based on experiments shown in Figs. 6b-e. In Fig. 6c we plot the dependence of the three detected precession frequencies on the external magnetic field applied along the [010] and [110] crystal axes. At saturation fields, which for the 7% Mn-doped sample are $\gtrsim 70$ mT, the equilibrium magnetization vector is aligned with $H_{\rm ext}$ and Eq. (1) with $\varphi = \varphi_{\rm H}$ can be used to fit the data. We emphasize that all six displayed dependences $f_n(H_{\rm ext})$ for $n = 0$, 1, and 2, and $\varphi_{\rm H} = 45^\circ$ and 90° can be accurately fitted by one set of magnetic anisotropy constants. We can therefore use Eq. (2) to convert the measured frequency spacing of individual SWRs to ΔH_n. In Fig. 6d we show that ΔH_n in our optimized epilayers is proportional to n^2 as expected for the Kittel modes

in homogeneous films.

The magnetic homogeneity and the applicability of Eq. (2) in our epilayers is further confirmed by the following experiments: We prepared three samples by etching the original 48 nm thick (Ga,Mn)As film down to the thicknesses of 39, 29 and 15 nm, respectively. As seen in Fig. 6b, the frequency f_0 is independent of the film thickness which confirms that it corresponds to the uniform precession mode and that the film is homogeneous, i.e., the magnetic anisotropy constants do not vary across the width of the (Ga,Mn)As epilayer. Note that this is again in striking contrast with the vertical gradient of magnetic anisotropies reported, e.g., in Ref. 46 on a $\sim$ 500 nm thick unoptimized material. (For another direct evidence of the crucial role of the growth parameters on the material uniformity compare also results of previous muon spin relaxation measurements in Ref. 47 and in Ref. 48.)

The spacing ΔH_1 shown in Fig. 6e scales as L^{-2} and the values of D extracted from the n-dependence of the resonant field spacings in the $L = 48$ nm epilayer (see Fig. 6d) and from the L-dependence of ΔH_1 (see Fig. 6e) give the same $D = 2.43 \pm 0.15$ meVnm^2. Identical value of the spin stiffness was also obtained from measurements in an optimized epilayer grown with the same doping and thickness of 18 nm in which we detected the frequencies f_0 and f_1 and applied Eq. (2). These measurements confirm the reliability of extracted values of the spin stiffness. We note that the SWR frequencies are determined with high accuracy in our measurements and that the indicated error bars in Fig. 4b reflect the uncertainty of the film thickness. As shown in Fig. 4b, we observe a consistent, weakly increasing trend in D with increasing doping and values of D between 2 and 3 meVnm^2 in the studied ferromagnetic samples with nominal doping 3.8-9%. (Note that apart from the difficulty of exciting magnetization precession in the very low and high-doped samples with stable easy-axes, the measurements of D were unfeasible on the lower doping side of the series because of the increasing damping and the corresponding inability to detect the higher SWR modes.) As mentioned in the discussion of Fig. 1 we have tested the inapplicability of the SWR experiments for the direct determination of the spin stiffness in thick non-uniform materials (see Supplementary Figure S5). The observed number of modes and the field dependent frequencies are non-systematic in these unoptimized materials and ΔH_n do not show the quadratic scaling with n of the Kittel modes of Eq. (2) (see Supplementary Figure S6 and Supplementary Discussion for more details).

Similar to the Gilbert damping constant, our measured spin stiffness constant in the

optimized (Ga,Mn)As epilayers is comparable to the spin stiffness in conventional transition metal ferromagnets.[49] The large values of the spin stiffness of the order meVnm^2 are also consistent with model Hamiltonian and *ab initio* calculations[28,50–52] which all consider or obtain the band structure of the ferromagnetic (Ga,Mn)As with merged valence and impurity bands.[6] On the other hand, for carriers localized in a narrow impurity band the expected spin stiffness would be small in a dilute moment system like (Ga,Mn)As, in which the magnetic coupling between remote Mn moments is mediated by the carriers.[53]

Discussion

We have presented a systematic study demonstrating the crucial role of the careful synthesis optimization for understanding the intrinsic semiconducting and magnetic properties of (Ga,Mn)As. Micromagnetic parameters of (Ga,Mn)As measured on our carefully optimized materials show values which are characteristic of common band ferromagnets and all the observed semiconducting and magnetic properties are consistent with the microscopically established electronic structure of (Ga,Mn)As with merged impurity and valence bands. By recognizing that the bands are merged, i.e. overlapped and mixed, in the optimized ferromagnetic (Ga,Mn)As materials, the distinction between a "valence" and "impurity" bands becomes mere semantics with no fundamental physics relevance. Simultaneously, it is important to keep in mind that the moderate acceptor binding energy of Mn_{Ga} shifts the insulator-to-metal transition to orders of magnitude higher doping densities than in the case of common shallow non-magnetic acceptors. Disorder and correlation effects, therefore, play a comparatively more significant role in (Ga,Mn)As than in degenerate semiconductors with common shallow dopants and any simplified one-particle band picture of ferromagnetic (Ga,Mn)As can only represent a proxy to the electronic structure of the material.

Methods

Optimized materials synthesis. Because of the highly non-equilibrium nature of the heavily-doped ferromagnetic (Ga,Mn)As, the growth and post-growth annealing procedures have to be individually optimized for each Mn-doping level in order to obtain films which are as close as possible to idealized uniform (Ga,Mn)As mixed crystals with the minimal density of compensating and other unintentional defects. An extensive set of characterization measurements has to accompany the synthesis to guarantee that the materials show systematic doping trends; monitoring the thermodynamic Curie point singularities is essen-

tial for assuring the uniformity and high magnetic quality of the materials.[11,15,54,55] When omitting the above procedures, extrinsic impurities and sample inhomogeneities can yield non-systematic doping trends and conceal the intrinsic magnetic properties of (Ga,Mn)As.

Our (Ga,Mn)As layers were grown at the growth rate of approximately 0.2 monolayers/second. The Mn flux, and hence the nominal Mn doping x, was determined by measuring the ratio of the beam equivalent pressures (BEP) of Mn and Ga sources before each growth. The Mn content was cross-checked by secondary ion mass spectroscopy (SIMS) and by comparing the growth rates of GaAs and (Ga,Mn)As measured by the oscillations of the reflection high-energy electron diffraction (RHEED). There are two critical growth parameters of (Ga,Mn)As: the substrate temperature, and the As-to-(Ga+Mn) flux ratio.[4,14,15,56] At the typical temperatures of ~ 200°C neither an optical pyrometer nor a radiatively coupled temperature sensor are applicable. Instead, we use the GaAs band-edge spectrometer to measure the substrate temperature and the predictive substrate heater control to stabilize the temperature during the growth. For a given As:(Ga+Mn) ratio the substrate temperature fully determines the growth regime: the growth proceeds two-dimensionally at low temperatures, and turns irreversibly into the 3D growth mode when a critical temperature is exceeded. The scatter of the critical substrate temperature for given doping x and As:(Ga+Mn) ratio is remarkably small, typically less than 2°C. For a larger As flux, the 2D/3D transition occurs at higher temperature. The highest quality samples are grown in a narrow window around the 1:1 stoichiometric As:(Ga+Mn) ratio and at the substrate temperature approaching as close as possible from below the 2D/3D critical temperature for given x. The As:(Ga+Mn) ratio was adjusted by the As-cell valve, and calibrated using the As-controlled RHEED oscillations.

The next important factor determining the quality of the resulting (Ga,Mn)As materials are post-growth annealing conditions.[4,15,54] The common trends in annealing (at temperatures close to the growth temperature) suggest the presence of competing mechanisms. One mechanism yields the increase of T_c and is ascribed in a number of reports to the removal of charge and moment compensating interstitial Mn impurities.[57,58] The removal is slowed down by the growth of an oxide surface layer during annealing[54] and an additional mechanism can eventually yield reduction of $T_{\rm C}$ after sufficiently long annealing times, depending on the annealing temperature. The origin of this detrimental mechanism may be in Mn clustering or in the competition between the non-equilibrium (Ga,Mn)As phase and the equilibrium

MnAs second phase. Because of the competing mechanisms, the absolutely highest Curie temperature for the given nominal doping is achieved at intermediate annealing temperature and time. The remaining critical parameter of the synthesis is the epilayer thickness.[54] For a given nominal doping, the highest attainable T_C is reached only in thin films, typically thinner than ∼50 nm.

An increase of T_C is not the only parameter followed to ascertain that a sample is of high quality. A key characterization tool are the thermodynamic Curie point singularities.[11] The development of sharply vanishing magnetization $M(T)$ at T_C and the onset of the singularity in $d\rho/dT$ are well correlated with increasing T_C and conductivity within the annealing sequence.

Magneto-optical experiments. A Ti:sapphire laser was used as a light source. Laser pulses, with the time width of 200 fs and the repetition rate of 82 MHz, were tuned to 1.64 eV, i.e. above the semiconductor band gap, in order to excite magnetization dynamics by photon absorption. A schematic diagram of the experimental set-up is shown in Supplementary Figure S7. The output of a femtosecond laser is divided into a strong pump pulse and a weak probe pulse that are focused to a same spot on the sample. The pump pulses were usually circularly polarized (with a helicity controlled by a wave plate) and the probe pulses were linearly polarized. The measured MO signals correspond to the probe polarization rotation induced by the pump pulses. The experiment was performed close to the normal incidence geometry (angle of incidence $\theta_i = 2^\circ$ and 8° for pump and probe pulses, respectively) with a sample mounted in a cryostat, which was placed between the poles of an electromagnet. All the MO data were measured at temperature of 15 K, at pump excitation intensity 30-40 μJcm^{-2}, and they correspond to the helicity-independent part of the measured signal.[40] The external magnetic field H_{ext} was applied in the sample plane at an angle φ_H with respect to the [100] crystallographic direction in the sample plane (see Supplementary Figure S7). Prior to all time-resolved experiments, we always prepared the magnetization in a well-defined state by first applying a strong saturating magnetic field at an angle φ_H and then reducing it to the desired magnitude of H_{ext}. There are several microscopic mechanisms that can lead to a precession of magnetization due to the impact of pump laser pulse. In particular, very recently we reported on the precession of magnetization due to optical spin-transfer torque[40] and optical spin-orbit torque.[59] However, the most common mechanism,

which is responsible for the oscillatory MO signals measured in the majority of (Ga,Mn)As samples at low excitation intensities, is the change of the sample magnetic anisotropy due to the pump-induced temperature increase[59] that is schematically shown in Supplementary Figure S8. The most important point from the perspective of the present paper is that the precession of magnetization induced by the laser pulses is determined by the magnetic anisotropy of the sample which makes this method an all-optical analog to FMR[60] (see Supplementary Equations S2-S19 in Supplementary Discussion).

Determination of micromagnetic parameters. All micromagnetic parameters reported here were deduced from a single magneto-optical pump-and-probe experiment. In particular, the anisotropy fields were determined by a fitting of the theoretically derived dependence of the precession frequency on the external magnetic field (Supplementary Equations S13-S15) to the experimentally obtained data (see Supplementary Figure S9). For all the investigated samples, we supplemented this method by two additional experimental techniques that provide information about the samples magnetic anisotropy, namely the probe-polarization dependence of the MO precession signal amplitude (see Supplementary Figure S10) and SQUID magnetometry (see Supplementary Figure S11). This enabled us to increase the precision of the magnetic anisotropy determination (see Supplementary Figure S12) even further. The Gilbert damping constant can be deduced from the precession signal damping using the Landau-Lifshitz-Gilbert (LLG) equation (see Supplementary Equations S2-S4, S10, and S16) and the experimentally measured values of MO coefficients of the polar Kerr effect and magnetic liner dichroism (see Supplementary Figure S13); examples of the data are shown in Supplementary Figure S14. Finally, the spin stiffness is obtained from the mutual spacing of the spin wave resonances (see Supplementary Figure S15) which are present in the measured oscillatory MO signals (see Supplementary Figure S16). The inapplicability of this spin stiffness determination to thick (Ga,Mn)As epilayers (see Supplementary Figure S5) is illustrated in Supplementary Figure S6.

---

[1] Ohno, H. *et al.* (Ga,Mn)As: a new diluted magnetic semiconductor based on GaAs. *Appl. Phys. Lett.* **69**, 363-365 (1996).

[2] Hayashi, T., Tanaka, M., Seto, K., Nishinaga, T. & Ando, K. III-V based mag-

netic(GaMnAs)/nonmagnetic(AlAs) semiconductor superlattices. *Appl. Phys. Lett.* **71**, 1825-1827 (1997).

[3] Van Esch, A. *et al.* Interplay between the magnetic and transport properties in the III-V diluted magnetic semiconductor $Ga_{1-x}Mn_xAs$. *Phys. Rev.* **B 56**, 13103-13112 (1997).

[4] Ohno, H. Making nonmagnetic semiconductors magnetic. *Science* **281**, 951-956 (1998).

[5] Jungwirth, T., Sinova, J., Mašek, J., Kučera, J. & MacDonald, A. H. Theory of ferromagnetic (III,Mn)V semiconductors. *Rev. Mod. Phys.* **78**, 809-864 (2006).

[6] Mašek, J. *et al.* Microscopic analysis of the valence band and impurity band theories of (Ga,Mn)As. *Phys. Rev. Lett.* **105**, 227202(1)-227202(4) (2010).

[7] Burch, K. S. *et al.* Impurity band conduction in a high temperature ferromagnetic semiconductor. *Phys. Rev. Lett.* **97**, 087208(1)-087208(4) (2006).

[8] Tang, J.-M. & Flatté, M. E. Magnetic circular dichroism from the impurity band in III-V diluted magnetic semiconductors. *Phys. Rev. Lett.* **101**, 157203(1)-157203(4) (2008).

[9] Dobrowolska, M. *et al.* Controlling the curie temperature in (Ga,Mn)As through location of the fermi level within the impurity band. *Nature Mater.* **11**, 444-449 (2012).

[10] Samarth, N. Battle of the bands. *Nature Mater.* **11**, 360-361 (2012).

[11] Novák, V. *et al.* Curie point singularity in the temperature derivative of resistivity in (Ga,Mn)As. *Phys. Rev. Lett.* **101**, 077201(1)-077201(4) (2008).

[12] Walowski, J. *et al.* Intrinsic and non-local Gilbert damping in polycrystalline nickel studied by Ti : sapphire laser fs spectroscopy. *J. Phys. D: Appl. Phys.* **41**, 164016(1)-164016(10) (2008).

[13] Liu, Y. *et al.* Optically induced magnetization dynamics and variation of damping parameter in epitaxial Co2MnSi Heusler alloy films. *Phys. Rev.* **B 81**, 094402(1)-094402(12) (2010).

[14] Myers, R. C. *et al.* Antisite effect on hole-mediated ferromagnetism in (Ga,Mn)As. *Phys. Rev.* **B 74**, 155203(1)-155203(9) (2006).

[15] Wang, M. *et al.* Achieving high Curie temperature in (Ga,Mn)As. *Appl. Phys. Lett.* **93**, 132103(1)-132103(3) (2008).

[16] Singley, E. J. *et al.* Electronic structure and carrier dynamics of the ferromagnetic semiconductor $Ga_{1-x}Mn_xAs$. *Phys. Rev.* **B 68**, 165204(1)-165204(14) (2003).

[17] Mack, S., Myers, R. C., Heron, J. T., Gossard, A. C. & Awschalom, D. D. Stoichiometric growth of high Curie temperature heavily alloyed GaMnAs. *Appl. Phys. Lett.* **92**, 192502(1)-192502(3) (2008).

[18] Jungwirth, T. *et al.* Low-temperature magnetization of (Ga,Mn)As semiconductors. *Phys. Rev.* **B 73**, 165205(1)-165205(12) (2005).

[19] Sinova, J. *et al.* Magnetization relaxation in (Ga,Mn)As ferromagnetic semiconductors. *Phys. Rev.* **B 69**, 085209(1)-085209(6) (2004).

[20] Khazen, K. *et al.* Anisotropic magnetization relaxation in ferromagnetic $Ga_{1-x}Mn_xAs$ thin films. *Phys. Rev.* **B 78**, 195210(1)-195210(8) (2008).

[21] Rappoport, T. G. *et al.* Anomalous behavior of spin wave resonances in $Ga_{1-x}Mn_xAs$ thin films. *Phys. Rev.* **B 69**, 125213(1)-(9) (2004).

[22] Zhou, Y.-Y. *et al.* Magnetic anisotropy, spin pinning, and exchange constants of (Ga,Mn)As films. *IEEE T. Magn.* **43**, 3019-3021 (2007).

[23] Liu, X., Zhou, Y. Y. & Furdyna, J. K. Angular dependence of spin-wave resonances and surface spin pinning in ferromagnetic (Ga,Mn) As films. *Phys. Rev.* **B 75**, 195220(1)-195220(8) (2007).

[24] Bihler, C., Schoch, W., Limmer, W., Goennenwein, S. T. B. & Brandt, M. S. Spin-wave resonances and surface spin pinning in $Ga_{1-x}Mn_xAs$ thin films. *Phys. Rev.* **B 79**, 045205(1)-045205(11) (2009).

[25] Potashnik, S. J. *et al.* Saturated ferromagnetism and magnetization deficit in optimally annealed (Ga,Mn)As epilayers. *Phys. Rev.* **B 66**, 012408(1)-012408(4) (2002).

[26] Gourdon, C. *et al.* Determination of the micromagnetic parameters in (Ga,Mn)As using domain theory. *Phys. Rev.* **B 76**, 241301(1)-241301(4) (2007).

[27] Wang, D. M. *et al.* Light-induced magnetic precession in (Ga,Mn)As slabs: Hybrid standing-wave Damon-Eshbach modes. *Phys. Rev.* **B 75**, 233308(1)-233308(4) (2007).

[28] Werpachowska, A. & Dietl, T. Theory of spin waves in ferromagnetic (Ga,Mn)As. *Phys. Rev.* **B 82**, 085204(1)-085204(15) (2010).

[29] Zemen, J., Kučera, J., Olejník, K. & Jungwirth, T. Magneto crystalline anisotropies in (Ga,Mn)As: a systematic theoretical study and comparison with experiment. *Phys. Rev.* **B 80**, 155203(1)-155203(29) (2009).

[30] Oiwa, A., Takechi, H. & Munekata, H. Photoinduced magnetization rotation and precessional motion of magnetization in ferromagnetic (Ga,Mn)As. *J. Supercond. Nov. Magn.* **18**, 9-13 (2005).

[31] Wang, D. M. *et al.* Light-induced magnetic precession in (Ga,Mn)As slabs: Hybrid standing-wave damon-eshbach modes. *Phys. Rev.* **B 75**, 233308(1)-233308(4) (2007).

[32] Takechi, H., Oiwa, A., Nomura, K., Kondo, T. & Munekata, H. Light-induced precession of ferromagnetically coupled Mn spins in ferromagnetic (Ga,Mn)As. *Phys. Status Solidi C* **3**, 4267-4270 (2007).

[33] Qi, J. *et al.* Coherent magnetization precession in GaMnAs induced by ultrafast optical excitation. *Appl. Phys. Lett.* **91**, 112506(1)-112506(3) (2007).

[34] Qi, J. *et al.* Ultrafast laser-induced coherent spin dynamics in ferromagnetic $Ga_{1-x}Mn_xAs$/GaAs structures. *Phys. Rev.* **B 79**, 085304(1)-085304(8) (2009).

[35] Rozkotová, E. *et al.* Light-induced magnetization precession in GaMnAs. *Appl. Phys. Lett.* **92**, 122507(1)-122507(3) (2008).

[36] Rozkotová, E. *et al.* Coherent control of magnetization precession in ferromagnetic semiconductor (Ga,Mn)As. *Appl. Phys. Lett.* **93**, 232505(1)-232505(3) (2008).

[37] Hashimoto, Y. & Munekata, H. Coherent manipulation of magnetization precession in ferromagnetic semiconductor (Ga,Mn)As with successive optical pumping. *Appl. Phys. Lett.* **93**, 202506(1)-202506(3) (2008).

[38] Hashimoto, Y., Kobayashi, S. & Munekata, H. Photoinduced precession of magnetization in ferromagnetic (Ga,Mn)As. *Phys. Rev. Lett.* **100**, 067202(1)-067202(4) (2008).

[39] Kobayashi, S., Suda, K., Aoyama, J., Nakahara, D. & Munekata, H. Photo-induced precession of magnetization in metal/(Ga,Mn)As systems. *IEEE Trans. Magn.* **46**, 2470-2473 (2010).

[40] Němec, P. *et al.* Experimental observation of the optical spin transfer torque. *Nature Phys.* **8**, 411-415 (2012).

[41] Tesařová, N. *et al.* Direct measurement of the three dimensional magnetization vector trajectory in GaMnAs by a magneto-optical pump-and-probe method. *Appl. Phys. Lett.* **100**, 102403(1)-102403(3) (2012).

[42] Ingvarsson, S. *et al.* Role of electron scattering in the magnetization relaxation of thin $Ni_{81}Fe_{19}$ films. *Phys. Rev.* **B 66**, 214416(1)-214416(5) (2002).

[43] Rantschler, J. O. *et al.* Effect of $3d$, $4d$, and $5d$ transition metal doping on damping in permalloy thin films. *J. Appl. Phys.* **101**, 033911(1)-033911(5) (2007).

[44] Gilmore, K., Idzerda, Y. U. & Stiles, M. D. Spin-orbit precession damping in transition metal ferromagnets. *J. Appl. Phys.* **103**, 07D303(1)-07D303(6) (2008).

[45] Kittel, C. Excitation of spin waves in a ferromagnet by a uniform rf field. *Phys. Rev.* **110**, 1295-1297 (1958).

[46] Son, H. *et al.* Vertical gradient of magnetic anisotropy in the ferromagnetic semiconductor (Ga,Mn)As film. *Appl. Phys. Lett.* **96**, 092105(1)-092105(3) (2010).

[47] Dunsiger, S. R. *et al.* Spatially homogeneous ferromagnetism of (Ga, Mn)As. *Nature Mater.* **9**, 299-303 (2010).

[48] Storchak, V. G. *et al.* Spatially resolved inhomogeneous ferromagnetism in GaMnAs diluted magnetic semiconductors: A microscopic study by muon spin relaxation. *Phys. Rev. Lett.* **101**, 027202(1)-027202(4) (2008).

[49] Collins, M. F., Minkiewicz, V. J., Natans, R., Passell, L. & Shirane, G. Critical and spin-wave scattering of neutrons from iron. *Phys. Rev.* **179**, 417-430 (1969).

[50] König, J., Jungwirth, T. & MacDonald, A. H. Theory of magnetic properties and spin-wave dispersion for ferromagnetic (Ga,Mn)As. *Phys. Rev.* **B 64**, 184423(1)-184423(8) (2001).

[51] Brey, L. & Gómez-Santos, G. Magnetic properties of GaMnAs from an effective Heisenberg Hamiltonian. *Phys. Rev.* **B 68**, 115206(1)-115206(11) (2003).

[52] Bouzerar, G. Magnetic spin excitations in diluted ferromagnetic systems: the case of $Ga_{1-x}Mn_xAs$. *Europhys. Lett.* **79**, 57007(1)-57007(5) (2007).

[53] MacDonald, A. H., Schiffer, P. & Samarth, N. Ferromagnetic semiconductors: moving beyond (Ga,Mn)As. *Nature Mater.* **4**, 195-202 (2005).

[54] Olejník, K. *et al.* Enhanced annealing, high Curie temperature and low-voltage gating in (Ga,Mn)As: a surface oxide control study. *Phys. Rev.* **B 78**, 054403(1)-054403(4) (2008).

[55] Jungwirth, T. *et al.* Systematic study of Mn-doping trends in optical properties of (Ga,Mn)As. *Phys. Rev. Lett.* **105**, 227201(1)-227201(4) (2010).

[56] Foxon, C. T. *et al.* The growth of high quality GaMnAs films by MBE. *J. Mater. Sci.* **15**, 727-731 (2004).

[57] Yu, K. M. *et al.* Effect of the location of Mn sites in ferromagnetic $Ga_{1-x}Mn_xAs$ on its curie temperature. *Phys. Rev.* **B 65**, 201303(1)-201303(4) (2002).

[58] Edmonds, K. W. *et al.* High Curie temperature GaMnAs obtained by resistance-monitored annealing. *Appl. Phys. Lett.* **81**, 4991(1)-4991(3) (2002).

[59] Tesařová, N. *et al.* Experimental observation of the optical spin-orbit torque (2012). http://arXiv.org/abs/1207.0307.

[60] van Kampen, M. *et al.* All-optical probe of coherent spin waves. *Phys. Rev. Lett.* **88**, 227201(1)-227201(4) (2002).

Corresponding author

Correspondence and requests for materials should be addressed to Tomas Jungwirth, e-mail: jungw@fzu.cz, Institute of Physics ASCR, v.v.i., Cukrovarnická 10, 162 53 Praha 6, Czech Republic.

Acknowledgments

We acknowledge theoretical assistence of Pavel Motloch and support from EU ERC Advanced Grant No. 268066 and FP7-215368 SemiSpinNet, from the Ministry of Education of the Czech Republic Grants No. LM2011026, from the Grant Agency of the Czech Republic Grant No. 202/09/H041 and P204/12/0853, from the Charles University in Prague Grant No. SVV-2012-265306 and 443011, from the Academy of Sciences of the Czech Republic Preamium Academiae, and from U.S. grants ONR-N000141110780, NSF-MRSEC DMR-0820414, NSF-DMR-1105512.

Author contributions

Sample preparation: V.N., K.O., R.P.C.; experiments and data analysis: N.T., P.N., E.R., D.B., P. M., K.O, T.J., B.L.G.; data modeling: P.N., F.T.; theory: J.Z., T.J., J.S.; writing: T.J., P.N., J.S.; project planning: P.N., T.J.

Additional information

Competing financial interests: The authors declare no competing financial interests.

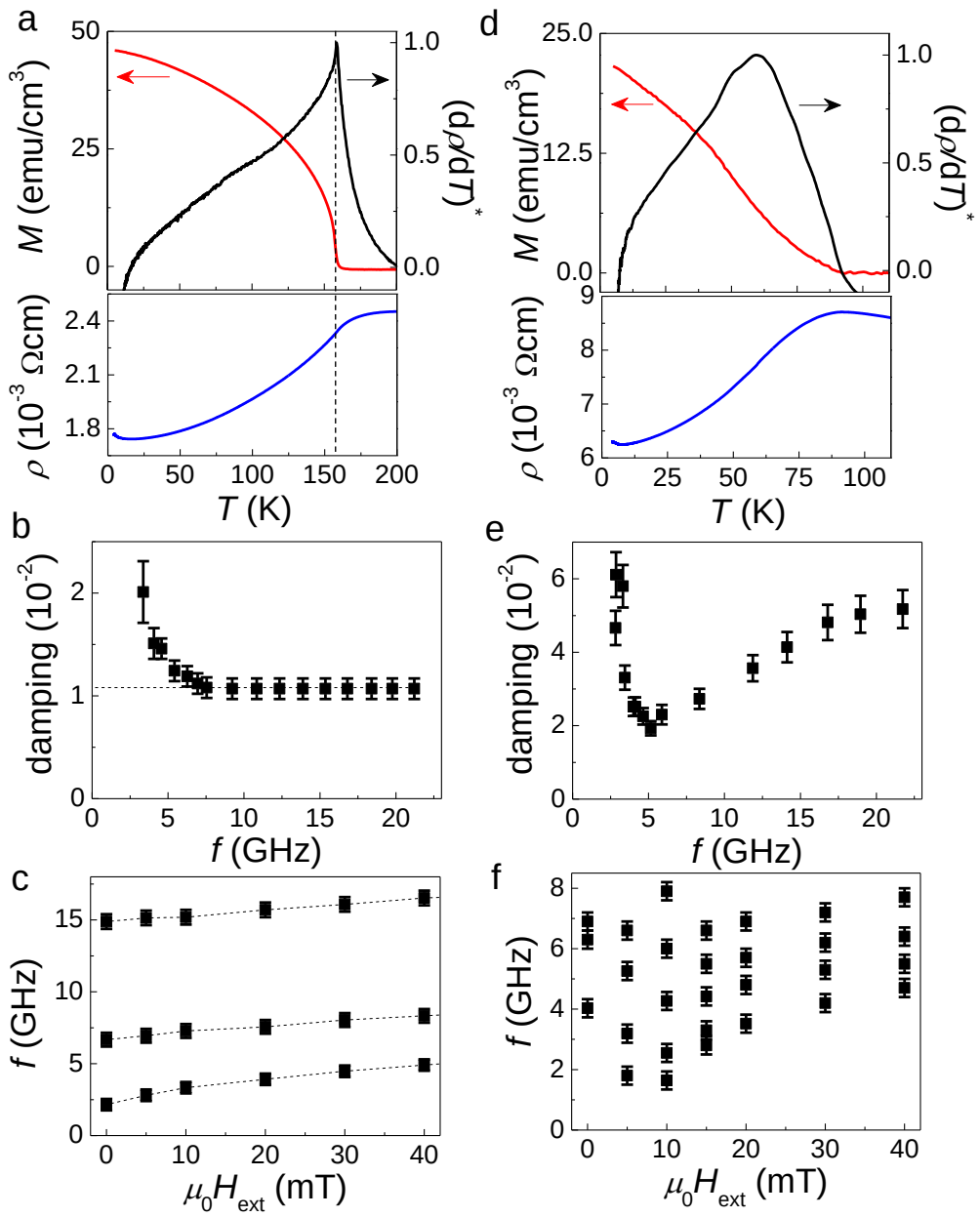

FIG. 1: **Demonstration of the essential role of the careful optimization of (Ga,Mn)As synthesis.** **a**, Magnetization M (red line), temperature derivative of the resistivity normalized to the peak value $(d\rho/dT)^*$ (black line), and resistivity $\rho(T)$ (blue line)of an optimized 20 nm thick epilayer with 7% nominal Mn-doping. **b** and **c**, Frequency dependence of the damping factor and field dependence of the spin-wave resonant frequencies of the same sample. Dotted line in **b** highlights the Gilbert constant value; dotted lines in **c** highlight the $n = 0$, 1,and 2 Kittel spin-wave modes. **d** – **f**, Same as **a** – **c** for a material differing by having only one of the synthesis parameters not optimized (epilayer thickness of 500 nm too large). Gilbert constant and Kittel modes cannot be inferred from **e** and **f**. The error bars correspond to standard deviations and depict the overall uncertainty in the determination of the displayed value from the experimentally measured data.

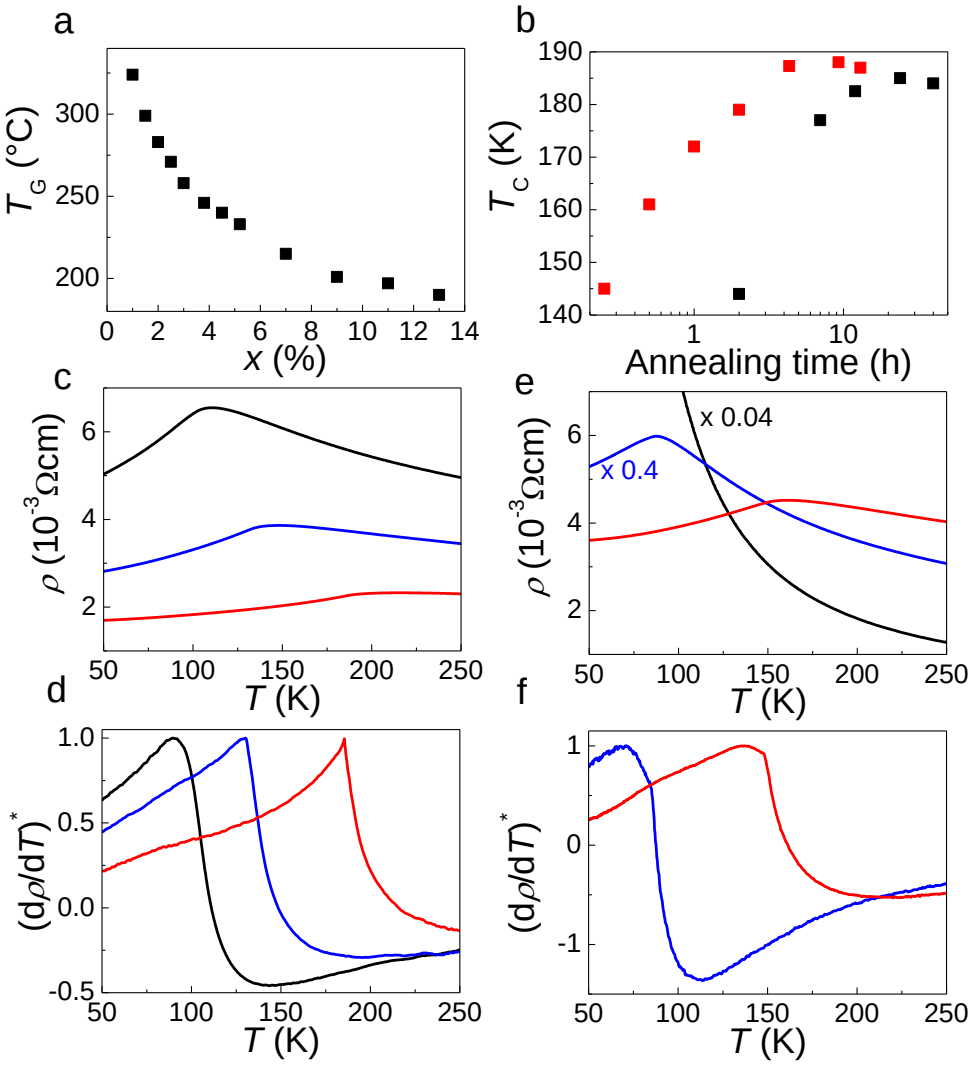

FIG. 2: **Individual optimization for each nominal Mn-doping of the growth temperature and of the annealing temperature and time.** **a**, Optimal growth temperature T_G as a function of the nominal Mn-doping x. **b**, Dependence of the Curie temperature T_C on the annealing time for two annealing temperatures $T_A = 160°C$ (red points) and 140°C (black points) in a 15 nm thick (Ga,Mn)As epilayer with 13% nominal Mn doping grown at optimal T_G. **c**, **d**, Resistivity $\rho(T)$ and temperature derivative of the resistivity normalized to the peak value $(d\rho/dT)^*$ in the $x = 13\%$ epilayer grown at optimal T_G in the as-grown state (black line), for optimal T_A and annealing time 0.5h (blue line), and for optimal T_A and optimal annealing time of 8h (red line). **e**, **f**, Same as **c**, **d**, for a $x = 13\%$ epilayer grown at 10° below optimal T_G; $\rho(T)$ for the as-grown state and for the annealing time 0.5h are multiplied by the numerical factors depicted in the figure for clarity; $(d\rho/dT)^*$ is not plotted for the as-grown insulating and paramagnetic sample.

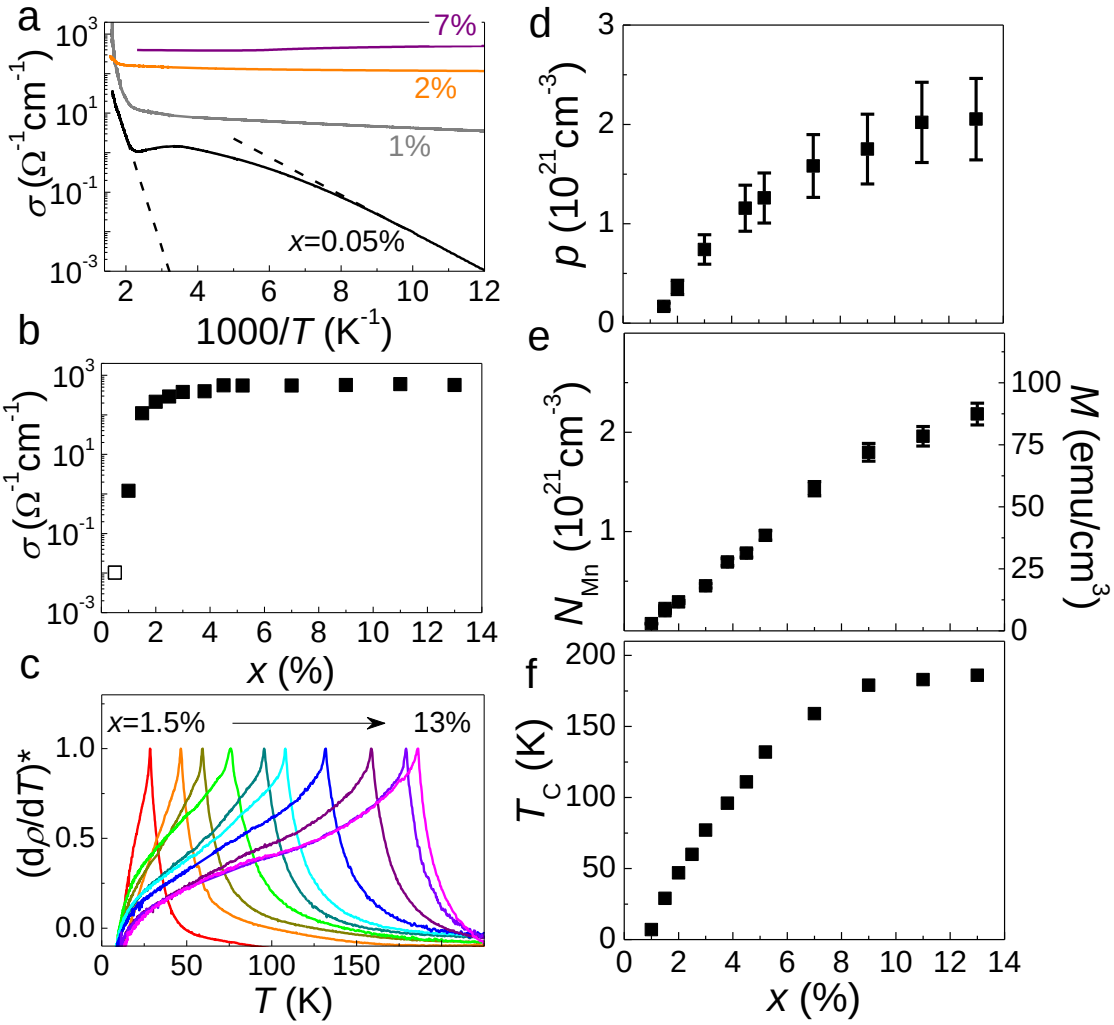

FIG. 3: **Doping trends in the series of optimized (Ga,Mn)As epilayers. a**, Temperature dependence of the conductivity $\sigma(T)$ of optimized (Ga,Mn)As epilayers with depicted nominal Mn doping. Dashed lines indicate the activated parts of $\sigma(T)$ of the insulating paramagnetic (Ga,Mn)As with 0.05% Mn doping, corresponding to the Mn acceptor level and the band gap, respectively. **b**, Conductivity at 4 K as a function of the nominal Mn doping. Open symbol corresponds to a paramagnetic sample. **c**, Sharp Curie point singularities in the temperature derivative of the resistivity in the series of optimized ferromagnetic (Ga,Mn)As epilayers with metallic conduction and x =0.5, 2, 2.5, 3, 3.8, 4.5, 5.2, 7, 9, and 13%. **d-f**, hole density p, magnetization M and corresponding Mn moment density N_{Mn}, and Curie temperature T_{C} as a function of the nominal Mn doping in the series of optimized (Ga,Mn)As epilayers.

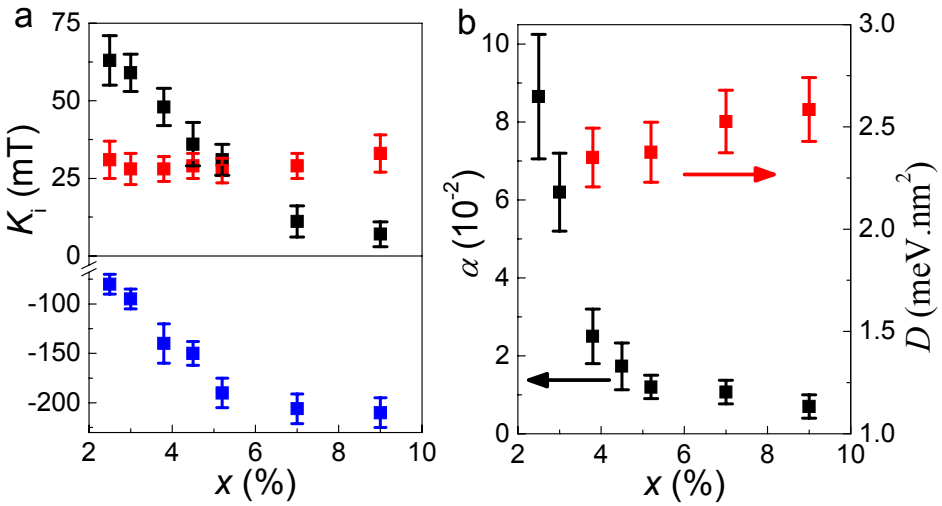

FIG. 4: **Micromagnetic parameters of optimized epilayers of ferromagnetic (Ga,Mn)As. a,** Dependence of anisotropy fields K_c (black points), K_u (red points), and K_{out} (blue points) on nominal Mn doping. **b,** Dependence of the Gilbert damping constant α and the spin stiffness constant D on nominal Mn doping.

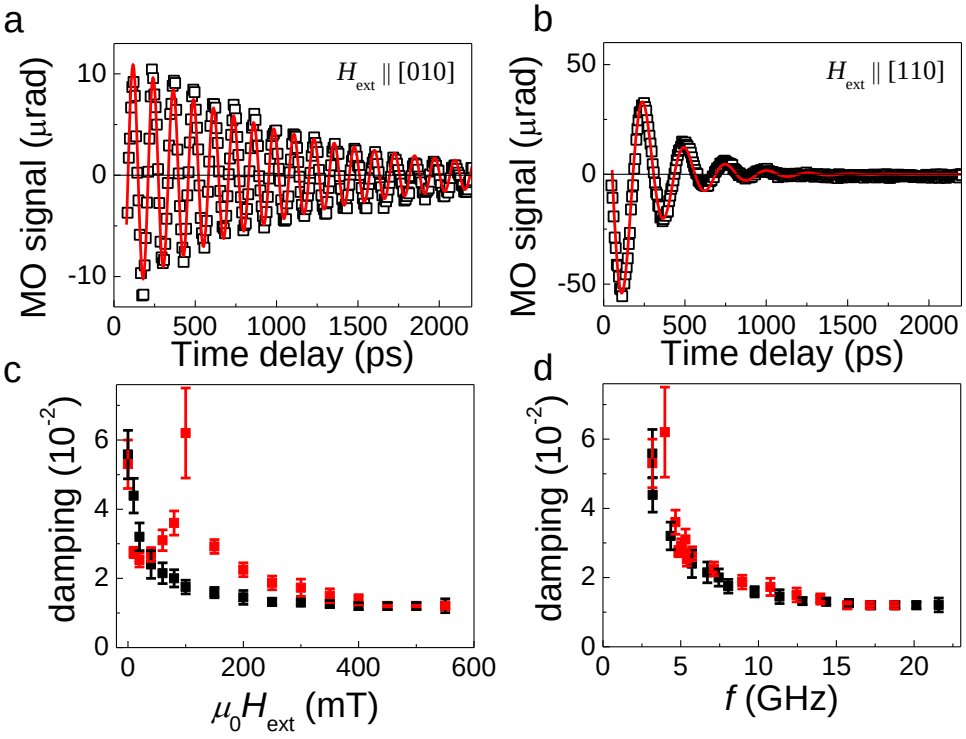

FIG. 5: **Determination of the Gilbert damping constant. a,b,** Oscillatory part of the magneto-optical signal (points) measured in a 18 nm thick epilayer with 5.2% nominal Mn doping for external magnetic field $\mu_0 H_{\mathrm{ext}} = 100$ mT applied along the crystallographic directions [010] and [110]; lines are fits by the Landau-Lifshitz-Gilbert equation. **c,d,** Dependence of the magnetization precession damping factor on the external magnetic field and on the precession frequency for fields applied along the [010] (black points) and [110] (red points) crystallographic directions.

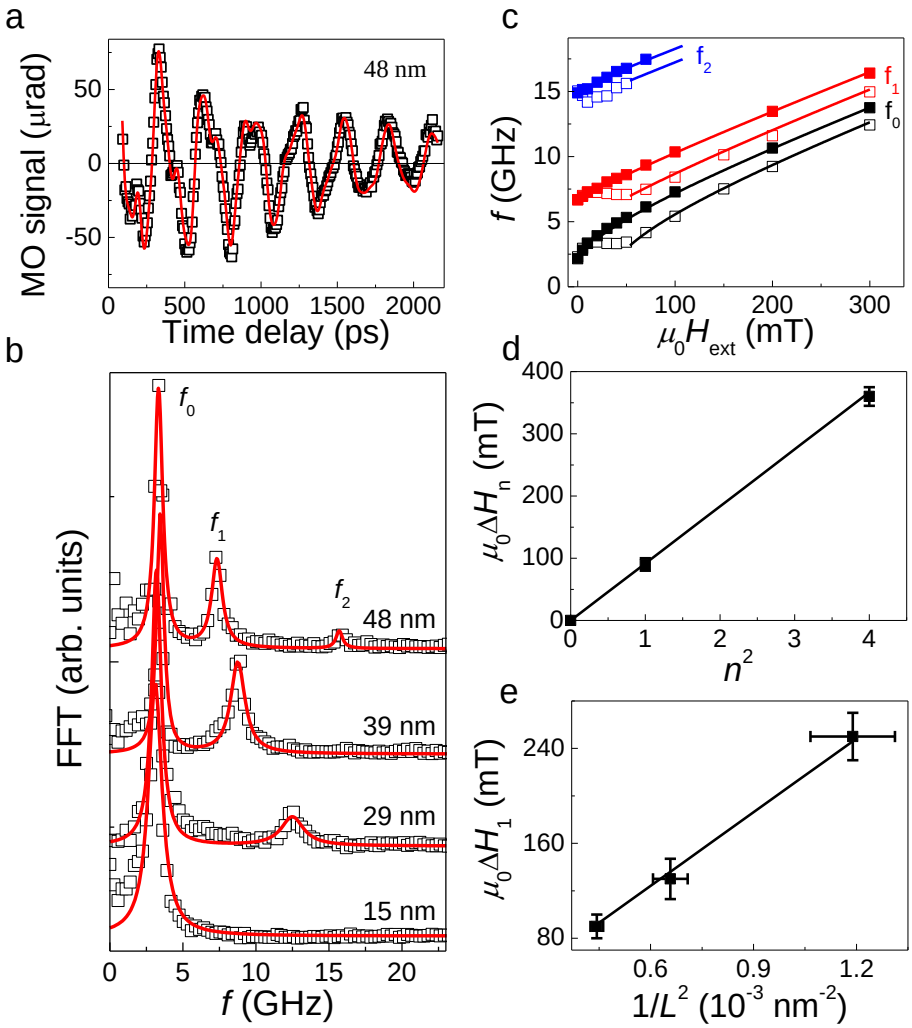

FIG. 6: **Determination of the spin stiffness constant.** **a,** Oscillatory part of the magneto-optical signal (points) measured in a 48 nm thick epilayer with 7% nominal Mn doping for external magnetic field $\mu_0 H_{\rm ext} = 20$ mT applied along the [010] crystallographic direction; line is a fit by a sum of three damped harmonic functions. **b,** Fourier spectra of oscillatory magneto-optical signals (points) measured for $\mu_0 H_{\rm ext} = 20$ mT applied along the [010] crystallographic direction in samples prepared by etching from the 48 nm thick epilayer. The curves are labeled by the film thicknesses, normalized, and vertically off-set for clarity; lines are fits by a sum of Lorentzian peaks. **c,** Dependence of the measured precession frequency on the magnetic field for fields along the crystallographic directions [010] (solid points) and [110] (open points) in the 48 nm thick epilayer; lines are fits by Eq. (1). **d,** Dependence of the measured mode spacing on square of the mode number in the 48 nm thick epilayer. **e,** Dependence of the spacing between the two lowest modes (ΔH_1) on the film thickness. Lines in **d** and **e** are fits by Eq. (2) with spin stiffness $D = 2.43$ meV nm^2.

APPENDIX 9

Experimental setup for the time-resolved MO spectroscopy measurements

All the time-resolved measurements presented in this thesis were done in the experimental setup described in Fig. A9.1. The titan-sapphire laser was used to generate ultrashort laser pulses (width of the pulse ~ 200 fs) with a repetition rate of 82 MHz. The laser system can be tuned in the spectral range of 720 – 1050 nm, but we typically used the wavelength λ = 760 nm (phonon energy hv = 1.63 eV) which is sufficient to excite (Ga,Mn)As above the band gap. The laser pulses were divided by the beam splitter into two parts – the stronger pump pulse and the weaker probe pulse. The pump pulse was time-delayed by a computer-controlled delay line with respect to the probe pulse. The intensity of the laser pulses was individually adjusted in both arms by the neutral density filters. The polarization state was controlled by the polarizers and the wave plates (half and quarter wave plates), where the pump pulses were typically circularly polarized and the probe pulses were polarized linearly. The laser beams were focused on the sample in a near normal incidence geometry (the angles of incidence, measured from the normal of the sample, for pump and probe beams were 3º and 9º, respectively). The samples were glued on the cold finger (by a silver paste which enabled a good thermal conductivity) of a closed-cycle cryostat. The samples were typically cooled down to 15 K. The samples were placed between the poles of the electromagnet, which could generate a magnetic field (H_{ext}) up to ~ 600 mT.

After reflection from the sample, the probe pulses were analyzed in the optical bridge (while the reflected pump beam was blocked). The basic principle of the optical bridge is, that the linear polarization of the probe beam is divided by a polarizing beam splitter into *s*- and *p*-orthogonal polarizations (usually a half wave plate is placed in front of the beam splitter that can be used to adjust an equal intensities of the *s*- and *p*- polarized beams). Each of the polarizations is deflected into different arms of the optical bridge where they are separately detected by photodiodes. The output signals from the photodiods are transferred to differential preamplifiers where the sum and the difference from the individual signals are computed. These differential and sum signals are further amplified and both are processed by the lock-in amplifiers, that were synchronized to the reference signal from the optical chopper. The chopper was placed in the pump beam, so the detected signal reflects only the magneto-optical signal changes induced by the pump pulses.

The sum signal provides information about the pump-induced reflectivity change of the sample $\Delta R(t)$ that can by expressed as [93]:

$$\frac{\Delta R(t)}{R_0} \approx \frac{\Delta I_p(t)+\Delta I_s(t)}{I_0^p+I_0^s}, \qquad \text{(A1)}$$

where R_0 is the static reflectivity of the sample, ΔI_p (ΔI_s) is the pump-induced change of the intensity in the *p*- (*s*-) polarized arm of the optical bridge with respect to intensities without the pump pulse I_0^p (I_0^s).

The difference signal is related to the pump-induced rotation of the polarization plane $\Delta\theta$ (or to the pump-induced ellipticity, if a quarter wave plate is placed in front of the half wave plate in the optical bridge) that can be expressed as [93]:

$$\Delta\theta(t) = \frac{\Delta I_p(t) - \Delta I_s(t)}{2(I_0^p + I_0^s)}. \qquad \text{(A2)}$$

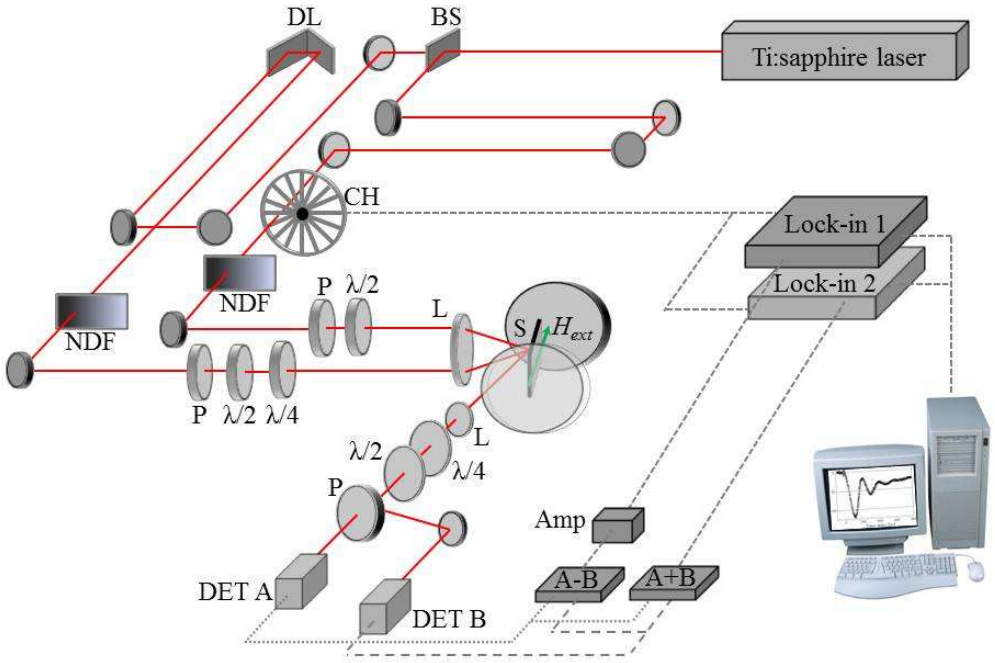

Fig. A9.1: Experimental setup for the time-resolved MO measurements. The meaning of the abbreviations is the following: BS – beam splitter, DL – delay line, CH – chopper, NDF – neutral density filter, P – polarizer, λ/2 – half wave plate, λ/4 – quarter wave plate, L – lens, S – sample, H_{ext} – external magnetic field generated between the poles of the electromagnet, DET A (B) – silicon detectors, A-B, A+B – differential preamplifiers, AMP – preamplifier, lock-in 1 (2) – phase sensitive lock-in amplifier.